UNIVERSITÀ
DEGLI STUDI
DI PADOVA

Sede Amministrativa: Università degli Studi di Padova

Dipartimento di
SCIENZE CHIMICHE

CORSO DI DOTTORATO DI RICERCA IN: SCIENZE MOLECOLARI
CURRICOLO: CHIMICO
CICLO XXX

FUNDAMENTAL PROPERTIES OF THE MOLECULAR Au CLUSTERS

Coordinatore: Ch.mo Prof. Leonard Prins
Supervisore: Ch.mo Prof. Flavio Maran

Dottorando: Mikhail Agrachev

Table of Contents

Abstract

Monolayer-protected gold clusters (MPCs) are a very interesting and fascinating class of compounds, from the points of view of both the fundamental science and their possible applications. They are composed of a gold core, with a diameter smaller than a few nanometers, and are surrounded by a protecting organo-thiolate monolayer, bonded by covalent Au-S bonds. Due to their dimensions, these systems exhibit properties in between those of molecules and nanoparticles, therefore displaying unique physical and chemical behaviors. In this Thesis, some properties of the most stable and well-known molecular MPC are addressed and studied. The investigation focuses on fundamental features, including solid-state properties, optical behavior, reactivity and especially their magnetic properties. The investigation of the latter constitutes the major part of this work. Particular attention is dedicated to the effect of ligands on these phenomena. The main tool of our investigation was electron paramagnetic resonance (EPR) spectroscopy, which was used to study these MPCs both in solution and in the solid state. The topics addressed are to understand the magnetic interactions between gold core and the capping ligands in solutions phase and ferromagnetic and antiferromagnetic interactions between clusters in the solid state. Another magnetic resonance technique, nuclear magnetic resonance, was used for the study of the ligand exchange kinetics. The data obtained from a number of experimental techniques and computational calculations were used in conjunction with these two main tools.

Riassunto

I cluster d'oro protetti da monostrato (MPC) sono una classe di composti molto interessante e affascinante, sia dal punto di vista della ricerca di base, che delle loro possibili applicazioni. Sono composti da un *core* di oro, con un diametro inferiore a pochi nanometri e sono circondati da un monostrato organo-tiolato, legato con legami covalenti Au-S. A causa delle loro dimensioni, questi sistemi esibiscono proprietà a metà strada fra quelle di molecole e nanoparticelle, mostrando quindi comportamenti fisici e chimici unici. In questa Tesi sono state studiate alcune proprietà del MPC più stabile e conosciuto. L'indagine è stata focalizzata su caratteristiche fondamentali, che includono proprietà di stato solido, comportamento ottico, reattività e in particolar modo le loro proprietà magnetiche. L'indagine di queste ultime costituisce la parte più rilevante di questo lavoro. Un'attenzione particolare è stata dedicata all'effetto dei leganti su questi fenomeni. Lo strumento principale della nostra indagine è stata la spettroscopia di risonanza paramagnetica elettronica (EPR), la quale è stata utilizzata per studiare questi sistemi sia in soluzione che allo stato solido. Gli argomenti trattati sono la comprensione delle interazioni magnetiche fra il *core* d'oro e i leganti in soluzione e delle interazioni ferromagnetiche e antiferromagnetiche fra cluster allo stato solido. Un'altra tecnica di risonanza magnetica, la risonanza magnetica nucleare, è stata usata per lo studio della cinetica di scambio di leganti. I dati ottenuti da alcune altre tecniche sperimentali e calcoli computazionali sono stati utilizzati in combinazione con questi due strumenti principali.

Chapter 1.
Introduction

1.1 Monolayer protected gold nanoclusters

1.1.1 From gold nanoparticles to nanoclusters

Research on colloidal gold nanoparticles dates back to the work by Michael Faraday in the middle of the nineteenth century. Its origins can be traced back to the publication of a paper focused on the study of a gold colloid prepared by a reaction between $HAuCl_4$(aq) and phosphorus (in ether).[1] Since then, these systems received an ever-growing attention by the scientific community. In the following years, many efforts have been done both from the synthetic point of view, in particular to achieve a precise dimensional control of the colloidal particles, and the theoretical point of view, to understand their outstanding stability, peculiar optical properties, structure etc.. In 1908, Gustav Mie published an important work,[2] in which he successfully modeled the optical behavior of colloidal gold nanoparticles by solving the Maxwell equations. Among the synthetic achievements, the method for hydrosol formation by reduction of $HAuCl_4$ with formaldehyde by Zsigmondy must be cited.[3] In the following decades a large amount of new physical-chemical properties and application of fine gold particles were discovered, such as, for instance, the huge enhancement of the Raman effect produced by colloidal gold nanoparticles,[4-7] which subsequently gave birth to the Surface Enhanced Raman Spectroscopy technique.[8] The most significant advances took place in the late 1990s. New synthetic routes and advanced analytical methods allowed achieving better control of the produced particles and a deeper understating of their structure and properties. Important applications were also developed, especially in the biomedical field, such as drug delivery, biosensors, tumor detection, photothermal agents and so on. [9-11]

The amount of research carried out over the years on these systems in the last two decades is enormous. Nevertheless, there is still a lot to be done from the point of view of synthetic control, analytical characterization and theoretical understanding. One of the major issues the researchers always had to deal with is the dimensional control of gold nanoparticles. Before the 1930s, the particles dimensions were commonly determined by methods such as ultramicroscopy,[3] X-ray diffraction (by means of the Scherrer method)[12] and ultracentrifugation (using the Stokes' law of sedimentation).[13] The latter two methods are still used today for some applications. However, with the invention of transmission electron microscopy (TEM) in the 1930s, these methods were largely substituted by this powerful

technique. [14-16] In addition to accurately measuring the particles dimensions, TEM microscopy also provides detailed information on their shape and, in many cases, crystalline structure.[17]

The ultimate goal was to obtain truly monodisperse nanoparticles, in which the dimensions are controlled at the atomic level and all the particles have exactly the same dimension, shape and structure. However, until recently, the researchers managed to obtain only more or less polydisperse systems, characterized by average dimensions, with a certain standard deviation always present. The issue was at least partially overcome in the 2000s, for ultrasmall gold nanoparticles, with dimensions ranging from a fraction of nanometer to about 2 nm.[18,19] Due to their tiny dimensions, atomically determined composition and often molecular behavior (this issue will be addressed below in detail), these systems are usually called gold nanoclusters to distinguish them from larger and poorly defined gold nanoparticles.[20] The term ”cluster” indicates the presence of metal-metal bonds and usually applies to objects smaller than the usual nanoparticles.

Because of their molecular, or “nearly molecular” characteristics, gold nanoclusters can be analyzed by typical “molecular” techniques. As a matter of fact, the dimensions and monodespersity of gold nanoclusters can be precisely evaluated by mass spectrometry, while their crystal structure can be accurately determined by single crystal X-ray diffractometry with additional information provided by Nuclear Magnetic Resonance (NMR) spectrometry. Electrochemistry and UV-visible spectrometry provide information on the energy levels of these systems.[21]

To be stable, the gold clusters must be protected by a molecular monolayer.[19,20] These clusters are thus called monolayer-protected clusters (MPCs). The most commonly used protecting ligands are the organothiolates, mainly because of the remarkable strength of the gold-sulfur bond.

Au MPCs are of paramount importance both from the point of view of applications and fundamental science. Concerning the latter, they could help increasing our understanding of the properties of gold nanoparticles in general, including the larger ones. In this field, some peculiar features are indeed still poorly understood and important questions remain unanswered. First, the exact role of the protecting monolayer is not completely clear. In particular, it is still not clearly established what exactly protects the nanoparticles surface, how the ligands are bonded to the Au core and, most importantly, what determines the stability of the monolayer-protected nanoparticles. Second, the structure and the properties of small nanoparticles diameters of <3 nm are not fully understood. In particular, a full

comprehension of the transition from the metallic behavior of larger nanoparticles to the molecular behavior peculiar of small clusters is still missing. An approach for describing the properties of the clusters-particles in the intermediate dimensional range is still to be found. Finally, many aspects of the shape-controlled self-assembly of the particles are still obscure: questions arise regarding the formation of anisotropic nanoparticles, on how the ligands bond to the metal core and whether this process is kinetically or thermodynamically driven.

As aforementioned, Au MPCs could potentially contribute to answering all these important questions.

The first atomically defined monolayer-protected cluster dates back to as far as 1969. It was a Au_{11} cluster protected with phosphine and thiocyanate ligands, specifically $Au_{11}(PPh_3)_7(SCN)_3$, prepared by Mason and his coworkers.[22] In the following decades many other gold clusters were found, such as $Au_{55}\{P(C_6H_5)_3\}_{12}Cl_6$, synthesized in 1981 by Schmid and his group.[23] An important step for the development of the field was the publication in 1983 by Nuzzo and Allara of a paper in which they observed the formation of a self-assembled monolayer on a gold surface.[24,25] Inspired by this work and the following studies on the same topic, Burst et al. developed in 1994 a method for the synthesis of thiolate-protected Au nanoparticles,[26] which became a real breakthrough for the field. It was now clear that the capping thiols are very efficient in stabilizing the small gold cores and preventing their aggregation. In the following years, the field of thiol-protected MPCs developed very quickly, with a huge amount of structures and properties being continuously discovered. [19-22]

Concerning the theoretical aspects, a turning point in the understanding of the properties of Au MPCs was the groundbreaking study by Häkkinen and his coworkers,[27] in which they showed that the electronic properties of many MPCs can be successfully described by the *superatom* concept. Using this model, not only they were able to rationalize the stability and some properties of several already isolated and experimentally characterized clusters, but they also managed to predict some stable structures, which were only later synthesized.

1.1.2 Superatom model

The superatom concept is based on the observation that the electronic properties of some metal clusters can be described, to a certain extent, using an approach similar to that commonly adopted for simple atoms. Before being applied to Au MPCs, this approach was successfully used to explain (and in many cases predict) the stability, natural abundance and

some chemical properties of both bare and coordinated gas-phase clusters,[28-30] most notably Al and Na clusters,[31] Ga-based metalloid clusters[32] and other simple systems.

The superatomic approach is based on the so-called *jellium electronic shell* model.[33] According to this model, in a metal cluster, the nuclei and the core electrons can be approximated as a uniform positively charged background, while the valence electrons are subject to the potential created by this overall charge and occupy a set of new electronic levels. In other words, within the superatom picture, the free electrons are considered to occupy a new set of orbitals, defined by the totality of cluster atoms, rather than by the individual atoms.[34,35] The superatomic orbitals can be obtained by solving the Schrödinger equation for a spherically symmetric square-well potential. Obviously, this approach holds only for highly symmetric clusters, such as many Au MPCs ($Au_{144}(SR)_{60}$, $Au_{102}(SR)_{44}$, $Au_{25}(SR)_{18}$ etc.). These superatomic orbitals strongly resemble the atomic orbitals in terms of symmetry, and so can be labeled according to their angular momentum, analogously to what is commonly done for the atomic orbitals. They are usually written in capital letters to distinguish them from the atomic orbitals. It turns out that the order of occupation of the superatomic orbitals does not follow the same order of atoms, dictated by the aufbau rule. The superatomic order of occupation is: $1S^2\ 1P^6\ 1D^{10}\ 2S^2\ 1F^{14}\ 2P^6\ 1G^{18}\ 2D^{10}\ 3S^2\ 1H^{22}$…, as opposed to the well-known atomic order: $1s^2\ 2s^2\ 2p^6\ 3s^2\ 3p^6\ 4s^2\ 3d^{10}$… The numbers (1, 2, 3…) indicate the number of radial nodes +1.

The validity of this approach was fully demonstrated by DFT calculations, in which the projection of the angular momentum was performed to attribute the orbital label.[32] (Figure 1.1)

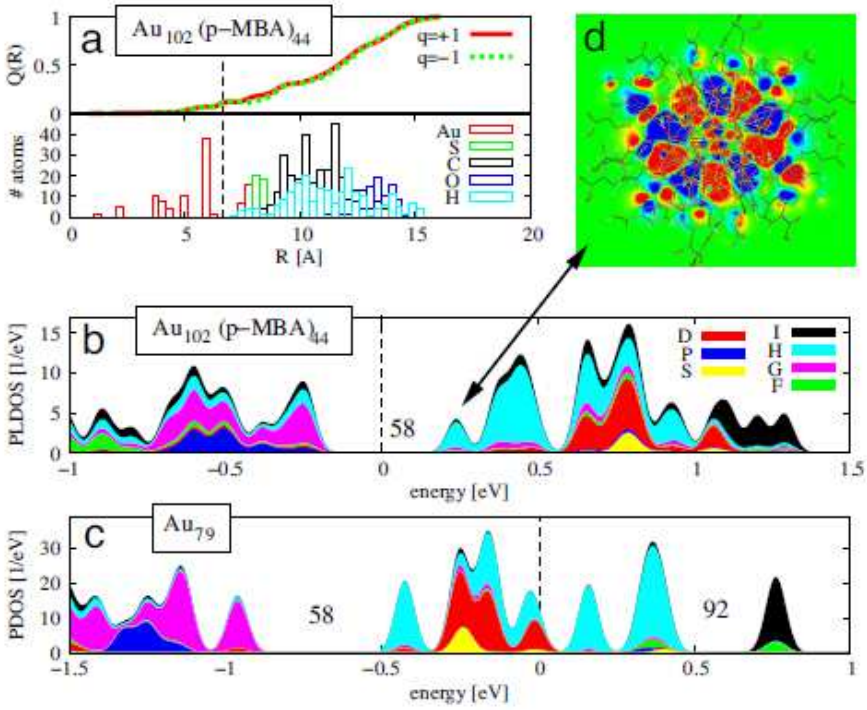

Figure 1.1. Electronic structure analysis of the Au_{102}(*p*-MBA)$_{44}$ cluster. (*a*) The radial dependence of the integrated induced charge upon removing (red curve) and adding (green curve) one electron to the neutral Au_{102}(*p*-MBA)$_{44}$ cluster (*Upper*), and the radial distribution of atoms (*Lower*) (*b*) The angular-momentum-projected local electron density of states for the Au_{79} core in Au_{102}(*p*-MBA)$_{44}$. (*c*) The angular-momentum-projected electron density of states for the bare Au_{79} without the Au-thiolate layer. (*d*) A cut-plane visualization of the LUMO state of the Au_{102}(*p*-MBA)$_{44}$ cluster. (From ref. 27).

As for the isolated atoms, some electronic configurations, in particular the closed-shell noble gas-like configurations, make the clusters particularly stable and chemically inert. Obviously, for bare, uncoordinated clusters the electron configuration of the cluster is fully determined by the number and the atomic electron configuration of the metal atoms. Instead, for ligand-protected clusters, in analogy with metal complexes, valence electrons can be transferred to the ligands and therefore closed-shell configuration can be restored even if the number of electrons in the corresponding bare cluster exceeds the noble gas configuration.

The electron count rule for superatom clusters is:

$$n = Nv_A - M - z \tag{1-1}$$

where n is the number of electrons, N is the number of metal atoms, v_A is the atomic valence, M is the number of electron withdrawing ligands and z is the overall charge of the cluster. With these labels, the cluster can be indicated as $A_N(X_ML_S)^z$, where L are weak (not electron withdrawing) ligands, which have the role of merely protecting the cluster. It is assumed that one electron is transferred for each electron-withdrawing X ligand.

Particularly stable clusters are obtained for some definite numbers of electrons n, corresponding to closed-shell configurations:

$n = 2, 8, 18, 34, 58, 92, 138, ...$

which are often called *magic numbers*. This approach predicts the stability and explains some chemical and physical properties of some of the most studied Au MPCs, such as, $Au_{102}(SR)_{44}$, $Au_{39}(PR_3)_{14}X_6^-$ and $Au_{25}(SR)_{18}^-$.

It must be stressed that the *electronic shell closing* just described is the leading factor for the stabilization of smaller clusters, larger clusters are mainly stabilized by *geometric shell closing*. Geometric closing refers to concentric polyhedral shells surrounding the (often icosahedral) cluster core, which geometrically stabilize the cluster.[36] The reason why this effect usually prevails for larger clusters is to be found in the nucleation mechanism:[37] if the clusters are small enough, the metal atoms are quite mobile, so they can rearrange to form the electronically more stable structures. When the clusters become too large, their motion is hindered, the core remains “frozen” and additional atoms superimpose over it in definite positions, forming the shell structure. A “borderline” cluster, for which both electronic and geometric shell closure seem to be important is $Au_{144}(SR)_{60}$.[27,36] It was actually observed that larger nanoclusters and nanoparticles tend to adopt the face centered cubic (FCC) structure typical of bulk gold. Eventually, translational symmetry inside the cluster starts to appear, marking a behavior even nearer to bulk gold. In this case, the term nanocrystals, instead of nanoparticles or nanoclusters, should be more appropriate. $Au_{144}(SR)_{60}$ and smaller clusters, instead, usually show highly symmetric, non-FCC structures, with no translational symmetry. Incidentally, the $Au_{144}(SR)_{60}$ cluster also seems to be a borderline between molecular and solid-state metallic behavior, as will be shown in the following paragraph.

1.1.3 Optical and electrochemical properties of Au MPCs

The investigation of MPCs is particularly fascinating because they cover the dimensional range which signs the transition from the solid-state to the molecular behavior, which means going from a world described by classical physics to a quantum mechanical world. Since the dimensions are atomically controlled, we can accurately follow this transition by different methods.

First, it can be clearly detected by the optical absorption of the MPCs. Large Au nanoparticles in the range of 4-20 nm notably show a single surface plasmon resonance (SPR) band at 520 nm, due to the collective electron charge oscillations, typical of metallic nanoparticles.[21] This

behavior can be explained by means of classical electrodynamics, solving the Maxwell equations. As the dimensions of the nanoparticles decrease, a gradual blue shift of the SPR peak is observed and the particles cannot be described as metallic anymore.[38,39,40] The SPR peak becomes damped and completely disappears below about 2 nm. For smaller nanoparticles, the spectrum changes completely, usually exhibiting several definite peaks, typical of the specific clusters. From the point of view of the electronic energy structure, this change corresponds to a transition from a continuum of energy levels, associated to solid-state metallic nanoparticles, to discrete energy levels, typical of molecular compounds. Using the available crystal structures, for many MPCs the DFT calculations allowed assigning the observed bands to specific transitions between the calculated energy levels.[39,41-44] In the following paragraph the energy levels and the interpretation of the UV-visible spectrum of $Au_{25}(SR)_{18}$ will be described, as this work is primarily focused on this cluster.

The transition from metallic to molecular behavior can also be successfully monitored by electrochemical methods. As with the optical spectra, also in this case the gradual passage from a continuum of electrochemical driving forces to a few discrete voltammetric peaks can be clearly observed. Between these two extremes, the energy levels become progressively more distant and thus also the energy difference between the lowest unoccupied molecular orbital (LUMO) and the highest occupied molecular orbital (HOMO) gradually increases, giving rise to more separated peaks.

One can define three voltammetric regimes, defined by Murray as bulk-continuum, quantized double layer charging and molecule-like.[45]

Concerning the first regime, typical of particles larger than 3-4 nm, the energy levels are near enough, compared to the thermal energy quantum, to be considered a continuum of states. In this case, performing an electrochemical experiment, a featureless, gradually rising amperometric current is observed.[46] Instead, particles prepared by the Brust-Shiffrin method, which allows a higher size control and the possibility of obtaining smaller MPCs, show a behavior typical of the second regime, labeled as quantized double layer charging. It consists in a series of regularly spaced voltammetric peaks, such as those exhibited by $Au_{144}(SR)_{60}$ (Figure 1.2). Here we see again that $Au_{144}(SR)_{60}$ can be considered as a borderline cluster, signing the transition from a continuum of states to discrete energy levels.

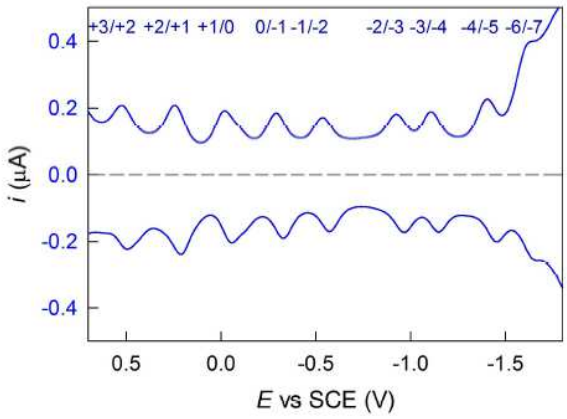

Figure 1.2. Typical differential pulse voltammetry behavior of 0.13 mM Au144(SC2H4Ph)60 in DCM/0.1 M TBAH. Glassy carbon electrode, 25 ℃.

For smaller MPCs, typically characterized by gold cores with diameters <1.6 nm, quantum confinement effects become even more pronounced and we enter in the third, molecule-like regime.[47,48,49] For these systems, electrochemical experiments show a very well-defined energy gap, associated with a molecular behavior. We will see this feature more in detail when we will deal with the specific properties of $Au_{25}(SR)_{18}$ in the following paragraph. Figure 1.3 shows the measured electrochemical gaps as a function of the number of Au atoms in the core of the clusters, nicely illustrating the trend and the transition between the three regimes we just discussed.

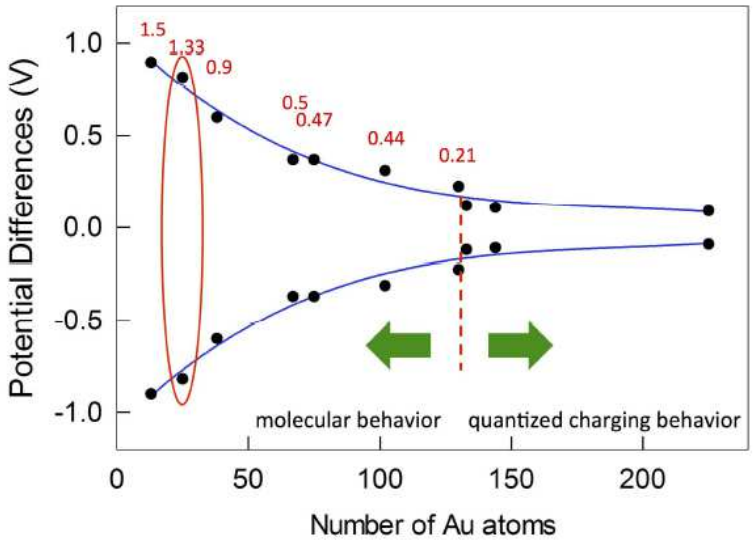

Figure 1.3. Electrochemical and optical gaps as function of the number of Au atoms. The blue curves have the only meaning of highlighting the trend.

1.1.4 Applications of Au MPCs.

The importance of Au MPCs for fundamental research was already stressed and will be further addressed in the following chapters, when we will deal with specific topics. Here, the importance of these systems for applications will be explained.

For the catalytic applications, bulk gold never gave any relevant results, because of its widely known inertness. However, in 1987 Haruta and his coworkers observed that supported Au nanoparticles are highly efficient catalyzers for carbon monoxide oxidation.[47] Subsequently many other catalytic applications of gold nanoparticles were found for several chemical reactions,[51-55] with higher efficiency for smaller particles (<5 nm).[56] One factor which can potentially reduce the catalytic efficiency of gold nanoparticles and MPCs is the presence of the protecting monolayer which doesn't allow the reactants to easily reach the active gold core. The ligands can be removed by calcination (supported on suitable substrates), but this may lead to unwanted aggregation of the particles. In any case, $Au_{25}(SR)_{18}$, can still successfully catalyze many solution reactions even with the protecting layer of ligands, such as CO_2 reduction[57] and CO oxidation,[58] oxidation of sulfides to sulfoxides[59] hydrogenation of α,β-unsaturated ketones and aldehydes,[60] or reduction of 4-nitrophenol.[61,62]. $Au_{25}(SR)_{18}$, is also promising in electrochemically induced homogenous redox catalysis, as shown by the Maran group[63,64] and others.[65-67]

The importance of gold nanoparticles in the biomedical field was already mentioned. This research branch was quite successful and a few applications are already in use in the biomedical practice. Surprisingly, compared to the huge amount of investigation on larger Au nanoparticles, the studies focusing on molecular Au MPCs are relatively limited. Nevertheless, there are some important reasons why these systems can be considered as highly promising for biomedical applications.[68-73] First, because of their very low toxicity, they are completely biocompatible and can be safely used in the medical practice. Second, since their dimensions can be accurately controlled at the atomic level, they could enter inside specific zones in the cell in a very selective way and therefore they can be potentially used in medical treatments (e.g. drug delivery) and diagnostics. Other characteristics, which make them interesting for the biomedical applications are: high luminescence, atomic precision, site-specific functionality and high permeability.

MPCs are also very promising for ultrahigh-resolution optical imaging, since they exhibit strong nonlinear optical processes, such as two-photon absorption and two-photon fluorescence.[76-82] They have several advantages compared to the more commonly used

organic materials, i.e. their stability and non-toxicity. Also their ability to bind to DNA, shown by some researchers,[72,83-85] can be potentially used for this aim. Other advantages are ultrasmall size,[72,87-89] color tunability,[87-89] NIR luminescence, [90-91] long lifetime[92] etc..

Zheng and his group showed possible applications of gold MPCs as fluorescent nanoprobes for cancer detection, Kidney functional imaging and chemical sensing.[92-98] Ackerson and his group extensively investigated the absorption, biodistribution, metabolism, excretion and the pharmacokinetic properties of $Au_{25}(SR)_{18}$ and $Au_{102}(SR)_{44}$ clusters in a murine model system, with some very promising results.[99] Additional important work on photoluminescent nanoclusters was performed by Xie and Zhang.[100]

The penetration of MPCs inside the cells was also quite extensively studied.[101] It was shown that it does not lead to the cell death, but to higher cellular metabolism and proliferation. Xie and his coworkers recently showed that MPCs can be potentially used as radiosensitizers for cancer radiotherapy, without damaging healthy tissues.[102]

Other applications of gold MPCs were also suggested: chemical sensors, [103,104] light-emitting devices (LEDs) [105] and others. The applications which are of major interest for this work will be presented in the following chapters, dedicated to the specific topics.

1.2. Structure and properties of $Au_{25}(SR)_{18}$ MPC

1.2.1. Structure of $Au_{25}(SR)_{18}$

$Au_{25}(SR)_{18}$ is one of the most stable and well characterized Au MPCs. It is small enough to display a molecular behavior, such as a definite HOMO-LUMO transition.[45,106] This cluster is well characterized from the crystallographic, optical and electrochemical point of view. Nevertheless, some aspects are still not clear, especially those related to its solid-state properties.

The structure of $Au_{25}(SR)_{18}$ was determined in 2009 by XRD: the Au core of the cluster is formed by a Au_{13} centered icosahedron surrounded by six –(SR)-Au-(SR)-Au-(SR)- staple units with the 12 Au atoms stellated on the 12 faces of the core (Fig. 1.3).[107,108] Thus two groups of ligands can be distinguished: the 12 "inner" ligands, in which the sulfur is bonded to one stellated Au atom and one core Au atom and the 6 "outer" ligands, in which the sulfur is bonded to two stellated Au atoms (Figure 1.4)

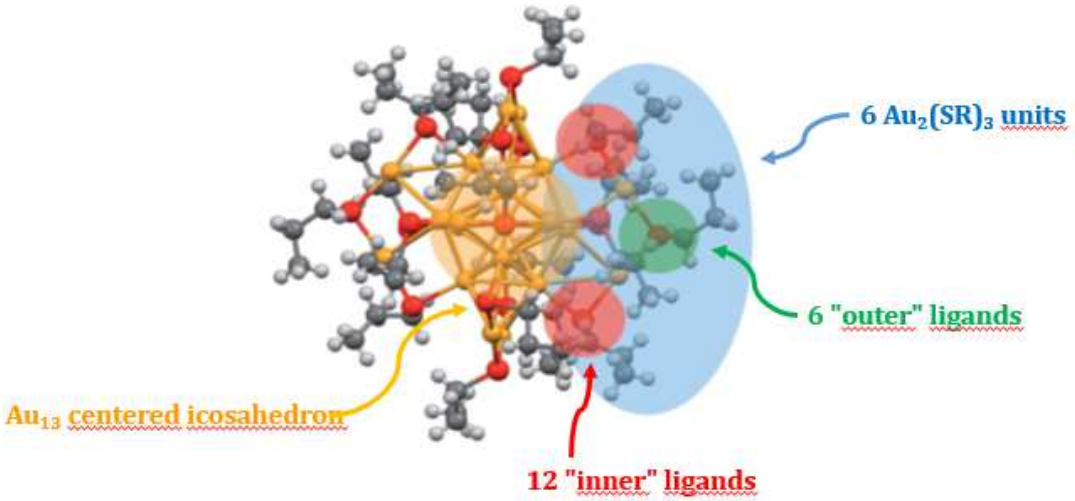

Figure 1.4. Structure of $Au_{25}(SR)_{18}$. core Au atoms (dark yellow), S atoms (red), C atoms (dark grey), C atoms (light grey), The metal core, staples, outer and inner units are evidenced in dark yellow, blue, green and red respectively.

Some fundamental properties of $Au_{25}(SR)_{18}$ will be briefly outlined in the following paragraphs. Many of these concepts, in particular those closely related to the experimental results of this Thesis, will be treated in more detail in the following chapters.

1.2.2. Electronic structure and optical absorption spectrum of $Au_{25}(SR)_{18}$

The optical spectrum of $Au_{25}(SR)_{18}$ (figure 1.5 B) shows several characteristic absorption peaks, which are a clear indication of the fact that we are dealing with a molecular compound. Accordingly, the UV-vis spectrum does not exhibit the usual SPR band at 510 nm, typical of larger metallic Au nanoparticles. The spectrum was extensively studied in great detail and all the spectral peaks were assigned to specific transitions between the calculated energy levels (figure 1.5).

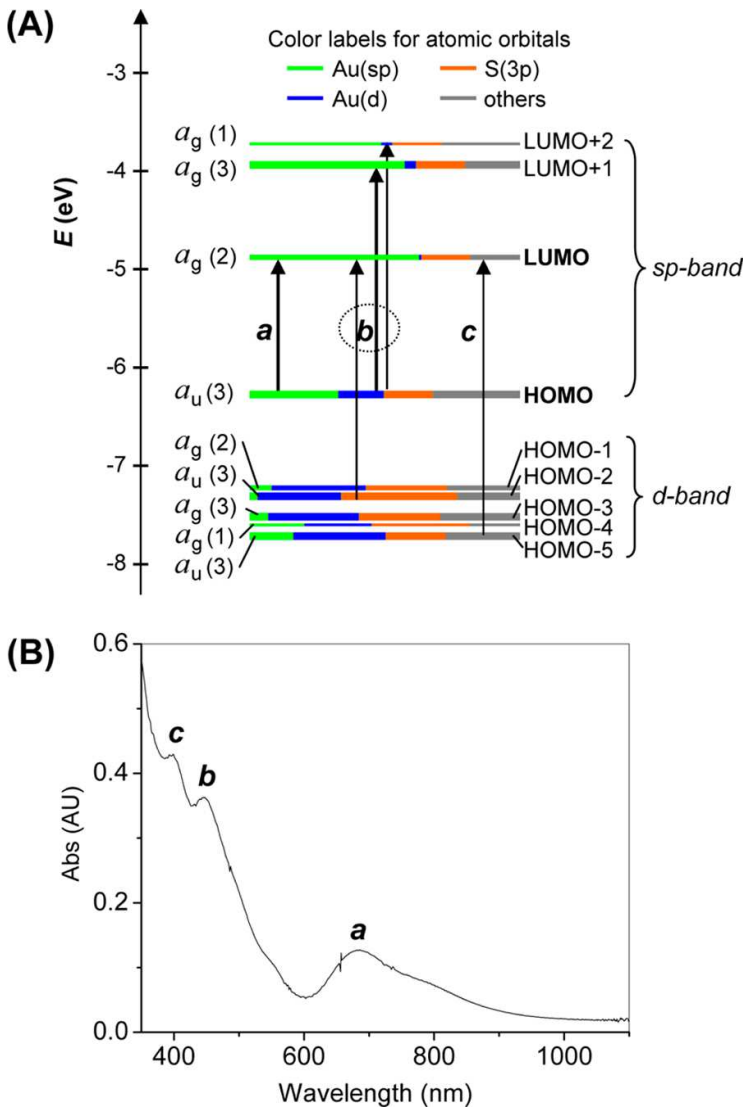

Figure 1.5. (A) Kohn-Sham orbital energy level diagram for a model compound $Au_{25}(SH)_{18}^-$.. Each KS orbital is drawn to indicate the relative contributions of the atomic orbitals of Au (6sp) in green, Au (5d) in blue, S (3p) in yellow, and others in gray. The left column of the KS orbitals shows the orbital symmetry and degeneracy (in parenthesis); the right column shows the HOMO and LUMO sets. (B) (from ref. 39)

On the basis of the highly symmetric structure of the $Au_{25}(SR)_{18}$ clusters one could expect that it can be successfully described by the superatomic model, described previously. The cluster can be seen as an octahedral complex with the icosahedral Au_{13} core (which can be approximated as having a spherical symmetry), complexed by six covalently bond $Au_2(SR)_3$ staples. DFT calculations based on the experimentally determined crystal structure of the cluster were performed to verify this assumption.[39,109] According to equation (1-1), if we assume that the superatomic approximation holds, the electron shell closure is obtained for the negatively charged cluster $Au_{25}(SR)_{18}^-$, with an electron count giving n=8. For this reason,

the first calculations were performed on this anionic compound, since one could expect it to be the nearest to an ideal superatom.

As a matter of fact, the DFT calculations, performed for the first time by Aikens[39,110] show that the superatomic approach successfully explains the electronic structure of the frontier and a few higher and lower energy orbitals. In particular, the HOMO is approximately triply degenerate, corresponding, in the framework of the superatomic approximation, to a set of P orbitals. According to the calculations, these orbitals are essentially due to s orbitals of the Au atoms and are mainly delocalized over the Au_{13} core. The LUMO and LUMO+1 consist respectively in a doubly and triply degenerate set of orbitals, corresponding, in the superatomic approach, to the five D orbitals, split in a t_{2g} and a e_g –like subsets by an approximately octahedral ligand field created by the six $Au_2(SR)_3$ staples. These orbitals are also essentially composed by atomic Au(s) orbitals (Figure 1.5 a).

About 1 eV below the LUMO, a series of closely spaced orbitals is located, extending for nearly 2 eV, constituting the so-called ligand band. Actually, this band arises from the ligand shell atomic orbitals, specifically Au(5d) and S(3p) of the $Au_2(SR)_3$ staples.

At still lower energies, another set of closely spaced orbitals lies, namely the d band, mainly due to Au(d) orbitals of the Au atoms constituting the Au_{13} core.

The calculated UV-vis absorption spectrum perfectly reproduces the experimental one. On its basis, all the peaks can be attributed to definite transitions. The strong peak at 1.63 eV is due to the HOMO – LUMO (P – D) transition. The peak at 2.60 eV instead arises from the HOMO – LUMO+1 transition (which is also P – D, according to the superatomic interpretation, since the D orbitals are split by the ligand field). The weak absorption peak at 2.48 eV and the strong peak at 2.97 eV originate from the transition between the ligand band and the superatomic D orbitals.

The validity of the superatomic interpretation was further demonstrated in the study by Hakkinen and his coworkers.[109] The character of the molecular orbitals in terms of their angular momentum was determined by projecting them onto spherical harmonics placed at the center of the cluster, revealing a P-character for the HOMO and a D-character for the LUMO, thus confirming again the superatomic assumption.

Although, as we just saw, the superatomic approach explains fairly well the electronic structure and optical behavior of $Au_{25}(SR)_{18}$ cluster, some deviations from this ideal model were also pointed out. One feature, which was experimentally observed in the UV-vis spectrum, is the splitting of the strong peak corresponding to the HOMO-LUMO transition.

This splitting manifests as a shoulder at room temperature and is particularly evident at lower temperatures.

Several theoretical explanations of this observation were suggested. The DFT calculations performed by Aikens pointed out that, increasing the ligands length, the conformation of the ligands changes and the ligand field distorts quite significantly from the octahedral symmetry.[110] In the analyzed cases, this leads to a S6 symmetry, in which the P orbitals split in two subsets: two doubly degenerate orbitals at lower energy and, 0.12-0.13 eV higher, a single non-degenerate orbital. A splitting of the two sets of the D orbitals was also predicted: they would split in three sets, two doubly degenerate and a non-degenerate orbital, split by 0.54 and 0.17 eV respectively.

Maran and his coworkers also investigated the origin of the splitting of the superatomic P orbitals both experimentally and theoretically, in particular its dependence on the charge of the cluster and its effect on magnetism.[111] Indeed, the splitting of the P orbitals have dramatic effects on the cluster magnetism and on its EPR spectra. These aspects will be discussed further in more detail, since they are of paramount importance for this Thesis. Here we just briefly report some concepts necessary for the understating of the problem. From the electron count performed on the negatively charged cluster it turned out that it is a closed-shell superatom, in which the P orbitals are full, being filled with 6 electrons. According to this model, the neutral cluster is expected to have 5 electrons, with one electron unpaired. Therefore, it is expected to be paramagnetic and consequently EPR-active. Actually, experimentally it gives a very reproducible EPR signal, which will be extensively studied in detail in this Thesis. Using the same approach, one could expect also the positively charged cluster to be paramagnetic: with its 4 electrons situated in the three P orbitals it would have two unpaired electrons, leading to a triplet spin state, which should be visible by EPR. Although such a signal was apparently observed by one group,[113] a later study by Maran and his coworkers clearly demonstrated that $Au_{25}(SR)_{18}^{+}$ is EPR-silent and therefore diamagnetic, with no unpaired electrons.[111,112] This was explained both experimentally, using electrochemistry, and theoretically, using the DFT calculations, as a direct effect of the P orbitals splitting (Figure 1.6). The results showed that the small P splitting $Au_{25}(SR)_{18}^{-}$, already observed by Aikens, becomes more pronounced in $Au_{25}(SR)_{18}^{+}$: the residual double degeneracy is lost and the energy of one of the two degenerate orbitals increases by 0.12 eV. The splitting further increases considerably in $Au_{25}(SR)_{18}^{+}$, with the high-energy non-degenerate orbital shifting at a still higher energy by nearly 0.2 eV. In this situation, the triplet

state is not thermally accessible: the high energy orbital remains empty and the four electrons completely fill the two low energy orbitals, with no unpaired electrons left. This clearly explains the absence of EPR signals for $Au_{25}(SR)_{18}^{+}$.

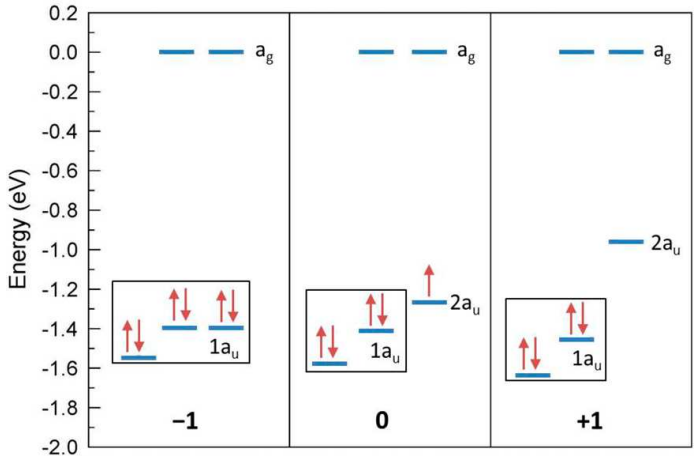

Figure 1.6. Orbital diagrams in $Au_{25}(SCH_3)_{18}^{z}$ (z = −1, 0, +1).

Ackerson and his coworkers came to a similar conclusion, based on their XRD studies, combined with SQUID magnetometry and DFT calculations, on $Au_{25}(SR)_{18}$ cluster in the same oxidation states (-1, 0, +1).[114] They observed a similar increase of the HOMO-LUMO gap and attributed it to the cluster core distortion, interpreted, in analogy with a common phenomenon observed for metal complexes, as a Jahn-Teller effect, which minimizes the system energy by the removing the degeneracy.

The changes of the electronic structure with the charge can be nicely monitored experimentally with UV-vis spectroscopy, as shown in figure 1.7. The oxidation method adopted is based on a procedure developed by the Maran group and consists in the use of the very reactive bis(pentafluorobenzoyl) peroxide as oxidant. It acts as a very efficient electron acceptor by a two-electron concerted dissociative electron-transfer process. Zhu's and Jin's groups also performed the oxidation by means of the oxoammonium cation.[115]

As already mentioned, the UV-vis spectrum of $Au_{25}(SR)_{18}$ is very reproducible. It does not depend on the ligands used and on solvent, which means that these factors don't substantially affect the electronic structure of the cluster. For these reasons, UV-vis is very efficient in assessing the purity, monodispersity, charge state and concentration of the cluster and therefore it can be routinely used for this aim.

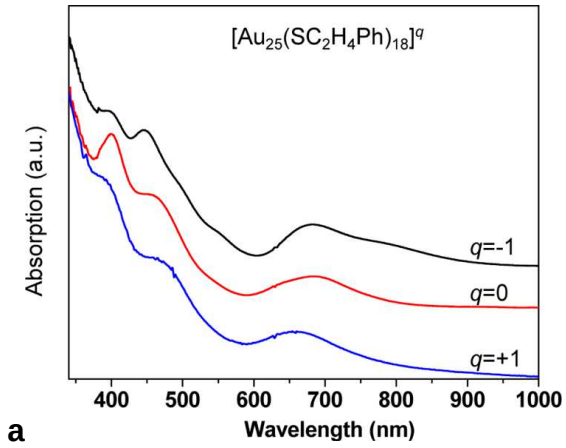

a

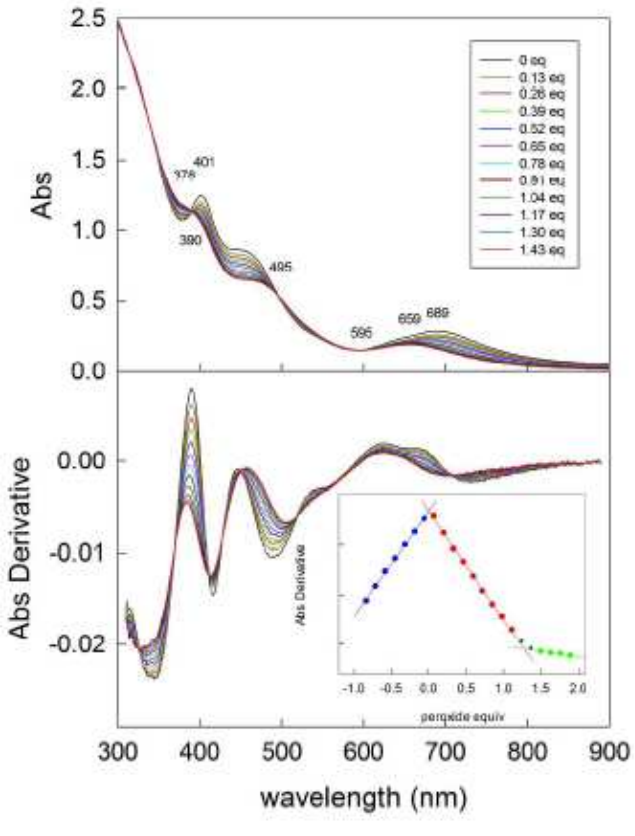

b

Fig. 1.7. a) UV−vis spectra of phenylethanethiolate-protected $Au_{25}(SR)_{18}$ clusters of different charge states. b) Effect of the addition of bis(pentafluorobenzoyl) peroxide on the UV-vis absorbance spectrum (upper graph) and corresponding derivative (lower graph) of 0.023 mM $Au_{25}(SR)_{18}^{0}$ in DCM.

The P splitting issue was also addressed by De-en Jiang and his collaborators.[116] While all the calculations reported above were performed at the scalar relativistic level, they performed full relativistic calculations on the negatively charged cluster in order to study the possible effects of the spin-orbit interaction (see Chapter 4). They discovered that a HOMO splitting of

about 0.2, in good accordance with the experimental value, appears with the full-relativistic approach, which they did not detect with the scalar relativistic calculations. Therefore, they entirely attributed the degeneracy removal of the P orbitals to the spin-orbit interaction by drawing an analogy with the spin-orbit driven splitting of atomic p orbitals.

The P orbitals splitting and the evaluation of the different phenomena contributing to it were studied in this Thesis and will be treated in depth in Chapter 4.

1.2.3. NMR spectrum of $Au_{25}(SR)_{18}$

The NMR spectra of $Au_{25}(SR)_{18}$ with different R ligands and different charges (-1, 0, +1) were analyzed in detail by the Murray's[117] and Maran's groups.[111] The $Au_{25}(SC_2H_4Ph)_{18}$ was studied particularly in depth, also for different solvents and different temperatures. All the NMR signals were attributed by using one-dimensional ^1H and ^{13}C NMR, as well as two-dimensional techniques, such as COrrelation SpectroscopY (COSY), Total Correlation SpectroscopY (TOCSY), Heteronuclear Multiple Bond Correlation spectroscopy (HMBC) and Heteronuclear Multiple Quantum Correlation spectroscopy (HMQC). The analysis of the resonances was favored by the fact that the oxidant bis(pentafluorobenzoyl) does not introduce additional protons. Both the spectra of the neutral and negatively charged cluster (in the form of $[n\text{-}Oct_4N^+][Au_{25}(SC_2H_4Ph)_{18}^-]$) clearly showed the presence of two non-equivalent groups of protons, corresponding to inner and outer ligands, which were already known from the crystallographic structure, as described previously. The NMR spectra of the neutral $Au_{25}(SC_2H_4Ph)_{18}^0$ is characterized by remarkable differences between the corresponding chemical shifts, with respect to the negatively charged cluster. This effect is due to the paramagnetic nature of the neutral cluster and is called the hyperfine shift. It arises from the interaction between the nuclear spins of the protons and the electron spin of the unpaired electron present in the neutral cluster. This interaction and its effects on the NMR, as well as on the EPR spectra, will be explained in greater detail in the following chapter. As we saw previously, DFT showed that the singly occupied molecular orbital (SOMO) is mainly localized in the gold core, therefore one could expect the NMR signals corresponding to protons nearer to the core to be more shifted (Fig. 1.8). As a matter of fact, the effect is more pronounced for the α protons (the nearest to the S atoms) of the inner ligands, which shift to lower fields by about 25 ppm. In addition, the temperature dependence of the NMR signals of the paramagnetic clusters is heavily affected by the hyperfine coupling: a dramatic line sharpening, accompanied by a remarkable low-field shift with increasing temperature are

observed (Fig. 1.8). This effect is due to the contribution of the hyperfine coupling to the spin relaxation processes, as will be explained in the following chapter. DFT calculations were in accordance with the experimental NMR chemical shifts and gave a first indication of the spin density delocalization to the ligand monolayer.

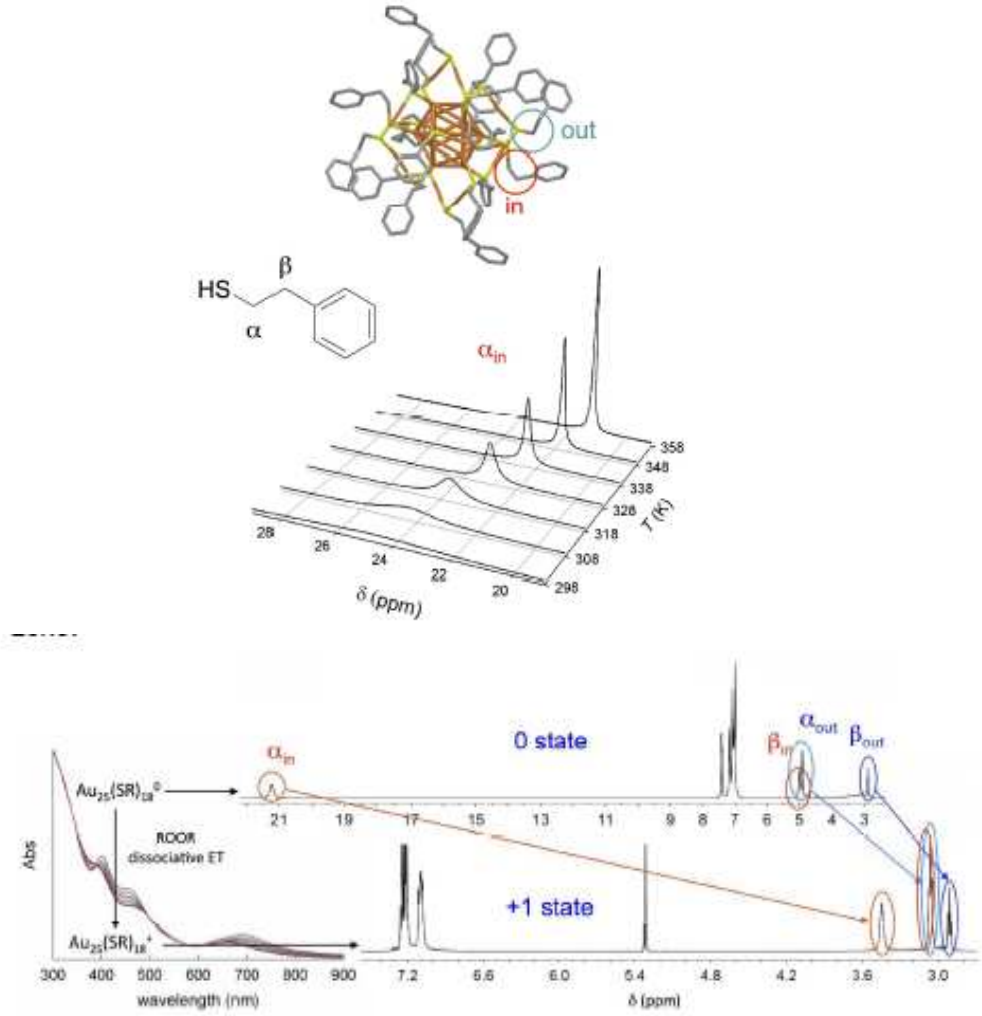

Figure 1.8. 1H NMR spectrum of monodisperse 3 mM Au25(SC2H4Ph)18 0 in toluened as a function of temperature. The spectra (ref. 79) only show the (· -CH2)in zone. 1H NMR spectrum of 3 mM Au25(SC2H4Ph)18 0 (upper graph, in toluened8, 358 K) and Au25(SC2H4Ph)18 + (lower graph, dichloromethane-d2, 298 K) obtained by quantitative oxidation of the former.

The spectrum of the cationic $Au_{25}(SC_2H_4Ph)_{18}^0$ cluster is very similar to the spectrum of the anionic one, pointing to the fact that this cluster is diamagnetic, in accordance with the previously mentioned EPR results.[112]

The same spectral analysis was performed on a series of clusters protected with alkyl chains of different length, specifically: $Au_{25}(SC_2H_5)_{18}$, $Au_{25}(SC_3H_7)_{18}$, $Au_{25}(SC_4H_9)_{18}$ and longer chains.[118,120]

1.2.4. Magnetic behavior of $Au_{25}(SR)_{18}$

The charge-dependent magnetic behavior of the $Au_{25}(SC_2H_5)_{18}$ clusters in solution was assessed by both NMR and EPR spectroscopies. It was shown that the only paramagnetic state is the neutral one, whereas the anionic and the cationic ones are diamagnetic.[111,112] The continuous wave (CW) EPR spectrum of $Au_{25}(SC_2H_4Ph)_{18}^0$ was published for the first time by Zhu and his collaborators.[119] The EPR spectrum appears below 100 K and consists in a very broad, highly anisotropic line (Fig. 1.9). The experimental spectrum was simulated, by using a rhombic, nearly axial g tensor (g_x=2.56, g_y=2.36, g_z=1.82). Such an anisotropic signal could seem strange for a highly symmetric system, as the MPC we are dealing with. Nevertheless, it is in agreement with the superatomic interpretation, according to which the SOMO is a set of P orbitals. Moreover, the calculated g values, were in accordance with the experimental values.

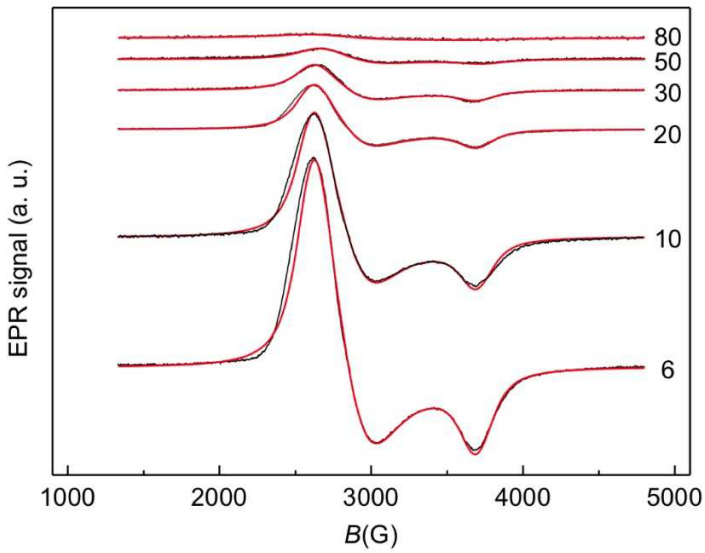

Figure 1.9. Typical spectrum of $Au_{25}(SR)_{18}^0$ (R=C_2H_4Ph in this case) in toluene at different temperatures (in K). Experiment (black) and simulations (red).

CW-EPR spectra of $Au_{25}(SR)_{18}^0$ with several other ligands were described.[120.121] and the observed signal turned out to be virtually the same in all the cases. This in agreement with

the previous conclusion, made on the basis of NMR measurements and DFT calculations, that the SOMO is mostly localized in the Au core (see previous paragraphs). It is thus clear that CW-EPR provides very useful information on the structural, magnetic and electronic properties of the cluster. However, it must be stressed that this technique does not allow to resolve the hyperfine couplings, which carry the information on spin density delocalization, indicating how much the SOMO is spread on the ligand monolayer. The solution of this issue, which involves the use of an advanced pulsed EPR technique, i.e. pulsed Electron-Nuclei Double Resonance (ENDOR), will be addressed further in Chapter 3. The possibility of using ENDOR for measuring the hyperfine couplings in $Au_{25}(SR)_{18}^0$ were shown by Maran and his group in an investigation on the smallest $Au_{25}(SR)_{18}$ cluster ever synthesized, i.e. $Au_{25}(SC_2H_5)_{18}$.[121] This work was focused on the core structure, therefore the hyperfine couplings with the ^{197}Au nuclei (which have I=3/2) were measured. As will be explained in Chapter 2, nuclei with I>3/2 give rise to quadrupolar interactions, therefore signals due to these interactions were observed on the ENDOR spectrum, in addition to those due to the hyperfine couplings (Fig. 1.10). The spectra were successfully simulated with DFT-calculated parameters, dynamically averaged to reproduce the experimental conditions, and were in accordance with the XRD crystal structure. The analysis led to some important results. In particular, the fact that the ENDOR spectra could be satisfactorily simulated only with the parameters pertaining to EtSH, and not, for example MetSH ligands, demonstrates the remarkable influence of the ligands on the SOMO, which was never detected by other techniques. Moreover, it was shown that the 12 Au atoms of the icosahedron are not equivalent, but split into two non-equivalent groups of 8 and 4 atoms. This was attributed to small distortions from the perfect icosahedral symmetry, which is probably also dictated by the ligands.

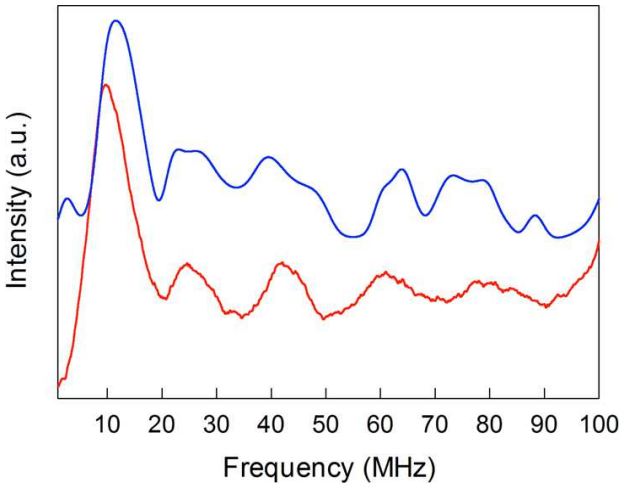

Figure 1.10. Davies ENDOR spectrum of a frozen 0.5 mM solution of Au25(SEt)18 0 in toluene at 5.5 K (red line). The blue line shows the corresponding simulation based on the hyperfine and quadrupole components obtained by DFT.

Previously to this Thesis, the solid-state magnetic behavior of $Au_{25}(SR)_{18}^0$ was very poorly investigated. Previous SQUID and EPR measurements on $Au_{25}(SC_2H_4Ph)_{18}^0$ powders led to the conclusion that this cluster is still paramagnetic in the solid-state and no significant interactions take place.[114,121] This will be discussed in more detail in Chapter 4, dealing with our findings on the magnetic properties of $Au_{25}(SC_2H_4Ph)_{18}^0$. Regarding other ligands, an important discovery was made by the Maran group in 2014, concerning the $Au_{25}(SC_4H_9)_{18}^0$ cluster.[122] They found out, by a combined XRD-EPR-DFT study, that, while in solution these MPCs are magnetically non-interacting, and therefore paramagnetic, in the solid state they form linear 1D chains, in which the single clusters are antiferromagnetically coupled (figure 1.11). We observed this phenomenon also for ligands of different length, and these new findings will be described in Chapter 5.

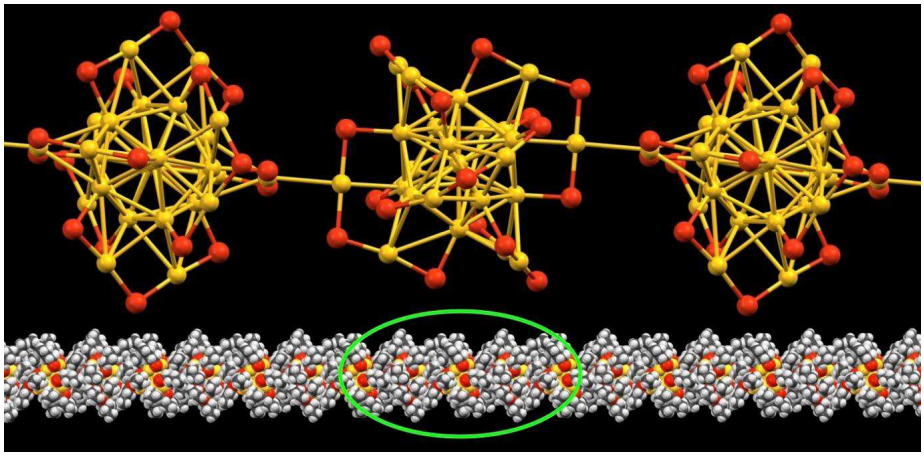

Figure 1.11. Formation of the antiferromagnetic $[Au_{25}(SBu)_{18}]_n$ polymer.

1.3 Aims and outline of the Thesis.

In this Thesis, some fundamental properties of the $Au_{25}(SR)_{18}$ MPCs are investigated, with a particular focus on magnetic properties. We wanted to rationalize some unique characteristics, arising from interactions between clusters, such as their solid-state properties and reactivity, starting from the properties of the isolated MPCs. One of the main goals of this work was to understand the role of the ligands monolayer in affecting the properties of the isolated clusters and, especially, for the intercluster interactions. The following chapters focus on a series of aspects.

Chapter one. In the first chapter, the general features of gold MPCs were introduced, with particular attention to $Au_{25}(SR)_{18}$, on which this Thesis is focused. First, the history of studies on nanodimensional gold particles was briefly outlined. Then, the structural features of MPCs were reported, in connection with some of their fundamental properties, which were subsequently reviewed. Finally, some applications of these systems suggested so far were described, with a wide literature review.

Chapter two. Some fundamental magnetic properties of matter are briefly introduced, which constitute the basis for the understanding of the following chapters. In the second part of this chapter, the basic description of the EPR technique and instrumentation is described, as well as a few hints on NMR applied to paramagnetic compounds. All these concepts are largely used for the interpretation and theoretical analysis of the experimental data throughout this Thesis.

Chapter three. In this chapter, isolated clusters in solution are investigated. Specifically, the protecting ligand monolater is investigated by means of an advanced EPR technique. So far, a clear understanding of the fine interactions between the cluster core and the capping monolayer has remained elusive, despite the importance of the latter in interfacing the former to the surrounding medium. In this chapter, a very sensitive methodology is described, that enables comprehensive assessment of these interactions. Pulse electron nuclear double resonance (ENDOR) was employed to study the interaction of the unpaired electron with the protons of the alkanethiolate ligands in four structurally related paramagnetic $Au_{25}(SR)_{18}^{0}$ clusters (R = ethyl, propyl, butyl, 2-methylpropyl). Whereas some of these structures were known, we present the first structural description of the highly symmetric $Au_{25}(SPr)_{18}^{0}$ cluster.

Through knowledge of the structural data, the ENDOR signals could be successfully related to the types of ligand and the distance of the relevant protons from the central gold core. We found that orbital distribution affects atoms that can be as far as 6 Å from the icosahedral core. Simulations of the spectra provided the values of the hyperfine coupling constants. The resulting information was compared with that provided by ^{1}H NMR spectroscopy, and DFT calculations provided useful hints to understanding differences between the ENDOR and NMR results. It is shown that the unpaired electron can be used as a very precise probe of the main structural features of the interface between the metal core and the capping ligands.

Chapter four. Whereas the previous chapter focused on the magnetic properties of the isolated clusters in solution, in this chapter the solid state magnetic behavior of the same cluster, protected with a different ligand ($Au_{25}(SCH_2CH_2Ph)_{18}^0$) was studied. Several research groups have observed magnetism in monolayer-protected gold-cluster samples, but the results were often contradictory and thus a clear understanding of this phenomenon is still missing. Previous magnetometry studies performed on this cluster only detected paramagnetism. We used samples representing a range of crystallographic orders and studied their magnetic behaviors by electron paramagnetic resonance (EPR). As a film, $Au_{25}(SCH_2CH_2Ph)_{18}^0$ displays paramagnetic behavior but, at low temperature, ferromagnetic interactions are detectable. One or few single crystals undergo physical reorientation with the applied field and display ferromagnetism, as detected through hysteresis experiments. A large collection of microcrystals is magnetic even at room temperature and shows distinct paramagnetic, superparamagnetic, and ferromagnetic behaviors. Simulation of the EPR spectra shows that both spin-orbit coupling and crystal distortion are important to determine the observed magnetic behaviors. DFT calculations carried out on single cluster and periodic models predict values of spin-orbit coupling and crystal-splitting effects in agreement with the EPR derived quantities. Magnetism in gold nanoclusters is thus demonstrated to be the outcome of a very delicate balance of factors. To obtain reproducible results, the samples must be (i) controlled for composition and thus be monodisperse with atomic precision, (ii) of known charge state, and (iii) well defined also in terms of crystallinity and experimental conditions.

Chapter five. This chapter also focuses on the magnetic properties of $Au_{25}(SR)_{18}$ clusters in the solid state, as the previous chapter. Here we studied alkanethiolates of different length, some of which were studied in the third Chapter, focusing on the isolated clusters in solution.

It was reported a few years ago by the Maran group that in the crystalline form, when a butylthiol ligand is used, the paramagnetic clusters arrange in such a way to form linear one-dimensional chains, in which the neighboring clusters interact antiferromagnetically. Here we show that the same phenomenon is observed also for longer chains (pentylthiol, heptylthiol), although the strength of the intercluster magnetic exchange interaction and the corresponding blocking temperatures are different. For shorter ligands, instead, such as ethylthiol and propylthiol, linear chains are not formed and the clusters interact ferromagnetically. Other phenomena related to the formation of polymeric cluster chains were studied: spin relaxation and photoinduced electron transfer, both between clusters and between a cluster and TiO_2 nanoparticles.

Chapter six. In this chapter, additional properties of the protecting ligand monolayer are explored, in particular those concerning ligand exchange reactions. The thiolated ligands protecting molecular gold nanoclusters split into families determined by the way sulfur binds to Au atoms belonging to the core and/or an outer shell. In this study we used $Au_{25}(SR)_{18}$ clusters and selected thiols to assess the reactivity of the inner and outer ligand families. Our goal was to focus on intrinsic reactivities and thus care was taken to control steric and electronic effects associated with the thiols. Moreover, to make the reactive sites of the monolayer as accessible as possible, we used a newly prepared $Au_{25}(SR)_{18}$ cluster (SR = propanethiolate), whose single-crystal X-ray crystallographic structure is described in Chapter 3. The study was carried out by ^1H NMR spectroscopy and mass spectrometry. Through full NMR knowledge of clusters and ligand types, a careful kinetic analysis of the exchange reactions could be carried out for three thiols. The results highlight a remarkable site- and thiol-dependent exchange, but also the importance of taking into account statistical factors.

1.4. References

1. Faraday, M. The Bakerian Lecture: Experimental Relations of Gold (and Other Metals) to Light. *Philos. Trans. R. Soc. London* **1857**, *147*, 145− 181.
2. Mie, G. Beiträge zur Optik Trüber Medien, *Speziell Kolloidaler Metallösungen. Ann. Phys.* **1908**, *330*, 377−445.
3. Zsigmondy, R. Colloids and the Ultramicroscope, a Manual of Colloid Chemistry and Ultramicroscopy; John Wiley & Sons: New York, 1909.
4. Fleischmann, M.; Hendra, P. J.; McQuillan, A. J. Raman Spectra of Pyridine Adsorbed at a Silver Electrode. *Chem. Phys. Lett.* **1974**, *26*, 163−166.
5. Albrecht, M. G.; Creighton, J. A. Anomalously Intense Raman Spectra of Pyridine at a Silver Electrode. *J. Am. Chem. Soc.* **1977**, *99*, 5215−5217.
6. Jeanmaire, D. L.; Van Duyne, R. P. Surface Raman Spectroelectrochemistry. *J. Electroanal. Chem. Interfacial Electrochem*. **1977**, *84*, 1−20.
7. Creighton, J. A.; Blatchford, C. G.; Albrecht, M. G. Plasma Resonance Enhancement of Raman Scattering by Pyridine Adsorbed on Silver or Gold Sol Particles of Size Comparable to the Excitation Wavelength. *J. Chem. Soc., Faraday Trans. 2* **1979**, *75*, 790−798.
8. Freeman, R. G.; Grabar, K. C.; Allison, K. J.; Bright, R. M.; Davis, J. A.; Guthrie, A. P.; Hommer, M. B.; Jackson, M. A.; Smith, P. C.; Walter, D. G.; Natan, M. J. Self-Assembled Metal Colloid Monolayers: An Approach to SERS *Substrates. Science* **1995**, *267*, 1629−1632.
9. Arvizo, R.; Bhattacharya, R.; Mukherjee, P. Gold nanoparticles: Opportunities and Challenges in Nanomedicine. *Expert Opin Drug Deliv.* **2010**, *7(6)*, 753–763.
10. Dykman; L.A., Khlebtsov, N.G. Gold Nanoparticles in Biology and Medicine: Recent Advances and Prospects *Acta Naturae*. **2011,** *3(2),* 34–55.
11. Cai, W; Gao, T.; Hong, H.; Sun, J. Applications of gold nanoparticles in cancer nanotechnology *Nanotechnol Sci Appl.* **2008**, *1*, 17–32.
12. Scherrer, P. Nachr. Ges. Wiss. Goettingen, *Math.-Phys. Kl.* **1918**, *1918*, 98−100.
13. Svedberg, T.; Pedersen, K. O. The Ultracentrifuge; Elsevier: Amsterdam, 1940.
14. Turkevich, J.; Hillier, J. Electron Microscopy of Colloidal Systems. *Anal. Chem.* **1949**, *21*, 475−485.

15. Turkevich, J.; Stevenson, P. C.; Hillier, J. A Study of the Nucleation and Growth Processes in the Synthesis of Colloidal Gold. *Discuss. Faraday Soc.* **1951**, *11*, 55−75.

16. Turkevich, *J. Colloidal Gold. Part I. Gold Bull*. **1985**, *18*, 86−91.

17. Jin, R.; Cao, Y.; Mirkin, C. A.; Kelly, K. L.; Schatz, G. C.; Zheng, J. G. Photoinduced Conversion of Silver Nanospheres to Nanoprisms. *Science* **2001**, *294*, 1901−1903.

18. Qian, H.; Zhu, M.; Wu, Z.; Jin, R. Quantum Sized Gold Nanoclusters with Atomic Precision. Acc. Chem. Res. **2012**, *45*, 1470−1479.

19. Jin, R. Atomically Precise Metal Nanoclusters: Stable Sizes and Optical Properties. Nanoscale **2015**, *7*, 1549−1565.

20. Jin, J.; Zhu, Y.; Qian, Y. Quantum-Sized Gold Nanoclusters: Bridging the Gap between Organo metallics and Nanocrystals *Chem. Eur. J.* **2011**, *17*, 6584 – 6593.

21. Jin, R.; Zeng, C.; Zhou, M.; Chen, Y. Atomically Precise Colloidal Metal Nanoclusters and Nanoparticles: Fundamentals and Opportunities *Chem. Rev.* **2016**, *116*, 10346−10413.

22. M. McPartlin, R. Mason, L. Malatesta, Novel Cluster Complexes of Gold(0)-Gold(I) *J. Chem. Soc. D* **1969**, 334.

23. Schmid, G.; Pfeil, R.; Boese, R.; Bandermann, F.; Meyer, S.; Calis, G. M. H.; Vandervelden, W. A. [Au55{P(C6H5)3}12Cl6] – A Gold Cluster of Unusual Size. *Chem. Ber*. **1981**,*114*, 3634-3642.

24. Nuzzo, R. G.; Allara, D. L. Adsorption of Bifunctional Organic Disulfides on Gold Surfaces. *J. Am. Chem. Soc.*, **1983**, *105*, 4481-4483.

25. Love, J. C.; Estroff, L. A.; Kriebel, J. K.; Nuzzo, R. G.; Whitesides, G. M. Self-Assembled Monolayers of Thiolates on Metals as a Form of Nanotechnology. *Chem. Rev.* **2005**, *105*, 1103-1169.

26. Brust, M.; Walker, M.; Bethell, D.; Schiffrin, D. J.; Whyman, R. Synthesis of thiol-derivatised Gold Nanoparticles in a Two-Phase Liquid-Liquid System. *J. Chem. Soc., Chem. Commun.* **1994**, 801-802.

27. Walter, M.; Akola, J.; Lopez-Acevedo, O.; Jadzinsky, Pablo D.; Calero, G.; Ackerson, C.J.; Whetten, R.L.; Grönbeck, H.; Häkkinen H. A unified view of ligand-protected gold clusters as superatom complexes. *Proc. Natl. Acad. Sci. U.S.A.* **2008**, *105(27)*, 9157-9162.

28. de Heer W.A. The physics of simple metal clusters: Experimental aspects and simple models. *Rev. Mod. Phys.* **1993**, 65, 611–675.

29. Reveles, J.U.; Khanna S.N.; Roach, P.J.; Castleman, A.W. *Proc. Natl. Acad. Sci. USA* **2006**, 103, 18405–18410.

30. Bergeron, D.E.; Roach, P.J.; Castleman, A.W., Jr; Jones, N.O.; Khanna, S.N. Al cluster superatoms as halogens in polyhalides and as alkaline earths in iodide salts. *Science* **2005**, 307, 231–235.

31. Kiran, B; Jena, P.; Li, X.; Grubisic, A.; Stokes, S. T.; Ganteför, G. F.; Bowen, K. H.; Burgert, R.; Schnöckel, H. Magic rule for Al_nH_m magic clusters. *Phys. Rev. Lett.,* **2007**, *98*, 256802(1–4).

32. Hartig, J.; Stösser, A.; Hauser P., Schnöckel H. A metalloid $[Ga_{23}\{N(SiMe_3)_2\}_{11}]$ cluster: The jellium model put to test. *Angew Chemie Int Ed*, **2007**, *46*, 1658–1662.

33. Knight W.D.; Clemenger K.; de Heer W.A.; Saunders W.A.; Chou M.Y.; Cohen M.L. *Phys Rev Lett.* **1984**, *52*, 2141–2143.

34. Reveles, J. U.; Khanna, S. N.; Roach, P. J.; Castleman, Jr., A. W. Multiple valence superatoms *Proc Natl Acad Sci U S A*. **2006**, *103 (49)*, 18405–18410.

35. Muñoz-Castro A., Arratia-Perez R. Spin-orbit effects on a gold-based superatom: a relativistic Jellium model *Phys Chem Chem Phys.* **2012**, *14 (4)*, 1408-1411.

36. Tofanelli, M. A.; Ackerson C. J. Superatom Electron Configuration Predicts Thermal Stability of $Au_{25}(SR)_{18}$ Nanoclusters *J. Am. Chem. Soc.*, **2012**, *134 (41)*, 16937–16940.

37. Martin, T. P.; Bergmann, T.; Goehlich, H.; Lange, T. Shell structure of clusters *J. Phys. Chem.*, **1991**, *95 (17)*, 6421–6429.

38. Alvarez, M. M.; Khoury, J. T.; Schaaff, T. G.; Shafigullin, M. N.; Vezmar, I.; Whetten, R. L. Optical Absorption Spectra of NanocrystalGold Molecules. *J. Phys. Chem. B* **1997**, *101*, 3706−3712.

39. Zhu, M.; Aikens, C. M.; Hollander, F. J.; Schatz, G. C.; Jin, R. Correlating the Crystal Structure of a Thiol-Protected Au25 Cluster and Optical Properties. *J. Am. Chem. Soc.* **2008**, *130*, 5883−5885.

40. Yau, S. H.; Varnavski, O.; Goodson, T., III. An Ultrafast Look at Au Nanoclusters. *Acc. Chem. Res.* **2013**, *46*, 1506−1516.

41. Knoppe, S.; Malola, S.; Lehtovaara, L.; Bürgi, T.; Häkkinen, H. Electronic Structure and Optical Properties of the Thiolate-Protected $Au_{28}(SMe)_{20}$ Cluster. *J. Phys. Chem. A* **2013**, *117*, 10526−10533.

42. Zeng, C.; Liu, C.; Pei, Y.; Jin, R. Thiol Ligand-Induced Transformation of $Au_{38}(SC_2H_4Ph)_{24}$ to $Au_{36}(SPh\text{-}t\text{-}Bu)_{24}$. *ACS Nano* **2013**, *7*, 6138−6145.

43. Watzky, M. A.; Finney, E. E.; Finke, R. G. Transition-Metal Nanocluster Size vs Formation Time and the Catalytically Effective Nucleus Number: A Mechanism-Based Treatment. *J. Am. Chem. Soc.* **2008**, *130*, 11959−11969.

44. Wiseman, M. R.; Marsh, P. A.; Bishop, P. T.; Brisdon, B. J.; Mahon, M. F. Homoleptic Gold Thiolate Catenanes. *J. Am. Chem. Soc.* **2000**, *122*, 12598−12599.

45. Murray, R. W. Nanoelectrochemistry: Metal Nanoparticles, Nanoelectrodes, and Nanopores. *Chem. Rev.* **2008**, *108*, 2688-2720.

46. Ung, T.; Giersign, M.; Dunstan, D.; Mulvaney, P. Spectroelectrochemistry of Colloidal Silver. *Langmuir* **1997**, *13*, 1773-1782.

47. Hicks, J. F.; Miles, D. T.; Murray, R. W. Electrochemical and NMR Characterization of Octanethiol-Protected Au Nanoparticles. *J. Electroanal. Chem.* **2003**, *554*, 127-132.

48. Quinn, B. M.; Liljeroth, P.; Ruiz, V.; Laaksonen, T.; Kontturi, K. Electrochemical Resolution of 15 Oxidation States for Monolayer Protected Gold Nanoparticles. *J. Am. Chem. Soc.* **2003**, *125*, 6644-6645.

49. Holm, A. H.; Ceccato, M.; Donkers, R. L.; Fabris, L.; Pace, G.; Maran, F. Effect of Peptide Ligand Dipole Moments on the Redox Potentials of Au38 and Au140 Nanoparticles. *Langmuir* **2006**, *22*, 10584**-**10589.

50. Haruta, M.; Kobayashi, T.; Sano, H.; Yamada, N. Novel Gold Catalysis for the Oxidation of Carbon Monoxide. *Chem. Lett*. **1987**, *16*, 405-408.

51. Li, G.; Jin, R. Atomically Precise Gold Nanoclusters as New Model Catalysts. *Acc. Chem. Res.* **2013**, *46*, 1749-1758.

52. Stephen, A.; Hashmi, K.; Hutchings, G. J. Gold Catalysis. *Angew. Chem., Int. Ed.* **2006**, *45*, 7896-7936.

53. Stratakis, M.; Garcia, H. Catalysis by Supported Gold Nanoparticles beyond Aerobic Oxidative Processes. *Chem. Rev.* **2012**, *112*, 4469-4506.

54. Ma, G.; Binder, A.; Chi, M.; Liu, C. Jin, R.; Jiang, D.; Fan, J.; Dai, S. Stabilizing Gold Clusters by Heterostructured Transition-Metal Oxide– Mesoporous Silica Supports for Enhanced Catalytic Activities for CO Oxidation. *Chem. Commun*. **2012**, *48*, 11413-11415.

55. Della Pina, C. D.; Falletta, E.; Rossi, M. Update on Selective Oxidation using Gold. *Chem. Soc. Rev.* **2012**, *41*, 350-369.

56. Valden, M.; Lai, X.; Goodman, D. W. Onset of Catalytic Activity of Gold Clusters on Titania with the Appearance of Nonmetallic Properties. *Science* **1998**, *281*, 1647-1650.

57. Kauffman, D. R.; Alfonso, D.; Matranga, C.; Qian, H.; Jin, R. Experimental and Computational Investigation of Au25 Clusters and CO2: A Unique Interaction and Enhanced Electrocatalytic Activity. *J. Am. Chem. Soc.* **2012**, *134*, 10237- 10243.

58. Nie, X.; Qian, H.; Ge, Q.; Xu, H.; Jin, R. CO Oxidation Catalyzed by Oxide- Supported Au25(SR)18 Nanoclusters and Identification of Perimeter Sites as Active Centers. *ACS Nano* **2012**, *6*, 6014-6022.

59. Li, G.; Qian, H.; Jin, R. Gold Nanocluster-Catalyzed Selective Oxidation of Sulfide to Sulfoxides. *Nanoscale*, **2012**, *4*, 6714-6717.

60. Zhu, Y.; Qian, H.; Drake, B. A.; Jin, R. Atomically Precise Au25(SR)18 Nanoparticles as Catalysts for the Selective Hydrogenation of α,β-Unsaturated Ketones and Aldehydes. *Angew. Chem., Int. Ed.* **2010**, *49*, 1295-1298.

61. Yamamoto, H.; Yano, H.; Kouchi, H.; Obora, Y.; Arakawa, R.; Kawasaki, H. *N,N*-Dimethylformamide-stabilized Gold Nanoclusters as a Catalyst for the Reduction of 4-Nitrophenol. *Nanoscale* **2012**, *4*, 4148-4154.

62. Shivhare, A.; Ambrose, S. J.; Zhang, H.; Purves, R. W.; Scott, R. W. J. Stable and Recyclable Au25 Clusters for the Reduction of 4-Nitrophenol. *Chem. Commun.* **2013**, *49*, 276-278.

63. Antonello, S.; Holm, A. H.; Instuli, E.; Maran, F. Molecular Electron-Transfer Properties of Au38 Clusters. *J. Am. Chem. Soc.* **2007**, *129*, 9836.

64. Antonello, S.; Hesari, M.; Polo, F.; Maran, F. Electron Transfer Catalysis with Monolayer Protected Au25 Clusters. *Nanoscale* **2012**, *4*, 5333-5342.

65. Chen, W.; Chen, S. Oxygen Electroreduction Catalyzed by Gold Nanoclusters. *Angew. Chem. Int. Ed*. **2009**, *48*, 4386-4389.

66. Kumar, S. S.; Kwak, K.; Lee, D. Amperometric Sensing Based on Glutathione Protected Au25 Nanoparticles and Their pH Dependent Electrocatalytic Activity. *Electroanalysis* **2011**, *23*, 2116-2124.

67. Liu, Z.; Xu, Q.; Jin, S.; Wang, S.; Xu, G. Electron Transfer Reaction Between Au25 Nanocluster and Phenothiazine-Tetrachloro-*p*-Benzoquinone Complex *Int*. *J. Hydrog. Energy* **2013**, *38*, 16722-16726.

68. Saha, K.; Agasti, S. S.; Kim, C.; Li, X.; Rotello, V. M. Gold Nanoparticles in Chemical and Biological Sensing. *Chem. Rev.* **2012**, *112,* 2739-2779.

69. Howes, P. D.; Chandrawati, R.; Sevens, M. M. Colloidal Nanoparticles as Advanced Biological Sensors. *Science* **2014**, *346*, 1247390-1-10.

70. George, A.; Shibu, E.; Maliyekkal, S. M.; Bootharaju, M.; Pradeep, T. Luminescent, Freestanding Composite Films of Au15 for Specific Metal Ion Sensing. ACS Appl. Mater. Interfaces 2012, 4, 639− 644.

71. Yuan, X.; Luo, Z.; Yu, Y.; Yao, Q.; Xie, J. Luminescent Noble Metal Nanoclusters as an Emerging Optical Probe for Sensor Development. *Chem. - Asian J.* **2013**, *8*, 858−871.

72. Tan, X.; Jin, R. Ultrasmall Metal Nanoclusters for Bio-Related Applications. *WIREs Nanomed. Nanobiotechnol.* **2013**, *5*, 569−581.

73. Zheng, J.; Zhou, C.; Yu, M. X.; Liu, J. B. Different Sized Luminescent Gold Nanoparticles. *Nanoscale* **2012**, *4*, 4073−4083.

74. Polavarapu, L.; Manna, M.; Xu, Q.-H. Biocompatible Glutathione Capped Gold Clusters as One- and Two-Photon Excitation Fluorescence Contrast Agents for Live Cells Imaging. *Nanoscale* **2011**, *3*, 429−434.

75. Ramakrishna, G.; Varnavski, O.; Kim, J.; Lee, D.; Goodson, T. Quantum-Sized Gold Clusters as Efficient Two-Photon Absorbers. *J. Am. Chem. Soc.* **2008**, *130*, 5032−5033.

76. Philip, R.; Chantharasupawong, P.; Qian, H.; Jin, R.; Thomas, J. Evolution of Nonlinear Optical Properties: From Gold Atomic Clusters to Plasmonic Nanocrystals. *Nano Lett.* **2012**, *12*, 4661−4667.

77. Knoppe, S.; Vanbel, M.; van Cleuvenbergen, S.; Vanpraet, L.; Bürgi, T.; Verbiest, T. Nonlinear Optical Properties of Thiolate- Protected Gold Clusters. *J. Phys. Chem. C* **2015**, *119*, 6221−6226.

78. Knoppe, S.; Häkkinen, H.; Verbiest, T. Nonlinear Optical Properties of Thiolate-Protected Gold Clusters: A Theoretical Survey of the First Hyperpolarizabilities. *J. Phys. Chem. C* **2015**, *119*, 27676− 27682.

79. Russier-Antoine, I.; Bertorelle, F.; Vojkovic, M.; Rayane, D.; Salmon, E.; Jonin, C.; Dugourd, P.; Antoine, R.; Brevet, P.-F. Non- Linear Optical Properties of Gold Quantum Clusters. The Smaller the Better. *Nanoscale* **2014**, *6*, 13572−13578.

80. Day, P. N.; Pachter, R.; Nguyen, K. A.; Bigioni, T. P. Linear and Nonlinear Optical Response in Silver Nanoclusters: Insight from a Computational Investigation. *J. Phys. Chem. A* **2016**, *120*, 507−518.

81. Link, S.; El-Sayed, M. A.; Schaaff, T. G.; Whetten, R. L. Transition from Nanoparticle to Molecular Behavior: A Femtosecond Transient Absorption Study of a Size-Selected 28 Atom Gold Cluster. *Chem. Phys. Lett.* **2002**, *356*, 240−246.

82. Miller, S. A.; Fields-Zinna, C. A.; Murray, R. W.; Moran, A. M. Nonlinear Optical Signatures of Core and Ligand Electronic States in $Au_{24}pdl_{18}$. *J. Phys. Chem. Lett.* **2010**, *1*, 1383−1387.

83. Tan, X.; Jin, R. Ultrasmall Metal Nanoclusters for Bio-Related Applications. *WIREs Nanomed. Nanobiotechnol.* **2013**, *5*, 569−581.

84. Jia, X.; Li, J.; Han, L.; Ren, J.; Yang, X.; Wang, E. DNA-Hosted Copper Nanoclusters for Fluorescent Identification of Single Nucleotide Polymorphisms. *ACS Nano* **2012**, *6*, 3311−3317.

85. Song, W.; Wang, Y.; Liang, R.-P.; Zhang, L.; Qiu, J.-D. Label- Free Fluorescence Assay for Protein Kinase Based on Peptide Biomineralized Gold Nanoclusters as Signal Sensing Probe. *Biosens. Bioelectron*. **2015**, *64*, 234−240.

86. Huang, C.-C.; Yang, Z.; Lee, K.-H.; Chang, H.-T. Synthesis of Highly Fluorescent Gold Nanoparticles for Sensing Mercury(II). *Angew. Chem., Int. Ed.* **2007**, *46*, 6824−6828.

87. Guevel, X. L.; Tagit, O.; Rodriguez, C. E.; Trouillet, V.; Pernia Leal, M.; Hildebrandt, N. Ligand Effect on the Size, Valence State and Red/near Infrared Photoluminescence of Bidentate Thiol Gold Nanoclusters. *Nanoscale* **2014**, *6*, 8091−8099.

88. Kawasaki, H.; Hamaguchi, K.; Osaka, I.; Arakawa, R. Ph- Dependent Synthesis of Pepsin-Mediated Gold Nanoclusters with Blue Green and Red Fluorescent Emission. *Adv. Funct. Mater.* **2011**, *21*, 3508−3515.

89. Zheng, B.; Zheng, J.; Yu, T.; Sang, A.; Du, J.; Guo, Y.; Xiao, D.; Choi, M. M. F. Fast Microwave-Assisted Synthesis of Auag Bimetallic Nanoclusters with Strong Yellow Emission and Their Response to Mercury(II) Ions. *Sens. Actuators, B* **2015**, *221*, 386−392.

90. Tang, Z.; Ahuja, T.; Wang, S.; Wang, G. Near Infrared Luminescence of Gold Nanoclusters Affected by the Bonding of 1, 4-Dithiolate Durene and Monothiolate Phenylethanethiolate. *Nanoscale* **2012,** *4*, 4119− 4124.

91. Lopez, A.; Liu, J. DNA-Templated Fluorescent Gold Nanoclusters Reduced by Good's Buffer: From Blue-Emitting Seeds to Red and near Infrared Emitters. *Can. J. Chem.* **2015**, *93*, 615−620.

92. Wu, Z.; Jin, R. On the Ligand Role in the Fluorescence of Gold Nanoclusters. *Nano Lett.* **2010**, *10*, 2568− 2573.

93. Yu, M.; Zheng, J. Clearance Pathways and Tumor Targeting of Imaging Nanoparticles. *ACS Nano* **2015**, *9*, 6655− 6674.

94. Liu, J.; Yu, M.; Zhou, C.; Yang, S.; Ning, X.; Zheng, J. Passive Tumor Targeting of Renal-Clearable Luminescent Gold Nanoparticles: Long Tumor Retention and Fast Normal Tissue Clearance. *J. Am. Chem. Soc.* **2013**, *135*, 4978−4981.

95. (595) Yu, M.; Zheng, J. Clearance Pathways and Tumor Targeting of Imaging Nanoparticles. *ACS Nano* **2015**, *9*, 6655−6674.

96. Yu, M.; Zheng, J. Clearance Pathways and Tumor Targeting of Imaging Nanoparticles. *ACS Nano* **2015**, *9*, 6655−6674.

97. Yu, M.; Zhou, J.; Du, B.; Ning, X.; Authement, C.; Gandee, L. Kapur, P.; Hsieh, J.-T.; Zheng, J. Noninvasive Staging of Kidney Dysfunction Enabled by Renal-Clearable Luminescent Gold Nanoparticles. *Angew. Chem., Int. Ed.* **2016**, *55*, 2787−2791.

98. Sun, S.; Ning, X.; Zhang, G.; Wang, Y.-C.; Peng, C.; Zheng, J. Dimerization of Organic Dyes on Luminescent Gold Nanoparticles for Ratiometric Ph Sensing. *Angew. Chem., Int. Ed.* **2016**, *55*, 2421−2424.

99. Wong, O. A.; Hansen, R. J.; Ni, T. W.; Heinecke, C. L.; Compel, W. S.; Gustafson, D. L.; Ackerson, C. J. Structure-Activity Relationships for Biodistribution, Pharmacokinetics, and Excretion of Atomically Precise Nanoclusters in a Murine Model. *Nanoscale* **2013**, *5*, 10525− 10533

100. Goswami, N.; Zheng, K.; Xie, J. Bio-NCs The Marriage of Ultrasmall Metal Nanoclusters with Biomolecules. *Nanoscale* **2014**, *6*, 13328−13347.

101. Zhang, J.; Fu, Y.; Conroy, C. V.; Tang, Z.; Li, G.; Zhao, R. Y.; Wang, G. Fluorescence Intensity and Lifetime Cell Imaging with Luminescent Gold Nanoclusters. *J. Phys. Chem. C* **2012**, *116*, 26561−26569.

102. Tay, C.; Yu, Y.; Setyawati, M.; Xie, J.; Leong, D. Presentation Matters: Identity of Gold Nanocluster Capping Agent Governs Intracellular Uptake and Cell Metabolism. *Nano Res.* **2014**, *7*, 805− 815.

103. Yong, Y.; Li, C.; Li, X.; Li, T.; Cui, H.; Lv, S. Ag7Au6 Cluster as a Potential Gas Sensor for CO, HCN, and NO Detection. *J. Phys. Chem. C* **2015**, *119*, 7534−7540.

104. Guan, G.; Cai, Y.; Liu, S.; Yu, H.; Bai, S.; Cheng, Y.; Tang, T.; Bharathi, M. S.; Zhang, Y.-W.; Han, M.-Y. High-Level Incorporation of Silver in Gold Nanoclusters: Fluorescence Redshift Upon Interaction with Hydrogen Peroxide and Fluorescence Enhancement with Herbicide. *Chem. - Eur. J.* **2016**, *22*, 1675−1681.

105. Koh, T.-W.; Hiszpanski, A.; Sezen, M.; Naim, A.; Galfsky, T.; Trivedi, A.; Loo, Y.-L.; Menon, V.; Rand, B. Metal Nanocluster Light- Emitting Devices with Suppressed Parasitic Emission and Improved Efficiency: Exploring the Impact of Photophysical Properties. *Nanoscale* **2015**, *7*, 9140−9146.

106. Parker,J. F.; Fields-Zinna, C. A.; Murray, R. W. The Story of a Monodisperse Gold Nanoparticle: $Au_{25}L_{18}$ *Acc. Chem. Res.* **2010**, *43*,1289.

107. Heaven, M. W.; Dass, A.; White, P. S.; Holt, K. M.; Murray,R. W. Crystal Structure of the Gold Nanoparticle $[N(C_8H_{17})_4][Au_{25}(SCH_2CH_2Ph)_{18}]$. *J. Am. Chem. Soc.* **2008**, *130*, 3754.

108. Zhu, M.; Eckenhoff, W. T.; Pintauer, T.; Jin, R. Conversion of Anionic $[Au_{25}(SCH_2CH_2Ph)_{18}]^-$ Cluster to Charge Neutral Cluster *via* Air Oxidation. *J.Phys. Chem. C* **2008**, *112*, 14221.

109. Akola, J.; Walter, M.; Whetten, R.L.; Häkkinen, H.; Grönbeck, H. On the Structure of Thiolate-Protected Au25*. J. Am. Chem. Soc.* **2008**, *130*, 3756-3757.

110. Aikens, C.M. Electronic Structure of Ligand-Passivated Gold and Silver Nanoclusters. *J. Phys. Chem. Lett.* **2011**, *2*, 99–104.

111. Venzo, A.; Antonello, S.; Gascón, J. A.; Guryanov, I.; Leapman, R. D.; Perera, N. V.; Sousa, A.; Zamuner, M.; Zanella, A.; Maran, F. Effect of the Charge State (z = –1, 0, +1) on the Nuclear Magnetic Resonance of Monodisperse $Au_{25}[S(CH_2)_2Ph]_{18}^z$ Clusters. *Anal. Chem.* **2011**, *83*, 6355–6362.

112. Antonello, S.; Perera, N. V.; Ruzzi, M.; Gascón, J. A.; Maran, F. Interplay of Charge State, Lability, and Magnetism in the Molecule-like $Au_{25}(SR)_{18}$ Cluster. *J. Am. Chem. Soc.* **2013**, *135*, 15585-15594.

113. Arash Akbari-Sharbaf, A.; Hesari, M.; Workentin, M. S.; Fanchini, G. *J. Chem. Phys.* **2013**, *138*, 024305−1−024305−5.

114. Tofanelli, M. A.; Salorinne, K.; Ni, T. W.; Malola, S.; Newell, B.; Phillips, B.; Häkkinen, H.; Ackerson, C. J. Jahn-Teller effects in $Au_{25}(SR)_{18}$. *Chem. Sci.* **2016**, *7*, 1882-1890.

115. Liu, Z.; Zhu, M.; Meng, X.; Xu, G.; Jin, R. Electron Transfer between $[Au_{25}(SC_2H_4Ph)_{18}]^-$ TOA^+ and Oxoammonium Cations. *J. Phys. Chem. Lett.* **2011**, *2*, 2104-2109.

116. Jiang, D.-e; Kühn, M.; Tang, Q.; Weigend, F. Superatomic Orbitals under Spin–Orbit Coupling. *J. Phys. Chem. Lett.* **2014**, *5*, 3286−3289.

117. Parker, J. F.; Choi, J.-P.; Wang, W.; Murray, R. W. Electron Self-exchange Dynamics of the Nanoparticle Couple $[Au_{25}(SC_2Ph)_{18}]^{0/1-}$ by Nuclear Magnetic Resonance Line-Broadening. *J. Phys. Chem. C* **2008**, *112*, 13976**–**13981.

118. Antonello, S.; Arrigoni, G.; Dainese, T.; De Nardi, M.; Parisio, G.; Perotti, L.; René, A.; Venzo, A.; Maran, F. Electron Transfer through 3D Monolayers on Au_{25} Clusters. *ACS Nano* **2014**, *8*, 2788–2795.

119. Zhu, M.; Aikens, C. M.; Hendrich, M. P.; Gupta, R.; Qian, H.; Schatz, G. C.; Jin, R. Reversible Switching of Magnetism in Thiolate-Protected Au_{25} Superatoms. *J. Am. Chem. Soc.* **2009**, *131*, 2490-2492.

120. Dainese, T.; Antonello, S.; Gascón, J. A.; Pan, F.; Perera, N. V.; Ruzzi, M.; Venzo, A.; Zoleo, A.; Rissanen, K.; Maran, F. $Au_{25}(SEt)_{18}$, a nearly "Naked" Thiolate-Protected Au_{25} Cluster: Structural Analysis by ENDOR and Single Crystal X-ray Crystallography. *ACS Nano* **2014**, *8*, 3904-3912.

121. Krishna, K. S.; Tarakeshwar, P.; Mujica, V.; Kumar, C. S. S. R. Chemically induced magnetism in atomically precise gold clusters. *Small* **2014**, *10*, 907-911.

122. De Nardi, M.; Antonello, S.; Jiang, D.; Pan, F.; Rissanen, K.; Ruzzi, M.; Venzo, A.; Zoleo, A.; Maran, F. Gold Nanowired: A Linear $(Au_{25})_n$ Polymer from Au_{25} Molecular Clusters. *ACS Nano* **2014**, *8*, 8505-8512.

Chapter 2.
Magnetic properties of materials and experimental techniques.

The main technique used in the work reported in this Thesis, Electron Paramagnetic Resonance (EPR), is a spectroscopic technique based on the absorption of microwave radiation by paramagnetic species in an applied magnetic field. By EPR it is possible to study organic radicals, defects in solids, transition metal complexes, triplet states and other systems with unpaired electrons. It is also particularly useful for the investigation of magnetic properties of unusual materials, such as gold nanoclusters. Before treating the theory underlying the EPR spectroscopy, a brief introduction to the magnetic properties of materials will be given, focusing on the features which will be subsequently encountered for our systems. For a more in depth treatment the reader can refer to the more comprehensive textbooks, on which this chapter is based.[1-4]

2.1 Magnetic properties of materials

2.1.1 General magnetic properties

Experimentally, the magnetic behavior of a material can be determined by applying an external magnetic field on this material. Macroscopically, a classification can be done based on the relative magnetic permeability, which quantifies the response of the material to the external magnetic field.

$$B = \mu_r B_0$$
$$\mu_r = \frac{\mu}{\mu_0} \qquad (2\text{-}1)$$

where μ is the magnetic permeability in the medium, μ_0 is the magnetic permeability in the vacuum, B_0 is the applied magnetic field and B is the measured magnetic field. The magnetic permeability is directly linked to another parameter often used for the characterization of magnetic properties, i.e. the magnetic susceptibility χ:

$$\mu_r = 1 + \chi$$
$$B = (1 + \chi) B_0 \qquad (2\text{-}2)$$

A substance is defined as diamagnetic if the χ value is low and negative (-10^{-4} – 0) and therefore the measured magnetic field is slightly lower than the applied one.

A substance is defined as paramagnetic if the χ value is low and positive (10^{-3} – 10^{-1}) and therefore the measured magnetic field is slightly higher than the applied one.

A ferromagnetic substance instead is characterized by a very high χ values (about 10^7), therefore the measured magnetic field is significantly higher than the applied one.

An antiferromagnetic substance instead has a $\chi = 0$, therefore the measured magnetic field is approximately equal to the applied one.

Diamagnetism is a classical property which is characteristic of all the substances. The other magnetic properties can add to the basic diamagnetic behavior (paramagnetism, ferromagnetism, antiferromagnetism…) allowing one to classify the compound on the basis of its macroscopic properties.

Microscopically, the magnetic properties of a substance are determined by the molecular electronic structure and can be accurately described by quantum mechanics.

From the quantum mechanical point of view, paramagnetism is observed when the system under study has at least one unpaired electron. Each electron is characterized by a magnetic moment, directly related to the spin angular momentum **S** and the orbital angular momentum **L**.

$$\boldsymbol{\mu}_e = -\frac{e}{2m_e}(\mathbf{L} + g_e\mathbf{S}) \qquad (2\text{-}3)$$

where e and m_e are respectively the charge and the electronic mass and g_e is an adimensional constant equal to about 2.0023 (free electron g factor), **S** is the spin angular momentum and **L** is the orbital angular momentum.

Corresponding operators are associated to **L** and **S**: the first one acts only on the orbital part of the wavefunction, while the second one acts only on the spin part.

Concerning the spin part, in accordance with quantum mechanics, it is indicated as an eigenfunction |S,Ms>, where S is the total spin quantum number and is integer or half-integer, and Ms is the magnetic quantum number with Ms=S, S-1, S-2 … -S. The application of the spin angular momentum operators $\hat{S}^2$ e $\hat{S}_z$ on these eigenfunctions allows one to obtain the square of the spin angular momentum and the projection of the angular momentum on the quantization axis (conventionally the z axis is chosen).

$$\hat{S}^2 \left| S, M_S \right\rangle = S(S+1)\hbar \left| S, M_S \right\rangle$$
$$\hat{S}_z \left| S, M_S \right\rangle = M_S \hbar \left| S, M_S \right\rangle \quad (2\text{-}4)$$

An analogous treatment is valid also for nuclear spins and orbital angular momentum. For a system with both spin and orbital momentum, the following Hamiltonian can be defined:

$$\hat{H} = \beta g \mathbf{J} \cdot \mathbf{B} \quad (2\text{-}5)$$

Where J is the total angular momentum operator equal to S + L and the *g* factor (called Landè factor) is given by

$$g = \frac{3J(J+1) + S(S+1) - L(L+1)}{2J(J+1)} \quad (2\text{-}6)$$

Where J is the total angular momentum quantum number given by J = S+L, S+L-1, …|S-L|. For non degenerate orbitals the orbital momentum is quenched and only the spin magnetic moment remains.

2.1.2 Spin-orbit coupling

The treatment reported above holds only if the spin and angular momenta don't interact strongly. If the interaction is appreciable (in particular stronger then the interaction between the single moments), the spin-orbit (SO) coupling term must be introduced:

$$\hat{H}_{SO} = \lambda \mathbf{S} \cdot \mathbf{L} \quad (2\text{-}7)$$

where λ is the SO coupling constant. When the spin-orbit term is put into the Hamiltonian, S, M_S and L, M_L are not good quantum numbers anymore, while J and M_J are. Moreover, SO interaction restores part of the angular momentum, by means of a second order admixture of an excited state to the wavefunction.

The spin-orbit interaction can be interpreted classically as the interaction between the spin of the electron and the magnetic field created by its orbital motion around the nucleus (or the orbital motion of another electron). Since the orbital motion strongly depends on the crystal electric field created by the lattice, the spin-orbit coupling contributes to the magnetocrystalline anisotropy, as will be seen further. For an electron

$$H_{SO} = \frac{-e\hbar}{2m^2c^2r}\frac{d\Phi}{dr}\mathbf{l} \cdot \mathbf{s} = \xi(r)\mathbf{l} \cdot \mathbf{s} \quad (2\text{-}8)$$

Where *c* is the speed of light, *r* is the distance from the nucleus, *ħ* is the reduced Plank constant, Φ is the electric potential, ξ, **l** and **s** are single-electron spin orbit coupling constant, spin and angular moments. For hydrogenoid atoms and centrosymmetric potentials

$$\xi(r) = \frac{-e\hbar}{2m^2c^2r}\frac{d\Phi}{dr} = \frac{Ze^2\hbar}{8\pi\varepsilon_0 m^2c^2r^3} \tag{2-9}$$

Where Z is the atomic number and ε_0 is the vacuum permittivity. For a many-electron many-atom systems with i electrons and j atoms:

$$H_\xi = \sum_j \left(\xi_i \sum_i l_i \cdot s_i \right)_j \tag{2-10}$$

The classical model provides an intuitive understanding of the SO coupling, but it doesn't give correct quantitative estimates. The correct way to introduce spin-orbit coupling is by starting from the relativistic Dirac equation which is the relativistic (Lorentz invariant) version of the Schrodinger equation.:

$$\hat{H} = \vec{\alpha} \cdot \vec{p} + \vec{\beta} m_e c^2 + V \tag{2-11}$$

$$\begin{gathered} \alpha_k = \begin{pmatrix} 0 & \sigma_k \\ \sigma_k & 0 \end{pmatrix} \qquad \beta_k = \begin{pmatrix} \mathbf{I} & 0 \\ 0 & -\mathbf{I} \end{pmatrix} \\ \sigma_x = \begin{pmatrix} 0 & 1 \\ 1 & 0 \end{pmatrix} \sigma_y = \begin{pmatrix} 0 & -i \\ i & 0 \end{pmatrix} \sigma_z = \begin{pmatrix} 1 & 0 \\ 0 & -1 \end{pmatrix} \end{gathered} \tag{2-12}$$

Where p is the linear momentum and V is the electric potential operator. The Dirac equation can be expanded to give a more familiar form: the zeroth order expansion gives the Pauli equation.

$$H_R = H_{NR} - \frac{p^4}{8c^2} + \frac{\Delta V}{8c^2} + \frac{1}{2c^2r}\frac{dV}{dr}\mathbf{l}\cdot\mathbf{s} \tag{2-13}$$

with the first term being the non-relativistic Hamiltonian, the second and the third ones the scalar relativistic mass-velocity and Darwin terms and the last-one the spin-orbit interaction. The term is identical to the classical one, only differing by a factor 2, which is from where the g factor turns out. The decimals (2.0023…) can be explained only by quantum electrodynamics.

Since ξ is directly proportional to the nuclear charge Z, we can expect the SO energy to become more important for heavier elements. And in effect, while for the first row transition elements the crystal field energy is dominant and SO can be treated as a perturbation, for the lanthanides we observe the opposite, i.e. the energies are mainly determined by SO and perturbed by the crystal field. For third row transition elements, such as gold, the two energies typically have comparable magnitudes.

As we will see further, SO coupling is very important for determining the magnetic properties of both isolated and interacting gold nanoclusters.

2.1.3 Paramagnetism

A macroscopic system is formed by an ensemble of magnetic moments and the observable quantity associated to it is the *magnetization*, which, in the case of non-interacting spin-only moments, can be defined as the density of net magnetic dipole moment for unit volume (*V*):

$$\mathbf{M} = \frac{1}{V}\sum_i \boldsymbol{\mu}_{Si} \tag{2-14}$$

In the absence of an external magnetic field, in materials which were not magnetized before, the magnetic dipoles are randomly oriented and the net magnetization is equal to zero. The application of a magnetic field causes a partial alignment of the moments, making an induced magnetization appear. In the presence of a net magnetization, every point of the sample experiences an overall field, given by the sum of the external applied field and a local field, deriving from the magnetization. The following relations hold:

$$\begin{aligned} \mathbf{B} &= \mathbf{B}_0 + \mu_0\mathbf{M} \\ \mathbf{B}_0 &= \mu_0\mathbf{H} \\ \mathbf{B} &= \mu_0(\mathbf{H}+\mathbf{M}) \end{aligned} \tag{2-15}$$

where **H** is the applied magnetic field intensity. In the case of paramagnetic substances, the single spins can be considered as non-interacting (magnetically diluted system) and the magnetization can be obtained by using the Boltzmann statistical distribution. From this treatment the following expression is derived for the modulus of magnetization:

$$M = \frac{N}{V}|\boldsymbol{\mu}|\,L(x) \tag{2-16}$$

where *L(x)* is the Langevin function, *V* is the sample volume, *N* is the number of magnetic moments present in the sample and |**μ**| is the modulus of the magnetic moment.

$$\begin{aligned} L(x) &= \coth x - \frac{1}{x} \\ x &= \frac{H|\boldsymbol{\mu}|}{k_B T} \end{aligned} \tag{2-17}$$

where k_B is the Boltzmann constant. For low enough fields and high enough temperatures, the magnetic susceptibility, defined in general as χ=dM/dH, is independent from the applied field and a linear correlation between **H** and **M** is obtained:

$$\mathbf{M} = \chi \mathbf{H} \tag{2-18}$$

With this approximation, χ is given by the Curie law:

$$\chi = \frac{N}{V}\frac{|\boldsymbol{\mu}|^2}{3k_B T} = \frac{C}{T} \tag{2-19}$$

where C is the Curie constant. Consequently, for pure paramagnets a linear plot of $1/\chi$ vs T is expected.

2.1.4 Ferromagnetism, antiferromagnetism

This treatment does not hold for magnetically ordered systems, since in this case the spin-spin interactions can not be neglected: indeed, these interactions are actually responsible for the magnetic ordering.

In particular, the most important interaction which makes a substance magnetically ordered is the exchange interaction. The effect of this interaction on the magnetization can be approximately described by the mean-field theory. In the mean-field approximation it is assumed that, because of the exchange interaction between the single spins, each magnetic moment experiences a field proportional to the magnetization, called the exchange field:

$$\mathbf{B}_E = \lambda' \mathbf{M} \tag{2-20}$$

where λ' is a constant independent of temperature. At a certain temperature, called the *Curie temperature*, T_C, the spontaneous magnetization vanishes, because the exchange interactions are overcome by the thermal agitation, the magnetic order is lost and a paramagnetic behavior is observed. In this case the magnetization is proportional to the total field, given by the sum of the applied and the exchange fields and is therefore given by

$$\mathbf{M} = \chi(\mathbf{B_0} + \mathbf{B}_E) \tag{2-21}$$

Combining the last equation with the Curie law, the following relation is obtained:

$$\chi = \frac{C}{T - T_C} \tag{2-22}$$

Where T_C is the Curie temperature given by $T_C = C\lambda'$. This is the Curie-Weiss law, which describes the variation of the magnetization vs temperature in the paramagnetic region above the Curie temperature. Actually, the temperature at which the transition from a paramagnetic to a magnetically ordered state takes place does not exactly correspond to the T_C parameter of the Curie-Weiss expression. For this reason, many authors adopt a different formalism, defining the former as the Curie temperature (T_C) and the latter as the Weiss parameter (θ).

Microscopically, the exchange interaction is a purely quantum interaction, which in the case of localized interacting spins is usually estimated by introducing the Heisenberg Hamiltonian.

$$\hat{H} = -2J_{12}\hat{\mathbf{S}}_1 \cdot \hat{\mathbf{S}}_2 \tag{2-23}$$

J_{12} is the Heisenberg exchange constant, related to the electronic exchange integral:

$$J_{sr} = \iint \varphi_s^*(1)\varphi_r^*(2)\frac{e^2}{r_{12}}\varphi_s(2)\varphi_r(1)dr_1 dr_2 \tag{2-24}$$

where r_{12} is the distance between the two electrons and $\varphi_r(1)$, $\varphi_s(2)$ etc. indicate the first electron with function φ_r, the second electron with function φ_s etc.. It can be shown by mean-field theory that in general J is related to T_C in the following way:

$$J = \frac{3k_B T}{2zS(S+1)} \tag{2-25}$$

where z is the number of nearest neighbors of each spin in the lattice. If the constant J_{12} is positive, the configuration with parallel magnetic moments has a lower energy than the one with antiparallel moments. In this situation, the parallel configuration is more stable and, if the energy difference between the parallel and antiparallel configurations is high enough, the resulting macroscopic behavior of the material is ferromagnetic. If J_{12} is negative the opposite is true and the material is an antiferromagnet. If the interacting spins inside a lattice have different S quantum numbers, and therefore the magnetic moments have different magnitudes, another kind of magnetic behavior can be present, called ferrimagnetism. It takes place when the magnetic moments are aligned antiparallelly, but, since they do not cancel out, a net magnetic moment results. The different magnetic behaviors are illustrated in Figure 2.1:

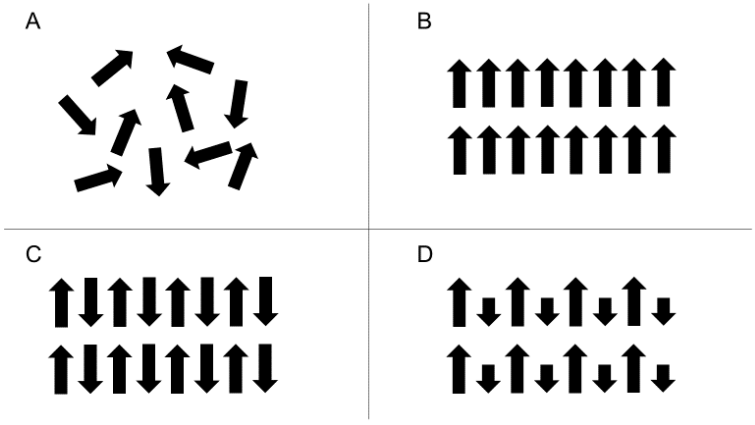

Figure 2.1. Pictorial depiction paramagnetic (a), ferromagnetic (b), antiferromagnetic (C) and ferrimagnetic (d) behaviors.

We can easily distinguish between the different magnetic behaviors from a $1/\chi$ vs T plot (Figure 2.2). While the pure magnetically diluted paramagnets following the Curie law show a linear plot with 0 intercept, ferromagnets follow the Curie-Weiss law. They still show linearity above T_C, but with a positive intercept, since J (and consequently T_C) is positive. At lower temperatures a deviation from linearity is observed. For antiferromagnets J is negative and so above the Néel temperature T_N a linear plot with a negative intercept is observed. At T_N there is a singularity and below T_N χ starts decreasing again ($1/\chi$ increasing), in contrast with what is observed for ferromagnets. This is because for ferromagnets the low-energy state is the one with parallel spins, and thus higher magnetization, while for antiferromagnets the low-energy state is the one with antiparallel spins and thus lower magnetization. The Curie and Néel temperatures are characteristic of a specific material and depend primarily on the atomic spin and exchange interaction strength.

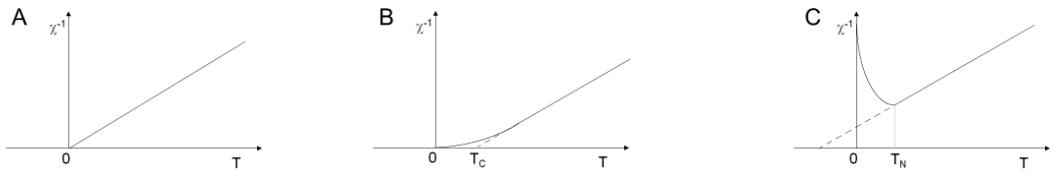

Figure 2.2. Curie-Weiss plots of the inverse of susceptibility vs T for a paramagnetic (A), ferromagnet (B), and antiferromagnetic (C).

Another peculiar feature of magnetically ordered materials is the fact that the magnetization is not homogenous in the whole sample: typically, they show a so-called *domain structure*. Inside each single domain (called *Weiss domain*), the magnetic moments are aligned by the exchange interaction and thus, in the ferromagnetic case, a domain has a net magnetization. Without an applied field, the magnetizations of the single domains are randomly oriented and therefore the overall magnetization of the material is equal to zero. The application of an external magnetic field causes the alignment of the magnetizations of the single domains, with a resulting net magnetization for the whole ferromagnetic sample (for antiferromagnets, since the magnetic moments are antiparallel, the magnetization of the single domains is approximately equal to zero and therefore also the overall magnetization of the material after the application of a magnetic field is negligible). The domains still remain partially aligned even after the magnetic field is removed, giving rise to a *remanent magnetization*, characteristic of ferromagnetic materials. In order to completely demagnetize the sample, a

negative field must be applied (directed in the opposite direction). The field value at which the magnetization is zero is called *coercitivity*.

The remanent magnetization and coercitivity can be clearly visualized in a M vs. B plot. We have seen that for pure paramagnets the field dependence of magnetization can be described by the Langevin function, which is independent on the field scan direction. This is not true for ferromagnets: if an alternating magnetic field loops are applied in opposite directions, closed magnetization curves are obtained, called hysteresis curves, which characterize the magnetic behavior of a substance. These curves are due to the rotation of the magnetic domains leading to a partial alignment with the applied field. Importantly, the first magnetization curve is different from all the following ones, because, as mentioned before, this is the only case in which the initial magnetization is equal to zero at B=0. Then the magnetization follows a non-linear curve until it reaches a saturation level, corresponding to the situation in which all the magnetic domains are aligned with the field direction. At this point the applied magnetic field intensity is decreased and the material retains a considerable degree of magnetization, which is consequently higher than for the first magnetization curve. When B=0 value is reached, the sample is not fully demagnetized, since the domains are only partially reorientated and a net magnetization is measured, corresponding to the remanent magnetization. Then the field direction is reversed and its intensity is increased until the coercitivity value is reached, when M=0. The field intensity is increased again until the saturation value in the opposite direction is reached. Subsequently the same steps are performed in the opposite direction and the hysteresis loop is thus completed (Figure 2.3).

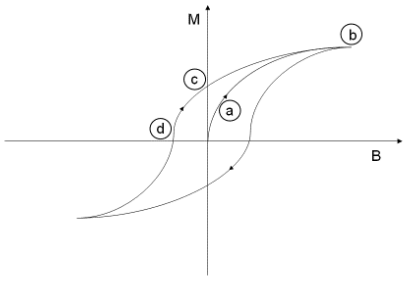

Figure 2.3. Typical hysteresis curve for a ferromagnetic material. a) First mgnetization curve; b) saturation magnetization; c) remanent magnetization; d) coercitivity.

2.1.5 Superparamagnetism

The magnetic properties of magnetic particles are strongly dependent on their dimensions. If the particles are large enough, the material exhibits a domain structure and a typical bulk magnetic behavior (ferromagnetism, antiferromagnetism, ferrimagnetism). Particles with dimensions smaller than those of a Weiss domain, usually of the order of a few nanometers, are instead single domain and show a peculiar behavior, which is intermediate between paramagnetism and ferromagnetism and which is called *superparamagnetism*. The limit radius for a spherical single-domain particle to be stable is given by:

$$R = \frac{6\sqrt{AK}}{\mu_0 M_S^2} \tag{2-26}$$

where *A* is the exchange stiffness, *K* is the magnetic anisotropy constant, which we will talk about in the next paragraph, μ_0 is the permeability in vacuum and M_S is the saturation magnetization.

The magnetization of a superparamagnetic particle fluctuates between some (usually two) preferential directions, corresponding to energy minima (Fig. 2.4), in each moment determining a distribution of populations of energy states corresponding to different orientations. In other words, the single spins of a particle are not independent (as in paramagnetic materials), and they reorient under thermal agitation in a correlated way: the particle behaves as a sort of giant spin. The superparamagnetic relaxation time is defined as the time it takes for the magnetization to return to equilibrium after a perturbation, such as the application of an external magnetic field. At equilibrium the populations are given by the Boltzmann distribution. The temperature dependence of the relaxation time is given by the Néel-Arrhenius law:

$$\tau = \tau_0 \exp\left(\Delta E / k_B T\right) \tag{2-27}$$

where τ_0 is of the order of 10^{-10}-10^{-13} and is only weakly dependent on temperature and ΔE is the energy barrier between the two easy directions of magnetization.

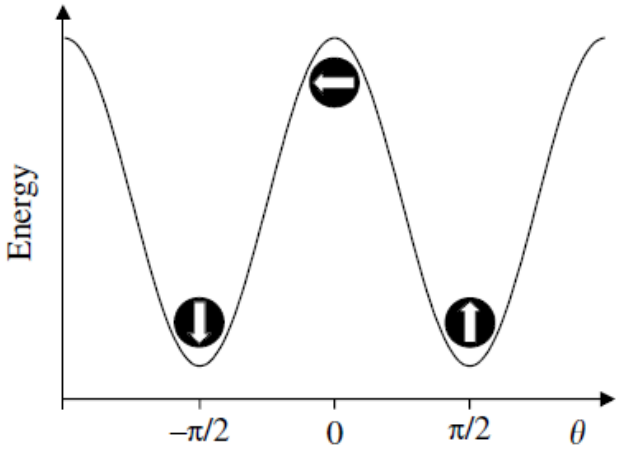

Figure 2.4. Energy vs angle between magnetization and easy axis direction for a superparamagnetic particle with axial magnetocrystalline anisotropy (from Gatteschi, D; Sessoli, R., Villain, J. Molecular nanomagnets, Oxford Press 2006),

This energy difference is primarily due to the *magnetecrystalline anisotropy energy*, which is linked to the interaction of the particle spin with the crystal lattice. This interaction reflects the crystallographic symmetry of the system and is generally phenomenologically estimated as a series expansion in polar coordinates. For an axial system it can be written in the following way:

$$E(\theta) = KV \sin^2 \theta \tag{2-28}$$

where K is the magneticrystalline anisitropy constant we already encountered, V is the particle volume and θ is the angle between the magnetization vector and the easy direction of magnetization, corresponding to a minimum of magnetocrystalline anisotropy energy (Figure 2.4). The energy barrier, which corresponds to the maximum of the function, in this case is equal to KV.

The anisotropy energy, together with the exchange energy, have a tremendous importance for magnetic phenomena. The usual Heisenberg exchange interaction is expressed by the $J\mathbf{S_1S_2}$ and is thus isotropic. Actually, anisotropic exchange exists as well, expressed by the Dzyaloshinsky-Moriya term $D\mathbf{S_1xS_2}$ but it can often be neglected. Therefore, if we consider only the exchange interaction, we get the alignment of the single spins resulting in a total magnetization, but no preferential direction for this magnetization. In order to explain why a ferromagnetic material can be magnetized in certain definite directions we have to introduce the magnetic anisotropy energy. Microscopically the anisotropy energy is given by many contributions, such as the dipolar spin-spin interactions, shape and strain contributions and

other. However, for the transition metals and rare earths the anisotropy energy is mainly determined by the spin-orbit interaction.

The anisotropy energy due to spin-orbit coupling can be calculated using the second order perturbation theory.

$$\Delta E_{SO} = \sum_{exc} \frac{\left|\langle exc | H_{SO} | gr \rangle\right|^2}{E_{gr} - E_{exc}} \tag{2-29}$$

from which the uniaxial anisotropy constant can be roughly estimated as

$$K_1 \approx \frac{\xi^2}{W} \tag{2-30}$$

where *gr* and *exc* stand for ground and excited states and *W* is the total bandwidth. Now let's see what happens if a weak external magnetic field is applied: the two energy minima corresponding to θ=0° and θ=180° are now not degenerate anymore, and therefore two different relaxation times can be defined for the two magnetization directions:

$$\tau^{\pm} = \tau_0^{\pm} \exp\left(\Delta E^{\pm} / k_B T\right) \tag{2-31}$$

with

$$\begin{aligned} \tau^{\pm} &= \tau_0^{\pm} \exp\left(\Delta E^{\pm} / k_B T\right) \\ \Delta E^{\pm} &= KV\left(1 \pm h\right)^2 \\ \tau_0^{\pm} &= \tau_0 \left(1 - h^2\right)^{-1} \left(1 \pm h\right)^{-1} \\ h &= \frac{\mu B}{2KV} \end{aligned} \tag{2-32}$$

For h<<1 the approximation $\tau_0^{\pm} \approx \tau_0$ holds.

The Néel-Arrhenius law is a good approximation for high enough temperatures, when thermal agitation kT is much higher than the energy barrier and causes the fluctuation of magnetization between the two energy minima (superparamagnetic behavior). At lower temperatures the Néel-Arrhenius law does not hold anymore and below a specific temperature, called blocking temperature, the material becomes ferromagnetic. According to the usual Néel-Arrhenius law, since the anisotropy energy barrier is proportional to the particle volume, the blocking temperature depends on the particles dimensions. Moreover, it also depends on the measurement time: obviously, one can see the same particle as blocked if $\tau_m << \tau$, or as superparamagnetic if $\tau_m >> \tau$. Therefore, the blocking temperature is rigorously defined as the temperature at which $\tau_m = \tau$ and is equal to:

$$T_B = \frac{\Delta E}{k_B \ln\left(\frac{\tau_m}{\tau_0}\right)} \tag{2-33}$$

Near the blocking temperature, hysteresis phenomena can be observed even for single domain particles. Indeed, relaxation becomes so slow, compared to the measurement time, that magnetization remains blocked in one of the local minima and different curves are recorded for upwards and downwards scans.

2.2. EPR spectroscopy

2.2.1. Zeeman interaction

In the first part of the chapter, the quantum mechanical formalism was introduced, describing the electronic and nuclear spin angular moments. These momenta are characterized by a spin principal quantum number S and a magnetic quantum number M_S, assuming $2S+1$ integer or half-integer values from S to $-S$. For a single electron $S=1/2$ and therefore only $M_S=1/2$ and $M_S=-1/2$ are possible. These two states are respectively indicated as α and β. In the preceding paragraph it was stated that for charged particles, such as electrons and atomic nuclei, a magnetic moment is associated to the spin angular moment, which is proportional to it by a constant specific of the considered particle (gyromagnetic ratio). The application of an external field B_0 removes the spin degeneration because of an interaction occurring between the field and the magnetic moment associated to the spin. In the quantum mechanical formalism, this interaction (Zeeman interaction) is expressed, for B_0 parallel to the z axis, by the following Hamiltonian. [5-7]

$$\hat{H} = -\hat{\mu} B_0 = g_e \gamma_e B_0 \hat{S}_z \tag{2-34}$$

where γ_e is the gyromagnetic ratio given by $e/2m_e$ (e and m_e are respectively the electron charge and mass) and g_e is the free electron g factor, already defined previously in this chapter. Applying this operator to the α and β, according to equations, the following eigenvalues are obtained:

$$\begin{aligned} E_\alpha &= \frac{1}{2} g_e \beta_e B_0 \\ E_\beta &= -\frac{1}{2} g_e \beta_e B_0 \end{aligned} \tag{2-35}$$

Where β_e is the already defined Bohr magneton, equal to $\gamma_e \hbar$. The degeneration removal of the spin states in the presence of an external magnetic field is called Zeeman effect. This

effect makes the transitions between the α and β states possible when the energy of the incident radiation is equal to the difference between the two levels (resonance condition):

$$h\nu = \Delta E = g_e \beta_e B_0 \tag{2-36}$$

In general, for the EPR transitions the following selection rules are applied:

$$\begin{aligned} \Delta M_S &= \pm 1 \\ \Delta M_I &= 0 \end{aligned} \tag{2-37}$$

i.e. the electron spin secondary quantum number must change by a unity, while the nuclear spins remain unchanged.

For instrumental reasons, in a continuous wave (CW) EPR experiment the resonance condition is obtained by varying the static magnetic field B_0, while the microwave frequency is fixed, as shown in the following diagram (Figure 2.5):

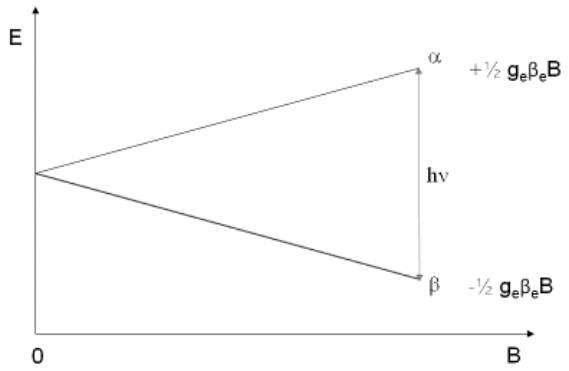

Figure 2.5. Energy vs magnetic field diagram, representing the Zeeman splitting of the spin states of a single unpaired electron..

2.2.2 Spin-orbit interaction in EPR: g tensor and zero field splitting

We have seen previously that in most real atomic or molecular systems, the electron is not free and one must take into account the orbital angular moment associated to its motion and the spin-orbit interaction. Therefore, the new complete Hamiltonian is:

$$\hat{H} = \beta_e (\hat{\mathbf{L}} + g_e \hat{\mathbf{S}}) \cdot \mathbf{B}_0 + \lambda \hat{\mathbf{L}} \cdot \hat{\mathbf{S}} \tag{2-38}$$

Since the orbital and spin-orbit operators, acting on the spatial part are present, this Hamiltonian is not a pure spin Hamiltonian. For the EPR purposes, it is often convenient to deal with pure spin Hamiltonians, since the spectral analysis and interpretation is much easier. For this aim, the operators acting on the spin coordinates are usually substituted by

their expectation values. This can be done by applying the perturbation theory, calculating the average spin-orbit interaction on the spatial part of the electronic states and considering this interaction as a first and second order perturbation to the spatial electronic Hamiltonian. With some math one obtains that the Hamiltonian (2-38) can be simply rewritten as

$$\hat{H} = \beta_e \hat{\mathbf{S}} \cdot \mathbf{g} \cdot \mathbf{B}_0 \tag{2-39}$$

g is a 3x3 tensor

$$\mathbf{g} = \begin{pmatrix} g_{xx} & g_{xy} & g_{xz} \\ g_{yx} & g_{yy} & g_{yz} \\ g_{zx} & g_{zy} & g_{zz} \end{pmatrix} \tag{2-40}$$

with each element given by

$$g_{ij} = 2.0023\left(\delta_{ij} - \lambda \Lambda_{ij}\right) \tag{2-41}$$

and

$$\Lambda_{ij} = \Lambda_{ji} = \sum_{n \neq 0} \frac{\langle 0 | \hat{L}_i | n \rangle \langle n | \hat{L}_i | 0 \rangle}{E_n - E_0} \tag{2-42}$$

Where L_i is the orbital angular momentum operator along the i-th direction, E_n is the energy of the n-th electronic level and E_0 is the energy of the fundamental electronic level.

For transition metals, the same kind of interaction (spin-orbit interaction) gives rise also to another term, which appears in the spin Hamiltonian for paramagnetic systems with S>1/2: the Zero Field Splitting (ZFS) coupling:

$$\hat{H}_{ZFS} = \hat{\mathbf{S}} \cdot \mathbf{D} \cdot \hat{\mathbf{S}} \tag{2-43}$$

The name Zero Field Splitting derives from the fact that this interaction partially removes the degeneracy of the M_S states even in the absence of a magnetic field. The same effect is produced by the dipolar interaction for organic radicals. However, for transition metals, the spin-orbit interaction is much stronger than the dipolar one, therefore ZFS is completely determined by the former.

Applying the same perturbative approach already used for the **g** tensor, it can be shown that the elements of the **D** tensor (also a 3x3 matrix) are given by

$$D_{ij} = \lambda^2 \Lambda_{ij} \tag{2-44}$$

The **D** tensor is symmetrical and has a trace equal to zero, therefore it can be diagonalized, orienting the reference frame in such a way that all the matrix elements are equal to zero, except the diagonal ones (D_x, D_y and D_z). In this case, there are only two independent terms

describing the ZFS (fine) interaction. It is convenient to use the following parameters, expressed as a function of the three values, which diagonalize **D**.

$$D = -\frac{3}{2} D_z$$
$$E = \frac{D_y - D_x}{2} \tag{2-45}$$

And the ZFS term can be written as:

$$\hat{\mathbf{S}} \cdot \mathbf{D} \cdot \hat{\mathbf{S}} = D\left[\hat{S}_z^2 - \tfrac{1}{3} S\left(S+1\right)\right] + E\left(\hat{S}_x^2 - \hat{S}_y^2\right) \tag{2-46}$$

The D parameter takes into account the tetragonal distortion of the system, while the E parameter indicates the degree of orthorhombic distortion and is comprised between 0 (no orthorhombic distortion) and D/3 (maximum orthorhombic distortion).

It is important to stress that the results obtained so far hold only if the spin-orbit interaction is much weaker than the energy splitting due, for example to the crystal field, so that it can be considered a weak perturbation. This is certainly true for first and second series transition metal elements. However, these formulas are not valid for some systems, such as the ones containing heavy atoms (third series transition metals, rare earths), as we shall see in the discussion of the experimental results.

The **g** matrix can be diagonalized to find the following matrix in the principal reference framework:

$$\mathbf{g} = \begin{pmatrix} g_x & 0 & 0 \\ 0 & g_y & 0 \\ 0 & 0 & g_z \end{pmatrix} \tag{2-47}$$

where g_x, g_y and g_z are called principal g values. The fact that **g** is a tensor implies that the EPR spectrum becomes anisotropic, i.e. characterized by different *g* values depending on the relative orientation of the principal axes of the spin system and the applied magnetic field B_0. Experimentally, a shift of the EPR line is observed by rotating the sample with respect to the magnetic field, because of the change of the resonace condition. The principal *g* values correspond to the g values measured with the field aligned respectively with the *x*, *y* and *z* principal axes. Depending on the symmetry of the paramagnetic system, three cases can be distinguished:

1. $g_x = g_y = g_z$: cubic symmetry
2. $g_x = g_y \neq g_z$: axial symmetry
3. $g_x \neq g_y \neq g_z$: orthorombic symmetry

For a generic orientation the g value is given by

$$g(\vartheta,\phi) = \sqrt{\sin^2\vartheta\cos^2\phi g_x^2 + \sin^2\vartheta\sin^2\phi g_y^2 + \cos^2\vartheta g_z^2} \quad (2\text{-}48)$$

where θ and φ are the polar angles describing the orientation of $\mathbf{B_0}$ with respect to the principal axes of the **g** tensor.

What was just stated is true for a single crystal, but is not valid for a polycrystalline or amorphous glassy sample. In both these cases the sample is formed by an ensemble of randomly oriented paramagnetic species and the overall spectrum consists of the superposition of all the signals corresponding to the different orientations. Powder and glass samples usually give very broad spectra. Nevertheless, the magnetic geometry (cubic, axial, orthorhombic) and the principal g values can be determined from them, since they give specific lineshapes and spectral features at fields corresponding to the principal *g* values.

2.2.3 Hyperfine interaction

Additionally to the Zeeman interaction and to the Zero field splitting interaction, another important interaction in EPR spectroscopy is the hyperfine interaction. It originates from the coupling of the magnetic moment associated with the electron spin with that associated with the spin of nearby nuclei. Hyperfine coupling can be expressed by the following spin Hamiltonian:

$$\hat{H} = \hat{\mathbf{S}} \cdot \mathbf{A} \cdot \hat{\mathbf{I}} \quad (2\text{-}49)$$

where **A** is a 3x3 tensor, called the hyperfine coupling tensor and **I** the nuclear spin. It is due to the sum of two different electron-nuclei interactions: the isotropic Fermi Contact interaction and the dipole-dipole electron-nuclei interaction and it can thus be written as

$$\mathbf{A} = a_{iso}\mathbf{1}_3 + \mathbf{T} \quad (2\text{-}50)$$

where a_{iso} is the Fermi contact constant and **T** is the dipolar tensor. The Fermi contact constant is given by

$$a_{iso} = \tfrac{2}{3}\mu_0 g_e \beta_e \beta_n \left|\psi(0)\right|^2 \quad (2\text{-}51)$$

As already said, this term is isotropic and proportional to the probability of finding the unpaired electron in the position of the nucleus $|\psi(0)|^2$. This is directly possible only for unpaired electrons with *s* character. Nevertheless, this coupling can be observed also for other systems through spin polarization mechanism, in which polarization is induced through bond atoms.

The second term of the hyperfine coupling matrix, i.e. the anisotropic **T** tensor, arises from the classical interaction between the magnetic dipoles associated with electron and nuclear spins respectively. Quantum mechanically this interaction is expressed by the following Hamiltonian, corresponding to the classical dipolar interaction energy:

$$\hat{H}_{dip} = \frac{\mu_0}{4\pi\hbar} g_e \beta_e g_n \beta_n \left[\frac{\hat{\mathbf{S}} \cdot \hat{\mathbf{I}}}{r^3} - \frac{3(\hat{\mathbf{S}} \cdot \mathbf{r})(\hat{\mathbf{I}} \cdot \mathbf{r})}{r^5} \right] \tag{2-52}$$

where r is the electron-nucleus distance. The expression holds for isotropic g_e and g_n. It is clear that this interaction depends both on the electron-nuclei spin distance and orientation. By collecting the distance dependence into the T parameter, this Hamiltonian can be written in this simplified form:

$$\hat{H}_{dip} = \frac{\mu_0}{4\pi\hbar} \frac{g_e \beta_e g_n \beta_n}{r^3} \begin{pmatrix} -1 & 0 & 0 \\ 0 & -1 & 0 \\ 0 & 0 & 2 \end{pmatrix} = \begin{pmatrix} -T & 0 & 0 \\ 0 & -T & 0 \\ 0 & 0 & 2T \end{pmatrix} \tag{2-53}$$

It can be easily shown, using the following complete Hamiltonian, with only isotropic coupling

$$\hat{H} = g_e \beta B S_z - g_N \beta_N B I_z + \hbar a S I \tag{2-54}$$

that, for and S=1/2 system interacting with a nucleus with spin I=1/2, such as a proton, the energies are given by:

$$E(M_S, M_I) = g_e \beta B M_S - g_N \beta_N B M_I + \hbar a M_S M_I \tag{2-55}$$

This leads to two allowed EPR transitions, following the selection rules $\Delta M_S=1$, $\Delta M_I=0$, corresponding to the following energies:

$$\Delta E = g_e \beta B \pm \frac{1}{2} \hbar a_{iso} \tag{2-56}$$

Experimentally, this manifests in the line splitting. For a general case of m sets of n equivalent nuclei with spin I_i, the hyperfine coupling gives rise to a splitting into $\Pi_i^m(2n_iI_i+1)$ lines.

2.2.4 Continuous wave EPR experiment and relaxation

For the description of some phenomena, in particular the typical Continuous Wave (CW) EPR experiment, a semiclassical model for electron magnetic resonance is useful. The model can be rigorously applied to the macroscopic magnetization vector **M**, representing the overall magnetic moment of the system (as detailed previously). At the thermal equilibrium, in

the presence of a static magnetic field $\mathbf{B_0}$ applied along the z axis, the α and β spin levels have different energies and are populated according to the Boltzmann statistics:

$$\frac{P_\beta}{P_\beta} \propto \exp\frac{(E_\alpha - E_\beta)}{kT} = \exp\frac{g_e\beta_e B_0}{kT} \qquad (2\text{-}57)$$

From this population difference a non-zero **M** component along the *z* axis turns out ($M_z=M_0\neq0$). The M_x and M_y components are instead equal to zero because of the random orientation of the magnetic moments with respect to these axes.

According to the classical model, the static field $\mathbf{B_0}$ causes a torque on the **M** vector, which in turn causes a time evolution of the magnetization, described by the following equation:

$$\frac{d\mathbf{M}}{dt} = \gamma\mathbf{M}\times\mathbf{B}_0 \qquad (2\text{-}58)$$

In a static magnetic field, the solution of this equation represents a rotation of **M** around the direction of $\mathbf{B_0}$ (precession motion, figure 2.6) with a typical frequency ω^0 (Larmor frequency), given by $\omega_0=\gamma B_0$.

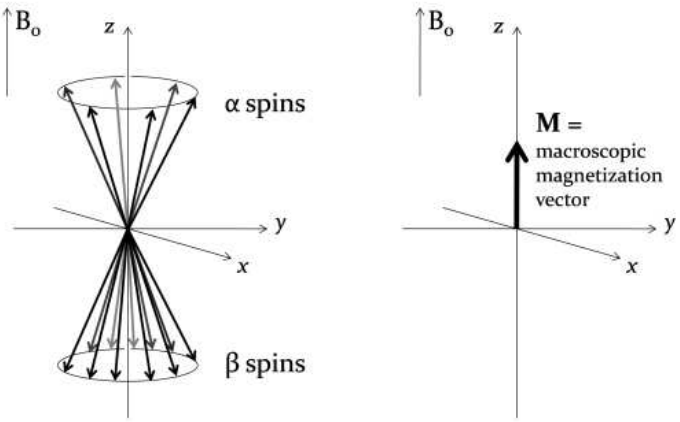

Figure 2.6. Vector representation of the spins subject to an external magnetic field and the overall magnetization (adopted from Bruker manual).

If, additionally to the static field $\mathbf{B_0}$ along *z*, an oscillating $\mathbf{B_1}$ field in the xy plane is introduced, due to the microwave radiation, a rotation around $\mathbf{B_1}$ adds to the precession around $\mathbf{B_0}$ and the **M** vector undergoes a spiral motion towards the *xy* plane (nutation). This nutation motion towards the *xy* plane is opposed by irreversible relaxation processes, which tend to bring **M** back to the initial thermal equilibrium position, i.e. aligned along the static field $\mathbf{B_0}$. In particular, the M_z component returns to M_0 (thermal equilibrium value) with a characteristic

time T1 (longitudinal, or spin-lattice relaxation), while M_x and M_y return back to zero with a characteristic time T2 (transverse, or spin-spin relaxation).

These processes can be included in the phenomenological Bloch equations:

$$\begin{aligned}\frac{dM_x}{dt} &= \gamma(M_y B_z - M_z B_y) - \frac{M_x}{T_2} \\ \frac{dM_y}{dt} &= \gamma(M_z B_x - M_x B_z) - \frac{M_x}{T_2} \\ \frac{dM_z}{dt} &= \gamma(M_x B_y - M_y B_x) - \frac{M_z - M_0}{T_1}\end{aligned} \tag{2-59}$$

These equations can be solved after performing a change of the reference frame, in which the *x*, *y* and *z* axes lab frame is substituted by a rotating frame, in which the new *x*' and *y*' axes rotate around the *z* (*z*=*z*') axis with the frequency of the microwave radiation ω. In this reference frame $\mathbf{B_1}$ appears as static and is assumed for simplicity to be aligned with *x*.

In these stationary conditions, typical of a continuous wave EPR experiment, the system of the phenomenological Bloch equations is easily solved and it can be shown that in this model the CW-EPR signal is simply proportional to the magnetization along y. The EPR signal therefore appears to be described by the following equation:

$$\chi''(\omega) = 1/2\,\chi_0\omega_0 T_2 \frac{1}{1+(\omega-\omega_0)^2 T_2^2 + \gamma^2 B_1^2 T_1 T_2} \tag{2-60}$$

where χ' is the magnetic susceptibility along *y*, to which the EPR signal is proportional. The magnetic susceptibility is often defined as a complex quantity and χ'' is its imaginary part:

$$\chi = \chi' + i\chi'' \tag{2-61}$$

At low microwave power, which is proportional to B_1^2, the susceptibility, and therefore the EPR intensity, increases with increasing intensity. However, at high powers, the signal broadens and becomes weaker. This is due to the last term at the denominator of the previous equation, which is particularly important for paramagnetic species with long relaxation times. This phenomenon is called saturation. Far from the saturation conditions, this term can be neglected and the equation for the susceptibility is given by:

$$\chi'' = \frac{\gamma M_0 (1/T_2)}{(1/T_2)^2 + (\gamma B_0 - \omega)^2} \tag{2-62}$$

In the CW-EPR experiment, the χ'' observable is measured by sweeping the B_0 field and its variation with B_0, is described by (2-62): it's a line, called Lorentzian, centered at the field corresponding to the ω frequency and characterized by a linewidth which is inversely

proportional to T2 (homogeneous linewidth). For instrumental reasons, due to the signal modulation system, in EPR the first derivative of χ' is recorded during the experiment.

In the solid-state the EPR line is often given by a convolution of several EPR signals, each due to species characterized by slightly different surroundings and interactions, giving rise to slightly different physical parameters, such as the *g* factor. This phenomenon causes the so-called the inhomogeneous line broadening.

2.2.5 Magnetic resonance in magnetically ordered systems

Ferromagnetic electron resonance (FMR) is observed when a ferromagnetic sample is placed into an external magnetic field and irradiated with a microwave frequency equal to the precession frequency of the magnetization of the system.[8] Differently from the paramagnetic systems, ferromagnets exhibit a spontaneous magnetization $\mathbf{M_S}$, due to alignment of the spins produced by the exchange interaction, giving rise to an intrinsic magnetic field, which is present even in the absence of an external magnetic field. For this reason, some additional phenomena must be considered for these systems. First of all, the demagnetizing fields must be taken into account. These fields are due to a purely classical effect and oppose to the sample magnetization when a magnetic field is applied. Together with the magnetic anisotropy, the demagnetizing fields are of fundamental importance in the hysteresis phenomena. For an isotropic sample the demagnetizing field can be expressed in the following way:

$$\mathbf{B}_d = -N_d \mathbf{M} \tag{2-63}$$

Where N_d is the demagnetizing factor. However, this expression can be rigorously used only for spherical samples. Indeed, the demagnetizing field reflects the sample shape and for anisotropic samples it must be written as a tensor. For an ellipsoidal sample with principal axes corresponding to the cartesian axes, it is given by a diagonal tensor:

$$\mathbf{N}_d = \begin{pmatrix} N_d^x & 0 & 0 \\ 0 & N_d^y & 0 \\ 0 & 0 & N_d^z \end{pmatrix} \tag{2-64}$$

Consequently, the demagnetizing field can be expressed as:

$$\mathbf{B}_d = -\mu_0 \mathbf{N}_d \mathbf{M} = -\mu_0 \begin{pmatrix} N_d^x & 0 & 0 \\ 0 & N_d^y & 0 \\ 0 & 0 & N_d^z \end{pmatrix} \begin{pmatrix} M_x \\ M_y \\ M_z \end{pmatrix} = -\mu_0 \left(N_d^x M_x \mathbf{i} + N_d^y M_y \mathbf{j} + N_d^z M_z \mathbf{k} \right) \tag{2-65}$$

and the total magnetic field sensed by the sample magnetization during an FMR experiment is given by:

$$\mathbf{B} = \mathbf{B}_0 + \mathbf{B}(t) + \mathbf{B}_d \tag{2-66}$$

where $\mathbf{B_0}$ is the usual static external magnetic field ($\mathbf{B_0}=B_0\mathbf{k}$) and $\mathbf{B}$(t) is the oscillating magnetic field associated with the radiation ($\mathbf{B}(t)=\mathbf{B_1}e^{i\omega t}$). The magnetic anisotropy is neglected for the moment.

Neglecting relaxation, the magnetization motion equation for a ferromagnet is obtained by substituting to total field (2-66) into (2-58):

$$\frac{d\mathbf{M}}{dt} = \gamma\mathbf{M}\times\left(\mathbf{B}_0 + \mathbf{B}(t) + \mathbf{B}_d\right) \tag{2-67}$$

Assuming that: 1) the magnetization does not move away remarkably from the equilibrium ($\mathbf{M}=\mathbf{M_s}$, saturation magnetization); 2) a stationary regime takes place, in which $\mathbf{M_x}=\mathbf{M_x}(0)e^{i\omega t}$ and $\mathbf{M_y}=\mathbf{M_y}(0)e^{i\omega t}$; 3) the oscillating radiation field can be neglected ($\mathbf{B}(t)=0$), equation (2-67) can be solved, to give:

$$\omega_0 = \gamma\left\{\left[B_0 + \mu_0\left(N_d^y - N_d^z\right)M_s\right]\left[B_0 + \mu_0\left(N_d^x - N_d^z\right)M_s\right]\right\}^{1/2} \tag{2-68}$$

with $M_z=M_s$. Equation (2-68) gives the resonance frequency of a ferromagnetic system. From this equation it turns out that the resonance condition is obtained for two different values of B_0 and this explains the typical complex and highly asymmetric lineshape of the ferromagnetic EPR (FMR) signals. This effect is visible only for non-spherical particles: indeed, for a spherical sample $N_d^x=N_d^y=N_d^z=1/3$ and $\omega_0=\gamma B_0$.

In most magnetic materials also magnetic anisotropy must be necessarily taken into account. This can be done by introducing the magnetic anisotropy field $\mathbf{B_a}$. The total magnetic field acting on the sample now becomes:

$$\mathbf{B} = \mathbf{B}_0 + \mathbf{B}(t) + \mathbf{B}_d + \mathbf{B}_a \tag{2-69}$$

In the simple case of spherical particles, where the demagnetizing field ($B_d=0$) can be neglected and for $B_1=0$ we obtain:

$$\omega_0 = \gamma\left(B_0 + B_a\right) \tag{2-70}$$

In this case ferromagnetic resonance can be observed also without applying the external field and the resonance frequency is proportional to the anisotropy field.

Neglecting all the contributions to magnetic anisotropy, except the magnetocrystalline contribution, for a system with axial symmetry, $B_a=2K_1/M$, where K_1 is the first order

magnetocrystalline anisotropy constant. For systems with different symmetries higher order anisotropy constants must be introduced.

The magnetization motion of a ferromagnet is more correctly described by the Landau-Lifshiz equation, which takes into account also the specific ferromagnetic relaxation process.

$$\frac{d\mathbf{M}}{dt} = \gamma \mathbf{M} \times \mathbf{B} - \frac{\lambda''}{|\mathbf{M}|^2} \mathbf{M} \times (\mathbf{M} \times \mathbf{B}) \tag{2-71}$$

where λ'' is a phenomenological relaxation constant (not to be mistaken with the spin-orbit coupling and the exchange field constants). From this equation, the following expression for the imaginary part of the susceptibility is obtained in the case of a soft ferromagnet:

$$\chi'' = \frac{1}{\pi} \Delta_B B_0^2 \frac{\left[\left(B_0^2 + \Delta_B^2 \right) B^2 + B_0^4 \right]}{\left[\left(B_0^2 - B_0 \right)^2 B_0^2 + \Delta_B^2 B^2 \right] \left[\left(B_0^2 + B_0 \right)^2 B_0^2 + \Delta_B^2 B^2 \right]} \tag{2-72}$$

where Δ_B is the full linewidth at half height.

The EPR spectra of superparamagnetic particles show some peculiar features distinguishing them from the spectra of other magnetic compounds. While retaining the typical asymmetric lineshape of ferromagnetic signals, in addition they exhibit a characteristic temperature dependence, consisting in a broadening and a low-field shift of the resonance line with lowering the temperature. This behavior can be intuitively explained in the following way: high temperatures promote thermal fluctuations of the magnetization of single particles (the thermal energy is higher than the magnetocrystalline anisotropy energy) and therefore, the EPR spectra show an average situation, giving rise to narrower lines. At lower temperatures, the magnetization is limited (the thermal energy is lower than the anisotropy energy) and the magnetization vectors are “frozen” in different orientations, corresponding to energy minima. The spectrum is therefore given by the convolution of signals corresponding to the different orientations and consequently the lines are broader.

Different models were developed, which more or less rigorously describe the superparamagnetic resonance phenomenon, most based on a classical approach [9-12]. In this thesis a quantum mechanical approach was used,[13,14] and further developed. It will be presented in Chapter 4, dedicated to the ferromagnetism in Au_{25} clusters.

2.2.6 Pulsed EPR

In addition to the continuous wave EPR experiments, in which a field sweep is performed and the response of the system is measured for each applied field value, it is possible to use EPR

in the pulse mode, similarly to what is done in modern NMR experiments. Nevertheless, as will be explained below, there are some substantial differences with respect to NMR, especially in the possibilities offered by the two techniques.[15,16]

In CW-EPR techniques the microwave power is very low ($B_1 << B_0$) and the sweep is slow, so that the system is only slightly perturbed and is able to return to equilibrium before the field is changed. Instead, in pulse experiments short (10-100 ns) and strong microwave pulses are used, which allow to significantly perturb the magnetization from its equilibrium state. As a matter of fact, when a pulse is applied, the magnetization starts a precession around the B_1 field, rotating by an angle $\theta = \gamma B_1 t_p$, where t_p is the pulse time length. By varying the pulse length and power (proportional to B_1^2), it is thus possible to rotate the magnetization by a desired angle: 90°, bringing it to the *xy* plane ($\pi/2$ pulse), by 180° (π pulse) etc.. From the point of view of the spin energy levels, a $\pi/2$ pulse corresponds to equaling the α and β populations, while a π pulse corresponds to inverting the populations.

It was already mentioned that there are some significant differences between pulsed EPR and pulsed in NMR, which are part of the reason why the former didn't completely replace the continuous wave technique, as happened for the latter. The first difference is the fact that the electron spin relaxation is usually much faster than the nuclear spin relaxation. The first consequence of this fact is that part of the magnetization (the one which relaxes faster) is lost: it is completely relaxed in the instrumental dead time, which is necessarily introduced to prevent the damage of the detector from the very intense radiation just after the pulse. The second consequence is that in pulse EPR we don't have enough time to perform the complex pulse sequences, which are commonly used in NMR. Moreover, the EPR signals cover a much wider spectral range than common NMR signals, therefore it is usually not possible to excite the entire spectrum with pulses of available length ($\Delta\nu_{eff} = 1/6\tau_p$). Even with the shortest pulses we are able to excite only a small portion of the spectrum, so the Fourier transformed free induction decay (FID) procedure commonly used in NMR is not usually useful. Instead, in most pulse EPR techniques the electron spin echo is measured, i.e. the spontaneous microwave emission by a paramagnetic sample after the application of a series of microwave pulses.

In all the pulse sequences three distinct phases may be distinguished:

1. Preparation: a series of pulses with controlled delays generate non-equilibrium magnetization (populations and coherences).

2. Evolution: the non-equilibrium magnetization is allowed to evolve; in this phase the delays between pulses are usually varied during the experiment.
3. Acquisition: the pulses applied in this phase bring the magnetization to the xy plane, so it can be detected.

Among the most common pulse sequences we find the two- and three-pulse spin echo sequences.

In the two-pulse sequence (Hahn sequence), a $\pi/2$ and a π pulse are sequentially applied on a sample placed in the static magnetic B_0 field. The spin echo appears after a time equal to 2τ, where τ is the time between the two pulses. The spin echo formation can be easily explained by using the classical vector model in the rotating frame, as illustrated in figure 2.7:

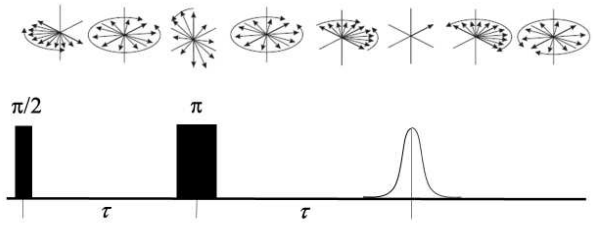

Figure 2.7. Two-pulse Hahn spin-echo sequence with a pictorial depiction of the magnetization dynamics (partially adopted from Bruker manual).

After the first $\pi/2$ pulse, applied along the y rotating axis direction, the magnetization, which is initially aligned with the *z* axis is brought to the *xy* plane, specifically along *–x*. This is the preparation period, in which the spin populations are equaled and coherence is induced. At this point the relaxation processes begin, which leads to the loss of coherence, bringing the M_x and M_y values back to zero and M_z back to its equilibrium value M_0. At the same time, the magnetic moments characterized by slightly different Larmor frequencies, which contribute to the overall magnetization, start dephasing. The loss of coherence is induced by transverse relaxation (T_2), different Larmor frequencies and inhomogeneity of the B_0 field. Then the evolution period starts, in which the π pulse applied along x after a time τ rotates the magnetization by 180°, bringing it to *–y* (M_y is converted to M_{-y}). Then, since the sense of rotation of the magnetization vectors is the same as before, after the same time τ, the magnetization vectors rephase and a signal maximum is observed, corresponding to the spin echo, which in this case is called Hahn echo. In this way coherence is only partially recovered, because the T_2 relaxation processes are random. Moreover, the magnetization in

the *xy* plane is decreased because of the T_1 relaxation. In the solid state other additional processes contribute to the echo decay, such as instantaneous diffusion and spin diffusion.

In the three-pulse sequence, schematized in figure 2.8, three $\pi/2$ pulses are applied along *x*. The time between the first and the second pulses is indicated as τ, while the time between the second and the third pulses is indicated as t_1. As in the two pulse sequence, first of all the magnetization is transferred from *z* to *-x* by the first $\pi/2$ pulse. After a time τ, during which the usual processes leading to the loss of coherence take place, the second $\pi/2$ pulse brings the magnetization to *z*. This leads to a population inversion with respect to the initial situation. The magnetization stored along *z* then undergoes T_1 relaxation, which is usually significantly slower than T_2 relaxation. After the evolution time T, magnetization is brought back to the *xy* plane (specifically along *x*) by the third, last $\pi/2$ pulse. Finally, similarly to the two-pulse sequence, the magnetization vectors are refocused, partially recovering the coherence and a stimulated echo is detected after a time τ.

Actually, the three-pulse sequence gives rise to several echoes, as illustrated in figure 2.8, because of the formation of different coherences which refocus at different times. The commonly used echo is the so-called stimulated echo, which is the one appearing after a time equal to τ after the third pulse. The other echoes can be removed by using specific pulse sequences, such as a two-step or four-step phase cycling.

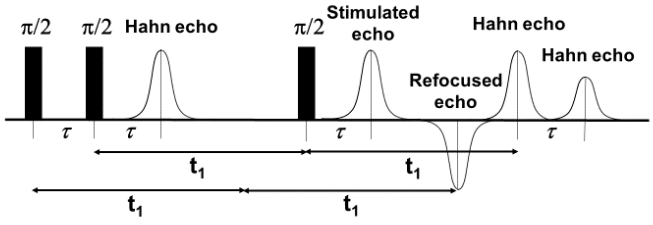

Figure 2.8. Three-pulse spin-echo sequence.

A very common pulsed EPR experiment consists in a B_0 field scan, in which, for each field a spin-echo sequence is performed and the integrated area under the echo is measured. Since this area is proportional to the magnetization of the spin system, what is obtained is an EPR spectrum which is “in absorption” and not a derivative, as for a typical CW-EPR experiment. The EPR spectra recorded in this way are called echo-detected EPR spectra. The acquirement of echo-detected spectra is useful when one wants to eliminate some signals.

This can be done by selecting the right parameters, with which only the magnetization due to the species of interest is brought to the *xy* plane and gives rise to an echo.

2.2.7 Pulsed Electron Nuclear Double Resonance

As previously explained, from a simple CW-EPR spectrum it is theoretically possible to obtain the hyperfine coupling constants with the nuclei surrounding the electronic spin under study. However, since each coupling splits an EPR line in two or more lines ($\Pi_i^m(2n_iI+1)$ lines for m sets of n equivalent nuclei with spin *I*), for systems with many nuclei and different hyperfine couplings, the spectrum can be very complex and often only a single broad line is visible, in which no coupling can be observed. However, there are some pulsed EPR techniques which allow to solve this issue by greatly simplifying the spectrum and its interpretation. One of these techniques is pulsed Electron Nuclear Double Resonance (pENDOR).

ENDOR can be considered a hybrid EPR-NMR technique, since it requires the use of both microwave and radiofrequency radiation. Specifically, a sample is placed in a static magnetic field, as in all the EPR experiments, and a microwave radiation is applied to induce the saturation of a specific EPR transition ($\Delta M_S=1$, $\Delta M_I=0$), which corresponds to equaling the two populations. Additionally, an RF radiation is applied to induce NMR transitions ($\Delta M_S=0$, $\Delta M_I=1$), which have the effect of desaturating the EPR transition. For an S=1/2, I=1/2 system, when $\nu>>A$, two resonance lines are obtained at $\nu+A$ and $\nu-A$. In the opposite case ($\nu<<A$) the transitions are observed at frequencies $A+\nu$ and $A-\nu$. In any case, this significantly reduces the number of lines compared to CW-EPR (from 2^n to 2n for n non-equivalent I=1/2 nuclei).

ENDOR experiments can be performed both in CW and pulse mode. The CW-ENDOR spectra are recorded in the way just described, by sweeping the RF frequency, instead of the B_0 field as in the typical CW-EPR experiment. However nowadays, since pulsed ENDOR techniques were developed, the CW-ENDOR technique is much less commonly used. As a matter of fact, pulse ENDOR techniques have several advantages over CW-ENDOR: higher resolution, less artifacts, easier saturation, possibility of measuring lower hyperfine constants.

There are two main pulse sequences which are commonly used in pulsed ENDOR: Davies ENDOR sequence and Mims ENDOR sequence.

During the preparation period of the Davies ENDOR technique (Fig. 2.9),[17] a selective π microwave pulse is applied to invert the electron spin magnetization relative to a specific EPR

transition, thus creating a sort of “hole” in the EPR spectrum. During the evolution period, no MW pulses are applied, but a T time long selective RF π pulse is applied to invert a specific NMR transition, which corresponds to transferring the magnetization to the other M_S spin manifold and thus eliminating the population difference created by the first MW pulse (refilling the hole). The detection period consists in a two-pulse spin echo sequence, which brings the M_z component of the magnetization to the *xy* plane allowing to measure the magnetization restored during the mixing period.

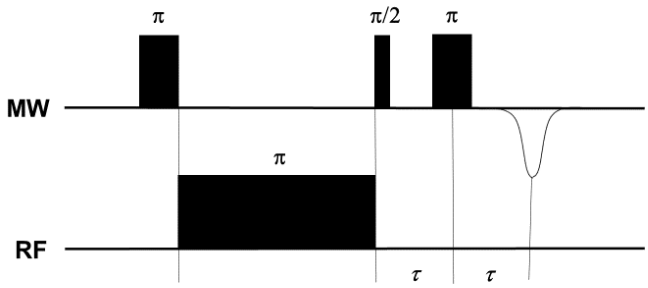

Figure 2.9. Davies-ENDOR pulse sequence.

The Mims ENDOR pulse sequence is basically a stimulated three pulse echo sequence,[18] in which a π RF pulse is applied during the T delay time. The Mims sequence has the advantage of detecting lower hyperfine couplings, compared to Davies ENDOR, but has the drawback of being affected by blind spots at $\tau=2k\pi/a$, where *k* is an integer, making several measurements at different fields necessary. This sequence will not be discussed in further detail, since it was not used in the present work.

2.3 Parmagnetic Nuclear Magnetic Resonance Spectroscopy

2.3.1 Nuclear Magnetic Resonance

The general theory underlying Nuclear Magnetic Resonance (NMR) spectroscopy is very similar to the basis of EPR spectroscopy, outlined in the previous section. While in EPR we are dealing with electron spins, NMR is concerned with nuclear spins. Due to the huge difference between electron and nuclear mass, the gyromagnetic ratios are very different and therefore the energy difference between the Zeeman-split levels is much lower. This have some important consequences: first of all, a higher wavelength radiation must be used,

specifically in the radiofrequency range. Second, small energy differences give rise to small population differences and consequently low sensibility. The use of higher fields to overcome this issue is one of the main concerns in NMR spectroscopy.

Although the general theory is quite similar, there are remarkable differences between the EPR and the NMR experimental setups. As already mentioned previously, in the most common ^{1}H and ^{13}C NMR experiments, it is possible to excite all the nuclear resonances with a single $\pi/2$ RF pulse and then obtain the whole spectrum by Fourier transforming the measured decaying and oscillating signal, called Free Induction Decay (FID). This is not possible in EPR, because of the broader spectral range, which does not allow the excitation with pulses of instrumentally feasible length. For this reason, the time-consuming CW mode, still widely adopted in EPR, is not used in NMR anymore since many decades and all the experiments are performed only in pulse mode.

Compared to EPR, which is a very powerful, but a highly specific technique, NMR is much more widespread. Due to its ability to precisely detect both through-bond and through-space interactions, it allows the determination of connectivity and relative positions of atoms in a molecule. For these reasons it became one of the basic tools of organic chemists for the identification of new compounds and an important technique for protein structure determination.

The two main quantities, which allow such a precise identification, are the chemical shift and the J-coupling. The former is the NMR equivalent of the *g* factor, arising from the particular magnetic environment of the resonant nuclei. It consists in a shift of the proton resonance with respect to the Larmor frequency and allows a first identification of functional groups. The latter is an interaction between nuclear spins, arising from the hyperfine coupling between nuclear spins and the spins of the electrons nearby. By an analysis of line multiplicity and intensity of the different resonances, it is usually possible to univocally determine (at least for small molecules) the molecular structure from an NMR spectrum. If the assignment is ambiguous, advanced NMR techniques are often used, such as the 2D techniques: Correlation Spectroscopy (COSY), Total Correlation Spectroscopy (TOCSY), Heteronuclear Single Quantum Correlation (HSQC), Heteronuclear Multiple Quantum Correlation (HMQC), Heteronuclear Multiple Bond Correlation (HMBC) etc..

2.3.2. 2D Nuclear Magnetic Resonance

As already mentioned, a 1D pulse NMR experiment consists in a single 90° pulse, which has the right length to excite all the Larmor frequencies of interest. The magnetization is thus brought on the *xy* plane and the FID is detected. The frequency-domain NMR spectrum is obtained by performing a Fourier transform of the FID.

For particularly complex systems, with a high amount of interacting protons, the 1D NMR spectra are usually composed by many highly overlapping signals, which can hardly be interpreted. In this case, 2D NMR techniques are often very useful to disentangle and univocally assign the different signals.

A typical 2D NMR experiment consists in the same phases we already observed for a generic pulsed experiment, described previously for EPR, i.e. preparation, evolution, mixing and detection. However, in this case the evolution time is not fixed, but is varied continuously. In particular, the time intervals between specific pulses are changed, depending on the specific experiment. In this way a series of FIDs are obtained, one for each evolution time, which represents the second dimension, the first one being the detection time, in which the FID decays. The Fourier transform is then performed in both dimensions and the 2D spectrum is thus obtained. Depending on the experiment, the spectrum can show both diagonal and off-diagonal peaks, representing correlations of a signal with itself and with other signals. The latter are of major interest, since they carry information on interactions between magnetic nuclei and allow to determine the connectivity and structure of the molecule. Indeed, these peaks are due to the magnetization transfer between the nuclei, obtained by means of a series of pulses during the mixing time. The magnetization can be transferred both by scalar (through-bond) coupling and dipolar (through-space) interactions.

Here a few common 2D NMR techniques are briefly illustrated in which the scalar coupling mechanism is employed. These techniques were used in the last chapter of this Thesis.

The simplest 2D experiment is the Correlation Spectroscopy (COSY) pulse sequence, which is shown in Fig. 2.10:

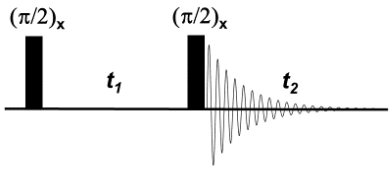

Figure 2.10. COSY pulse sequence.

In this experiment, only correlations between protons which are up to three bonds apart can be observed. By studying the correlations between all the different signals, the connectivity between the functional groups can be often successfully determined. However, for an unambiguous analysis the use of a complementary technique is often necessary, specifically the Total Correlation Spectroscopy (TOCSY). The TOCSY pulse sequence is shown in Fig. 2.11:

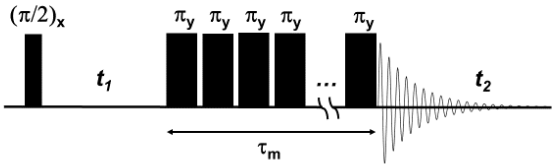

Figure 2.11. COSY pulse sequence.

The sequence is very similar to the COSY sequence. However, in this case the spin lock series of pulses spreads the magnetization over the whole scalar-coupled spin systems. Therefore, the correlations between all the protons belonging to the same spin system are visible, in addition to those bond to the directly connected carbons.

Both COSY and TOCSY are homonuclear techniques, since only proton nuclear spins are manipulated by the pulse sequences. In addition, more advanced, heteronuclear techniques are also available, in which magnetization is transferred between different nuclei, typically ^{1}H and ^{13}C.

Similarly to the homonuclear techniques we have just seen, Heteronuclear Single Quantum Correlation (HSQC) and Heteronuclear Multiple Quantum Correlation (HMQC) pulse sequences give rise to off-diagonal correlation peaks between a carbon signal and its directly bond protons, while the Heteronuclear Multiple Bond Correlation (HMBC) technique provides correlations with all the protons pertaining to the same spin system. The HMQC and HMBC pulse sequences, used in the present work, are shown in Fig. 2.12:

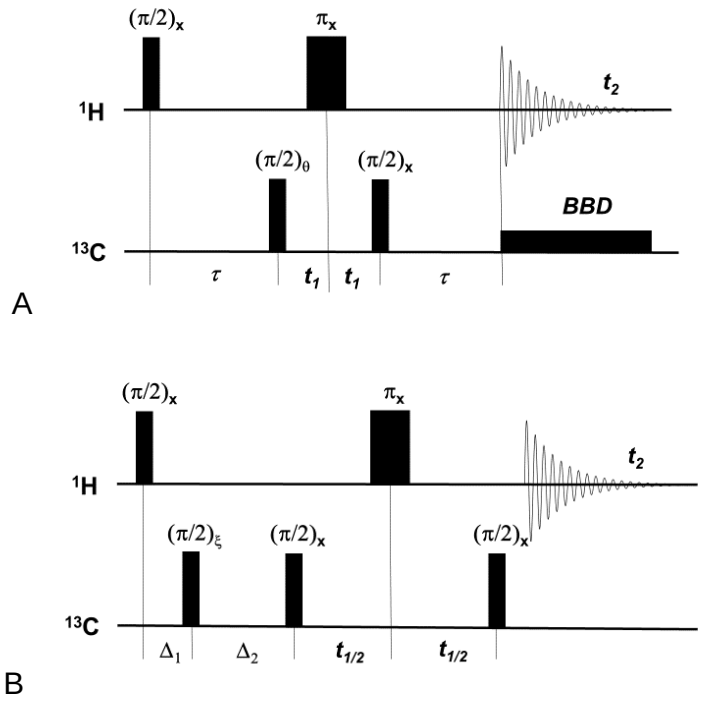

Figure 2.12. HMQC (A) and HMCB (B) pulse sequences.

2.3.3. Hyperfine shift in paramagnetic NMR.

Since NMR is a widely known and used technique, further details on general NMR basics will not be reported here and reader is addressed to the huge amount of literature on the subject.[19-21] Here we will focus only on the peculiar features observed in the NMR spectra of paramagnetic compounds.

The unpaired electron spin affects both the position (chemical shift) of the NMR signal and its linewidth. Both these effects are due to the hyperfine coupling between nuclear and electronic spins, which, as we saw in previous paragraphs, gives rise to line splitting in CW-EPR and ENDOR. The reason why in NMR the hyperfine coupling manifests as a line shift and broadening, and not a splitting, as in EPR, is the spin relaxation rate. It was already mentioned that electronic spin relaxation is much faster than nuclear spin relaxation. Therefore, from the electron point of view, the electron spin always sees a definite nuclear spin. This leads to different situations, depending on the relative orientations of the electron and nuclear spins and consequently to a line splitting. This effect is observed in CW-EPR and ENDOR spectra. Instead, from the point of view of the nucleus, because of the fast electron spin relaxation, the nuclear spin sees an average population of electron spin levels. For a

nucleus coupled to an electron spin only by isotropic hyperfine coupling, in the high field approximation ($\gamma\mu_B B >> A$) the hyperfine coupling contribution to the chemical shift is given by[22]

$$\delta^{con} = \frac{A}{\hbar \gamma_I B} \langle S_z \rangle \tag{2-72}$$

Using the statistical mechanics for calculating the average of S_z, it turns out that it is given by the Curie law, which is a result already obtained classically previously. Finally, one obtains:

$$\delta^{con} = \frac{A}{\hbar} \frac{g_e \beta S(S+1)}{3\gamma_I k_B T} \tag{2-73}$$

Another contribution to the hyperfine shift is the pseudocontact interaction, due to the dipolar coupling between electron and nuclear magnetic moments. This interaction is distance- and orientation-dependent and is averaged in fluid solution.

2.3.4. Nuclear spin relaxation in paramagnets

The presence of electron spins considerably increases the relaxation rate of nuclear spins. Enhanced relaxation affects the linewidth of NMR signals, analogously to what was reported for the EPR lines in the previous paragraph, leading to a remarkable line broadening in paramagnetic compounds.

Several relaxation mechanisms are responsible for this effect. The first one is due to electron spin relaxation. We just saw that the electron spin relaxation is significantly faster than the nuclear one. Therefore, from the point of view of the nuclear spin, the electron spins will switch continuously between the different M_S states. Changes of M_S imply changes of the orientation of electron magnetic moment, which, in turn, give rise to fluctuating magnetic fields, causing nuclear spin relaxation. As for the chemical, shifts, also the relaxation mechanisms involve both Fermi contact and dipolar interaction. Another mechanism contributing to the overall relaxation rate is the molecular rotation. If the rotation is faster than spin relaxation, the nucleus sees the electron spin with the same M_S, but in different orientations. This provides an additional fluctuating magnetic field causing the nuclear spin relaxation. Other mechanisms involve the interaction of the nuclear spin with the magnetic moment, arising from the average Boltzmann population of the Zeeman levels and also changing orientation with rotation (Curie spin relaxation) and the chemical exchange.

The temperature dependence of the relaxation rate must be underlined, which causes a line narrowing at high temperature. This and the other phenomena reported above will be used in

the following chapter, dealing with the experimental results on Au_{25} clusters protected with different alchyl ligands in solution.

2.4 References

1. Buschow, K.H.J., de Boer, F.R. *Physics of Magnetism and Magnetic Materials*; Springer: Berlin, 2003.

2. Ashcroft, N.W., Mermin, N.D. *Solid State Physics*; Saunders College: Philadelphia, 1976.

3. Orchard, A.F. *Magnetochemistry*; Oxford University Press: Oxford, 2003.

4. Aharoni, A. *Introduction to the theory of ferromagnetism*; 2 ed., Oxford University Press, 2001.

5. Atherton, N.; Atherton, M.W. *Electron spin resonance: theory and applications*, Ellis Horwood Chichester 1973.

6. Brustolon, M. *Electron paramagnetic resonance: a practitioner's toolkit*, John Wiley & Sons 2009.

7. Weil, J.A., Bolton, J.R. *Electron paramagnetic resonance: elementary theory and practical applications*, Wiley-Interscience 2007.

8. Vonsovskii, S.V. *Ferromagnetic Resonance*, Pergamon: Oxford, 1966**.**

9. Berger, R.; Bissey, J.-C.; Kliava, J. Lineshapes in magnetic resonance spectra *J. Phys.: Condens. Matter*, **2000**, *12*, 9347–9360.

10. Morais, P.C.; Tronconi, A.L.; Neto, K.S. Electron paramagnetic resonance linewidth of superparamagnetic particles *J. Appl. Phys.*, **1984**, *55*, 10.

11. Raikher, Y.L.; Stepanov, V.I. Ferromagnetic resonance in a suspension of single-domain particles. *Phys. Rev. B*, **1994**, *50 (9)*, 6250-6259.

12. Berger, R.; Kliava, J.; Bissey, J.-C.; Baïetto, V. Magnetic resonance of superparamagnetic iron-containing nanoparticles in annealed glass. *J. Appl. Phys.*, **2000**, *87*, 7389.

13. Fittipaldi, M.; Sorace, L.; Barra, A.-L.; Sangregorio, C.; Sessoli, R.; Gatteschi, D. Molecular nanomagnets and magnetic nanoparticles: the EMR contribution to a common approach *Phys. Chem. Chem. Phys.*, **2009**, *11*, 6555-6568

14. Noginova, N.; Chen, F.; Weaver, T.; Giannelis, E.P.; Bourlinos, A.B. Atsarkin, V.A. Magnetic resonance in nanoparticles: between ferro- and paramagnetism. *J. Phys. Condens. Matter.* **2007**, *19(24)*, 246208.

15. Schweiger, A.; Jeschke. G. *Principles of pulse electron paramagnetic resonance*,

Oxford University Press, Great Clarendon Street, Oxford, OX 2 6 DP, UK, 2001.

16. Schweiger, A. Pulsed Electron Spin Resonance Spectroscopy: Basic Principles,Techniques, and Examples of Applications [New Analytical Methods (43)], *Angew. Chem. Intern. Ed. in En.***1991**, *30*, 265-292.

17. Davies, E. A new pulse ENDOR technique, *Phys. Lett. A*. **1974** *47*, 1-2.

18. Mims, W. Pulsed ENDOR experiments, *Proc. Royal Soc. Lon..Ser. A, Math. Phys. Sci.* **1965**, 452-457.

19. Levitt, M.H. *Spin Dynamics: Basics of Nuclear Magnetic Resonance* John Wiley & Sons Inc Print on; 2nd ed. 2008.

20. Keeler, J. *Understanding NMR Spectroscopy* 2nd Ed. John Wiley & Sons Inc Print on; 2010.

21. Gunther, W. *NMR Spectroscopy: Basic Principles, Concepts and Applications in Chemistry*, 3rd Ed. John Wiley & Sons Inc Print on; 2010.

22. Bertini, I.; Luchinat, C.; Parigi, G. *Solution NMR of Paramagnetic Molecules Applications to Metallobiomolecules and Models Current Methods in Inorganic Chemistry* Elesevier, Amsterdam, 2001

Chapter 3.
A Magnetic Look into the Protecting Layer of Au_{25} Clusters

3.1. Introduction

As described in detail in Chapter 1, in monolayer-protected gold clusters (MPCs) with gold cores of diameter <1.6 nm the number of Au atoms is sufficiently small to make them display molecular features. This makes the study of their fundamental properties as particularly fascinating and often intriguing.[1-5] Instrumental to these studies has been the possibility of preparing molecule-like gold MPCs in an atomically precise form, as assessed by mass spectrometry and single-crystal X-ray crystallography.[6] The structure of $Au_{25}(SR)_{18}$ clusters, by far the most well known among molecular clusters, is based on a 13 gold-atom icosahedral core surrounded by 6 $Au_2(SR)_3$ units, with minor differences induced by the charge state (-1, 0, and +1) and the ligands,[7-11] even when the linear polymer $(Au_{25})_n$ forms.[12] Several molecular features of $Au_{25}(SR)_{18}$ clusters have been studied in detail, such as the characteristic electrochemical behavior[13-15] and charge-dependent optical[16] and nuclear magnetic resonance (NMR) patterns.[17] Studies of their photophysical behavior,[18-21] chirality,[22] electron-transfer and redox-catalysis properties,[23-27] have been described. Several theoretical studies have been carried out and reviewed.[28-30] Whereas the as prepared anionic cluster $Au_{25}(SC_2H_4Ph)_{18}^-$ is a diamagnetic species, the corresponding, indefinitely stable neutral form $Au_{25}(SC_2H_4Ph)_{18}^0$ is paramagnetic. The effect of the unpaired electron was detected by ^1H and ^{13}C NMR at room temperature[17] or electron paramagnetic resonance (EPR) at temperatures typically lower than 100 K.[16,31] The Jin's group showed that the magnetic state can be switched off by reduction to diamagnetic $Au_{25}(SC_2H_4Ph)_{18}^-$.[31] Similarly, we demonstrated by both NMR[17] and EPR[16] that oxidation to cation $Au_{25}(SC_2H_4Ph)_{18}^+$ generates a diamagnetic species. DFT calculations indicated that the magnetic behavior is controlled by significant splitting of the relevant orbital energy levels.[17]

The NMR spectrum of the three charge states evidenced very profound charge-induced variations in the position and shape of the peaks.[17] Most notably, some of the ligands' resonances undergo a significant downfield shift upon formation of paramagnet $Au_{25}(SR)_{18}^0$.

This was first observed by the Murray's group[32] and then perfected by us through identification of all resonances as a function of temperature or ligand type.[10,12,17,26] In this context, it is important to stress that the 18 thiolated ligands present in the 6 $Au_2(SR)_3$ half-crowns (or staples) capping the central Au_{13} core split into a group of 12 inner and 6 outer ligands. Here, inner refers to the fact that the two terminal SR groups of –(SR)–Au–(SR)–Au–(SR)– also bind to Au_{13}, whereas outer refers to the outmost, remaining thiolate of the half-crown. 1D and 2D NMR analysis allowed distinguishing between the two ligands' families, also on a quantitative basis. There is a general consensus that the properties of molecular MPCs mostly depend on the number and relative position of the gold atoms.[5,6] On the other hand, NMR evidence and corresponding DFT calculations indicated that the singly occupied molecular orbital (SOMO) spreads onto the first groups of the thiolated ligands. Very recent studies also concluded that the ligand structure/composition can be a factor affecting the optical behavior of molecular and larger MPCs.[33,34] These results thus indicate that the highest occupied and the lowest unoccupied MOs (HOMOs and LUMOs) are not just limited to the Au_{13} core, as often implicitly assumed, but rather involve to some extent the ligands. Another example is provided by the optical spectrum of Au_{25} capped by thiophenolate-type ligands, which shows band shifts[35] and a small decrease of the HOMO-LUMO gap compared to that of Au_{25} capped by alkanethiolates, for which the spectrum does not depend on the ligand length:[26] this effect shows that changing the carbon type at the α position to sulfur affects the electronic properties of the cluster. The way by which the capping ligands interact with the core, the shape and spreading of the chemically relevant orbitals, and the actual environment experienced by molecules or ions penetrating the monolayer[15] are expected to be crucial factors also for understanding the catalytic effects of ultrasmall clusters[27] on a truly molecular basis.

Very recently, we illustrated the remarkable potentialities of pulse electron nuclear double resonance (ENDOR).[10] This technique is a very sensitive way of performing ENDOR[36] and is meant to characterize hyperfine coupling (A) between an unpaired electron and nuclei nearby. This interaction consists of isotropic and anisotropic parts: the former is a through-bond contribution that depends on the number and type of bonds involved, whereas the latter depends on both through-bond and through-space (electron-dipole/nuclear-dipole) interactions. In the ENDOR spectrum, a doublet of lines is associated with a magnetic nucleus with nuclear spin $I = 1/2$. When $A < 2\nu$, where ν is the nucleus Larmor frequency□

the doublet is centered at v and the separation between the two lines is A. On the other hand, for $A > 2v$ the doublet is centered at $A/2$ and the separation between the two lines is $2v$. The Larmor frequency v depends only on the magnetic field B at which the ENDOR spectrum is recorded, according to the relation $v = \gamma_I B/(2\pi)$, where γ_I is the nucleus gyromagnetic ratio. For larger nuclear spins, such as for ^{197}Au whose $I = 3/2$, the quadrupolar and hyperfine interactions split the ENDOR lines further. This was experimentally verified in the ENDOR analysis of $Au_{25}(SEt)_{18}^0$.[10] The hyperfine interaction between the unpaired electron and the gold atoms could be assessed quantitatively, and the ENDOR results could be nicely reproduced by density functional theory (DFT) calculations, which could be particularly precise due to the very small thiolate used.

Here, we describe a methodology and results that accurately enabled assessing the spin density and, therefore, the distribution of the SOMO in $Au_{25}(SR)_{18}^0$ clusters. We employed pulse ENDOR to study the interaction of the unpaired electron with the protons of the alkanethiolate ligands, an approach that was never described before. The resulting information was compared with that obtained by ^{1}H NMR spectroscopy of how and how much the chemical shifts change when the charge state of the cluster is varied from -1 to 0. DFT calculations provided useful hints in understanding differences between the ENDOR and NMR results. We noted that by reducing the temperature to 5 K, a pronounced increase of spin-polarization occurs. It is thus shown that the unpaired electron can be used as a particularly sensitive probe of the main structural features of the interface between the metal core and the capping ligands, leading to establish a very precise and consistent picture of these complex systems.

3.2 Results and Discussion

We used a series of related $Au_{25}(SR)_{18}^{0/-1}$ clusters. The ligands were chosen to provide a progressive variation of the chain length from two to four carbon atoms, as shown in Chart 3.1. The single crystal structures of the SEt and SBu protected clusters were available from previous work, whereas that of $Au_{25}(SPr)_{18}^0$ is described here for the first time. The effect of branching was checked by changing a hydrogen atom with a methyl group at the β position: for this ligand, 2-methyl-1-propanethiolate, we will use the notation SMePr to stress both methyl branching and that the fully extended chain length is the same as that of SPr.

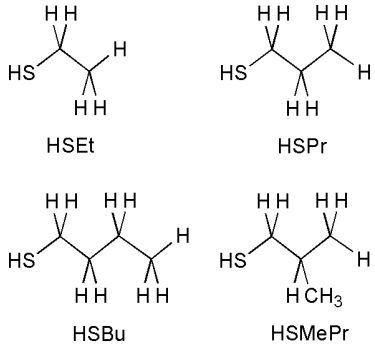

Chart 1. Thiols.

Starting from sulfur, the carbon atoms and associated hydrogen atoms are defined as α, β, γ, and δ; the second CH_3 group of HSMePr is denoted as γ′. Monodisperse samples of the four $Au_{25}(SR)_{18}^-$ clusters were prepared, and the clusters were oxidized according to a method already described.[10] Full characterization of the purified neutral clusters was carried out by a combination of matrix-assisted laser desorption ionization time-of-flight mass spectrometry, UV-vis absorption spectroscopy, differential-pulse voltammetry, and ^{1}H NMR spectroscopy techniques. $Au_{25}(SPr)_{18}$ and $Au_{25}(SMePr)_{18}$ are new clusters.

3.2.1 Electrochemistry

The experiments were conducted by cyclic voltammetry, using a 1 mM solution of the cluster. The peak current (i_p) measured at low scan rates (v) allowed determining the diffusion coefficient D by using the equation that relates $i_p/v^{1/2}$ to $D^{1/2}$.[36] The radius of the MPC (r_{MPC}) was calculated from D by using the Stokes–Einstein–Sutherland equation, $D = k_B T/6\pi\eta r_{MPC}$, where k_B is the Boltzmann constant and η is the solvent viscosity. In Figure 3.1, the D and the r_{MPC} values are compared with those, previously obtained,[15] of $Au_{25}(SEt)_{18}$, $Au_{25}(SPr)_{18}$, and $Au_{25}(SBu)_{18}$.

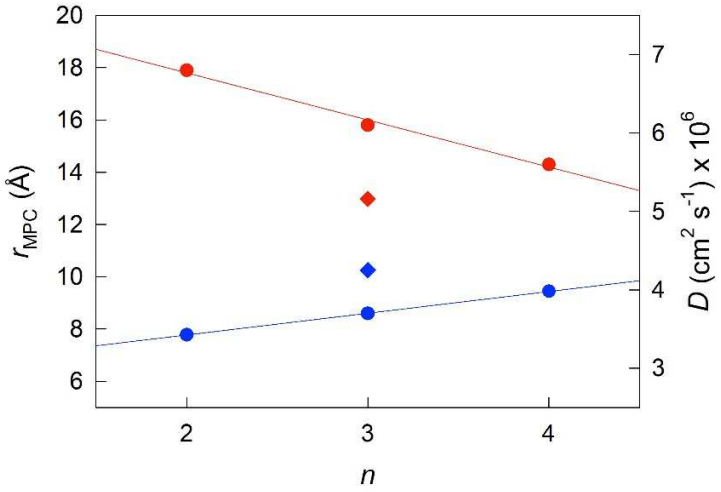

Figure 3.1. Dependence of the diffusion coefficient D (red circles, scale on right) and the MPC radius r_{MPC} (blue circles, scale on left) on the number of carbon atoms (n) forming the main ligand chain.

3.2.2 X-ray diffractometry

$Au_{25}(SPr)_{18}^0$ crystallizes (Fig. 3.2c) in trigonal space group P-3, with three cluster molecules in the unit cell. This MPC is highly symmetric with a 3-fold rotoinversion axis running through the central Au atom. As for the other known $Au_{25}(SR)_{18}$ structures,[7-12] the 25 gold atoms can be regarded as being formed by two shells composed by an Au_{13} icosahedral core, consisting of a central Au atom with 12 Au atoms directly interacting with it, and an outer shell of 12 Au atoms bound to thiolate groups to form –(SR)–Au–(SR)–Au–(SR)– motifs (Fig. 3.2a): The Au-Au bond- strength order is $Au_{central}$-Au_{ico} > Au_{ico}-Au_{ico} > Au_{ico}-Au_{staple}. These bonds correspond to average Au-Au

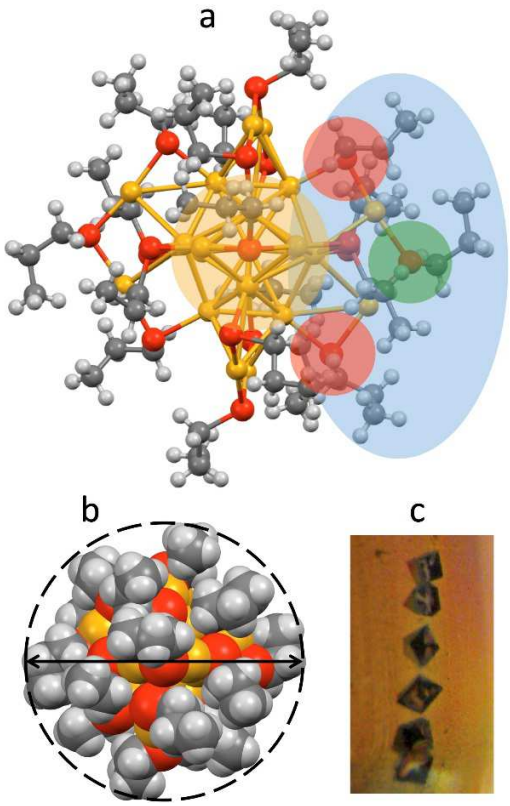

Fig. 3.2. (a) Projection showing the X-ray crystal structure of $Au_{25}(SPr)_{18}$. Au = yellow, S = red, C = gray, H = white. For clarity, the icosahedral core (yellow), one of the staples (blue), and the corresponding inner- (red) and outer-ligands (green) are highlighted. The positions of the chain carbons with respect to sulfur are also indicated. (b) Space-filling model; the dashed line and the arrow highlight the approximately spherical shape and the average diameter (1.72 nm). (c) Single crystal bricks (ca. 1 mm) from which the structure was solved.

bond lengths of 2.784, 2.927 and 3.163 Å, respectively. It is worth noting that there is a significantly shorter Au_{ico}-Au_{ico} bond (2.7746 Å) and a relatively longer Au_{ico}-Au_{staple} bond (3.3206 Å). We found this feature also in the closely related SEt and SBu analogues.[10,12] Concerning the orientation of the carbon chains with respect to the plane of the same half-crown, $Au_{25}(SPr)_{18}^0$ features the first case of a Au_{25} cluster where only alternate orientations are observed. The space-filling model (Fig. 3.2b) illustrates that the ligands are quite folded around the gold core, thereby forming a relatively thin monolayer, at least in the solid state. Evidence for the formation of quite thin capping monolayers was previously gathered also in solution, through electron-transfer measurements[26] of a series of monodisperse $Au_{25}(SC_nH_{2n+1})_{18}$ clusters with n varying from 2 to 18. Of particular importance for the current investigation, from the structures of $Au_{25}(SEt)_{18}^0$, $Au_{25}(SPr)_{18}$, and $Au_{25}(SBu)_{18}^0$ we could calculate the average distances (mediated over the six staples) of the corresponding hydrogen atoms for both the inner and outer ligands. In this connection, it is worth noting that

the average radii (r_{MPC}) of these three clusters nicely match those calculated from the Stokes-Einstein-Sutherland equation, $D = k_B T/6\pi\eta r_{MPC}$, where D is the electrochemically determined diffusion coefficient,[15] k_B is the Boltzmann constant, and η is the solvent viscosity: for $Au_{25}(SEt)_{18}^0$, $Au_{25}(SPr)_{18}$, and $Au_{25}(SBu)_{18}^0$ we find the couple of values 8.3 and 7.8, 8.6 and 8.6, 10.2 and 9.4 Å, respectively.

3.2.3 NMR spectroscopy

The following NMR spectroscopy data (δ) were obtained in benzene-d_6 at 298 K. For the four anionic clusters, the ^{1}H NMR signals pertaining to the tetra-*n*-octylammonium cation, *n*-Oct_4N^+, are found at: 3.09 (8H, 4 NCH_2), 1.55, 1.45, 1.40, 1.39, 1.37 and 1.41 (48H, 4 x 6CH_2), 0.98 (12H, 4CH_3). As already observed,[10] the ^{13}C NMR signals for the α_{in} and β_{in} resonances occur at very large absolute δ values whose determination would require exceedingly long acquisition times, which goes beyond the scope of the present investigation.

$Au_{25}(SEt)_{18}$

[*n*-Oct_4N^+][$Au_{25}(SEt)_{18}^-$].^{1}H NMR: : 3.879 (q, 24H, α_{in}), 3.139 (q, 12H, α_{out}), 1.710 (t, 36H, β_{in}), 1.362 (t, 18H, β_{out}). ^{13}C NMR: 33.0 (12C, α_{in}), 28.6 (6C, α_{out}), 21.8 (12C, β_{in}), 19.5 (6C, β_{out}).

$Au_{25}(SEt)_{18}^0$.^{1}H NMR: 25.4 (very br s, 24H, α_{in}), 4.900 (br s, 12H, α_{out}), 4.121(br s, 36H, β_{in}), 1.19 (t, 18H, β_{out}). ^{13}C NMR: 35.5 (6C, α_{out}), 27.9 (6C, β_{out}).

$Au_{25}(SPr)_{18}$

[*n*-Oct_4N^+][$Au_{25}(SPr)_{18}^-$]. ^{1}H NMR: 3.885 (t, 24H, α_{in}), 3.15 (t, 12H, α_{out}), 2.213 (sextet, 24H, β_{in}), 1.894 (sext, 12H, β_{out}), 1.227 (t, 36H, γ_{in}), 0.980 (t, 18H, γ_{out}). ^{13}C NMR: 40.23 (12C, α_{in}), 36.18 (6C, α_{out}), 30.15 (12C, β_{in}), 28.36 (6C, β_{out}), 14.39 (6C, γ_{out}), and 13.90 (12C, γ_{in}).

$Au_{25}(SPr)_{18}^0$. ^{1}H NMR: 25.0 (very br s, 24H, α_{in}), 4.924 (br s, 12H, α_{out}), 3.381 (br s, 24H, β_{in}), 2.132 (br t, 36H, γ_{in}), 1.689 (sext, 12H, β_{out}), 1.019 (t, 18H, γ_{out}). ^{13}C NMR: 40.22 (6C, α_{out}), 36.22 (6C, β_{out}), 23.08 (12C, γ_{in}) and 14.39 (6C, γ_{out}).

$Au_{25}(SBu)_{18}$

[*n*-Oct_4N^+][$Au_{25}(SBu)_{18}^-$]. ^{1}H NMR: 3.933 (t, 24H, α_{in}), 3.226 (t, 12H, α_{out}), 2.207 (m, 24H, β_{in}), 1.912 (m, 12H, β_{out}), 1.732 (m, 24H, γ_{in}), 1.485 (m, 12H, γ_{out}), 1.072 (t, 36H, δ_{in}), 0.881 (t, 18H, δ_{out}). ^{13}C NMR: 29.24 (12C, α_{in}), 38.92 (6C, α_{out}), 40.98 (12C, β_{in}), 31.57 (6C, β_{out}), 22.71 (12C, γ_{in}), 21.85 (6C, γ_{out}), 13.78 (6C, δ_{out}), and 14.37 (12C, δ_{in}).

$Au_{25}(SBu)_{18}^0$. ^{1}H NMR: 25.0 (very br s, 24H, α_{in}), 5.067 (m, 12H, α_{out}), 3.484 (br m, 24H, β_{in}), 1.739 (m, 12H, β_{out}), 2.562 (m, 24H, γ_{in}), 1.561 (m, 12H, γ_{out}), 1.595 (br t, 36H, δ_{in}), 0.779 (t, 18H, δ_{out}). ^{13}C NMR: 38.3 (6C, α_{out}), 45.03 (6C, β_{out}), 31.09 (12C, γ_{in}), 23.3 (6C, γ_{out}), 17.19 (12C, δ_{in}), and 14.75 (6C, δ_{out}).

$Au_{25}(SMePr)_{18}$

[*n*-Oct_4N^+][$Au_{25}(SMePr)_{18}^-$]. ^{1}H NMR: 3.840 (br s, 24H, α_{in}), 3.084 (d, 12H, α_{out}), 2.387 (12H, sept, β_{in}), 2.156 (6H, sept, β_{out}), 1.353 (72H, d, γ_{in}), 1.113 (36H, d, γ_{out}). ^{13}C NMR: 46.6 (6C, α_{in}), 42.6 (6C, α_{out}), 34.5 (12C, β_{in}), 33.2 (6C, β_{out}), 22.6 (24C, γ_{in}), 22.1 (12C, γ_{out}).

$Au_{25}(SMePr)_{18}^0$. ^{1}H NMR: 14.39 (very br s, 24H, α_{in}), 4.973 (br s, 12H, α_{out}), 2.24 (12H, sept, β_{in}), 1.856 (6H, sept, β_{out}), 2.31 (72H, broad s, γ_{in}), 1.151 (36H, d, γ_{out}). ^{13}C NMR: 44.01 (6C, α_{out}), 31.2 (6C, β_{out}), 22.1 (24C, γ_{in}), 15.2 (12C, γ_{out}).

The 12 inner and the 6 outer ligands experience a different chemical environment and thus show distinct NMR spectroscopy signals. When the cluster is in its paramagnetic state, differences are enhanced, especially for those resonances related to the proton and carbon atoms closer to the gold core. We studied the spectra of the selected clusters in either charge state, using benzene-d_6 as the solvent. Fig. 3.3 illustrates for the case of $Au_{25}(SPr)_{18}$ the most salient differences in chemical shift as one goes from the paramagnetic to the diamagnetic states.

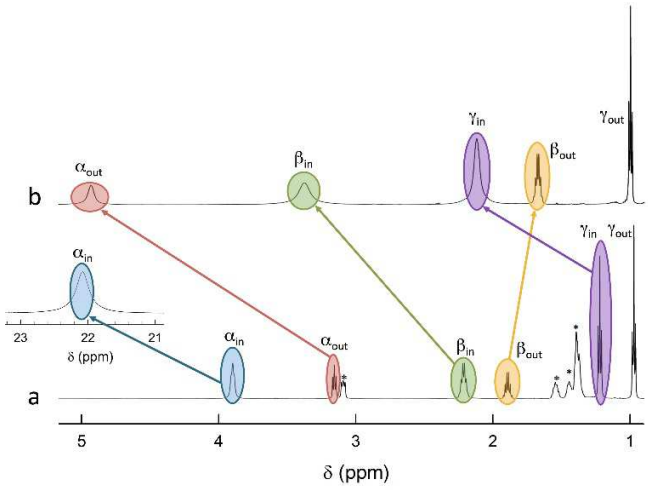

Fig. 3.3. (a) ^{1}H NMR spectrum of [n-Oct$_4$N$^+$] [Au$_{25}$(SPr)$_{18}^-$] at 25 ℃. The peaks marked with a star refer to n -Oct$_4$N$^+$. (b) ^{1}H NMR spectrum of Au$_{25}$(SPr)$_{18}^0$ at 25 ℃; the portion of the spectrum showing the (α-CH)$_{in}$ protons (at 70 ℃) is offset and enlarged.

The most significant effect of the one-electron oxidation of the native cluster is to shift downfield the NMR peaks pertaining to the protons in positions α, β and γ (except for Au$_{25}$(SEt)$_{18}$, which has no γ groups) of the inner ligands, and in positions α and (to a small extent) γ of the outer ligands; instead, the β protons of the outer ligands undergo an upfield shift. As to Au$_{25}$(SMePr)$_{18}$, we observed the same charge-dependent effect (Fig. 3.4). For the three clusters of known crystallographic structure, the chemical shift differences ($\Delta\delta = \delta_{radical} - \delta_{anion}$) are displayed in Fig. 3.5 as a function of the average distance between the central Au atom to the two or three hydrogen atoms of the specific resonance, averaged for the six half-crowns. The positive differences roughly obey an exponential dependence on distance (taking into account the error on the latter), as already commented upon for Au$_{25}$(SBu)$_{18}$.[12] The NMR shifts observed upon changing the charge state from -1 to 0 are related to the contact interaction of the nuclear magnetic moments with the unpaired electron, and can thus be taken as a measure of how far the spin density spreads outside the Au$_{13}$ core. [17]

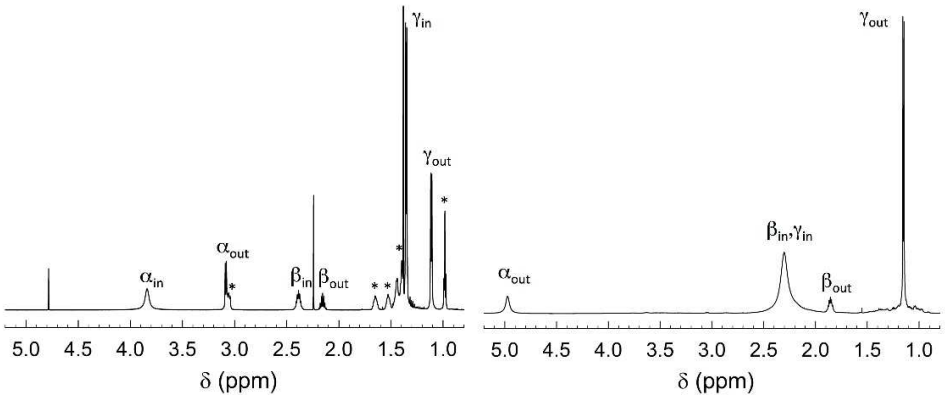

Figure 3.4. a) ^{1}H NMR spectrum of 3 mM [*n*-Oct$_4$N$^+$][Au$_{25}$(SMePr)$_{18}^-$] at 25℃. The asterisks mark the *n*-Oct$_4^+$ cation. b) ^{1}H NMR spectrum of 3 mM Au$_{25}$(SMePr)$_{18}^0$ at 25℃. The overlapping β_{in} and γ_{in} resonances split at higher temperatures.

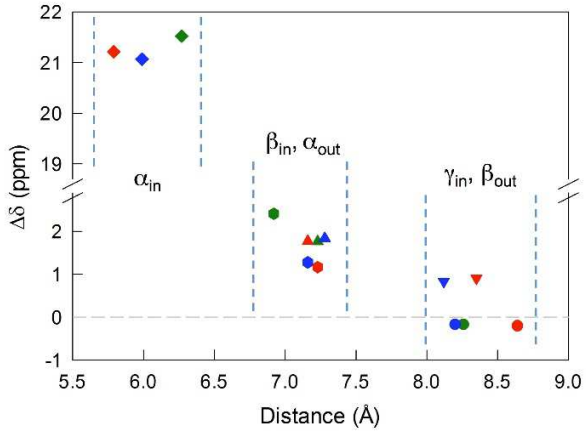

Fig. 3.5. Plot of the Δδ values for Au$_{25}$(SR)$_{18}$, obtained at 298 K, against the average crystallographic distance of the specific proton type from the central Au atom. The color codes for the R groups are: Et, green; Pr, red; Bu, blue. The resonances are indicated as: (α-CH)$_{in}$, ◆; (β-CH)$_{in}$, ⬢; (α-CH)$_{out}$, □; (γ-CH)$_{in}$, □; (β-CH)$_{out}$, □. For clarity, a scale break has been inserted into the Δδ scale and vertical dashed lines group the protons at similar distances.

The Δδ values can be used to estimate the isotropic hyperfine coupling constant *A* according to the relationship (eq. 3-1):[37]

$$\Delta\delta = Ag\beta_e\, S(S+1)/(3\hbar\gamma_I k_B T) \qquad (3\text{-}1)$$

where $\hbar$ is the reduced Planck constant, β_e is the Bohr magneton, γ_I is the proton nuclear gyromagnetic ratio, and *g* is the isotropic *g* value for the unpaired electron. The latter can be exactly calculated as $g = (g_{xx}+g_{yy}+g_{zz})/3$, where g_{xx}, g_{yy}, and g_{zz} are the main values of the *g*-

tensor. For $Au_{25}(SBu)_{18}^0$, they are 1.78, 2.40, and 2.56, respectively,[12] and the same values are found for $Au_{25}(SEt)_{18}^0$:[10] therefore, we used these values also for the other clusters. By using these values and 298 K, $\Delta\delta$ can be expressed as 29.74 (ppm/MHz) $\times$ *A* (MHz). We note that eq. 1 holds true provided the pseudo-contact contribution to the chemical shifts of the ligand protons is negligible; this is indeed supported by the remarkable agreement observed between NMR chemical shifts and DFT calculations of the electron spin-density.[17] Table 3.1 shows the so-calculated *A* values.

3.2.4 ENDOR spectroscopy

ENDOR experiments were carried out at 5 K in frozen solutions of 0.5 mM $Au_{25}(SR)_{18}^0$ in toluene. The spectra of the four clusters (Fig. 3.6) show a large background between 2 and 20 MHz due to an ENDOR line of gold atoms.[10] By focusing on the region between 8 and 16 MHz, as shown in Fig. 3.7a for $Au_{25}(SBu)_{18}^0$, one can notice the presence of three symmetrical line doublets centered at the Larmor frequency *v*. For the protons at a magnetic field of 0.29 T, the latter is 12.34 MHz, which is the frequency at which ENDOR spectra were acquired. The three symmetric doublets are marked by brown (outer), green (middle), or red (inner) lines. Similar ENDOR spectra are observed for the other clusters capped by linear-chain thiolates, but the relative intensity ratios are different.

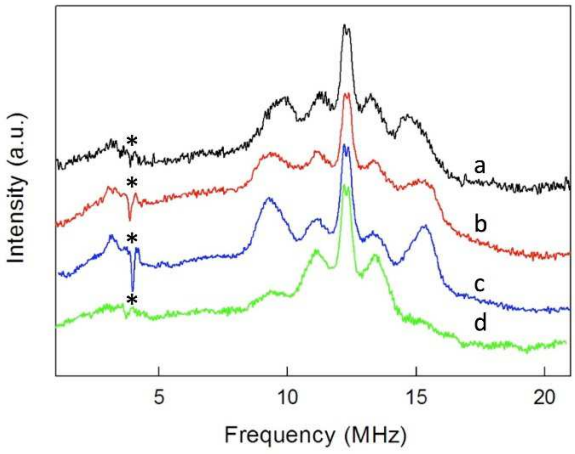

Fig. 3.6. ^{1}H ENDOR spectra of (a) $Au_{25}(SEt)_{18}^0$, (b) $Au_{25}(SPr)_{18}^0$, (c) $Au_{25}(SBu)_{18}^0$, and (d) $Au_{25}(SMePr)_{18}^0$ in toluene solution at 5 K. For clarity, the spectra have been offset. The asterisks mark background signals due to the probe head.

Table 3.1. ENDOR parameters obtained from the simulation of the spectra of $Au_{25}(SR)_{18}^{0}$.

Ligand and position	A[a](kHz)	A[b,c](MHz)	T_{xx}[c,d](MHz)	T_{yy}[c,d](MHz)	T_{zz}[c,d](MHz)	n[e]
SEt						
(α-CH)$_{in}$	723	n.d.[f]				
(β-CH)$_{in}$	81.1	-4.2	-0.8	-2.7	3.5	36
(α-CH)$_{out}$	59.2	-1.6	-0.9	-0.9	1.8	12
(β-CH)$_{out}$	-5.78	-0.24	-0.01	-0.01	0.02	14[g]
SPr						
(α-CH)$_{in}$	713	n.d.[f]				
(β-CH)$_{in}$	39.3	-5.5	-1.2	-1.2	2.4	24
(α-CH)$_{out}$	59.7	-2.0	-0.6	-0.6	1.2	12
(β-CH)$_{out}$	-6.89	-0.24	-0.01	-0.01	0.02	14[g]
SBu						
(α-CH)$_{in}$	708	n.d.[f]				
(β-CH)$_{in}$	42.9	-5.8	-0.7	-0.7	1.4	24
(α-CH)$_{out}$	61.9	-2.2	-0.6	-0.6	1.2	12
(β-CH)$_{out}$	-5.82	-0.24	-0.01	-0.01	0.02	16[g]
SMePr						
(α-CH)$_{in}$	355	n.d.[f]				
(β-CH)$_{in}$	-4.94	-5.5	-1.2	-1.2	2.4	12
(α-CH)$_{out}$	63.5	-2.8	-0.6	-0.6	1.2	12
(β-CH)$_{out}$	-10.1	-0.22	-0.01	-0.01	0.02	28[f]
(γ-CH)$_{in}$	31.9	-2.0	-0.5	-0.5	1.0	60

[a] From NMR measurements at 298 K, using eq. 1. [b] From ENDOR measurements at 5 K. [c] The error associated with the simulations is ca. 0.1 MHz; for (α-CH)$_{in}$ it is ca. 1 MHz. [d] T_{xx}, T_{yy}, and T_{zz} are the main values of the anistropic hyperfine tensor. [e] n is the number of equivalent nuclei corresponding to the best simulation. [f] Not determined: see text. [g] As discussed in the text, this number is affected by further contributions.

The simplest case to analyze is $Au_{25}(SEt)_{18}^0$. The two proton types and the two ligand families generate four groups of equivalent protons: 24 $(\alpha\text{-CH})_{in}$, 36 $(\beta\text{-CH})_{in}$, 12 $(\alpha\text{-CH})_{out}$, and 18 $(\beta\text{-CH})_{out}$. These groups should give raise to four doublets of lines. Three doublets of lines are clearly observed and positioned symmetrically around the Larmor frequency, whereas a broad line is observed at ca. 3 MHz (Fig. 3.6, trace a). The latter could be attributed to the low-frequency part of a doublet of lines pertaining to the most strongly coupled protons. However, the corresponding high-frequency component, which should occur at ca. 21 MHz, is almost undetectable in the spectra (not shown). Furthermore, in the region around 3 MHz hyperfine couplings from ^{13}C nuclei could also contribute. This makes uncertain the attribution of this feature to a proton line.

For $Au_{25}(SEt)_{18}^0$, the average crystallographic distance between the alkanthiolate protons and the central gold atom increases in the order 6.27 $(\alpha\text{-CH})_{in}$, 6.92 $(\beta\text{-CH})_{in}$, 7.23 $(\alpha\text{-CH})_{out}$, and 8.26 Å $(\beta\text{-CH})_{out}$. The $(\alpha\text{-CH})_{in}$ protons are closer to the gold cluster than the other protons and, therefore, they should give rise to the most strongly coupled doublet. In the hypothesis the 3 MHz line is a proton line, this could be related to the $(\alpha\text{-CH})_{in}$, in keeping with the aforementioned NMR results. However, the ENDOR lines of the $(\alpha\text{-CH})_{in}$ protons could be simply undetectable, which is indeed not unusual for strongly coupled nuclei. The $(\beta\text{-CH})_{out}$ protons are located at the largest distance from the center of the Au core and are attributed to the inner lines. The distances characterizing the $(\beta\text{-CH})_{in}$ and $(\alpha\text{-CH})_{out}$ proton groups are quite similar, in the solid state at least, and thus a direct assignment is difficult. This problem can be addressed by simulation of the ENDOR outer, middle and inner doublets. The spectrum of $Au_{25}(SEt)_{18}^0$ is well simulated (red line in Fig. 3.7b) by using the parameters shown in Table 3.1, in which a ratio of 36:12 for the intensity of the outer and middle doublets is considered. This ratio corresponds to the ratio between the nuclei $(\beta\text{-CH})_{in}$ and $(\alpha\text{-CH})_{out}$. The position of the doublets also is in agreement with the crystallographic relative distances from the central Au atom, which for this cluster are 6.92 vs 7.23 Å. This allows assigning the outer, middle and inner doublets to $(\beta\text{-CH})_{in}$, $(\alpha\text{-CH})_{out}$, and $(\beta\text{-CH})_{out}$, respectively. Regarding the $(\beta\text{-CH})_{out}$ protons, the simulation provides a number, 14, that does not fully agree with that expected, 18. For weak couplings, however, some differences are not unusual because the ENDOR selectivity effect reduces the ENDOR line intensity, whereas the presence of the proton-free Larmor line (a single line associated with the solvent protons) could contributes to

the inner doublet by increasing the line intensity.[38] Depending on the prevailing effect, either a decrease or an increase in intensity may occur.

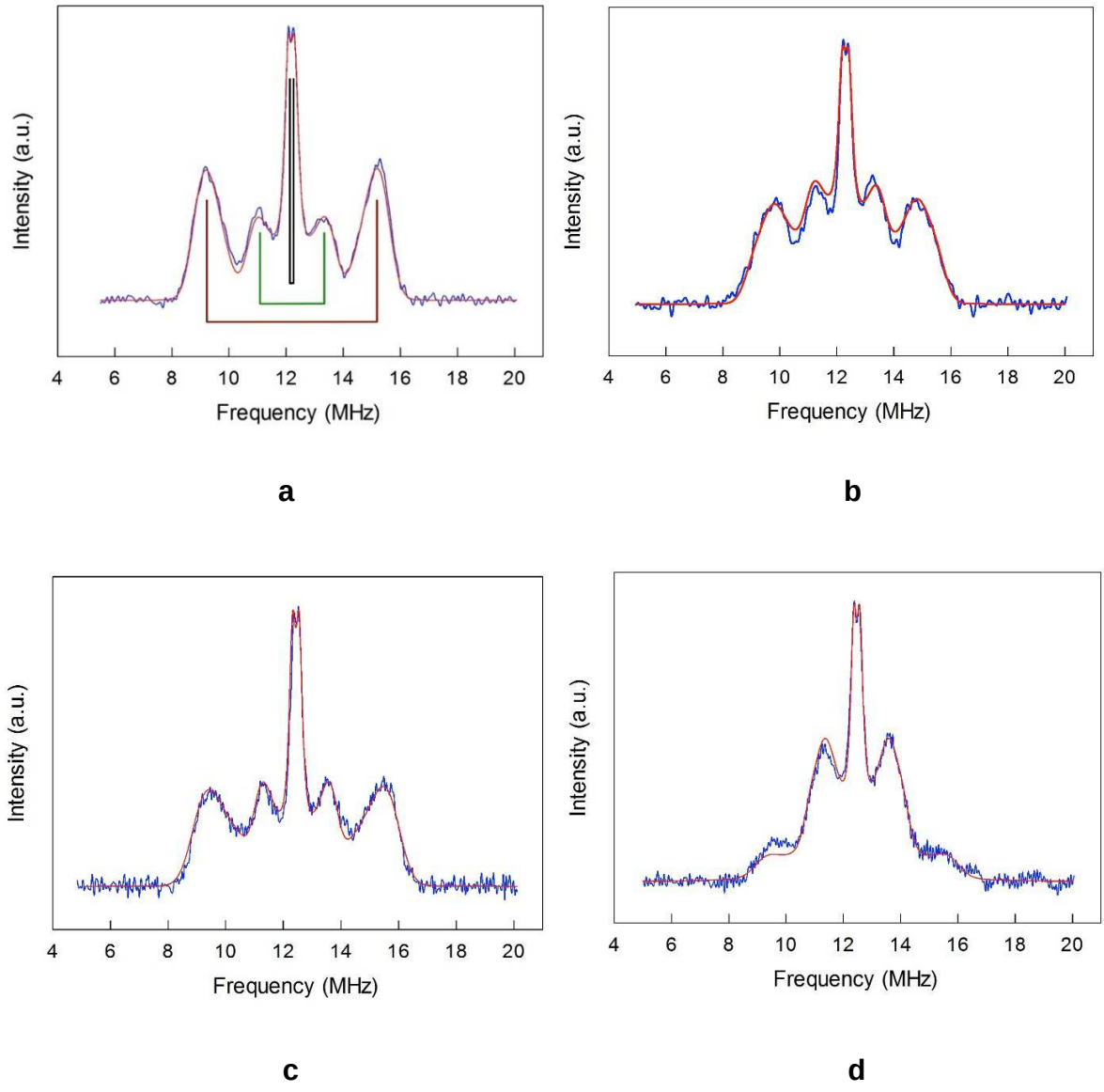

Fig. 3.7. Baseline-corrected ^{1}H-ENDOR spectrum (blue) and simulation (red) for $Au_{25}(SBu)_{18}^{0}$ (a), $Au_{25}(SEt)_{18}^{0}$ (b) $Au_{25}(SPr)_{18}^{0}$ (c) and $Au_{25}(SMePr)_{18}^{0}$ (d) in toluene at 5 K. The lines mark the outer (brown), middle (green), and inner (black) proton ENDOR doublets.

For the other clusters, we assign the $(\beta\text{-CH})_{in}$ and $(\alpha\text{-CH})_{out}$ doublets as for $Au_{25}(SEt)_{18}^{0}$; for $(\alpha\text{-CH})_{in}$, the above considerations about the broad peak at 3 MHz are also valid. The crystallographic distances of the $(\beta\text{-CH})_{in}$ and $(\alpha\text{-CH})_{out}$ groups from the cluster's center are

similar, *i.e.,* 7.23 and 7.16 Å ($Au_{25}(SPr)_{18}^0$), and 7.16 and 7.28 Å ($Au_{25}(SBu)_{18}^0$), respectively. In addition to the signals already discussed, the ENDOR spectrum of $Au_{25}(SPr)_{18}^0$ is liable to show a contribution also from the 36 $(\gamma\text{-CH})_{in}$, whose average crystallographic distance is 8.35 Å, and thus shorter than that of the $(\beta\text{-CH})_{out}$ protons, 8.64 Å; a similar outcome is observed for $Au_{25}(SBu)_{18}^0$ whose values are 8.12 and 8.20 Å, respectively. However, we could still simulate the spectrum of $Au_{25}(SPr)_{18}^0$ well (Fig. 3.7c) by using for the outer and middle doublets an ENDOR intensity ratio of 24:12, which corresponds to the number of equivalent $(\beta\text{-CH})_{in}$ and $(\alpha\text{-CH})_{out}$ protons. Apparently, no $(\gamma\text{-CH})_{in}$ protons need to be taken into account. In fact, according to the NMR results, the $(\gamma\text{-CH})_{in}$ protons could have a hyperfine coupling smaller than that of the $(\alpha\text{-CH})_{out}$ protons but still detectable. However, the room-temperature NMR data cannot be directly compared with the low-temperature ENDOR data. At room temperature, the random motion of the alkyl chain is fast, with the $(\gamma\text{-CH})_{in}$ atoms moving often closer to the metal core than the $(\beta\text{-CH})_{in}$ atoms, but NMR spectroscopy only probes the average contact shift. Electron-transfer[26] and diffusion-coefficient[15] measurements provided evidence for the ligand chains being quite mobile in solution; for example, the *D* values yield r_{MPC} values smaller than the average radius of the same clusters as calculated from the crystallographic structure. At 5 K, however, whereas the ligands' motion is very limited by the frozen glassy solution, $(\gamma\text{-CH})_{in}$ can still be present in different conformations. It is thus conceivable that the ENDOR doublet of the $(\gamma\text{-CH})_{in}$ protons is associated with a wide conformational distribution (larger than that experienced by the β- and, even more, the α-groups) and this would cause significant line broadening and thus spreading of the signal under the outer and middle doublets.

To shed further light onto this issue, it is useful to compare the ENDOR spectra of $Au_{25}(SPr)_{18}^0$ and $Au_{25}(SMePr)_{18}^0$ (Fig. 3.8). Whereas in the latter there are 72 $(\gamma\text{-CH})_{in}$ protons that can contribute to the spectrum, the $(\beta\text{-CH})_{in}$ and $(\beta\text{-CH})_{out}$ protons are only 12 and 6, respectively, *i.e.*, one half than those in $Au_{25}(SPr)_{18}^0$. Fig. 3.8 shows that in $Au_{25}(SMePr)_{18}^0$ the ENDOR lines of the outer doublet are indeed significantly smaller than those of $Au_{25}(SPr)_{18}^0$, and this confirms that for all clusters the outer doublet is consistently associated with the $(\beta\text{-CH})_{in}$ protons. The increase in the middle doublet is particularly worth noting. This increase is attributed to a strong contribution from the $(\gamma\text{-CH})_{in}$ protons: compared to those in $Au_{25}(SPr)_{18}^0$, in $Au_{25}(SMePr)_{18}^0$ these protons have a narrower conformational

distribution due to the steric hindrance introduced by the second methyl group. Hindrance not only makes these methyl groups less mobile but also the whole monolayer stiffer and thus the MPC larger. Support to this view comes from the electrochemical determination of the *D* in dicholoromethane (see Fig. 3.1) and, thus, r_{MPC} values of $Au_{25}(SMePr)_{18}^0$: they are 5.16 x 10^{-6} cm^2 s^{-1} and 10.3 Å, respectively, whereas for $Au_{25}(SPr)_{18}^0$ (which has the same fully extended length but more fluid chains in the monolayer) they corresponding values are 6.15 x 10^{-6} cm^2 s^{-1} and 8.6 Å.[15] The simulation of the ENDOR spectrum of $Au_{25}(SMePr)_{18}^0$ (Fig. 3.7d) was carried out as summarized in Table 3.1. The number of protons required to obtain the best fit to the inner signals is indeed significantly larger than 6, which in this specific cluster corresponds to the particularly small number of $(\beta\text{-CH})_{out}$ protons. We note, however, that the average crystallographic distance for the $(\gamma\text{-CH})_{out}$ protons in $Au_{25}(SPr)_{18}^0$ and $Au_{25}(SBu)_{18}^0$ is 8.9 Å and thus only slightly larger than for the $(\beta\text{-CH})_{out}$ protons. A weak coupling is thus expected also for the $(\gamma\text{-CH})_{out}$ protons: for $Au_{25}(SMePr)_{18}^0$ these protons are particularly numerous, 36, and this could make their contribution to the inner ENDOR lines quite significant. This hypothesis is reasonable but not quantifiable also because of the aforementioned problems associated with weak couplings.

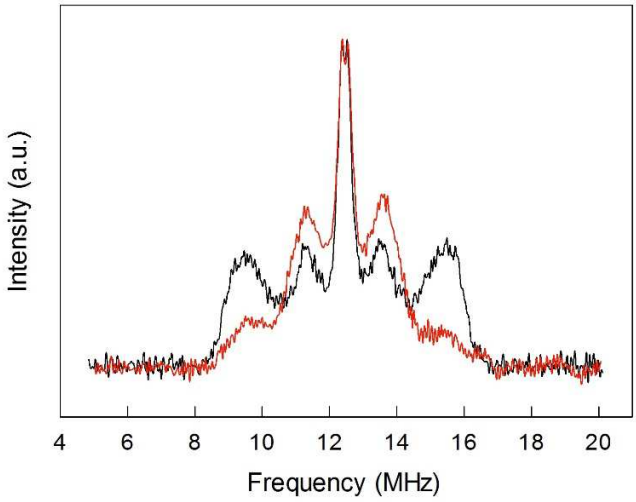

Fig. 3.8. Comparison between the normalized ENDOR spectrum of $Au_{25}(SPr)_{18}^0$ (black line) and $Au_{25}(SMePr)_{18}^0$ (red line). For comparison, the spectra were normalized for the height.

Regarding $Au_{25}(SBu)_{18}^0$ (Fig. 3.7a), the most evident new feature is that the outer lines are higher than the middle lines. However, the number of protons causing an ENDOR line is related to the area, not to the line height. The simulation results in a ratio of 24:12 between the outer and middle lines, in agreement with the attribution of the outer line to $(\beta\text{-CH})_{in}$ and

the middle line to (α-CH)$_{out}$; the outer lines are just narrower than in $Au_{25}(SEt)_{18}^0$ and $Au_{25}(SPr)_{18}^0$. As for $Au_{25}(SPr)_{18}^0$, conformational distribution would make the contribution of the (γ-CH)$_{in}$ protons spread in the region pertaining to the outer and middle lines. As a matter of fact, the Stokes radius of this cluster, 9.4 Å, is smaller than that of the stiffer $Au_{25}(SMePr)_{18}^0$ cluster. Regarding the (β-CH)$_{out}$ protons, the best fit to the inner lines is obtained by using a number of protons, 16, larger than 12. Interestingly, also for $Au_{25}(SPr)_{18}^0$ the number is larger, 14. We believe that the reason is as already described for $Au_{25}(SMePr)_{18}^0$, *i.e.*, a non vanishingly small contribution from the (γ-CH)$_{out}$ protons.

3.2.5 Electron-Nucleus Interaction

The isotropic coupling is proportional to the spin density on the nucleus. The simulations of the ENDOR spectra provide both the isotropic and the anisotropic hyperfine values. The latter are mainly related to the magnetic dipole-dipole interaction between electron and nucleus, therefore providing geometrical information. This interaction can be described by three main values, T_{xx}, T_{yy} and T_{zz}, called hyperfine tensor main values, which are specific for each nucleus.[39] Here, the axes *x,y,z* represent a main reference system whose origin is at the center of the electron spin-distribution (in our case, the gold-cluster center). The values of T_{xx}, T_{yy} and T_{zz} can be obtained by averaging spatially the dipole-dipole interaction over the spin distribution, according to the following equation (eq. 3-2), exemplified for *x*:

$$T_{xx} = -\frac{\mu_0}{4\pi} g_e \beta_e g_N \beta_N \left\langle \frac{R^2 - 3x^2}{R^5} \right\rangle \qquad (3\text{-}2)$$

where μ_0 is the vacuum permeability, R is the electron-nucleus distance, g_e is the electron g-factor, g_N is the nucleus g-factor, and β_N is the nuclear magneton. Analogous equations hold for *y* and *z*. From these equations, it results that $T_{xx} + T_{yy} + T_{zz} = 0$. If the spin-distribution is axially symmetric with respect the *z* direction, then $T_{xx} = T_{yy}$ and the hyperfine tensor main values are $T_{xx} = T_{yy} = -T$ and $T_{zz} = 2\,T$. Deviation from an axially symmetric distribution leads to a hyperfine tensor whose main values are [T_{xx}, T_{yy}, T_{zz}] with $T_{xx} \neq T_{yy}$.

Table 3.1 shows that the various proton types are consistently in the form [-*T*, -*T*, +2*T*], except for (β-CH)$_{in}$ in $Au_{25}(SEt)_{18}^0$ in which a [T_{xx}, T_{yy}, T_{zz}] form is observed, with a marked difference between T_{xx} and T_{yy}. With all cautions already discussed, if we assume that the feature at 3 MHz is due to (α-CH)$_{in}$ protons, its *A* can be estimated to be around 15-20 MHz.

This would be about one order of magnitude larger than the value pertaining to the $(\alpha\text{-CH})_{out}$ protons. In this connection, it is worth recalling that DFT calculations carried out for $Au_{25}(SCH_2CH_2Ph)_{18}^0$ showed that the spin density at $(\alpha\text{-CH})_{in}$ is one order of magnitude larger than at $(\alpha\text{-CH})_{out}$.[17] If we now compare the $(\beta\text{-CH})_{in}$ and the $(\alpha\text{-CH})_{out}$ isotropic hyperfine couplings for alkanethiolates of increasing length (Table 3.1, third column), we note an increase in the absolute value of *A,* particularly in the passage from Et to Pr. This suggests that the ligands are not completely indifferent to the spin distribution in $Au_{25}(SR)_{18}^0$, and thus to the SOMO structure.

Another aspect regards the sign of *A.* According to the theory, the isotropic hyperfine coupling with a nucleus is given by (eq 3-3):

$$A = \frac{2\mu_0}{3} g_e \beta_e g_N \beta_N (\rho_\alpha - \rho_\beta) \qquad (3\text{-}3)$$

where ρ_α is the direct spin-density and ρ_β is the spin-polarized density.[39] ρ_α is mainly contributed by the unpaired electron in the SOMO, whereas ρ_β is due to spin-polarization. The latter results from the tendency of the unpaired electron to withdraw electrons with the same spin, because of the favorable exchange interaction, and *vice versa.* If g_N is positive, which is true for protons, then a positive *A* is found for a dominant direct contribution from the SOMO, whereas a negative value is found if spin-polarization prevails.

From the simulations, we obtain the sign with respect to [T_{xx}, T_{yy}, T_{zz}], *i.e*., the pattern of the doublet does not change if we were to revert both the sign of *A* and [T_{xx}, T_{yy}, T_{zz}]. However, if we assume that the anisotropic interaction is mainly dipolar, then the form of the anisotropic tensor main values is [-*T*, -*T*, +2*T*] with *T*>0, and thus the sign of *A* is determined as shown in Table 1. Consequently, a negative value in *A* is an indication that *A* is mainly determined by spin-polarization through bonds, with a small contribution from direct spin density on the proton nuclei from the SOMO orbital, according to eq 5-3. We can thus speculate that the increase of |*A*| as one goes from Et to Bu is the result of a decreasing, positive contribution to the hyperfine coupling from the direct spin-density of the SOMO, suggesting again that in the Et cluster spin-density is more diffuse toward the ligands than in the Pr or Bu cases.

We can now compare these *A* values with those obtained from NMR measurements and the DFT-calculated spin density values obtained previously.[10,17] The ENDOR parameters in Table 3.1 differ from those obtained from the NMR signals in two ways: (i) in ENDOR, the

absolute values of *A* are significantly larger than the equivalent NMR values: 1.3-2.1 log units, except for $(\beta\text{-CH})_{in}$ in $Au_{25}(SMePr)_{18}^{0}$ whose value is 3.0 log units; (ii) some of the signs are different. Previous comparisons between the *A* values obtained from NMR and ENDOR measurements carried out in solution at the same or not very different temperature provided comparable values and the same signs for many radicals.[40] Our NMR and the ENDOR experiments, however, refer to very different conditions. In a previous comparison of this kind (for an iron-sulfur cluster),[41] similar NMR and ENDOR values were obtained, but the possibility that a strong temperature difference could lead to different results was also commented upon.[41] Additionally, we note that compared to previous investigations focusing on quite rigid radical structures and without particularly heavy atoms, here we considered entirely new systems composed of a gold nanocore and many flexible ligands.

To gain insights into this aspect, we performed *ab initio* molecular-dynamics (MD) calculations by using the Atom Centered Density Matrix Propagation molecular dynamics model (ADMP),[42] as implemented in Gaussian 09.[43] Because a converged finite-temperature sampling is exceedingly computational costly, we resorted to use a cluster model consisting of $Au_7(SCH_3)_6$, which is paramagnetic in the neutral state (Fig. 3.9, inset). The model consists of a 6 Au atom ring with a central gold core atom. We performed a 2 ps MD at 300 and 5 K with a time step of 0.001 fs. Snapshots were collected every 1 fs, for which we evaluated the isotropic Femi constant.

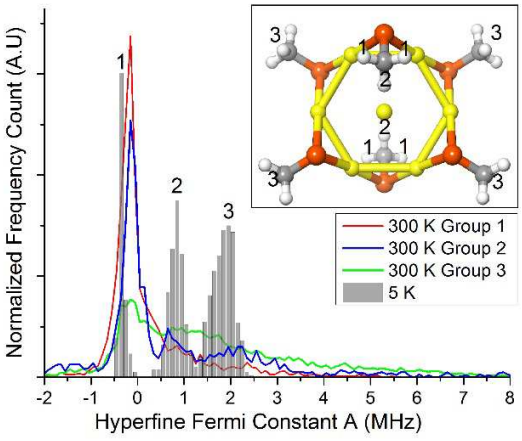

Fig. 3.9. Distribution of *A* values evaluated along an *ab initio* MD simulation at 300 K (colored lines) and 5 K (gray bars). Individual distributions have been normalized to have the same total area. Inset shows the Au_7 model used and the assignment of the different *A* values according to the proton type.

Despite its simplicity, the model contains protons with different values of *A*, ranging from negative to positive values. The values for protons in the group 2 and 3 (cf. inset to Fig. 3.9) come from the unpaired electron in the SOMO, whereas protons in groups 1 have negative values due to spin-polarization. At 300 K, thermal motion tends to reduce spin-polarization on group 1, whereas at 5 K there is a sharp distribution with a peak value (-0.35 MHz) more negative than the peak value at 300 K (-0.15 MHz). This is in qualitative agreement with the ENDOR results for $(\alpha\text{-CH})_{out}$ that show an overall decrease in the absolute value of *A*. Close inspection to the MD trajectories shows that at 5 K the rotation of the methyl groups is completely frozen in the global energy minimum, whereas at 300 K free rotations cause the direct effect of the spin electron and spin-polarization to roughly average out. The experimental and theoretical results thus point to the emergence, at very low temperature, of a pronounced increase of spin-polarization. These results, therefore, bring some rationale to the change in sign and magnitude observed by carrying out the hyperfine-coupling constant measurements at very different temperatures.

3.3 Conclusions

We used four structurally related paramagnetic Au_{25} clusters to determine how spin density and thus orbital distribution spread onto the protecting alkanethiolate ligands. The structures of two clusters were known, whereas that of the highly symmetric $Au_{25}(SPr)_{18}^0$ is described here for the first time. ^{1}H NMR and ENDOR measurements proved to be very sensitive in assessing how the unpaired electron interacts with progressively more distant protons, with significant differences between the types of ligand. Simulations provided the values of the corresponding hyperfine coupling constants. Interestingly, the experimental and DFT calculations results point to an increase of spin-polarization at very low temperature. The results show that the electron-proton interaction extends to the protons at the α, β, and γ positions, with a much stronger interaction for the ligands directly connected to the Au_{13} icosahedral core. We thus show for the first time that orbital distribution affects atoms that can be as far as 6 Å from the icosahedral core. This information is deemed as essential especially for properly describing the mechanisms of the many reactions already known to be catalyzed by molecular MPCs. As a final remark, we note that the strategy and methodologies here described are suitable to be applied to the study of other molecular clusters (regardless of the actual metal core composition) that already are in the form of free radicals or could generate them by electron transfer.

3.4 Experimental section

$Au_{25}(SEt)_{18}$ and $Au_{25}(SBu)_{18}$ were prepared as described previously.[10,12] The two new clusters, $Au_{25}(SPr)_{18}$ and $Au_{25}(SMePr)_{18}$, were synthesized and oxidized along similar lines, as described below.

3.4.1 Chemicals.

Hydrogen tetrachloroaurate trihydrate (Aldrich, 99.9%), tetra-*n*-octylammonium bromide (Aldrich, 98%), ethanethiol (Aldrich, 97%), sodium borohydride (Aldrich, 99%), tetrahydrofuran (THF, Sigma-Aldrich, 99.9%), toluene (Sigma-Aldrich, 99.7%), diethyl ether (Sigma-Aldrich, 99.8%), acetonitrile-d_3 (Aldrich, 99.8%, d_3), benzene-d_6 (Aldrich, 99.6%, d_6), and *trans*-2-[3-(4-*tert*-butylphenyl)-2-methyl-2-propenylidene] malononitrile (DCTB, Sigma-Aldrich, ≥98%) were used as received. For electrochemistry, dichloromethane (DCM, VWR, 99.8%) was freshly distilled over CaH2 and stored under an argon atmosphere. Tetra-*n*-butylammonium hexafluorophosphate (Fluka, 99%) was recrystallized from ethanol. Low conductivity water was milliQ Water pro analysis (Merck). Column chromatography was carried out using silica gel from Macherey-Nagel (MN-Kieselgel 60 M, 230-400 mesh).

3.4.2 Synthesis of $Au_{25}(SPr)_{18}$ and $Au_{25}(SMeBu)_{18}$.

0.50 g (1.27 mmol) of $HAuCl_4 \cdot 3H_2O$ was dissolved in 40 ml THF and then 0.833 g of tetra-*n*-octylammonium bromide (1.52 mmol, 1.2 equiv) were added to form a red solution. After stirring for 15 min at room temperature at moderate speed, magnetic stirring was increased to 100 rpm and then 0.460 ml (5.08 mmol, 4 equiv) of 1-propanethiol in 10 ml of THF was added dropwise. The resulting yellow solution became colorless in ca. 30 min. Magnetic stirring was increased to 600 rpm and a freshly prepared icy-cold aqueous solution (10 ml) of $NaBH_4$ (0.48 g, 12.7 mmol, 10 equiv) was added and this caused the resulting mixture to become black. After two days, the reaction mixture was filtered on paper and THF was evaporated to leave a reddish-brown oily solid covered by residual H_2O from aq. $NaBH_4$. The water phase was removed, and the solid was dissolved in toluene and washed with water (4 x 40 ml) in a separatory funnel. Toluene was evaporated, the solid was dissolved in 50 ml of DCM, and the resulting solution was left to rest overnight in the dark at 4℃. The white residue precipitated during this treatment was discarded and DCM was then evaporated. The resulting oily solid was further purified by dissolving it in a mixture of diethyl ether and

pentane to precipitate most of the residual tetraoctylammonium salt. The last traces of salt were eliminated by washing the product a few times with icy-cold methanol. The final product, [*n*-Oct_4N^+][$Au_{25}(SPr)_{18}^-$], is a dark-orange brown powder. For the NMR spectroscopy measurements, possible traces of the oxidized cluster, which could form by air oxidation during the methanol washes, were eliminated by rinsing the product a few times with pentane.

Oxidation of the as-prepared cluster to obtain the paramagnetic species $Au_{25}(SPr)_{18}^0$ was performed by a passage through a silica-gel chromatography column, using DCM as eluent and compressed air as the pushing gas. Upon injection of the orange solution of the anionic cluster in DCM into the column, the solution turned green while passing through the column. After evaporation of the solvent, the oxidized cluster appeared as a black-brownish powder. The cluster was further purified by washing thrice with acetonitrile, in which $Au_{25}(SPr)_{18}^0$ is insoluble. The resulting neutral cluster $Au_{25}(SPr)_{18}^0$ had the typical UV-vis behavior distinctly different from that of the corresponding anion, as already described for, *e.g.*, $Au_{25}(SEt)_{18}$.[S1] The expected molecular mass was observed by using matrix-assisted laser desorption ionization time-of-flight (MALDI-TOF) mass spectrometry.

$Au_{25}(SPr)_{18}^0$ was recrystallized by adding a drop of acetonitrile to a concentrated solution of the cluster in 1:2 toluene-pentane and leaving the solvents to evaporate for some days in the dark at room temperature. Its structure was resolved by X-ray diffraction., as described further

$Au_{25}(SMePr)_{18}$ was synthesized, purified, oxidized, and characterized, for both charge states, as already described in detail for $Au_{25}(SPr)_{18}$.

3.4.3 Mass spectrometry.

MALDI-TOF experiments were carried out with an Applied Biosystems 4800 MALDI-TOF/TOF spectrometer equipped with a Nd:YAG laser operating at 355 nm. The laser-firing rate was 200 Hz and the accelerating voltage was 25 kV. DCTB was used as the matrix. The clusters were dissolved in dichoromethane containing DCTB to obtain 0.1 mM solutions with a 1:400 MPC/matrix ratio. 2 μl of solution were dropcasted onto the sample plate and air-dried before loading into MALDI-TOF. The spectra were recorded using the reflectron positive- or negative-ion mode.

3.4.4 Electrochemistry

The electrochemical experiments were carried out in DCM containing 0.1 M *n*-tetrabutylammonium hexafluorophosphate, under an Ar atmosphere in a glass cell thermostatted at 25 ℃. The working electrode was a 0.0164 cm^2 glassy-carbon disk, the counter electrode was a Pt wire, and an Ag wire served as the quasi-reference electrode. The latter was then referenced against the KCl saturated calomel electrode, SCE. We used a CHI 660c electrochemical workstation. To minimize the ohmic drop between the working and the reference electrodes, we used the positive feedback correction.

3.4.5 NMR spectrometry

^1H and ^{13}C NMR spectroscopy measurements were carried out on 3 mM [*n*-Oct_4N^+][$Au_{25}(SR)_{18}^-$] or $Au_{25}(SR)_{18}^0$ in benzene-d_6 (100%, 99.96% d_6, Aldrich). We used a Bruker Avance DMX-600 MHz spectrometer equipped with a 5 mm TX-1 x,y,z-gradient powered, triple resonance inverse probe operating at 599.90 (^1H NMR) or 150.07 MHz (^{13}C NMR). The temperature was controlled at 298 K with a Bruker BVT-300 automatic temperature controller. Chemical shifts are in ppm units (δ□ with reference to tetramethylsilane used as an internal standard for both ^1H and ^{13}C NMR. The proton assignments were either already known or performed by standard chemical shift correlations and 2D correlation spectroscopy (COSY), total correlation spectroscopy (TOCSY), and nuclear Overhauser enhancement spectroscopy (NOESY) experiments. ^{13}C chemical shifts were obtained and assigned through heteronuclear multiple quantum coherence (HMQC) correlation experiments.

3.4.6 ENDOR spectroscopy.

For ENDOR measurements, the samples consisted in 100 µl of 0.5 mM $Au_{25}(SR)_{18}^0$ in toluene. Each solution was introduced into the EPR sample holder, a 3 (o.d.) x 2 mm (i.d.) quartz tube, and degassed through freeze-pump-thaw cycles in a vacuum line and sealed at low pressure (5 x 10^{-5} torr). The samples were frozen at 80 K and then introduced in the probehead. The experiments were carried out at 5 K. ^1H Pulsed ENDOR measurements were carried out with a Bruker Elexsys E580 instrument equipped with a Pulsed ENDOR dieletric probehead and an Oxford CF935 cryostat. We used the Davies pulse sequence, with 160 ns microwave inversion pulse and 80-160 ns pulse-sequence for electron-spin echo detection.

The radiofrequency pulse was 8-10 μs long and amplified with a 150 W RF Bruker amplifier. The spectra were recorded at the top of the Echo Detected EPR spectra (approximately 290 mT), with a RF scan ranging from 1 to 20 MHz, where the proton peaks were expected. The narrow spectral range and the long microwave pulses were chosen to spot and enhance ENDOR lines from ^{1}H with respect to ^{197}Au.[10] ENDOR simulations were performed with a homebuilt program running on the open-source Scilab-5.5.1 calculation package [http://www.scilab.org]. The narrow spectral range and the long microwave pulses were chosen to spot and enhance ENDOR lines from ^{1}H with respect to ^{197}Au.

3.4.7 X-ray crystallography.

Crystallographic data for $Au_{25}(SPr)_{18}^{0}$ were collected at 170 K with Mo *K*α radiation (λ = 0.71073 Å) by using an Agilent SuperNova diffractometer equipped with Atlas CCD area detector. For data measurement and processing the CrysAlisPro software[44] was employed. The intensities were corrected for absorption with analytical numeric absorption correction method[45]. The structure was solved by direct methods[46] integrated in the program of Olex2.[47] Full-matrix least-squares refinements on F^2 were carried out using SHELXL-2015.[48] Due to a very minor, yet significant on the gold atoms, around 95:5 positional disorder of the Au_{25} core was assigned. The SPr groups were not modeled accordingly but refined with full occupancy, yet they were constrained by “DFIX” and “ISOR” commands for reasonable geometry and thermal motion. In addition, one carbon atom (C2) in a SPr group in the asymmetric unit was found to be disordered over two sites and the two positions of the C2 atom (ratio 0.68:0.32) atom were constrained to have the same anisotropic thermal motion. The H atoms were calculated to their idealized positions with constrainted isotropic thermal factors (1.2 or 1.5 times of U_{eq}(C)) and refined as riding atoms. Crystal data for $Au_{25}(SPr)_{18}^{0}$: black plates, 0.0144 × 0.0405 × 0.0619 mm, FW = 6276.78, $C_{54}H_{126}Au_{25}S_{18}$, trigonal, space group R-3, a = 16.771(2) Å, b = 17.771(2) Å, c = 27.217(2) Å, α = 90°, β = 90°, γ = 120°, V = 7444(2) Å^3, Z = 3, D_c = 4.201 g/cm^3, F(000) = 8139, μ = 37.189 mm^{-1}, T = 170.00(10) K, $2\theta_{max}$ = 56.0°, 3240 reflections, 2181 with $I_o > 2\sigma(I_o)$, R_{int} = 0.0346, 190 parameters, 68 restraints, GoF = 0.986, R_1 = 0.0474 [$I_o > 2\sigma(I_o)$], wR_2 = 0.0935 (all reflections), -2.034 < Δρ < 1.608 e/Å^3. The structure has been deposited to the Cambridge Crystallographic Data Centre with CCDC number 1453036, and the data can be obtained free of charge *via* www.ccdc.cam.ac.uk/data_request/cif.

3.4.8 Molecular Dynamics simulations.

Ab initio MD was carried out at the Density Functional Theory level using the generalized gradient approximation (GGA) and the PBE exchange-correlation functional. LANL2DZ (19 valence electrons) was employed for Au atoms, and the D90 basis set was used for (S, C, and H). All calculations were carried out with the program Gaussian 09, revision E.01.[43]

3.4 References

1. Parker, J. F.; Fields-Zinna, C. A.; Murray, R. W. The story of a monodisperse gold nanoparticle: $Au_{25}L_{18}$. *Acc. Chem. Res.*, **2010**, *43*, 1289-1296.
2. Tsukuda, T. Toward an Atomic-Level Understanding of Size-Specific Properties of Protected and Stabilized Gold Clusters T. *Bull. Chem. Soc. Jpn*., **2012**, *85*, 151-168.
3. Qian, H.; Zhu, M.; Wu, Z.; Jin, R. Quantum sized gold nanoclusters with atomic precision. *Acc. Chem. Res.*, **2012**, *45*, 1470-1479.
4. Negishi, Y.; Kurashige, W.; Niihori, Y.; Nobusada, K. Isolation, structure, and stability of a dodecanethiolate-protected Pd(1)Au(24) cluster. *Phys. Chem. Chem. Phys.*, 2013, **15**, 18736-18751.
5. Jin, R. Atomically precise metal nanoclusters: stable sizes and optical properties. *Nanoscale*, **2015**, *7*, 1549**–**1565.
6. *Protected Metal Clusters: From Fundamentals to Applications*, ed. T. Tsukuda and H. Häkkinen, In Frontiers of Nanoscience, Elsevier, Amsterdam, 2015, Vol. 9.
7. Heaven, M. W.; Dass, A.; White, P. S.; Holt, K. M.; Murray, R. W. Crystal structure of the gold nanoparticle $[N(C_8H_{17})_4][Au_{25}(SCH_2CH_2Ph)_{18}]$. *J. Am. Chem. Soc.*, **2008**, *130*, 3754–3755.
8. Zhu, M.; Eckenhoff, W. T.; Pintauer T.; Jin, R. Conversion of Anionic $[Au_{25}(SCH_2CH_2Ph)_{18}]^-$ Cluster to Charge Neutral Cluster via Air Oxidation *J. Phys. Chem. C* **2008**, *112*, 14221–14224.
9. Zhu, M.; Aikens, C. M.; Hollander, F. J.; Schatz, G. C.; Jin, R. Correlating the crystal structure of a thiol-protected Au25 cluster and optical properties. *J. Am. Chem. Soc.*, **2008**, *130*, 5883–5885.

10. Dainese, T.; Antonello, S.; Gascón, J. A.; Pan, F.; Perera, N. V.; Ruzzi, M.; Venzo, A.; Zoleo, A.; Rissanen, K.; Maran, F. $Au_{25}(SEt)_{18}$, a nearly "Naked" Thiolate-Protected Au_{25} Cluster: Structural Analysis by ENDOR and Single Crystal X-ray Crystallography. *ACS Nano* **2014**, *8*, 3904-3912.

11. Tofanelli, M. A.; Salorinne, K.; Ni, T. W.; Malola, S.; Newell, B.; Phillips, B.; Häkkinen, H.; Ackerson, C. J. Jahn-Teller effects in $Au_{25}(SR)_{18}$. *Chem. Sci.* **2016**, *7*, 1882-1890.

12. De Nardi, M.; Antonello, S.; Jiang, D.; Pan, F.; Rissanen, K.; Ruzzi, M.; Venzo, A.; Zoleo, A.; Maran, F. Gold Nanowired: A Linear $(Au_{25})_n$ Polymer from Au_{25} Molecular Clusters. *ACS Nano* **2014**, *8*, 8505-8512.

13. Lee, D.; Donkers, R. L.; Wang, G.; Harper, A. S.; Murray, R. W. Electrochemistry and optical absorbance and luminescence of molecule-like Au38 nanoparticles. *J. Am. Chem. Soc.* 2004, **126**, 6193-6199.

14. Antonello, S.; Dainese, T.; Maran, F. *Electroanalysis* Exploring Collective Substituent Effects: Dependence of the Lifetime of Charged States of $Au_{25}(SC_nH_{2n+1})_{18}$ Nanoclusters on the Length of the Thiolate Ligands **2016**, *28*, 2771-2776.

15. Antonello, S.; Dainese, T.; De Nardi, M.; Perotti, L.; Maran, F. Insights into the Interface Between Electrolytic Solution and Gold Core in Molecular $Au_{25}(SR)_{18}$ Clusters. *ChemElectroChem.* **2016**, *3*, 1237**–**1244.

16. Antonello, S.; Perera, N. V.; Ruzzi, M.; Gascón, J. A.; Maran, F. Interplay of Charge State, Lability, and Magnetism in the Molecule-like $Au_{25}(SR)_{18}$ Cluster. *J. Am. Chem. Soc.* **2013**, *135*, 15585-15594.

17. Venzo, A.; Antonello, S.; Gascón, J. A.; Guryanov, I.; Leapman, R. D.; Perera, N. V.; Sousa, A.; Zamuner, M.; Zanella, A.; Maran, F. Effect of the Charge State (z = -1, 0, +1) on the Nuclear Magnetic Resonance of Monodisperse $Au_{25}[S(CH_2)_2Ph]_{18}^z$ Clusters. *Anal. Chem.* **2011**, *83*, 6355-6362.

18. Yau, S.H.; Varnavski, O.; Goodson III, An ultrafast look at Au nanoclusters. *Acc. Chem. Res.*, **2013**, *46*, 1506-1516.

19. Wang, S.; Zhu, X.; Cao, T.; Zhu, M. A simple model for understanding the fluorescence behavior of Au25 nanoclusters *Nanoscale*, **2014**, *6*, 5777**-**5781.

20. Mathew, A.; Varghese, E.; Choudhury, S.; Pal, S. K.; Pradeep, T. Efficient red luminescence from organic-soluble Au25 clusters by ligand structure modification *Nanoscale*, **2015**, *7*, 14305**–**14315.

21. Yuan, X.; Goswami, N.; Chen, W.; Yao, Q.; Xie, J. Insights into the effect of surface ligands on the optical properties of thiolated Au_{25} nanoclusters *Chem. Commun.*, **2016**, *52*, 5234-5237.

22. Knoppe, S.; Bürgi, T. Chirality in Thiolate-Protected Gold Clusters *Acc. Chem. Res.*, **2014**, *47*, 1318**–**1326.

23. Antonello, S.; Holm, A. H.; Instuli, E.; Maran, F. *J. Am. Chem. Soc.*, Molecular Electron-Transfer Properties of Au_{38} Clusters **2007**, *129*, 9836-9837.

24. Liu, Z.; Zhu, M.; Meng, X.; Xu, G.; Jin, R. Electron Transfer between $[Au_{25}(SC_2H_4Ph)_{18}]^-TOA^+$ and Oxoammonium Cations *J. Phys. Chem. Lett.*, **2011**, *2*, 2104**–**2109.

25. Antonello, S.; Hesari, M.; Polo, F.; Maran, F. Electron Transfer Catalysis with Monolayer Protected Au_{25} Clusters. *Nanoscale* **2012**, *4*, 5333**–**5342. S. Antonello, G. Arrigoni, T. Dainese, M. De Nardi, G. Parisio, L. Perotti, A. René, A. Venzo and F. Maran, *ACS Nano*, **2014**, *8*, 2788-2795.

26. Li, G.; Jin, R. Atomically Precise Gold Nanoclusters as New Model Catalysts. *Acc. Chem. Res.* **2013**, *46*, 1749-1758.

27. Akola, J.; Walter, M.; Whetten, R.L.; Häkkinen, H.; Grönbeck, H. On the Structure of Thiolate-Protected Au25*. J. Am. Chem. Soc.* **2008**, *130*, 3756-3757.

28. Jiang, D.-E. *Nanoscale*, The expanding universe of thiolated gold nanoclusters and beyond **2013**, *5*, 7149**–**7160.

29. Fernando, A.; Weerawardene, K. L. D. M.; Karimova, N. V.; Aikens, C. M. Quantum Mechanical Studies of Large Metal, Metal Oxide, and Metal Chalcogenide Nanoparticles and Clusters *Chem. Rev.*, **2015**, *115*, 6112**–**6216.

30. Zhu, M.; Aikens, C. M.; Hendrich, M. P.; Gupta, R.; Qian, H.; Schatz, G. C.; Jin, R. Reversible Switching of Magnetism in Thiolate-Protected Au_{25} Superatoms. *J. Am. Chem. Soc.* **2009**, *131*, 2490-2492.

31. Parker, J. F.; Choi, J.-P.; Wang, W.; Murray, R. W. Electron Self-exchange Dynamics of the Nanoparticle Couple $[Au_{25}(SC_2Ph)_{18}]^{0/1-}$ By Nuclear Magnetic Resonance Line-Broadening *J. Phys. Chem. C*, **2008**, *112*, 13976–13981.

32. Tlahuice-Flores, A.; Whetten, R. L.; Jose-Yacaman, M. Ligand Effects on the Structure and the Electronic Optical Properties of Anionic $Au_{25}(SR)_{18}$ Clusters *J. Phys. Chem. C*, **2013**, *117*, 20867–20875.

33. Crawford, S. E.; Andolina, C. M.; Smith, A. M.; Marbella, L. E.; Johnston, K. A.; Straney, P. J.; Hartmann, M. J.; Millstone, J. E. Ligand-Mediated “Turn On,” High Quantum Yield Near-Infrared Emission in Small Gold Nanoparticles *J. Am. Chem. Soc.*, **2015**, *137*, 14423−14429.

34. Guo, R.; Murray, R. W. Substituent Effects on Redox Potentials and Optical Gap Energies of Molecule-like $Au_{38}(SPhX)_{24}$ Nanoparticles *J. Am. Chem. Soc.*, **2005**, 127, 12140–12143.

35. Davies, E. A new pulse ENDOR technique, *Phys. Lett. A*. **1974** *47*, 1-2.

36. R. S. Nicholson, Shain, I. Theory of Stationary Electrode Polarography. Single Scan and Cyclic Methods Applied to Reversible, Irreversible, and Kinetic Systems, *Anal. Chem.* **1964**, *36*, 706– 723.

37. Bertini, I.; Luchinat, C.; Parigi, G. Magnetic susceptibility in paramagnetic NMR *Prog. Nucl. Magn. Reson. Spectrosc.*, 2002, **40**, 249-273.

38. Schweiger, A.; Jeschke, G. *Principles of pulse electron paramagnetic resonance*, Oxford University Press, Oxford, 2001.

39. Weil, J.; Bolton, J. R. *Electron paramagnetic resonance. Elementary Theory and Practical Applications*, 2nd ed., Wiley-Interscience, Hoboken, NJ, 2007, 50-51.

40. Nelsen, S. F.; Petillo, P. A.; De Felippis, J.; Wang, Y.; Chen, L.-J.; Yunta, M. J. R.; Neugebauer, F. A. Hydrogen splittings of bis-bicyclic hydrazine radical cations *J. Am. Chem. Soc.*, **1993**, *115*, 5608-5615.

41. Mouesca, J.-M.; Rius, G.; Lamotte, B.; Single-crystal proton ENDOR studies of the [Fe4S4]3+ cluster: determination of the spin population distribution and proposal of a model to interpret the 1H NMR paramagnetic shifts in high-potential ferredoxins *J. Am. Chem. Soc.*, **1993**, *115*, 4714-4731.

42. Iyengar, S. S.; Schlegel, H. B. ; Millam, J. M.; Voth, G. A.; Scuseria G. E.; Frisch, M. J. Ab initio molecular dynamics: Propagating the density matrix with Gaussian orbitals. II. Generalizations based on mass-weighting, idempotency, energy conservation and choice of initial conditions *J. Chem. Phys.*, **2001**, *115*, 10291-10302.

43. Frisch, M. J.; Trucks, G. W.; Schlegel, H. B.; Scuseria, G. E.; Robb, M. A. ; Cheeseman, J. R.; G. Scalmani, V. Barone, B. Mennucci, G. A. Petersson, H. Nakatsuji, M. Caricato, X. Li, H. P. Hratchian, A. F. Izmaylov, J. Bloino, G. Zheng, J. L. Sonnenberg, M. Hada, M. Ehara, K. Toyota, R. Fukuda, J. Hasegawa, M. Ishida, T. Nakajima, Y. Honda, O. Kitao, H. Nakai, T. Vreven, J. A. Montgomery, Jr., J. E. Peralta, F. Ogliaro, M. Bearpark, J. J. Heyd, E. Brothers, K. N. Kudin, V. N. Staroverov, R. Kobayashi, J. Normand, K. Raghavachari, A. Rendell, J. C.

Burant, S. S. Iyengar, J. Tomasi, M. Cossi, N. Rega, J. M. Millam, M. Klene, J. E. Knox, J. B. Cross, V. Bakken, C. Adamo, J. Jaramillo, R. Gomperts, R. E. Stratmann, O. Yazyev, A. J. Austin, R. Cammi, C. Pomelli, J. W. Ochterski, R. L. Martin, K. Morokuma, V. G. Zakrzewski, G. A. Voth, P. Salvador, J. J. Dannenberg, S. Dapprich, A. D. Daniels, Ö. Farkas, J. B. Foresman, J. V. Ortiz, J. Cioslowski,; Fox, D. J. Gaussian 9 (Revision E.01), Gaussian Inc., Wallingford, CT, 2009.

44. CrysAlisPro, version 1.171.37.35; Agilent Technologies Ltd: Yarnton, England, 2014.

45. Clark, R. C.; Reid, J. S. The analytical calculation of absorption in multifaceted crystals *Acta Crystallogr*., **1995**, A51, 887–897.

46. Sheldrick, G. M. A short history of SHELX. *Acta Crystallogr.*, **2008**, A64, 112–122.

47. Dolomanov, O. V.; Bourhis, L. J.; Gildea, R. J.; Howard, J. A. K.; Puschmann, H. OLEX2: a complete structure solution, refinement and analysis program *J. Appl. Cryst.*, **2009**, 42, 339–341.

48. Sheldrick, G. M. Crystal structure refinement with SHELXL *Acta Crystallogr*., **2015**, C71, 3-8

Chapter 4.

Magnetic Ordering in Gold Nanoclusters

4.1. Introduction

Over the past years, knowledge of most MPCs' properties has expanded very significantly. [1-6] However, an important property still poorly understood is gold nanomagnetism, despite magnetic nanoparticles and nanoclusters are of intrinsic importance and promising value in data storage, spintronics, quantum computing, optomagnetic devices, biomedical applications, and as magnetically recyclable nanocatalysts.[7-12]

Whereas bulk gold is known to be a typical diamagnetic material, upon decreasing the size down to the nanoscale a magnetic moment appears.[7-9] Since the first report by Hori *et al.*,[13] several papers described magnetic properties in gold nanoparticles, mostly thiolate MPCs prepared according to the two-phase synthesis by Brust *et al.*,[14] but the contradictory outcome of several of these results has been pointed out, reviewed, and discussed.[7-9] The observed magnetic behavior can indeed be very different. For example, Crespo *et al.*[15] and Donnio *et al.*[16] observed ferromagnetism in MPCs with diameters of 1.8-2.1 nm, whereas Yamamoto and Hori used clusters with a mean diameter of 1.9 nm and detected both superparamagnetism and Pauli paramagnetism.[17] Pauli paramagnetism, but no ferro- or superparamagnetism, was observed by Lear and his co-workers on nanoparticles of 1.8-1.9 nm.[18-20] Gréget *et al.* concluded that 1.9 nm large MPCs were diamagnetic, whereas larger particles (4.4 nm) were ferromagnetic.[21] Although ferromagnetism is generally detected when the MPC size decreases, Muños-Marquez *et al.* observed ferromagnetism in 2.1 nm clusters but diamagnetism in smaller clusters (1.4 nm).[22] It has been also observed that, depending on ligands, ~2 nm clusters may display ferromagnetism, paramagnetism, and diamagnetism.[23] Ferromagnetic behavior was observed for both films formed of bare Au clusters[24] and Au nanoparticles embedded in films of titania.[11] This astonishing variability in behavior is worsened by the observation that even particles of the same batch may display very different magnetizations. Sometimes different magnetic behaviors were observed even for samples prepared by using the same synthetic procedures and even by the same group.[9] In addition to these confusing results, some intriguing magnetic phenomena were also observed, such as an unusual dependence of the magnetization on temperature and dimensions of the particles

and a very high magnetic anisotropy.[16,25,26] Recent compilations of the different magnetic results obtained for Au nanoparticle or nanocluster systems, mostly ranging from 1 to 4 nm, are available.[24,27] From a theoretical viewpoint, gold magnetism has been related to a surface effect with an important orbital contribution to the magnetic moment.[28,29]

Nealon *et al*. discussed all these topics in particular detail and their analysis converged to the quite disappointing but nonetheless thought-provoking conclusion that nobody really knows to what extent and why some MPCs display an intrinsic magnetism.[9] Since the experimental results are often strange, discordant, and rarely reproducible, it is not surprising if a general explanation and even a qualitative understanding of these findings is still missing. We believe that this variegated, intriguing, and also confusing scenario is primarily due to the lack of control of the MPCs' composition, structure, charge state, and, as we will show here, crystallinity and morphology. Indeed, with very few exceptions to be discussed later, the majority of measurements were performed on Au nanoparticles lacking atomic precision (and thus possessing only an average dimension assessed through transmission electron microscopy images) and of undetermined charge state. Both these properties are closely linked to the magnetism of materials: by changing the dimension and the charge state, it is indeed possible to switch between different forms of magnetism. For example, the redox steps associated with charging of MPCs of hundreds of Au atoms can be so closely spaced[3,30] that removing or adding electrons can be easily triggered by oxygen or a mild reductant, as well as *via* intercluster disproportionation-comproportionation equilibria. Depending on the experimental conditions and material preparation, different magnetic states are thus possible. If the cluster stoichiometry is not controlled, further uncertainty is obviously introduced, as this increases very significantly the number of available redox couples in the whole sample.

MPCs with a gold core size of less than 1.5 nm display the same general features of molecules.[1-3,30] Important, most molecular MPCs can be prepared in a truly atomically monodisperse form.[1,2] The most well known and understood of them is $Au_{25}(SR)_{18}$.[31] Its structure is formed of a 13 gold-atom icosahedral core stabilized by 6 -(SR)-Au-(SR)-Au-(SR)- units (SR = thiolate).[32,33] Whereas anion $Au_{25}(SR)_{18}^-$ and cation $Au_{25}(SR)_{18}^+$ are diamagnetic, the neutral form $Au_{25}(SR)_{18}^0$ is paramagnetic.[34-36] For this charge state, which can be defined very precisely through electrochemistry or controlled redox reactions,[33,7,38] room temperature NMR spectroscopy shows that the spin density spreads onto the first ligand atoms and causes the corresponding resonances to undergo significant chemical shifts relative to the anionic or

cationic diamagnetic state.[35] Continuous-wave electron paramagnetic resonance (cw-EPR) experiments on frozen, glassy solutions show a broad peak detectable at temperatures lower than 100 K and displaying the typical features of a doublet state.[34,36] To complete the solution-phase magnetic picture, low-temperature electron nuclear double resonance (ENDOR) could assess the interactions of the unpaired electron with both gold[39] and hydrogen nuclei.[40] On the other hand, the knowledge of the magnetism of $Au_{25}(SR)_{18}^0$ in the solid state, *i.e.*, the physical state which most other gold magnetism data refer to, is far less advanced. According to superconducting quantum interference device (SQUID) magnetometry studies, $Au_{25}(SCH_2CH_2Ph)_{18}^0$ (hereafter, we will indicate phenylethanethiolate simply as SC2Ph) is as paramagnetic in the solid state[27,34,41] as in frozen solution.[33,35] Noteworthy, the nature of the capping ligand cannot be ignored. We have recently shown that by using *n*-butanethiolate ligands the resulting crystals are formed of a linear sequence of $Au_{25}(SBu)_{18}^0$ clusters interconnected by Au-Au bonds: overlap of the singly occupied molecular orbitals (SOMOs) of neighboring clusters allows coupling the individual spins with formation of an antiferromagnetic polymer, as revealed by EPR spectroscopy.[42] This result shows that possible interactions between paramagnets in the solid state should always be taken into consideration but also understood in terms of the crystallographic structure.

In this work, we describe the magnetic behavior of $Au_{25}(SC2Ph)_{18}^0$ in different solid-state forms, as assessed by EPR spectroscopy. In this connection, it is worth noting that SQUID has been the technique of choice for most of the previously quoted studies on molecular and non-molecular or non-atomically precise Au nanoparticles. This method allows detecting the susceptibility of the entire sample, which may be the result of different magnetic contributions (ferromagnetic, paramagnetic, diamagnetic, etc.). In EPR, on the other hand, only unpaired electrons are observed and, therefore, the diamagnetic contribution, which may be very significant, is completely removed. Moreover, different contributions to the overall magnetization can be often separated: for instance, ferromagnetic signals can be easily distinguished from most paramagnetic signals because they are characterized by completely different lineshape and temperature dependencies. In the past, consistent EPR studies have been carried out to study both molecular $Au_{25}(SR)_{18}$ or $Au_{25}(SR)_{18}$ doped with Pt, Pd, or Hg, and larger non-molecular Au nanoparticles.[19,20,34,36,39,42-45] It was also employed for studying magnetism of gold nanorods and nanoparticles, which showed ferromagnetic signals.[46,47] The potential of the EPR approach has been evidenced particularly well through the observation of

size-dependent signals for gold nanorods.[46] In most cases, on the other hand, analogous samples were found to be EPR-silent or showed very weak and hardly interpretable signals.[22,48] Our study takes advantage of using a cluster, $Au_{25}(SC2Ph)_{18}^{0}$, whose structure in the neutral state has been refined very recently[49] and whose magnetic properties in solution are well understood. The interactions between $Au_{25}(SC2Ph)_{18}^{0}$ clusters in the solid state were studied by using a combination of experimental and theoretical analyses. By carrying out a comparative study of the magnetic behavior of samples endowed of different morphology and crystallinity, we could detect and rationalize, for the first time, a series of magnetic behaviors. Independent EPR and density functional theory (DFT) calculations concur in pointing to the importance of spin-orbit (SO) coupling effects to explain the observed phenomena.

4.2. Results and discussion

$Au_{25}(SC2Ph)_{18}^{0}$ was prepared by oxidation of diamagnetic anion $Au_{25}(SC2Ph)_{18}^{-}$. By using methodologies that we devised and described previously, the oxidation was carried out either chromatographically[50] or electrochemically.[49] Each sample was meant to provide a specific example of different crystalline order and physical state: frozen solution, film, single crystal, immobilized single crystal, collection of 10 crystals, immobilized collection of 10 crystals, microcrystals. Figure 4.1 shows images of these samples.

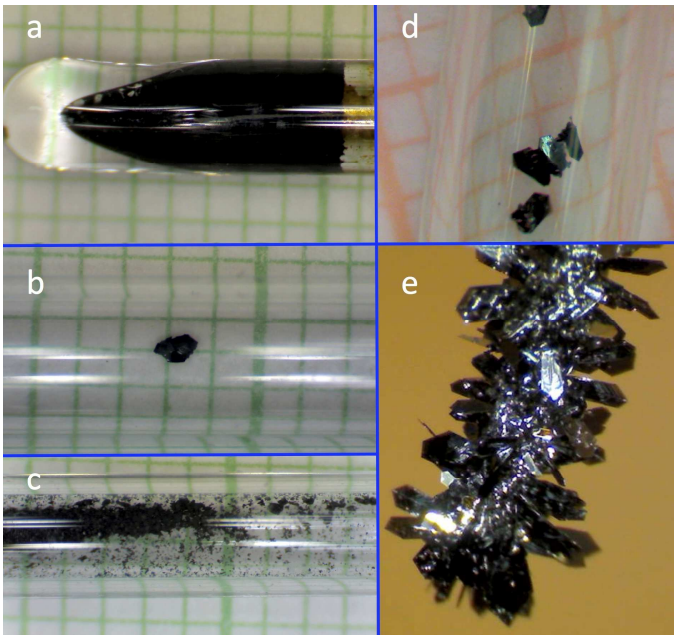

Figure 4.1. Images of the solid samples inside the EPR tubes: (a) film, (b) single crystal, (c) microcrystals, (d) collection of single crystals. For reference, the backgrounds are 1 mm graph papers. The single crystals were collected from those electrocrystallized on a 0.7 mm diameter gold-wire electrode (e).

4.2.1. Film

The $Au_{25}(SC2Ph)_{18}^{0}$ film was prepared inside the EPR tube by evaporation of the solvent from a dichloromethane solution. The film corresponds to a virtually amorphous solid and thus represents the lowest crystalline degree of the solid samples investigated herein. Figure 4.2 shows the EPR spectra (in black) obtained at temperatures ranging from 5 to 160 K, together with the corresponding simulations (in red). To evidence better the weak signals observed at temperatures larger than 60 K, the data in Figure 1a have been multiplied by a factor of 10.

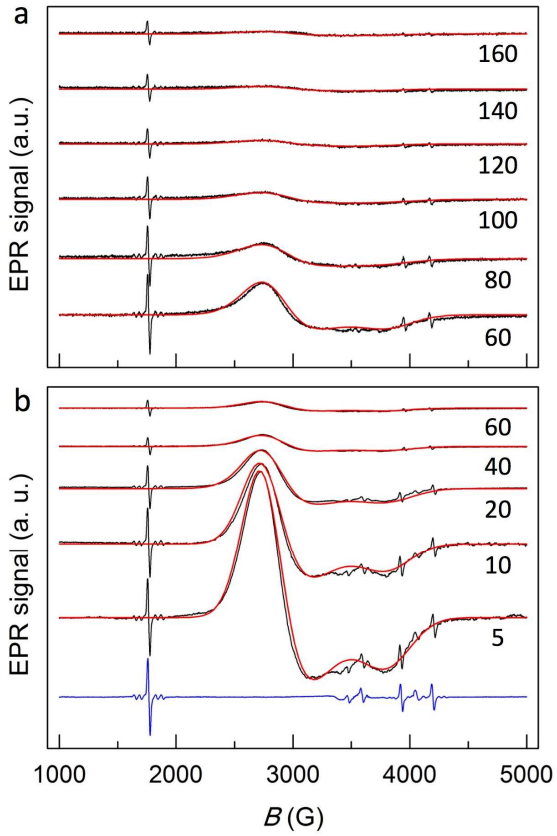

Figure 4.2. Experimental (black) and calculated (red) cw-EPR spectra of an $Au_{25}(SC2Ph)_{18}^{0}$ amorphous film at different temperatures (K), as indicated. In (a), the data have been multiplied by a factor of 10 with respect to those in (b). In (b), the blue trace corresponds to the EPR cavity at 5 K.

Each spectrum consists in a quite broad anisotropic line that can be well simulated by considering an ensemble of randomly oriented paramagnetic clusters with S = 1/2 and a Zeeman interaction described by an orthorombic *g*-tensor with principal values (at low temperatures) of 2.53 (x), 2.36 (y), and 1.82 (z); these values are very similar to those previously described for $Au_{25}(SC2Ph)_{18}^{0}$ in frozen solutions at similar temperatures, *i.e.*, 2.56, 2.36, and 1.82, respectively.[34,36] Figure 1 shows that an increase in temperature has the main effect of diminishing the intensity of the signal, which becomes barely detectable for temperatures larger than 160 K. This decrease is qualitatively similar to that already observed for the same cluster in frozen solution.[36] The main difference between the two cases (Figure 4.3 shows a direct comparison of the two spectra at 10 K) is that inhomogeneous broadening is more severe in the film than in the frozen solution. Indeed, the spectrum of the film could be simulated only by including some distribution for the y and the z components of the *g*-tensor, which correspond to the two negative peaks at 3000-4000 G; for 5 K we used fwhm (full width

at half maximum) values of 0.28 (g_y) and 0.15 (g_z) for y and z, respectively, whereas even larger fwhm values were used for higher temperatures. This distribution suggests the presence of weak orientation-dependent interactions in the film.

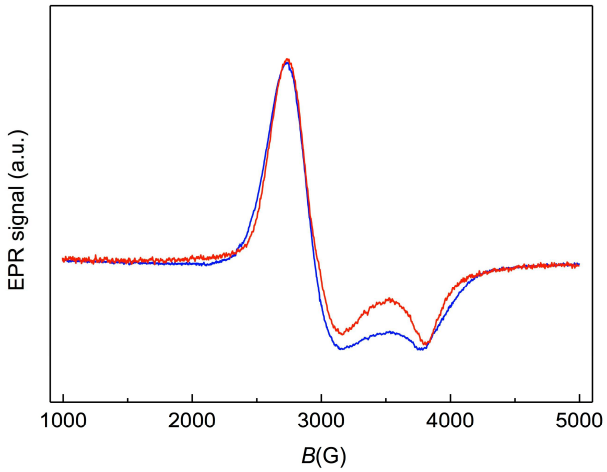

Figure 4.3. cw-EPR spectra of $Au_{25}(SC2Ph)_{18}^0$ at 10 K. The red trace shows a 2 mM dichloromethane solution, whereas the blue trace pertains to the film. For the sake of better comparison, the spectra were corrected for the signal of the EPR cavity and normalized on the maximum intensity.

Insights into this aspect can be obtained from the temperature dependence of the magnetic susceptibility (χ_m). For an ensemble of perfect, noninteracting paramagnets, χ_m is inversely proportional to the temperature, as described by the Curie law (eq 4-1):

$$\chi_m = \frac{N\beta^2 g_L^2 J(J+1)}{3k_B T} = \frac{C}{T} \qquad (4\text{-}1)$$

where the Curie constant C is composed of the number of spins N, the Bohr magneton β, the Landé factor g_L, the quantum number of the total magnetic moment J, and the Boltzmann constant k_B. The EPR signal can be integrated to obtain the corresponding EPR absorption spectrum, and further integration yields the so-called double integrated EPR intensity (I_{EPR});. I_{EPR} is proportional to χ_m and, therefore, as long as the Curie law is obeyed, a plot of I_{EPR}^{-1} vs T should be linear.

The best example of noninteracting paramagnetic MPCs is provided by clusters in a diluted frozen solution. Analysis of the data for 2 mM $Au_{25}(SC2Ph)_{18}^0$ in frozen dichloromethane[36]

shows that in the experimentally accessible temperature range (6 - 80 K) I_{EPR}^{-1} vs T is indeed quite linear (r^2 = 0.997), as shown in Figure 4.4.

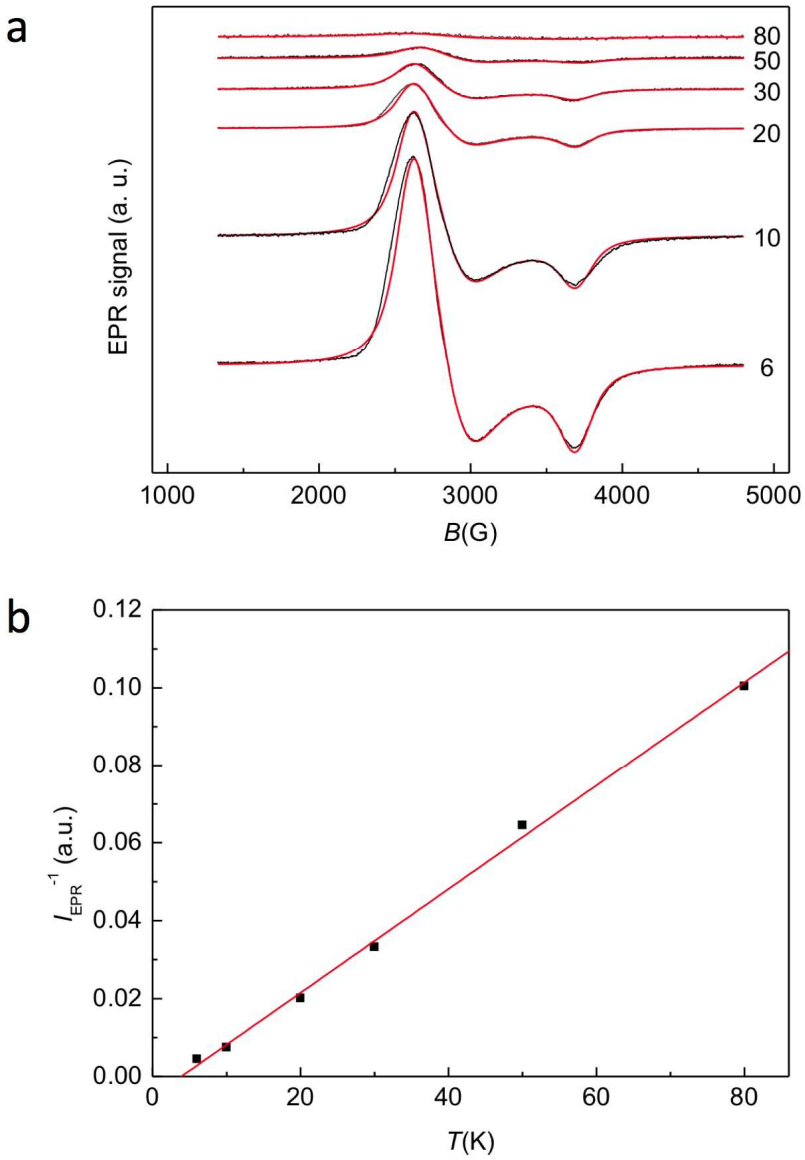

Figure 4.4. (a) cw-EPR spectra of 2 mM $Au_{25}(SC2Ph)_{18}^0$ in dichloromethane (black traces) at different temperatures (K), and corresponding simulations (red traces). (b) Plot of I_{EPR}^{-1} (inverse of the doubly integrated EPR signal) as a function of temperature.

In fact, the observation of a nonzero intercept at 4(1) K suggests that this system could be better described by the Curie-Weiss law (eq 4-2)

$$\chi_m = \frac{C}{(T - T_C)} \qquad (4\text{-}2)$$

where T_C is the intercept or Curie temperature, which marks the onset of magnetic interactions between the paramagnets. Although this T_C value is indeed very close to zero, we note that even at 2 mM concentration in frozen solution the distance between individual clusters is not particularly large: $Au_{25}(SC2Ph)_{18}^0$ has a radius of 13.2 Å[36] and a core radius of 4.9 Å,[32] and therefore, the mean Au-core edge-to-edge intercluster distance is 8.4 nm, whereas the mean Au-core edge-to-edge distance between the nearest neighbors[51] is only 4.2 nm. At this distance, a nonzero exchange coupling between the spins of neighboring clusters cannot be completely excluded.

Figure 4.5 shows the I_{EPR}^{-1} vs T plot for the film. Interestingly, whereas in the high temperature range the plot is quite linear (r^2 = 0.987), a net deviation from linearity occurs for T < 80 K, with an intercept of 63(4) K. This deviation is attributed to a weak ferromagnetic interaction between the spins of the individual clusters. The not-so-small intercept value is thus in keeping with a non-Curie behavior caused by partial parallel alignment of the spins, as described by eq 4-2. This shows that some interactions are clearly detectable in the solid-state, despite the structurally disordered film sample. This is indeed reasonable because the mean Au-core edge-to-edge intercluster distance in $Au_{25}(SC2Ph)_{18}$ films can be bracketed between 1 and 2 nm.[36,49,52]

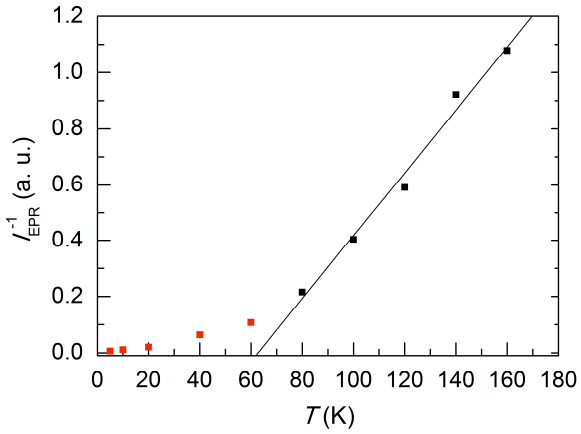

Figure 4.5. Dependence of the reciprocal of the double-integrated EPR intensity on the reciprocal of temperature. The solid line is the linear regression of the data (black square) at the higher temperatures.

4.2.2. Single crystals

A perfectly crystalline sample features the opposite case of an amorphous film. We used one single crystal obtained by electrocrystallization of $Au_{25}(SC2Ph)_{18}^0$.[49] Figure 4.6 shows that the spectrum consists in a narrow signal centered at about 2500 G. As the temperature increases, the signal becomes weaker, and virtually disappears for T > 35 K. The monocrystal signal (peaks at 2460-2630 G) and its temperature dependence are thus very different from those described for the amorphous film (peaks at 2700-3800 G).

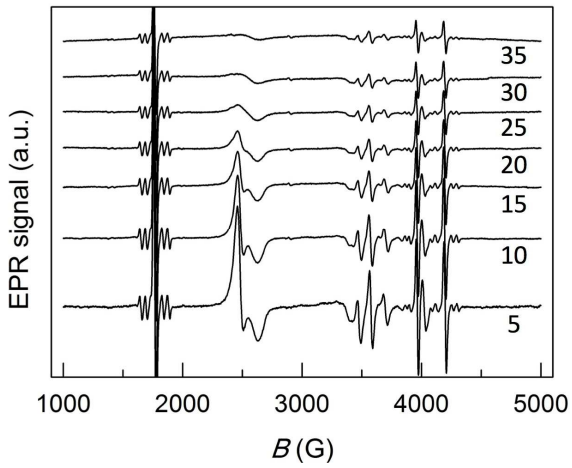

Figure 4.6. Effect of temperature (K) on the cw-EPR spectra of one single crystal of $Au_{25}(SC2Ph)_{18}^0$.

A single crystal of interacting paramagnets should be anisotropic and, therefore, one would expect to observe relevant spectral changes in both lineshape and position upon rotation of the EPR tube with respect to the direction of the applied magnetic field. We recorded a series of EPR spectra after progressively rotating the tube by 90°, and the results are shown in Figure 4.7a. Surprisingly, however, the spectrum did not change. A simple explanation of having an isotropic system is highly unlikely because the principal g tensor values optimized for the film and frozen-solution EPR spectra already evidenced a high degree of anisotropy. We suspected that the observed *apparent* isotropic behavior was caused by a physical reorientation of the crystal inside the tube, as expected for a ferromagnetic crystal that would minimize its magnetic energy by aligning its anisotropy axis along the direction of the applied field, with the result of observing the same spectrum at each orientation.

To confirm this hypothesis, we put one single crystal of similar size in an EPR tube and then added acetonitrile, a solvent in which the cluster is insoluble. Upon cooling, MeCN freezes and blocks the crystal from possible field-induced reorientations of the crystal. As clearly shown in

Figure 4.7b, the spectrum recorded upon a 90° rotation is completely different from the original spectrum (or, similarly, that obtained upon a 180° rotation), in full agreement with our hypothesis. The difference between the initial states of the two samples is attributed to the way by which the crystal gets immobilized by the frozen solvent in comparison with the free crystal, which can optimize its position with respect to the direction of the applied field.

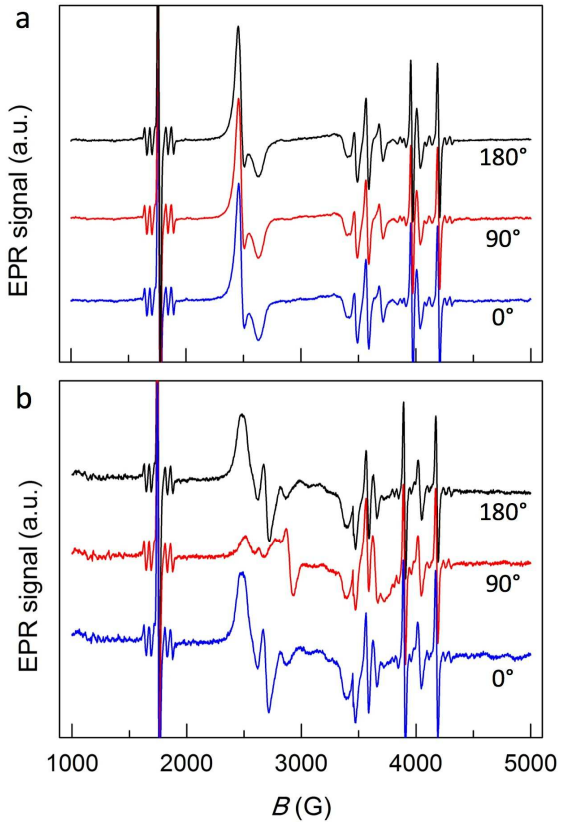

Figure 4.7. Orientation dependence of the cw-EPR spectra of one single crystal of $Au_{25}(SC2Ph)_{18}^{0}$ uncovered (a) or covered (b) by frozen MeCN. Within each graph, the EPR tube was rotated by 0 (blue), 90 (red), and 180° (black). T = 5 K.

To test the ferromagnetism hypothesis, we carried out EPR hysteresis experiments. A typical experiment consisted in an upward scan (from low to high fields) followed by a backward scan carried out after a time long enough (in this specific case, 30 min) for the system to reach equilibrium; this procedure makes the upward and the downward scans determined by the situations attained at low or high field, respectively. The experiment also included a third, upward scan (again, after a 30 min rest period) to check whether the first scan could be reproduced precisely: this was always verified. Differences between the upward and backward

spectra are caused by magnetization of the sample at high field value, and provide an important indication of ferromagnetism.

The hysteresis experiments showed that an effect is perceivable for T < 10 K. This effect is particularly evident at 5 K (Figure 4.8), at which the low-field signals in the upward and downward spectra are substantially different in both intensity and lineshape; as aforementioned, the first and the last upward scans are overlapping. These temperatures point to an apparent anisotropy energy on the order of 0.4-0.8 meV. No evident hysteresis, on the other hand, was detectable for the single crystal immobilized in frozen MeCN, whether by optimizing the orientation of the sample or after rotation by 90° (Figure 4.9). This behavior can be rationalized by considering that whereas the free single crystal can modify its orientation and thus optimize alignment of its anisotropy axis with the applied field (which maximizes hysteresis), in the second experiment the single crystal is blocked in a random orientation and, therefore, any hysteresis effect is significantly reduced.

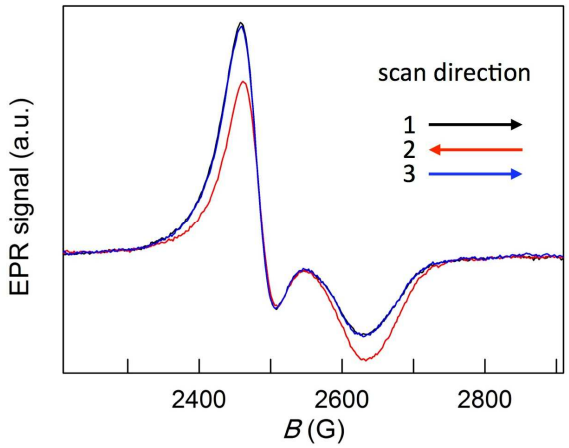

Figure 4.8. Hysteresis cw-EPR experiment for a $Au_{25}(SC2Ph)_{18}^{0}$ single crystal at 5 K. The direction and trace color of the three scans are indicated.

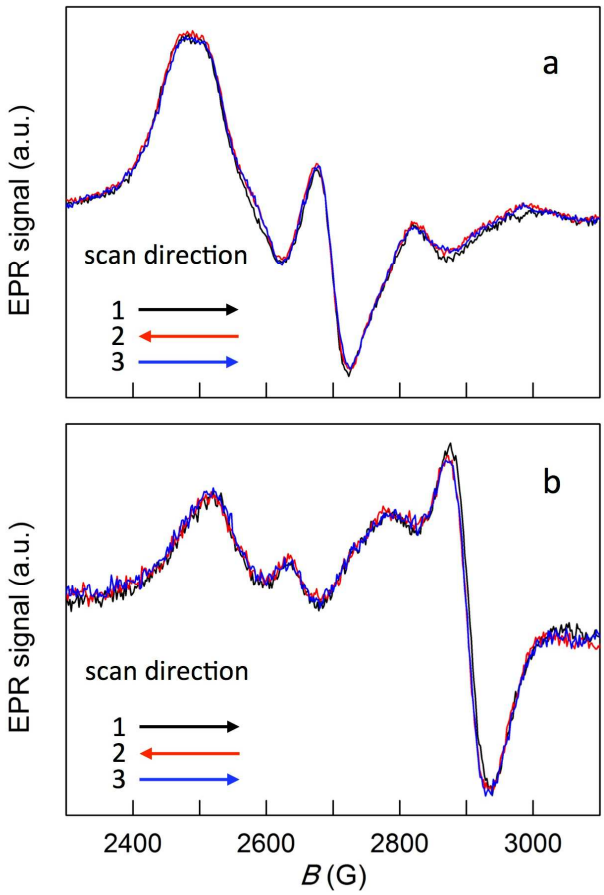

Figure 4.9. Hysteresis cw-EPR experiments for a $Au_{25}(SC2Ph)_{18}^{0}$ single crystal in frozen MeCN at 5 K. Graph (a) and (b) were taken at 0 and 90° rotation of the EPR tube, r espectively.

The effect of increasing the complexity of the experimental system was studied by using a collection of 10 single crystals with dimension comparable to those of the previous samples. Indeed, the presence of more than one crystal modifies the spectrum quite significantly. The same is true for a similar group of crystals trapped in frozen MeCN. As observed for the isolated single crystals, the hysteresis experiments (Figures 4.10 and 4.11) show that differences between the upward and downward traces is evident for the free crystals but not for the MeCN-frozen sample.

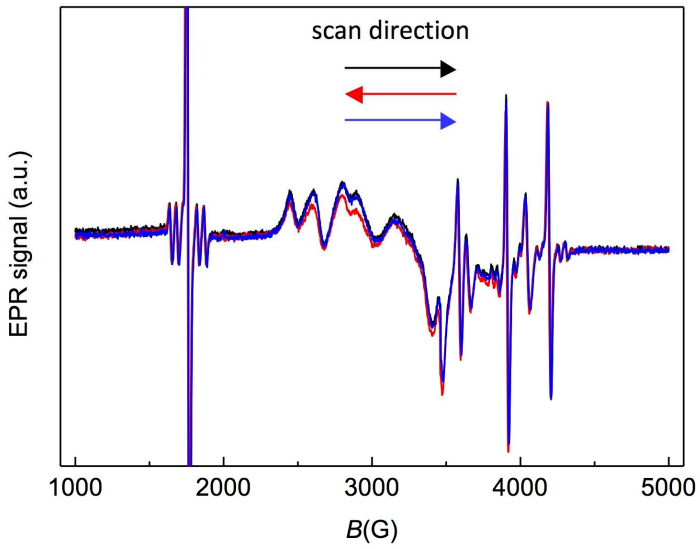

Figure 4.10. Hysteresis cw-EPR experiment for a group of 10 single crystals of $Au_{25}(SC2Ph)_{18}^{0}$ at 5 K. The direction and trace color of the three scans are indicated.

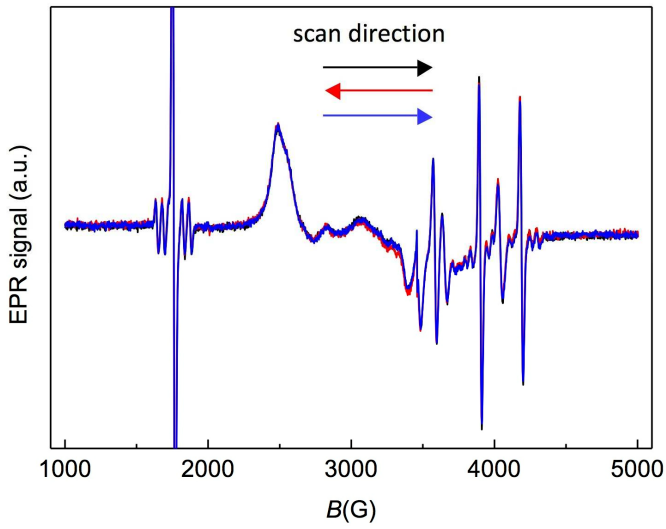

Figure 4.11. Hysteresis cw-EPR experiment for a group of 10 single crystals of $Au_{25}(SC2Ph)_{18}^{0}$ immobilized by frozen acetonitrile at 5 K. The direction and trace color of the three scans are indicated.

Comparison of the results obtained for the solid samples clearly shows that when the paramagnetic $Au_{25}(SC2Ph)_{18}^{0}$ clusters are in the crystalline state, the spins of the single clusters are no more independent. The observed effects on the EPR spectrum are due to a cooperative ferromagnetic ordering. These results and comparisons, including the behavior of

the film, thus provide compelling evidence for the onset of ferromagnetic behavior, as well as showing that the magnetic properties are very sensitive to the crystallinity and the physical state of the sample. As will be shown subsequently, also the lineshape of these signals are associated with the ferromagnetism of the single crystals.[53]

4.2.3. Microcrystals

We then studied a sample consisting of a very large ensemble of much smaller crystals, which will be denoted as microcrystals. This was meant to provide a sample somehow more similar to those typically used in SQUID measurements. The EPR spectra were recorded in a particularly wide temperature range (Figure 4.12), also because the temperature dependence of the spectral pattern proved to be quite complex.

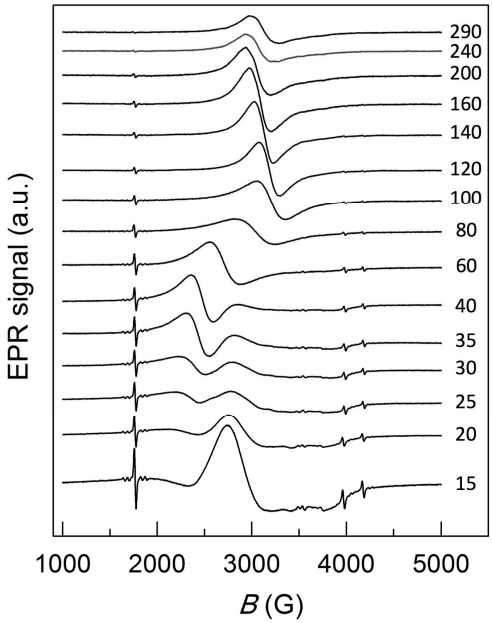

Figure 4.12. Effect of temperature (K) on the cw-EPR spectra of an $Au_{25}(SC2Ph)_{18}^{0}$ collection of microcrystals.

For temperatures decreasing from 100 K, the signal initially broadens and shifts to lower fields. This behavior is attributed to the onset of superparamagnetism, which is typical for small magnetically ordered particles.[54-57] In these systems, the exchange interaction and magnetic anisotropy generate a strong temperature-dependent inner field that adds to the applied external field. For uniaxial symmetry, the two opposite directions of the anisotropy axis correspond to the two minima of the anisotropy energy (E_{an}), which is the energy barrier to invert the direction of the magnetization. When $k_BT > E_{an}$, the temperature is high enough for

the magnetization to reverse its direction. This superparamagnetic behavior is somewhat similar to paramagnetism, but the coupled spins give rise to a higher magnetization. For $k_BT < E_{an}$, on the other hand, this magnetization flipping is hampered and the system becomes ferromagnetic; hysteresis is then usually observed, as it will be discussed in detail in the next paragraph. In addition to the superparamagnetic/ferromagnetic signal, the familiar paramagnetic signal becomes perceivable starting from 40 K, at ca. 2750 G, and its intensity progressively increases as temperature decreases, as already observed for the film and the frozen solution. It is finally worth mentioning that, when the temperature is increased above 100 K, the superparamagnetic signal is still present but displays the peculiar behavior of initially shifting to lower fields and then, for T > 200 K, to higher fields. This behavior is probably associated with the thermal population of higher energy spin states. In the following, however, we will specifically focus on the results obtained in a temperature range comparable to that explored for the other samples.

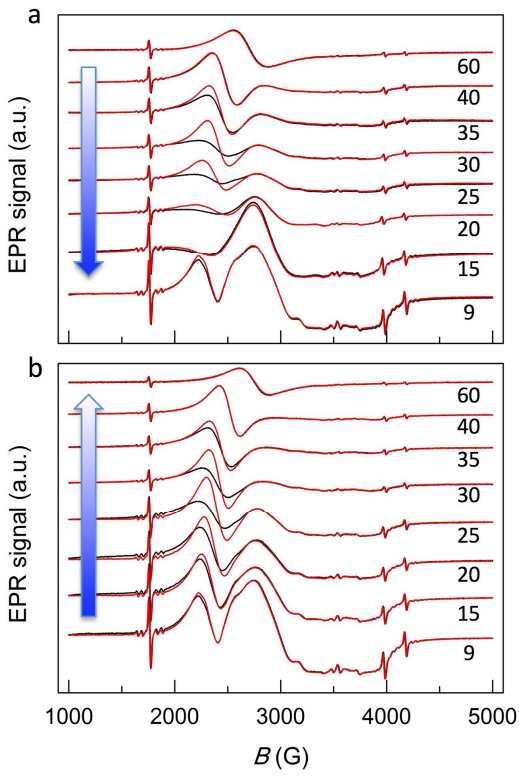

Figure 4.13. Hysteresis cw-EPR experiments for a large collection of $Au_{25}(SC2Ph)_{18}^0$ microcrystals. Panel (a) shows the effect of decreasing the temperature from 60 to 9 K; panel (b) the corresponding temperature increase. The black and the red traces indicate the low-to-high and high-to-low field directions, respectively.

Figure 4.13 shows the outcome of the hysteresis experiments. At each temperature we carried out the same sequence of three scans explained in the previous section. The third scan was always found to overlap precisely with the first scan and thus is not shown for clarity. As the temperature progressively decreases from 40 K (Figure 7a), the signals observed at 2000-2700 G for the upward and the downward scans are substantially different. The main effect is that in the downward spectra the signal is stronger and slightly shifted to higher fields. The hysteresis experiments thus show that the microcrystals display ferromagnetic behavior. Interestingly, hysteresis is observed at a higher temperature than for the large crystals. The magnetic anisotropy energy E_{an} of the microcrystals sample can be estimated on the order of ca. 3 meV, which is about one order of magnitude larger than the energy value observed for the single crystal. Indeed, this result would be quite unusual because both the magnetocrystalline and the magnetostatic anisotropy contributions to the overall magnetic anisotropy are expected to decrease as size decreases.[58] However, whereas for microcrystals we are dealing mostly with single-domain particles with uniform magnetization, for the much larger single crystal the magnetization is not uniform and the form of the anisotropy energy is conceivably more complex, with several local minima.[59] Indeed, the observation of very different spectra observed upon rotation of the immobilized crystals already indicates that the overall anisotropy of the single crystal (as well as that of a collection of large crystals) is certainly large. The comparatively low EPR field reachable (5000 G, *i.e.*, significantly less than in SQUID experiments) can only rotate part of the magnetization and overcome local anisotropies, with the result of giving rise to the small hysteresis observed. A size-controlled difference in anisotropy energy, on the other hand, might be explained on a different basis. $Au_{25}(SC2Ph)_{18}^{0}$ has only one spin s = 1/2 but the not-so-small radius of 13.2 Å.[36] This makes the saturation magnetization low, and the magnetostatic effects should not be particularly relevant. Simulation of the spectrum of the single crystal indicates that the surface contribution to magnetization must be taken into account, and therefore, that the surface anisotropy also should be important. Any surface effect is clearly even more important for the microcrystalline sample, which includes a significant fraction of tiny crystals. An increase of the magnetic anisotropy due to the surface effect was already observed.[60] Moreover, surface effects on magnetic moment and anisotropy have been inferred as important also for gold nanomagnetism.[61] The study of the connection between shape and magnetic properties is receiving attention also in the context of other metal nanoparticles.[62]

The fact that hysteresis apparently becomes less evident at the lowest temperatures is an artifact related to the rest time spent at the 5000 G. Due to the high anisotropy value compared to the thermal energy at these temperatures, the magnetization relaxation time (τ) becomes very long. If the rest time is not sufficiently long, at the beginning of the downward scan the magnetization has not yet completely relaxed, *i.e.*, the sample is still experiencing a situation somehow similar to that of the low-field equilibrium. An example of the effect of the rest time (at 20 K), which results in a slightly larger hysteresis, is provided in Figure 4.14. At even lower temperatures, increasing the rest time significantly becomes experimentally unfeasible. For example, use of the Neél-Arrhenius equation, $\tau = \tau_0 \exp(E_{an}/k_B T)$,[63] and the pertinent approximate E_{an} values shows that, at 10 K, the microcrystals' τ is at least one order of magnitude longer than for the single crystal (for which we waited 30 min). Finally, the persistence of the paramagnetic signal of isolated clusters, partially overlapping to the ferromagnetic signal, is attributed to the finest or the most amorphous fraction of the sample.

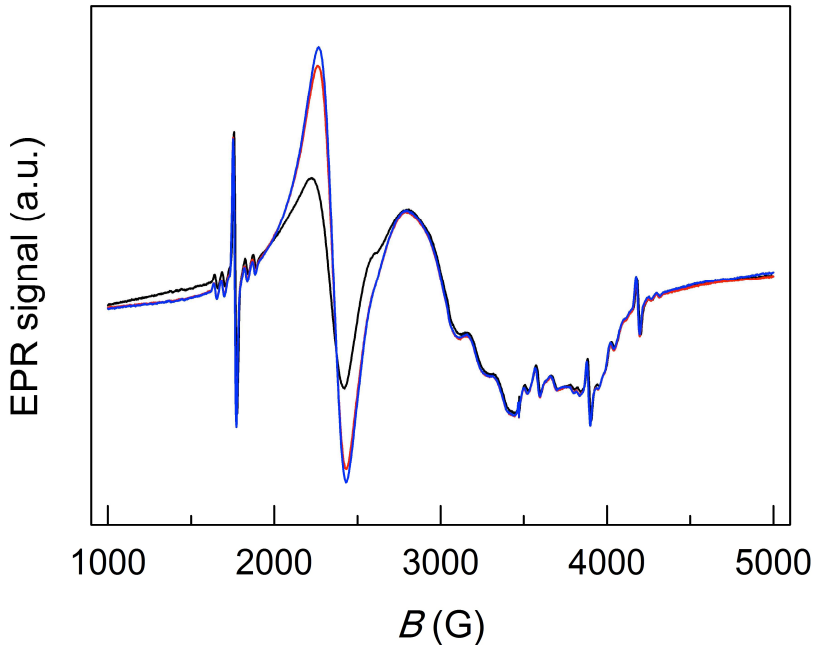

Figure 4.14. Example of the effect of the rest time on the hysteresis experiment carried out at 20 K for the $Au_{25}(SC2Ph)_{18}^0$ microcrystals. The two downward scans correspond to 30 min (red) and 60 min rest time (blue) after the upward scan (black).

An evident new spectral feature emerges upon reaching the lowest temperature explored. Figure 4.13a shows that as *T* decreases the ferromagnetic signal broadens and nearly

disappears upon reaching 15 K, whereas it sharpens abruptly at 9 K. Such a sudden change is typical of a phase transition or some other physical change in the sample. To gain insights into its nature, we recorded an additional set of hysteresis experiments by increasing the temperature from 9 K (Figure 4.13b). A comparison between the plots in Figure 4.13a,b shows that the spectra of the two sets are remarkably different. This difference could be attributed to a phase transition,[64] but this would reproduce the pattern when the experiment at the given temperature is repeated. Instead, the memory of the phenomenon that takes place at 9 K is evidently maintained in the subsequent experiments shown in Figure 4.13b, which indicates that an irreversible transformation occurred. It is also worth noting that once the temperature is > 40 K, virtually the same spectrum is observed, regardless of how that temperature was reached. The spectra become indistinguishable (we checked it up to 290 K by repeating the same patterns of Figure 6), essentially when hysteresis disappears. The same signal shape obtained at 9 K is observed also after the sample is kept for one day at room temperature. It only disappears upon physically removing, shaking and then reinserting the EPR tube into the cavity. The most plausible explanation of the phenomenon occurring at 9 K is thus a physical reorientation of the microcrystals, as similarly observed for the large crystal/s. The microcrystals would thus minimize their magnetic energy by aligning their anisotropy axes with the magnetic field, with the consequence of sharpening the signal. Once the crystals reorganize, the resulting orientation is maintained. This phenomenon takes place only at low temperature, because at higher temperatures the sample can minimize its energy by another relaxation mechanism, *i.e.*, partial alignment of the magnetization with the field. To do this, it must overcome an energy barrier due to magnetic anisotropy. At low temperature, this barrier is too high compared to the thermal energy and, therefore, the physical rotation mechanism prevails.

The measurements performed on the ensemble of microcrystals show that also this sample exhibits a ferromagnetic behavior, but in this case also a paramagnetic contribution due to weakly interacting clusters in less crystalline zones. These results confirm further that the observed ferromagnetic behavior is strongly affected by the physical characteristics of the samples. In the following sections we will address possible explanations of the observed behaviors.

4.2.4. Theoretical analysis of the EPR data

As explained in Chapter 2, the leading factor determining the orientation of the magnetization of a ferromagnetic particle in definite directions is the magnetic anisotropy energy. Microscopically, for heavy elements, the anisotropy energy is mainly determined by the SO interaction.[65] The SO coupling constant for an isolated cluster can be estimated from the CW-EPR spectra of the $Au_{25}(SC2Ph)_{18}^0$ film, which corresponds to the solid-state situation in which the clusters are comparatively more magnetically isolated. Thus, we developed a model by starting from the superatom concept[66] in which, for the diamagnetic anion, the highest occupied molecular orbitals (HOMOs) are viewed as consisting of three degenerate P-type superatomic orbitals, as detailed in Chapter 1. In fact, it was already discussed that this triple degeneracy is not strictly applicable as one orbital is found at a higher energy than the others;[36] this was also found by taking into account the effect of ligands on the frontier orbitals.[67] Even by assuming full degeneracy, it is clear that upon removal of one electron to form $Au_{25}(SC2Ph)_{18}^0$, which has an effective spin S = 1/2, further orbital splitting occurs. Degeneracy can be removed due to SO coupling[68] and/or distortions due to the crystal field and the Jahn-Teller effect.[41,69]

The total Hamiltonian is then given by eq 4-3:

$$\hat{H} = \lambda \mathbf{S}\cdot\mathbf{L} + D[3L_z^2 - L(L+1)] + g_e\beta\mathbf{S}\cdot\mathbf{B} + \beta\mathbf{L}\cdot\mathbf{B} \qquad (4\text{-}3)$$

where the four terms are the SO, the crystal field, the spin and the orbital Zeeman Hamiltonians (caused by the applied magnetic field), respectively; **S** and **L** are the spin and the orbital moment operators, L and L_z are the modulus and the z component operator of **L**, g_e is the electronic g factor, λ is the spin-orbit constant, D is the axial distortion parameter, and **B** is the applied magnetic field.

If the usual perturbation treatment is performed to correlate the principal values of the **g** tensor, considering SO as a perturbation to crystal field, no accordance with the experimental data is obtained: in effect, according to this treatment, g_{zz} must be equal to g_e (2.0023). Instead, the experimentally measured g_{xx}, g_{yy}, and g_{zz}, all substantially differ from the free electron g_e value.

The obvious conclusion is that the perturbation theory cannot be applied in this case. Since λ is directly proportional to the nuclear charge Z, we can expect the SO energy to become more important for heavier elements. And in effect, while for the first row transition elements the

crystal field energy is dominant and SO can be treated as a perturbation, for the lanthanides we observe the opposite, i.e. the energies are mainly determined by SO and perturbed by the crystal field. For third row transition metals, such as gold, the two energies probably have comparable magnitudes. In this case ì the only right way to find the energies is the numerical matrix diagonalization. In this way the EPR spectrum can be calculated and the simulation of the experimental spectrum can be performed, with the superatomic spin-orbit λ (for a p^5 configuration $\lambda=-\xi$) and the crystal field D constants as fitting parameters.

To calculate the spectrum of the $Au_{25}(SC_2H_4Ph)_{18}^0$ film, a code was written with Matlab. The Eigen energies were found by diagonalization of the Hamiltonian matrix (equation 4-3) at different fields corresponding to the experimental field values.

The resonance fields were obtained, which are the fields that match the EPR resonance condition at the experimental frequency of ~9.4 GHz. Boltzmann populations were considered and Gaussian lineshapes were used with a linewidth of 4 G. The spectrum was calculated, considering the transitions from the ground state, weighted by the transition probabilities, calculated as $|\langle\Psi_1|B_x|\Psi_2\rangle|^2$ and the Boltzmann population differences.

Since the amorphous film consists of an ensemble of randomly oriented clusters, the spectrum was calculated by integrating over all the possible orientations.

$$I(B)=\int_{\vartheta}\int_{\phi}\chi''[B-B_r(\vartheta,\phi)]\sin\vartheta d\vartheta d\phi \qquad (4\text{-}4)$$

Where χ'' is the single line absorption, calculated as explained above, B_r is resonance field, θ and ϕ are the angles defining the orientation of the applied magnetic field with respect to the cluster crystallographic axes.

The best fit was obtained using a g_e value of 1.9, slightly lower than the usual 2.0023 value, and this was attributed to a scalar relativistic mass effect, as explained below. The initial values of the parameters used in the fitting process were taken from previously reported energy splitting values. The lineshapes were best simulated by introducing a distribution of D values (D = 0.6 ± 0.4 eV), which is the equivalent of introducing a distribution of g in the aforementioned simulations performed with the Easyspin routines.

In our superatomic model, while the lineshape is well simulated by considering only the spin-orbit coupling and the Jahn-Teller-like distortion of the superatomic P orbitals, a slight shift of the resonances to lower fields is observed in the calculated spectrum, with respect to the experimental one. Such a shift can be reproduced by using a free electron g factor slightly

lower than the usual g_e=2.0023. This shift could be explained by introducing scalar relativistic effects. Indeed, since a relatively high spin-orbit constant value was found from the simulations, it is natural to expect that also the other relativistic effects must play an important role for the EPR spectrum. In particular, the line shift can be explained by considering the relativistic mass. For heavy elements (and probably more so for superatoms), the electron velocity becomes closer to the velocity of light and the relativistic mass must be used:

$$m = m_r \frac{1}{\sqrt{1-\frac{v^2}{c^2}}} \tag{4-5}$$

which is always higher than the electron rest mass m_r. because v is always lower than c. The Bohr magneton is thus given by

$$\mu_B' = \frac{e\hbar}{2m_e}\sqrt{1-\frac{v^2}{c^2}} = \mu_B\sqrt{1-\frac{v^2}{c^2}} \tag{4-6}$$

and the Zeeman Hamiltonian, determining the electron paramagnetic resonance becomes

$$\hat{H}_Z = \mu_B g_e B\sqrt{1-\frac{v^2}{c^2}} \tag{4-7}$$

Thus, in the relativistic case the resonance is observed at a higher field, compared to the non-relativistic one and this can explain the shift observed by EPR.

There are some reasons why relativistic effects, both scalar (mass-velocity) and higher order (spin-orbit), are expected to be particularly important on the superatomic P (SOMO) electron: first, the superatomic P orbitals mainly consist in atomic Au s orbitals and thus have a rather high probability of being near to the Au nuclei. This allows the electrons to experience a high nuclear charge and to acquire a high velocity (classically), which enhances the relativistic effects. Moreover, while the SOMO (superatomic P orbitals) is essentially delocalized on the Au_{13} core, the occupied orbitals below the SOMO mainly arise from the $Au_2(SR)_3$ staples. Therefore, the superatomic “nuclear” charge experienced by the unpaired SOMO electron is not strongly screened.

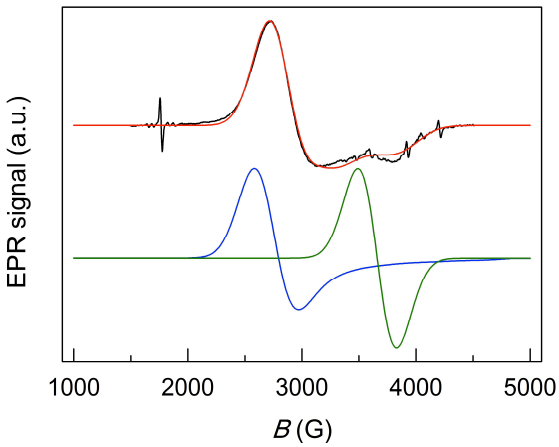

Figure 4.15. Simulations of the cw-EPR spectrum obtained at 5 K for the $Au_{25}(SC2Ph)_{18}^{0}$ film (black). The simulations include SO and distortion (red), only SO (blue), and only distortion (green).

The red trace in Figure 4.15 shows the simulation of the experimental spectrum as carried out by using both the λ and the D values as fitting parameters. Using the values of these parameters obtained from the best fitting ($|\lambda|$=0.8 eV, $|D|$=0.6 eV) the energy values of the splitted SOMO were calculated by means of the Hamiltonian (4-4). We find that, collectively, SO coupling and crystal-field distortion make the energy of the three now non-degenerate HOMOs span an overall difference of 0.26 eV, with the two lower levels splitted by 0.15 eV. This is an interesting result indeed because it provides new relevant information regarding the debated problem of the origin of orbital splitting upon formation of the Au_{25} SOMO. One view is that this is mainly due to the SO coupling,[68] while another asserts that it is a Jahn-Teller-like distortion effect.[41] In fact, according to our analysis of the EPR data, both SO coupling and distortion contribute by comparable amounts to the overall orbital splitting. As a further matter of fact, Figure 4.15 shows that the simulations carried out by including only the SO effect or the crystal-field term cannot reproduce the experimental spectrum.

In order to extract some reliable quantitative information from the EPR spectra of the single crystals, a model for the simulation of the hysteresis experiments had to be developed first.

There are two alternative ways to describe the EPR spectra of superparamagnetic systems: the classical model,[71-75] in which "macroscopic" quantities are introduced, such as the volume of nanoparticles, the saturation magnetization, the anisotropy energy, the demagnetizing fields etc.. This model allows to simulate the spectral shape and its temperature dependence quite correctly, and to get information about some important magnetic parameters and about the

shape and the dimensions of the nanoparticles. However, the introduction of a few empirical parameters with no clear physical meaning is necessary. The quantum mechanical model,[75,76] instead, describes the resonance phenomenon starting from the Spin Hamiltonian, and using "microscopic" parameters, such as the spin of a single center, total number of spins, zero field splitting parameters, which quantify the system anisotropy. This model is not able to describe some classical phenomena, such as the demagnetizing fields, but it does not require the use of empirical parameters and allows to simulate the transition from paramagnetism to superparamagnetism, increasing the number of interacting spins. However, there is no clue in literature on how to describe the EPR hysteresis, intended as the difference in spectral shape and intensity between upwards and backwards sweep. An approach to simulate this phenomenon is suggested here.

The model developed below is based on the quantum-mechanical approach, because it can possibly better describe what happens to systems with a few interacting spins, as in our case. As a drawback, the use of this approach implies that, when dealing with crystals, some macroscopic solid-state effects are necessarily neglected. Nevertheless, such effects are less important in systems with low magnetization, such as ours (only one spin s=1/2 for each cluster more than 1 nm large). Indeed, in this case magnetostatic effects and demagnetizing fields are generally weaker than the single-ion (or, in our case, single-cluster) properties, and can be reasonably neglected.

According to this approach, hysteresis is observed when the populations are not at equilibrium during the field sweep because of the long superparamagnetic relaxation times, which are linked to high magnetic anisotropy.

For an ensemble of strongly interacting spins, we can use the giant spin approximation, treating our system as a single spin with $S=\sum_i^n s_i$, where s_i is the spin of the single paramagnetic center (an $Au_{25}(SR)_{18}$ cluster in our case, with $s_i=1/2$) and n is the number of interacting paramagnetic centers.

So we start with writing the Spin Hamiltonian of our system:

$$\hat{H} = g\beta(\mathbf{B}\cdot\mathbf{S}) + \mathbf{S}\cdot\mathbf{D}\cdot\mathbf{S} \qquad (4\text{-}8)$$

Where **S** is the giant spin vector and **D** is the Zero Field Splitting tensor. The first term represents the Zeeman interaction, which is usually approximately isotropic for ferromagnets, while the second term is the Zero Field Splitting interaction, which in our case is due to the

spin-orbit coupling and can be linked to the magnetic anisotropy of the system. It can be also related to the magnetic anisotropy of the single paramagnetic centers. The axial anisotropy term is usually assumed as to be dominant, so we can write:

$$\hat{H} = g\beta(\mathbf{B}\cdot\mathbf{S}) + D(S_z^2 - S(S+1)/3) \tag{4-9}$$

where D is the axial Zero Field Splitting parameter. In the strong field approximation, valid if **B** is much larger than the Zero Field Splitting interaction (as usually happens), we can treat the second term as a perturbation.

The energy of a state with a certain m_S (m_S = -S, -S+1 ... S) with an applied field $B_{(1)}$ is

$$E_{m_s(1)} = -\hbar^2 D m_s^2 P_2(\cos\vartheta) + \hbar g\beta B_{(1)} m_s \tag{4-10}$$

where $P_2(\cos\theta)=(3\cos^2\theta-1)/2$ is the Legendre polynomial and θ is the angle between the applied field and the anisotropy axis.

The equilibrium population of an energy level (equal to the diagonal elements of the density matrix) is given by

$$\rho_{m_s(1),eq} = \frac{\exp(E_{m_s(1)}/k_B T)}{Z_{(1)}} \tag{4-11}$$

where k_B is the Boltzmann constant and $Z_{(1)}$ is the partition function:

$$Z_{(1)} = \sum_{m_s=-S}^{S} \exp(E_{m_s(1)}/k_B T) \tag{4-12}$$

Clearly the population of each level changes when we apply a field with intensity $B_{(2)}\neq B_{(1)}$: the relationship between the two equilibrium populations is

$$\rho_{m_s(1),eq} = \rho_{m_s(2),eq}\exp(\hbar g\beta\Delta B m_S) Z_{(2)} / Z_{(1)} \tag{4-13}$$

with $\Delta B=B_{(1)}-B_{(2)}$. Once a non-equilibrium population is obtained, the relaxation processes restore the equilibrium population with a characteristic time τ. Therefore, if we change the applied field before equilibrium is reached, we first have a non-equilibrium population which can be expressed as a function of time in the following way:

$$\rho_{m_s(2)} = (\rho_{m_s(1),eq} - \rho_{m_s(2),eq})\exp(-t/\tau) + \rho_{m_s(2),eq} \tag{4-14}$$

Substituting (4-13) into (4-14) we obtain:

$$\rho_{m_s(2)} = (\rho_{m_s(2),eq}\exp(\hbar g\beta\Delta B m_S) Z_{(2)} / Z_{(1)} - \rho_{m_s(2),eq})\exp(-t/\tau) + \rho_{m_s(2),eq} \tag{4-15}$$

and dividing by $\rho_{ms(2)eq}$ we define the *Hysteresis-polarization function* Π_2 as:

$$\Pi_2 = \frac{\rho_{m_s(2)}}{\rho_{m_s(2),eq}} = [\exp(\hbar g \beta \Delta B m_S) Z_{(2)} / Z_{(1)} - 1] \exp(-t/\tau) + 1 \tag{14-16}$$

As the sweeping velocity is given by the field shift in a certain amount of time, we have:

$$t = |\Delta B| / v_{scan} \tag{14-17}$$

and therefore we can write (4-16) as

$$\Pi_2 = [\exp(\hbar g \beta \Delta B m_S) Z_{(2)} / Z_{(1)} - 1] \exp(-|\Delta B| / \tau v_{scan}) + 1 \tag{4-18}$$

Going on with the field sweep, applying a $B_{(3)}$, one finds in a similar way:

$$\begin{aligned}
&\rho_{m_s(3)} = (\rho_{m_s(2)} - \rho_{m_s(3),eq}) \exp(-|\Delta B| / \tau v_{scan}) + \rho_{m_s(3),eq} \\
&\rho_{m_s(3)} = (\Pi_2 \rho_{m_s(2),eq} - \rho_{m_s(3),eq}) \exp(-|\Delta B| / \tau v_{scan}) + \rho_{m_s(3),eq} \\
&\rho_{m_s(2),eq} = \rho_{m_s(3),eq} \exp(\hbar g \beta \Delta B m_S) Z_{(3)} / Z_{(2)} \\
&\rho_{m_s(3)} = (\Pi_2 \rho_{m_s(3),eq} \exp(\hbar g \beta \Delta B m_S) Z_{(3)} / Z_{(2)} - \rho_{m_s(3),eq}) \exp(-|\Delta B| / \tau v_{scan}) + \rho_{m_s(3),eq} \\
&\Pi_3 = \frac{\rho_{m_s(3)}}{\rho_{m_s(3),eq}} = (\Pi_2 \exp(\hbar g \beta \Delta B m_S) Z_{(3)} / Z_{(2)} - 1) \exp(-|\Delta B| / \tau v_{scan}) + 1
\end{aligned} \tag{4-19}$$

Thus, we find for a general applied $B_{(n)}$ field:

$$\Pi_n = \frac{\rho_{m_s(n)}}{\rho_{m_s(n),eq}} = (\Pi_{(n-1)} \exp(\hbar g \beta \Delta B m_S) Z_{(n)} / Z_{(n-1)} - 1) \exp(-|\Delta B| / \tau v_{scan}) + 1 \tag{4-20}$$

with

$$n = \frac{B_1 - B_n}{\Delta B} \tag{4-21}$$

and Π_1=1 by definition, since we assume to start the field sweep from an equilibrium situation. This equation can be computationally solved in order to find Π_n for every applied field.

In this treatment, τ must still be defined. For this aim, the relaxation processes must be considered slightly more in detail.

The energy levels are graphically represented in Fig. 4.16. We observe that they are characterized by an energy maximum, which represents the anisotropy energy barrier to overcome in order to reach the equilibrium. When no external magnetic field is applied the curve is a symmetrical parabola ($E(m_S) = E(-m_S)$, Fig. 4.16a). When the B field is applied, the

energy levels on one side are lowered, while those on the other side are raised, so the populations of the m_S states are changed and the energy maximum is shifted (Fig. 4.16b).

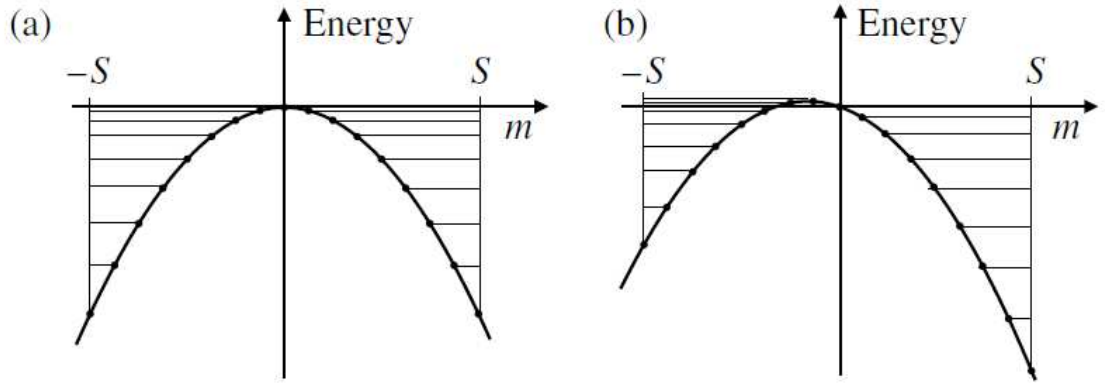

Fig. 4.16. Energy vs m_S diagram (a) with no applied field and (b) with an applied *B* field (from 57)

The energy maximum can be obtained by differentiating (4-10) and equaling the derivative to zero:

$$\frac{\partial E_{m_s(1)}}{\partial m_S} = \frac{\partial \hbar^2 D m_s^2 P_2(\cos\vartheta) + \hbar g \beta B_{(1)} m_s}{\partial m_S} = 0 \tag{4-22}$$

We obtain

$$m_{S\max} = (\hbar g \beta B_n) / (2|D| P_2(\cos\vartheta)) \tag{4-23}$$

and

$$E_{\max} = (\hbar g \beta B_n)^2 / (4|D| P_2(\cos\vartheta)) \tag{4-24}$$

Therefore, the energy barrier which a spin in an m_S level must overcome is given by:

$$\Delta E_{an} = (\hbar g \beta B_n)^2 / (4|D| P_2(\cos\vartheta)) + \hbar^2 D m_s^2 P_2(\cos\vartheta) - \hbar g \beta B_{(1)} m_s \tag{4-25}$$

If we assume that superparamagnetic relaxation is mainly a thermally activated process (as is usually the case), and the relaxation rate mainly depends on the probability to overcome the anisotropy energy barrier, we can apply the Néel-Arrhenius law:

$$\tau = \tau_0 \exp\left(\frac{\Delta E_{an}}{k_B T}\right) \tag{4-26}$$

and subsituting (4-25) into (4-26):

$$\tau = \tau_0 \exp\left(\frac{(\hbar g \beta B_n)^2 / (4|D| P_2(\cos\vartheta)) + \hbar^2 D m_s^2 P_2(\cos\vartheta) - \hbar g \beta B_{(1)} m_s}{k_B T}\right) \quad (4\text{-}27)$$

τ_0 is usually assumed to be weakly dependent on temperature.

Regarding the lineshape, instead of the usual Lorentzian or Gaussian functions, the following solution of the Landau-Lifshitz equation was used, which better describes the spin dynamics of a perfect soft ferromagnet:

$$\chi''(B) = \frac{1}{\pi} \frac{\left[\left(B_0^2 + \Delta_B^2\right) B^2 + B_0^4\right]}{\left[\left(B - B_0\right)^2 B_0^2 + \Delta_B^2 B^2\right]\left[\left(B + B_0\right)^2 B_0^2 + \Delta_B^2 B^2\right]} \quad (4\text{-}28)$$

For the single crystal spectra, the anisotropy axis was supposed to be parallel to the applied magnetic field, as explained before, and the spectrum is given by

$$I(B) = \sum_{m_S=-S}^{S} \chi''(B)[\rho_{m_S,eq}(B) P_{m_S}(B) - \rho_{m_S+1,eq}(B) P_{m_S+1}(B)] W_{m_S} \quad (4\text{-}29)$$

where

$$B_r = B_0 - \frac{(2m_S + 1) D \hbar}{g\beta}$$
$$B_0 = \frac{h\nu}{g\beta} \quad (4\text{-}30)$$
$$W_{m_S} = S(S+1) - m_S(m_S + 1)$$

The simulations of the monocrystal spectra recorded at 5 K, based on this model are shown in Fig. 4.17.

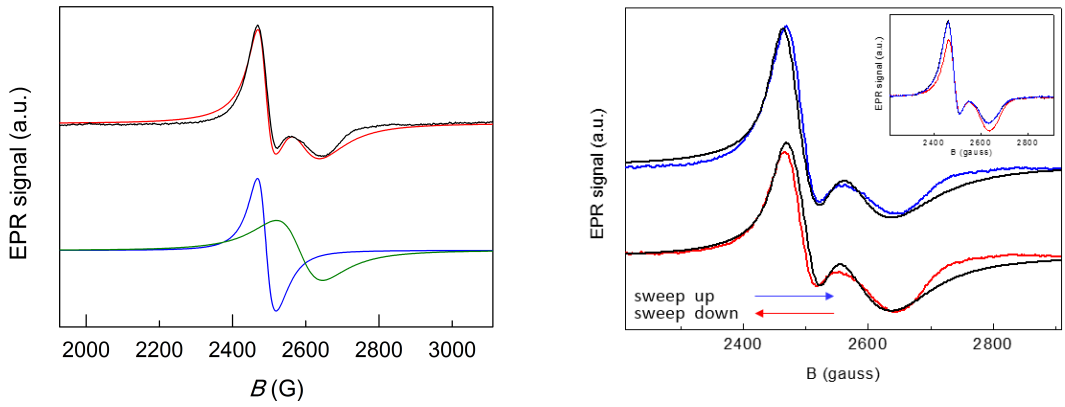

Figure 4.17. Simulations of the spectrum of the single crystal: the two components used for the simulations (left); simulations of the upwards and downwards field sweep (right).

The single crystal spectra could be simulated by two components with different values of magnetization, *g* factor and magnetic anisotropy, attributed to bulk and surface magnetization, as already observed in literature for analogous systems.[53] The values of the magnetic anisotropy parameters and the total spins were relatively low (S_1=8, D_1=8,5 MHz, S_2=6, D_2=5 MHz) This can be explained by considering the fact that with EPR hysteresis experiments we measure only local anisotropy barriers, overcome by only part of the magnetization. Indeed, in contrast with the typical magnetometry hysteresis experiment, here we apply the magnetic field only in one direction (only positive fields) and the fields are not very high. Instead the *g* values of both components were remarkably high (g_1=2.79, g_2=2.7).

The model used for the simulations successfully reproduces the experimental temperature and orientation dependence of the hysteresis: with the best fitting parameters for the monocrystal, the hysteresis decreases significantly when the temperature and the angle between the anisotropy axis and the applied magnetic field are increased, virtually disappearing at *T*=10 K and θ=90°.

These simulations also allowed to evaluate the effect of the SO coupling in the $Au_{25}(SC2Ph)_{18}^0$ crystals. In the previous paragraph, we determined a remarkable effect of the SO coupling in amorphous films. For ferromagnetic crystals the *g* value can be used to obtain similar information. From the simulations we obtained a mean *g* value of 2.745. The remarkable deviation from the free electron g_e value of 2.0023 indicates a high orbital moment and a substantial contribution of SO effects. Indeed, only large SO couplings allow the orbital moment not to be quenched by the crystal field. The ratio between the orbital and the spin moments can be calculated, using the Kittel equation:[70]

$$\frac{\mu_L}{\mu_S} = \frac{g-2}{2} \qquad (4\text{-}31)$$

For our system, this ratio is 0.37. It is worth mentioning that the importance of the orbital contribution to the observed magnetism is a feature that was already observed for large Au nanoparticles.[26]

4.2.5. DFT calculations

DFT simulations were performed to draw further insights into the magnetic properties of $Au_{25}(SR)_{18}$ and quantify to what extent magnetism is affected by the interplay of factors including spin-orbit coupling, Jahn-Teller symmetry breaking, and crystal assembly (*i.e.*, the

difference between the single cluster and its assembly in the crystal). To disentangle these effects, three different structural models were considered for the neutral $Au_{25}(SR)_{18}$ species: two of them consist of individual $Au_{25}(SCH_3)_{18}$ clusters, one where the $Au_{25}(SC)_{18}$ core was taken from the experimental crystal data[49] (adding and relaxing H atoms as needed) and a second one where the geometry of anionic $Au_{25}(SCH_3)_{18}^-$ was fully relaxed at the DFT/PBE0 level, and a third model of 4 $Au_{25}(SC2Ph)_{18}^0$ clusters in the unit cell. Hereafter, these models are denoted as $Au_{25}(SCH_3)_{18}^0$-crystal, $Au_{25}(SCH_3)_{18}^0$-anion, and $Au_{25}(SC2Ph)_{18}^0$-crystal, respectively. Transforming $Au_{25}(SC2Ph)_{18}^0$ into $Au_{25}(SCH_3)_{18}^0$ is a convenient way of reducing computational effort, and the comparison between the $Au_{25}(SCH_3)_{18}^0$-crystal and the $Au_{25}(SC2Ph)_{18}^0$-crystal models will assess the effect of this commonly used approximation. The Jahn-Teller symmetry breaking is absent in the anionic $Au_{25}(SCH_3)_{18}^-$, which is an electronic closed-shell species, and thus the comparison between the $Au_{25}(SCH_3)_{18}^0$-crystal and the $Au_{25}(SCH_3)_{18}^0$-anion models helps quantify Jahn-Teller effects. The NWChem package[77] was employed to simulate individual MPCs by using the hybrid B3LYP[78] exchange-correlation (xc) DFT functional at the scalar relativistic level or by treating the SO coupling effects within the zeroth-order relativistic approximation (ZORA)[79] and the van Wullen formalism.[80] To the best of our knowledge, this is the first time that a hybrid xc-functional and SO coupling are simultaneously employed to describe an MPC. The OPENMX package[81] using the Local Density Approximation (LDA)[82] was used for the solid-state non-spin-collinear calculations.

The orbital scheme predicted by these simulations is summarized in Figure 4.18. In the absence of Jahn-Teller symmetry breaking, the geometry of the $Au_{25}(SCH_3)_{18}^0$-anion model approximately corresponds to an S6 point symmetry group that presents triply degenerate superatomic 1P orbitals, although in the anion, as already noted,[36,68] a residual splitting between two higher-lying and one lower-lying orbital is present (~0.04 eV). Switching to the neutral species and introducing cluster deformation due to the Jahn-Teller effect in the $Au_{25}(SCH_3)_{18}^0$-crystal model completely lifts the degeneracy of the 1P orbitals, leaving a higher-lying SOMO, a HOMO-1 lower in energy by 0.04 eV, and a HOMO-2 further lower in energy by 0.09 eV. SO coupling increases further the orbital splitting by bringing the first and the second energy gaps to 0.12 and 0.15 eV, respectively. Due to SO coupling and Jahn-Teller effects, the three HOMOs are found to span an overall energy difference of 0.27 eV and the

splitting between the two lower levels to be 0.15 eV, in excellent agreement with the EPR derived values of 0.26 eV and 0.15 eV.

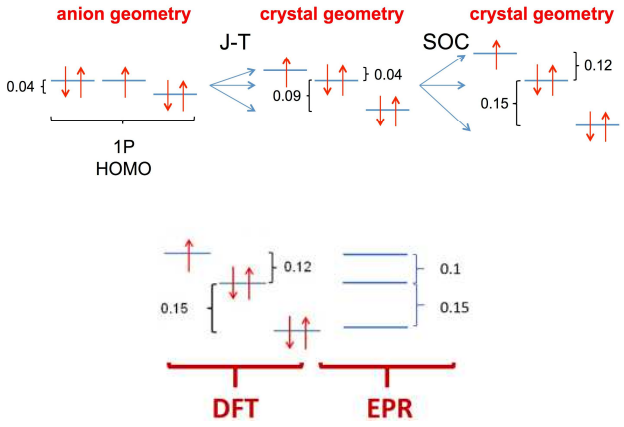

Figure 4.18. Diagram of DFT/B3LYP HOMO orbital energies (eV) in $Au_{25}(SCH_3)_{18}^0$ systems. From left to right: $Au_{25}(SCH_3)_{18}^0$ at the scalar-relativistic level in the $Au_{25}(SCH_3)_{18}^0$-anion geometry, $Au_{25}(SCH_3)_{18}^0$ at the scalar-relativistic level in the $Au_{25}(SCH_3)_{18}^0$-crystal geometry, which includes Jahn-Teller (J-T) effects, $Au_{25}(SCH_3)_{18}^0$ including SO coupling (SOC) in the $Au_{25}(SCH_3)_{18}^0$-crystal geometry. Below, comparison with the values obtained from the "superatomic" simulation of the EPR spectrum.

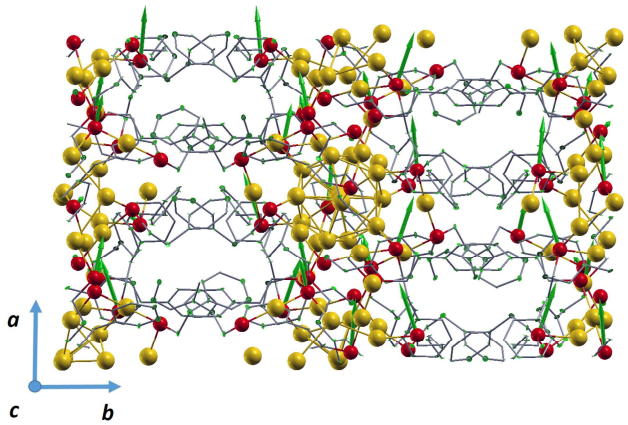

Figure 4.19**.** Schematic depiction of the direction and magnitude of atomic spins (green arrows) in the putative spin global minimum (the spins on the Au atoms are not shown as they would be out of scale). The image shows the unit cell as seen from direction *c*;[49] all clusters but for the central one are thus incomplete. The color codes are: the color codes are Au = yellow, S = red, C = grey. Au and S atoms and bonds are rendered as ball and stick, whereas C is rendered as stick style. H atoms have been removed for clarity.

Non-spin-collinear DFT/LDA calculations were performed on the $Au_{25}(SC2Ph)_{18}^0$-crystal model. Calculations in which spin modulus and orientation were relaxed starting from several initial orientations were first conducted to determine the preferential magnetization axis, which turns out to be the *z*-axis with a total spin component of 3.59 μ_B and a total orbital component of 1.25 μ_B per unit cell. This corresponds to a predicted ratio μ_L/μ_S of 0.35, in excellent agreement with the value calculated from the single-crystal spectrum simulation, 0.37. The direction and magnitude of atomic spins in the energetically most stable ferromagnetic solution so derived are schematically depicted in Figure 4.19. Noteworthy, the spin density is mostly located on Au atoms, but also extends on S and on both aliphatic and aromatic carbons. An exponentially decreasing delocalization of the spin moment from the Au/S MPC framework onto both aliphatic and aromatic C atoms has been noted and studied before.[35] Here we find that spin polarization is induced also on the phenyl groups, as shown in the form of the small arrows displayed on the rings in Figure 4.19; this long-range effect is likely due to a solid-state proximity effect by adjacent S atoms. This finding would thus rationalize the experimentally observed magnetism in the solid-state and its subtle dependence on crystallinity as due to the presence of oriented spin moments on neighboring π-stacked phenyl residues.[83] We were not able to locate the barrier for spin reorientation and thus the anisotropy energy. It is, however, worth mentioning that in our calculations we found another spin local minimum in which the magnetic moment is oriented along the *x*-axis (see Figure 4.18) with a total spin component per unit cell of 2.02 μ_B and a total orbital component per unit cell of 0.37 μ_B, nearly degenerate in energy with the spin global minimum.

4.3. Conclusions.

Magnetometry techniques are generally used to study the magnetic properties of materials, but have failed to provide coherent results for Au MPCs. The most important cause of discrepancy in previous studies was undoubtedly the lack of precise control on MPC stoichiometry and charge state. Interestingly, even for a controlled MPC such as paramagnetic $Au_{25}(SC2Ph)_{18}^0$, SQUID was unable to detect magnetic behaviors other than simple paramagnetism. Here we employ the more molecular experimental approach based on EPR spectroscopy, which allows separating different contributions to the magnetic susceptibility by focusing on clearly distinguishable signals and eliminating diamagnetic contributions.

By using samples meant to provide a range of specific examples of crystalline orders and physical states, we could detect paramagnetism, superparamagnetism, and ferromagnetism, as well as evidence physical reorganization of the samples as a function of the applied field. Besides rationalizing relevant phenomenological aspects, we carried out theoretical analyses. Simulations of the EPR spectra based on the superatom model showed that both SO coupling and crystal-field distortions play a role in determining the EPR properties of $Au_{25}(SC2Ph)_{18}^0$ in the solid state. The excellent agreement of the experimentally derived effects brought about by SO and crystal splitting, as well as the ratio between orbital and spin moments, with the outcome of complex first-principles simulations unequivocally supports the soundness of the present analysis. Calculations point to proximity effects in the solid state as the origin of magnetic interactions and the reason for their crucial dependence upon crystallinity.

We believe that this study provides a key to understand conflicting magnetic behaviors in solid MPC samples. Together with our previous findings concerning ligand-induced antiferromagnetic behavior in Au_{25} clusters,[42] it is now clear that several factors should be considered for effectively controlling the magnetic behavior of MPCs. As also discussed in the Introduction, for larger MPCs of unknown structure and possibly variable charge states the situation is more complex and probably definable only on a statistical basis. Regardless, the results here described for $Au_{25}(SC2Ph)_{18}^0$ could pave the way to enable controlled magnetism-related applications of gold MPCs, especially those based on the use of molecular MPCs.

4.4. Experimental section

4.4.1. $Au_{25}(SC2Ph)_{18}^0$ synthesis.

The synthesis of $Au_{25}(SC2Ph)_{18}$ was carried out in tetrahydrofuran. The details are as already described,[35] except for the addition of tetra-*n*-octylammonium (*n*Oct_4N^+) bromide, prior to the reduction steps, to the THF solution containing $HAuCl_4 \cdot 3H_2O$. The cluster was prepared as [*n*Oct_4N^+][$Au_{25}(SC2Ph)_{18}^-$] and purified by dissolving it in a mixture of diethyl ether (to precipitate most of the residual tetraoctylammonium salt), and by washing the product, obtained by evaporation of diethyl ether, with icy-cold methanol.

4.4.2. Preparation of the Film.

A sample of the so-prepared [*n*Oct_4N^+][$Au_{25}(SC2Ph)_{18}^-$] was quantitatively oxidized to form $Au_{25}(SC2Ph)_{18}^0$ by passage through a silica-gel chromatography column under aerobic conditions.[50] 4.0 mg of $Au_{25}(SC2Ph)_{18}^0$ was dissolved in 1 ml dichloromethane, and injected

into an EPR tube. The solvent was evaporated with a stream of nitrogen to leave an amorphous colored film covering the bottom wall of the tubing.

4.4.3. Preparation of the Single Cystals.

Large single crystals were prepared by electrocrystallization.[49] The experiments were carried out with a CHI 660c electrochemical workstation, under an Ar atmosphere in an air-tight glass electrochemical cell, at room temperature, and using 20 ml MeCN containing 0.1 M tetra-*n*-butylammonium hexafluorophosphate as the solvent-electrolyte system. The working electrode was a 0.75 mm diameter, 15 mm long gold wire and the counter-electrode was a Pt plate inserted into a glass holder separated from the analyte solution with a G3 glass frit and a plug of electrolyte-saturated methylcellulose gel.[84] The electrolysis was carried out at a constant current of 200 nA. The one-electron electrooxidation of 4.82 x 10^{-5} M $Au_{25}(SC2Ph)_{18}^{-}$ was carried out until 8% of the anion was still present in solution. Electrogenerated $Au_{25}(SC2Ph)_{18}^{0}$ is insoluble in MeCN and nicely deposits onto the electrode body to form a forest of single crystals. The single crystals were collected from the electrocrystallization experiment that led to the image shown in Figure 4.1. All pictures were taken with a Firefly GT800 High Precision Video Microscope.

4.4.4. Electron Paramagnetic Resonance.

The crystalline $Au_{25}(SCPh)_{18}^{0}$ samples, either one single crystal or a few crystals or many microcrystals, were introduced into 1.9 mm i.d. - 3.0 mm o.d. (used for the film and the microcrystals) or 2.9 mm i.d. - 3.9 mm o.d. (for all other samples) quartz tubes. The tubes containing the film or crystals were degassed by several freeze−pump−thaw cycles and sealed off under vacuum (5 × 10^{-5} Torr). X band cw-EPR spectra were recorded with a Bruker Elexsys E580 spectrometer equipped with a dielectric probehead. The temperature was controlled by a helium-continuous flow cryostat (Oxford CF935) and a variable-temperature controller unit (Oxford ITC-4). When the desired temperature was reached, the samples were thermalized before carrying out the actual experiments. All experimental data were collected under nonsaturating microwave conditions (microwave power: P_{MW} = 150 μW or lower). A modulation frequency of 100 kHz and amplitude (peak-to-peak) of 1 G were used for all spectra. The field scan rate was 47.68 G s^{-1}. Simulation of EPR spectra was carried out by using the Matlab 7.12 software platform. The ferromagnetic and the paramagnetic signals were simulated with *ad hoc* written codes based on the models developed in this paper. The

standard *g*-tensor-based simulations were performed using routines from the EasySpin toolbox.[85]

4.4 References

1. Protected Metal Clusters: From Fundamentals to Applications, In Frontiers of Nanoscience, Vol. 9; Tsukuda, T., Häkkinen, H., Eds.; Elsevier: Amsterdam, 2015.

2. Jin, R., Zeng, C., Zhou, M. & Chen, Y. Atomically Precise Colloidal Metal Nanoclusters and Nanoparticles: Fundamentals and Opportunities. *Chem. Rev.* **2016**, *116*, 10346-10413.

3. Antonello, S.; Maran, F. Molecular electrochemistry of monolayer-protected clusters. *Curr. Opin. Electrochem*. **2017**, *2*, 18-25.

4. Doane, T. L.; Burda, C. The unique role of nanoparticles in nanomedicine - imaging, drug delivery and therapy. *Chem. Soc. Rev*. **2012**, *41*, 2885 – 2911.

5. Tao, Y.; Li, M., Ren, J.; Qu, X. Metal Nanoclusters: Novel Probes for Diagnostic and Therapeutic Applications. *Chem. Soc. Rev.* **2015**, *44*, 8636-8663.

6. Li, G.; Jin, R. Atomically Precise Gold Nanoclusters as New Model Catalysts. *Acc. Chem. Res.* **2013**, *46*, 1749-1758.

7. Trudel, S. Unexpected Magnetism in Gold Nanostructures: Making Gold even more Attractive *Gold. Bull.* **2011**, *44*, 3-13.

8. Singh, R. Unexpected Magnetism in Nanomaterials. *J. Magnetism Magnetic. Mater.* **2013**, *346*, 58-73.

9. Nealon, G. L.; Donnio, B.; Gréget, R.; Kappler, J.-P.; Terazzi, E.; Gallani J.-L. Magnetism in Gold Nanoparticles. *Nanoscale* **2012**, *4*, 5244–5258.

10. Wang, D.; Astruc, D. Fast-growing field of magnetically recyclable nanocatalysts. *Chem. Rev.* **2014**, *114*, 6949-6985.

11. Granja, L. P.; Martinez, E. D.; Troiani, H.; Clément S.; Soler Illia G. J. A. A. Magnetic Gold Confined in Ordered Mesoporous Titania Thin Films: A Noble Approach for Magnetic Devices. *ACS Appl. Mater. Interfaces* **2017**, *9*, 965-971.

12. Hembury, M.; Chiappini, C.; Bertazzo, S.; Kalber, T. L.; Drisko, G. L.; Ogunlade, O.; Walker-Samuel, S.; Krishna, K. S.; Jumeaux, C.; Beard, P.; Kumar, C. S. S. R.; Porter, A. E.; Lythgoe, M. F.; Boissière, C.; Sanchez, C.; Stevens, M. M.; Langer, R. Gold-silica quantum

rattles for multimodal imaging and therapy. *Proc. Natl. Acad. Sci. U. S. A.* **2015***, 112*, 1959-1964.

13. Hori, H.; Teranishi, T.; Nakae, Y.; Seino, Y.; Miyake M.; Yamada, S. Anomalous magnetic polarization effect of Pd and Au nano-particles *Phys. Lett. A*, **1999**, *263*, 406-410.

14. Brust, M.; Walker, M.; Bethell, D.; Schiffrin, D. J.; Whyman, R. Synthesis of Thiol-derivatised Gold Nanoparticles in a Two-Phase Liquid-Liquid System. *J. Chem. Soc., Chem. Commun.* **1994**, 801-802.

15. Crespo, P.; García, M. A.; Fernández Pinel, E.; Multigner, M.; Alcántara, D.; De La Fuente, J. M.; Penadés, S.; Hernando, A. Fe impurities weaken the ferromagnetic behavior in Au nanoparticles. *Phys. Rev. Lett.* **2006***, 97*, 177203-1-4.

16. Donnio, B.; García-Vázquez, P.; Gallani, J.-L.; Guillon, D.; Terazzi, E. Dendronized ferromagnetic gold nanoparticles self-organized in a thermotropic cubic phase. *Adv Mater* **2007***, 19*, 3534-3539.

17. Yamamoto, Y.; Hori, H. Direct observation of the ferromagnetic spin polarization in gold nanoparticles: A review. *Rev. Adv. Mater. Sci.* **2006***, 12*, 23-32.

18. Cirri, A.; Silakov, A.; Lear B. J. Ligand Control over the Electronic Properties within the Metallic Core of Gold Nanoparticles *Angew. Chem. Int. Ed.* **2015**, *54*, 11750 –11753.

19. Cirri, A.; Silakov, A.; Jensen, L.; Lear, B. J. Chain Length and Solvent Control over the Electronic Properties of Alkanethiolate-Protected Gold Nanoparticles at the Molecule-to-Metal Transition. *J. Am. Chem. Soc.* **2016***, 138*, 15987-15993.

20. Cirri, A.; Silakov, A.; Jensen, L.; Lear, B. J. Probing ligand-induced modulation of metallic states in small gold nanoparticles using conduction electron spin resonance. *Phys. Chem. Chem. Phys.* **2016***, 18*, 25443-25451.

21. Gréget, R.; Nealon, G. L.; Vileno, B.; Turek, P.; Mény, C.; Ott, F.; Derory, A.; Voirin, E.; Rivière, E.; Rogalev, A.; Wilhelm, F.; Joly, L.; Knafo, W.; Ballon, G.; Terazzi, E.; Kappler, J.-P.; Donnio, B.; Gallani, J.-L. Magnetic properties of gold nanoparticles: a room-temperature quantum effect. *ChemPhysChem* **2012***, 13*, 3092-3097.

22. Muñoz-Márquez, M. A.; Guerrero, E.; Fernández, A.; Crespo, P.; Hernando, A.; Lucena, R.; Conesa, J. C. Permanent magnetism in phosphine- and chlorine-capped gold: From clusters to nanoparticles. *J. Nanopart. Res.* **2010***, 12*, 1307-1318.

23. Guerrero, E.; Muñoz-Márquez, M. A.; García, M. A.; Crespo, P.; Fernández-Pinel, E.; Hernando, A.; Fernández, A. Surface plasmon resonance and magnetism of thiol-capped gold nanoparticles. *Nanotechnology* **2008***, 19*, 175701–1-6.

24. Tuboltsev, V.; Savin, A.; Pirojenko, A.; Räisänen, J. Magnetism in nanocrystalline gold. *ACS Nano*, **2013**, *7*, 6691-6699.

25. Maitra, U.; Das, B.; Kumar, N.; Sundaresan, A.; Rao, C. N. R. Ferromagnetism exhibited by nanoparticles of noble metals. *ChemPhysChem* **2011***, 12*, 2322-2327.

26. Hernando, A.; Crespo, P.; García, M. A.; Fernández Pinel, E.; De La Venta, J.; Fernández, A.; Penadés, S. Giant magnetic anisotropy at the nanoscale: Overcoming the superparamagnetic limit. *Phys. Rev. B Condens. Matter Mater. Phys.* **2006***, 74*, 52403-1-4.

27. Krishna, K. S.; Tarakeshwar, P.; Mujica, V.; Kumar, C. S. S. R. Chemically induced magnetism in atomically precise gold clusters. *Small* **2014**, *10*, 907-911.

28. Hernando, A.; Crespo, P.; García, M. A. Origin of orbital ferromagnetism and giant magnetic anisotropy at the nanoscale. *Phys. Rev. Lett.* **2006***, 96*, 57206-1-4.

29. Hernando, A.; Crespo, P.; García, M. A.; Coey, M.; Ayuela, A.; Echenique, P. M. Revisiting magnetism of capped Au and ZnO nanoparticles: Surface band structure and atomic orbital with giant magnetic moment. *Phys. Status Solidi B Basic Res.* **2011***, 248*, 2352-2360.

30. Murray, R. W. Nanoelectrochemistry: Metal Nanoparticles, Nanoelectrodes, and Nanopores. *Chem. Rev.* **2008**, *108*, 2688–2720.

31. Parker, J. F.; Fields-Zinna, C. A.; Murray, R. W. The Story of a Monodisperse Gold Nanoparticle: $Au_{25}L_{18}$. *Acc. Chem. Res.* **2010**, *43*, 1289-1296.

32. Heaven, M. W.; Dass, A.; White, P. S.; Holt, K. M.; Murray, R. W. Crystal Structure of the Gold Nanoparticle $[N(C_8H_{17})_4][Au_{25}(SCH_2CH_2Ph)_{18}]$. *J. Am. Chem. Soc.* **2008**, *130*, 3754–3755.

33. Zhu, M.; Aikens, C. M.; Hollander, F. J.; Schatz, G. C.; Jin, R. Correlating the Crystal Structure of a Thiol-Protected Au_{25} Cluster and Optical Properties. *J. Am. Chem. Soc.* **2008**, *130*, 5883–5885.

34. Zhu, M.; Aikens, C. M.; Hendrich, M. P.; Gupta, R.; Qian, H.; Schatz, G. C.; Jin, R. Reversible Switching of Magnetism in Thiolate-Protected Au_{25} Superatoms. *J. Am. Chem. Soc.* **2009**, *131*, 2490-2492.

35. Venzo, A.; Antonello, S.; Gascón, J. A.; Guryanov, I.; Leapman, R. D.; Perera, N. V.; Sousa, A.; Zamuner, M.; Zanella, A.; Maran, F. Effect of the Charge State (z = **-**1, 0, **+**1) on the Nuclear Magnetic Resonance of Monodisperse $Au_{25}[S(CH_2)_2Ph]_{18}^z$ Clusters. *Anal. Chem.* **2011**, *83*, 6355-6362.

36. Antonello, S.; Perera, N. V.; Ruzzi, M.; Gascón, J. A.; Maran, F. Interplay of Charge State, Lability, and Magnetism in the Molecule-like $Au_{25}(SR)_{18}$ Cluster. *J. Am. Chem. Soc.* **2013**, *135*, 15585-15594.

37. Antonello, S.; Dainese, T.; De Nardi, M.; Perotti, L.; Maran, F. Insights into the Interface Between Electrolytic Solution and Gold Core in Molecular $Au_{25}(SR)_{18}$ Clusters. *ChemElectroChem.* **2016**, *3*, 1237**–**1244.

38. Antonello, S.; Hesari, M.; Polo, F.; Maran, F. Electron Transfer Catalysis with Monolayer Protected Au_{25} Clusters. *Nanoscale* **2012**, *4*, 5333**–**5342.

39. Dainese, T.; Antonello, S.; Gascón, J. A.; Pan, F.; Perera, N. V.; Ruzzi, M.; Venzo, A.; Zoleo, A.; Rissanen, K.; Maran, F. $Au_{25}(SEt)_{18}$, a nearly "Naked" Thiolate-Protected Au_{25} Cluster: Structural Analysis by ENDOR and Single Crystal X-ray Crystallography. *ACS Nano* **2014**, *8*, 3904-3912.

40. Agrachev, M., Antonello, S., Dainese, T., Gascón, J. A., Pan, F., Rissanen, K., Ruzzi, M., Venzo, A., Zoleo, A.; Maran, F. A Magnetic Look into the Protecting Layer of Au_{25} Clusters. *Chem. Sci.* **2016**, *7*, 6910-6918.

41. Tofanelli, M. A.; Salorinne, K.; Ni, T. W.; Malola, S.; Newell, B.; Phillips, B.; Häkkinen, H.; Ackerson, C. J. Jahn-Teller effects in $Au_{25}(SR)_{18}$. *Chem. Sci.* **2016**, *7*, 1882-1890.

42. De Nardi, M.; Antonello, S.; Jiang, D.; Pan, F.; Rissanen, K.; Ruzzi, M.; Venzo, A.; Zoleo, A.; Maran, F. Gold Nanowired: A Linear $(Au_{25})_n$ Polymer from Au_{25} Molecular Clusters. *ACS Nano* **2014**, *8*, 8505-8512.

43. Liao, L.; Zhou, S.; Dai, Y.; Liu, L.; Yao, C.; Fu, C.; Yang, J.; Wu, Z. Mono-mercury doping of Au25 and the HOMO/LUMO energies evaluation employing differential pulse voltammetry. *J. Am. Chem. Soc.* **2015***, 137*, 9511-9514.

44. Tian, S.; Liao, L.; Yuan, J.; Yao, C.; Chen, J.; Yang, J.; Wu, Z. Structures and magnetism of mono-palladium and mono-platinum doped $Au_{25}(PET)_{18}$ nanoclusters. *Chem. Commun.* **2016***, 52*, 9873-9876.

45. Song, Y.; Jin, S.; Kang, X.; Xiang, J.; Deng, H.; Yu, H.; Zhu, M. How a Single Electron Affects the Properties of the "non-Superatom" Au_{25} Nanoclusters. *Chem. Mater.* **2016***, 28*, 2609-2617.

46. Inagaki, Y.; Yonemura, H.; Sakai, N.; Makihara, Y.; Kawae, T.; Yamada, S. Magnetism of gold nanorods probed using electron spin resonance. *Appl. Phys. Lett.* **2016***, 109*, 72404-1-4.

47. Dutta, P.; Pal, S.; Seehra, M. S.; Anand, M.; Roberts, C. B. Magnetism in dodecanethiol-capped gold nanoparticles: Role of size and capping agent. *Appl. Phys. Lett.* **2007***, 90*, 213102-1-3.

48. Guerrero, E.; Muñoz-Márquez, M. A.; Fernández, A.; Crespo, P.; Hernando, A.; Lucena, R.; Conesa, J. C. Magnetometry and electron paramagnetic resonance studies of phosphine- and thiol-capped gold nanoparticles. *J. Appl. Phys.* **2010***, 107*, 64303-1-7.

49. Antonello, S.; Dainese, T.; Pan, F.; Rissanen, K.; Maran, F. Electrocrystallization of Monolayer-Protected Gold Clusters: Opening the Door to Quality, Quantity, and New Structures. *J. Am. Chem. Soc.* **2017**, *139*, 4168**–**4174.

50. Antonello, S.; Arrigoni, G.; Dainese, T.; De Nardi, M.; Parisio, G.; Perotti, L.; René, A.; Venzo, A.; Maran, F. Electron Transfer through 3D Monolayers on Au_{25} Clusters. *ACS Nano* **2014**, *8*, 2788–2795.

51. Chandrasekhar, S. Stochastic problems in physics and astronomy. *Rev. Mod. Phys.* **1943**, *15*, 1-89.

52. Carducci, T. M.; Murray, R. W. Kinetics and Low Temperature Studies of Electron Transfers in Films of Small (<2 nm) Au Monolayer Protected Clusters. *J. Am. Chem. Soc.* **2013**, *135*, 11351-11356.

53. Teale, R. W.; Pelegrini, F. Magnetic surface anisotropy and ferromagnetic resonance in single-crystal $GdAl_2$. *J. Phys. F: Metal Phys.* **1986***, 16*, 621-635.

54. Raikher, Yu. L.; Stepanov, V. I. The effect of thermal fluctuations on the FMR line shape in dispersed ferromagnets. *Sov. Phys. JETP* **1992**, *75*, 764-771.

55. Berger, R.; Kliava, J.; Bissey, J.-C.; Baïetto, V. Magnetic resonance of superparamagnetic iron-containing nanoparticles in annealed glass. *J. Appl. Phys.* **2000***, 87*, 7389-7396.

56. Noginov, M. M.; Noginova, N.; Amponsah, O.; Bah, R.; Rakhimov, R.; Atsarkin, V. A. Magnetic resonance in iron oxide nanoparticles: Quantum features and effect of size. *J Magn Magn Mater* **2008***, 320*, 2228-2232.

57. Fittipaldi, M.; Sorace, L.; Barra, A.-L.; Sangregorio, C.; Sessoli, R.; Gatteschi, D. Molecular nanomagnets and magnetic nanoparticles: The EMR contribution to a common approach. *Phys. Chem. Chem. Phys.* **2009***, 11*, 6555-6568.

58. Wei, D. Micromagnetics and Recording Materials. Springer: New York, 2012; pp 21-52.

59. Moon, T. S.; Merrill, R. T. Nucleation theory and domain states in multidomain magnetic material. *Phys. Earth Planet. Inter.* **1985***, 37*, 214-222.

60. Oyarzún, S.; Tamion, A.; Tournus, F.; Dupuis, V.; Hillenkamp, M. Size effects in the magnetic anisotropy of embedded cobalt nanoparticles: From shape to surface. *Sci. Rep.* **2015***, 5*, 14749-1-8.

61. Raghavender, A. T.; Hong, N. H.; Swain, B. S.; Jung, M.-H.; Lee, K.-J.; Lee, D.-S. Surface-induced magnetism in Au particles/clusters. *Mater Lett* **2012***, 87*, 169-171.

62. Di Paola, C.; D'Agosta, R.; Baletto, F. Geometrical Effects on the Magnetic Properties of Nanoparticles. *Nano Lett.* **2016**, *16*, 2885-2889.

63. Neél, L. Théorie du traînage magnétique des ferromagnétiques en grains fins avec application aux terres cuites, *Annales de Géophysique*, **1949**, *5*, 99-136.

64. Uhlír, V.; Arregi, J. A.; Fullerton, E. E. Colossal magnetic phase transition asymmetry in mesoscale FeRh stripes. *Nat. Commun.* **2016***, 7*, 13113-1-7.

65. Aharoni, A. Introduction to the Theory of Ferromagnetism. 2nd ed.; Oxford University Press: Oxford, 1996; 84-108.

66. Walter, M.; Akola, J.; Lopez-Acevedo, O.; Jadzinsky, P. D.; Calero, G.; Ackerson, C. J.; Whetten, R. L.; Grönbeck, H.; Häkkinen, H. A unified view of ligand-protected gold clusters as superatom complexes. *Proc. Natl. Acad. Sci. U.S.A.* **2008**, *105*, 9157−9162.

67. Aikens, C. L. Effects of Core Distances, Solvent, Ligand, and Level of Theory on the TDDFT Optical Absorption Spectrum of the Thiolate-Protected Au_{25} Nanoparticle. *J. Phys. Chem. A,* **2009**, *113*, 10811–10817.

68. Jiang, D.-e; Kühn, M.; Tang, Q.; Weigend, F. Superatomic Orbitals under Spin–Orbit Coupling. *J. Phys. Chem. Lett.* **2014**, *5*, 3286−3289.

69. Kwak, K.; Tang, Q.; Kim, M.; Jiang, D.-e.; Lee, D. Interconversion between Superatomic 6- Electron and 8- Electron Configurations of $M@Au_{24}(SR)_{18}$ Clusters (M = Pd, Pt). *J. Amer. Chem. Soc.* **2015**, *137*, 10833-10840.

70. Kittel, C. On the gyromagnetic ratio and spectroscopic splitting factor of ferromagnetic substances. *Phys. Rev.* **1949***, 76*, 743-748.

71. Berger, R.; Bissey, J.-C.; Kliava, J. Lineshapes in magnetic resonance spectra *J. Phys.: Condens. Matter*, **2000**, *12*, 9347–9360.

72. Morais, P.C.; Tronconi, A.L.; Neto, K.S. Electron paramagnetic resonance linewidth of superparamagnetic particles *J. Appl. Phys.*, **1984**, *55*, 10.

73. Raikher, Y.L.; Stepanov, V.I. Ferromagnetic resonance in a suspension of single-domain particles. *Phys. Rev. B*, **1994**, *50 (9)*, 6250-6259.

74. Berger, R.; Kliava, J.; Bissey, J.-C.; Baïetto, V. Magnetic resonance of superparamagnetic iron-containing nanoparticles in annealed glass. *J. Appl. Phys.*, **2000**, *87*, 7389.

75. Fittipaldi, M.; Sorace, L.; Barra, A.-L.; Sangregorio, C.; Sessoli, R.; Gatteschi, D. Molecular nanomagnets and magnetic nanoparticles: the EMR contribution to a common approach *Phys. Chem. Chem. Phys.*, **2009**, *11*, 6555-6568

76. Noginova, N.; Chen, F.; Weaver, T.; Giannelis, E.P.; Bourlinos, A.B. Atsarkin, V.A. Magnetic resonance in nanoparticles: between ferro- and paramagnetism. *J. Phys. Condens. Matter.* **2007**, *19(24)*, 246208.

77. Valiev, M.; Bylaska, E. J.; Govind, N.; Kowalski, K.; Straatsma, T. P.; Van Dam, H. J. J.; Wang, D.; Nieplocha, J.; Aprà, E.; Windus, T. L.; de Jong, W. NWChem: A comprehensive and scalable open-source solution for large scale molecular simulations. *Comput. Phys. Commun.* **2010**, *181*, 1477-1489.

78. P Becke, A. D. Density-functional thermochemistry. III. The role of exact exchange. *J. Chem. Phys.* **1993**, *98*, 5648−5652.

79. Nichols, P.; Govind, N.; Bylaska, E. J.; de Jong, W. A. Gaussian Basis Set and Plane-wave Relativistic Spin-Orbit Methods in NWChem. *J. Chem. Theory Comput*. **2009**, *5*, 491-499.

80. van Wullen, C.; Michauk, C. Accurate and efficient treatment of two-electron contributions in quasirelativistic high-order Douglas-Kroll density-functional calculations. *J. Chem. Phys.* **2005**, *123*, 204113.

81. Dui, T. V. T.; Ozaki, T. A three-dimensional domain decomposition method for large-scale DFT electronic structure calculations. *Comput. Phys. Commun*. **2014**, *185*, 777-789.

82. Ceperley, D. M.; Alder, B. J. Ground State of the Electron Gas by a Stochastic Method. *Phys. Rev. Lett*. **1980**, *45*, 566-569.

83. Nimmala, P. R.; Theivendran, S.; Barcaro, G.; Sementa, L.; Kumara, C.; Jupally, V. R.; Aprà, E.; Stener, M.; Fortunelli, A.; Dass, A. Transformation of $Au_{144}(SCH_2CH_2Ph)_{60}$ to $Au_{133}(SPh\text{-}tBu)_{52}$ Nanomolecules: Theoretical and Experimental Study. *J. Phys. Chem. Lett.* **2015**, *6*, 2134−2139.

84. Farnia, G.; Maran, F.; Sandonà, G.; Severin, M. G. Protonation kinetics of anionic intermediates in the electrochemical reduction of triphenylethylene: a disproportionation mechanism. *J. Chem. Soc., Perkin Trans. 2* **1982**, 1153-1158.

85. Stoll, S.; Schweiger, A. EasySpin, a Comprehensive Software Package for Spectral Simulation and Analysis in EPR. *J. Magn. Reson.* **2006**, *178*, 42–55.

Chapter 5.

Magnetic properties of 1D cluster chains modulated by alkyl ligand chain length

5.1. Introduction

As the results reported in Chapter 3 show, the type and length of ligands protecting the Au_{25} clusters are very important for the magnetic properties of isolated clusters in solution.[1] Moreover, our investigation of the magnetic properties of $Au_{25}(SC_2H_4Ph)^0$, discussed in the previous chapter, demonstrates that the nature and strength of the intercluster exchange interactions in the solid state are also strongly dependent on the ligands.[2] There we showed that Au_{25} crystals are ferromagnetic and that the appearance of ferromagnetism is likely determined by the stacking of the phenyl rings. Moreover, a few years ago it was discovered by our group[3] that, when protected by 18 n-butanethiolate (SBu) ligands, in the solid state Au_{25} forms linear 1D chains of antiferromagnetically coupled clusters, while still being paramagnetic in solution. Single crystal X-ray crystallography analysis has shown that the clusters are connected by single Au-Au bonds and that a twist-and-lock mechanism between neighboring clusters and capping ligands is responsible for the formation of the polymer (Figure 5.1). A comparison with the $Au_{25}(SEt)_{18}$ cluster (Et = ethyl) solid state structure, obtained in a previous investigation,[4] showed that this mechanism is possible only with ligands of a certain well-defined length. Intuitively, one could expect that the formation of 1D chains must be even more favored for shorter and thus less hindered ligands, such as EtSH. However, when the cluster is protected with this ligand, it remains monomeric in the solid-state conditions. This suggests that a minimum ligand length is required for the polymers to form.

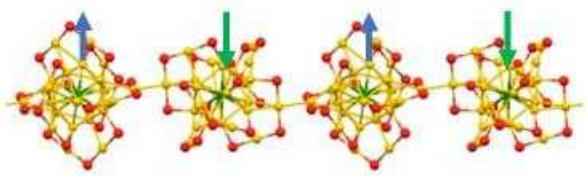

Figure 5.1. A fragment of a one-dimensional chain of clusters from the structure of $Au_{25}(SC_4H_9)_{18}$ crystal. The blue and green arrows indicate up and down spins respectively.

The antiferromagnetic coupling of the clusters in these 1D chains was experimentally demonstrated by EPR. The CW-EPR spectra of $Au_{25}(SBu)_{18}^0$ crystals gave completely different spectra, compared to those observed with other ligands, consisting of a broad, quite symmetric line, with no resonance shift with temperature, as opposed to the highly anisotropic paramagnetic signal of the amorphous films or the superparamagnetically shifted signal of the $Au_{25}(SC_2H_4Ph)_{18}^0$ microcrystals. More importantly, by performing the double integration and plotting the reciprocal of the integrals vs T, a peculiar trend was observed, in which the integrals, and consequently the susceptibility proportional to them, decreases with decreasing temperature. This is the opposite of what is observed for both paramagnetic and ferromagnetic materials and indicates an antiferromagnetic behavior instead. As explained in the introduction, for ferromagnets the exchange coupling constant *J* is positive and therefore the fundamental state consists in parallel spins and maximum magnetization. The higher energy states are characterized by progressively increasing number of antiparallel spins. Consequently, the magnetization decreases by increasing the temperature. On the contrary, for antiferromagnets *J* is negative. This implies preferentially antiparallel spin alignment and a consequent increase of magnetization with increasing temperature.

The double integrals vs T plot was fitted by the Bonner-Fisher function, which derives from a series expansion of the solution of the Ising Hamiltonian for 1D systems, which will be discussed later. An exchange coupling constant equal to 28 meV was obtained in this way, in full agreement with the DFT-calculated value of 27 meV. The same DFT calculations, based on the XRD structure, also successfully predicted an antiferromagnetic minimum energy state for the $Au_{25}(C_4H_9)_{18}^0$ cluster. The calculations also predicted that, by decreasing the intercluster distance, the non-magnetic (antiferromagnetic) state is further stabilized, while for longer distances the magnetic state becomes more stable. This trend must still be verified experimentally and is one of the aims of the work presented in this chapter. Thus, we decided to systematically investigate the ligand dependence of intercluster exchange interactions on alkyl chain length in the solid state.

The new fascinating monodimensional systems just described pave the way to many possible applications, in particular in the field of spintronics. Spintronics is a fast-growing technological and scientific field, which has the aim of developing electronics based on the

control of electron spin, instead of electron charge, on which traditional electronics is based.[5, 6] The urge of developing this new kind of electronics is due to the fact that at present transistors and other components of electronic devices has reached nanoscale dimensions and further reducing their size would lead to some serious issues. For instance, increased scorching heat would make the circuits hardly operable. Spintronics could overcome the first problem, since the use of spin currents imply much less heat dissipation. Additionally, spintronic devices exhibit several advantages, compared to traditional electronics, which make them very promising in this field. Some of these are: lower power consumption, increased compactness, faster spin manipulation, compared to charge manipulation, leading to increased read and write speed, long spin lifetime (of the order of nanoseconds).[6] Another very important feature offered by spintronics is the possibility of combining logic and storage functionalities in a single device. Indeed, information can be stored as one of the two possible spin orientations and this storage is non-volatile. This opens the way to using the spins as q-bits in quantum computers.[7]

Spin lifetime is very important in spintronics, as it determines how long the spin currents can travel and how much time is available for its manipulation. For this aim, the concept of spin-scattering length is of particular importance. It is defined as the distance covered by a spin-polarized electron, before it undergoes scattering processes, which change its spin orientation. Obviously, longer spin-scattering lengths are required for an efficient control of spin-currents. Experimentally, it was observed that this quantity varies widely for different materials, ranging from nanometers in the case of transition metals to micrometers for semiconductors. For this reason, semiconductor materials seem to be more suitable for spintronic applications.

Spin lifetime can also be increased by controlling spin relaxation processes, which as explained in the introduction, lead to the loss of spin polarization. This can be done, for example by suitably changing the structure and morphology of the material used for the construction of the spintronic device. It was shown recently in several studies,[8,9] that spin lifetime is considerably longer in semiconductor spin nanowires, compared to the corresponding bulk/film materials.

Another important issue in the field of spintronics is the efficient control of spin currents. Obviously, spins can be efficiently controlled by magnetic fields, but this method has some drawbacks: it is energetically very expensive and hardly scalable. Therefore, the use of

magnetic fields is being progressively abandoned and great efforts are spent to achieve an efficient manipulation of electron spins by electric fields.[10-12] The idea of independent spin and charge control is very appealing, however some issues regarding the all-electrical injection, transport, control and detection of spin-polarized currents still must be solved. Several methods have been developed, most of which exploit the spin-orbit coupling, which was introduced in Chapter 2. For example, applied voltages can be used to modify the spin-orbit interactions of the material, thus modifying the magnetic anisotropy (mainly determined by the spin-orbit interaction, as explained in Chapter 2) and rotating the magnetization to a new minimum energy orientation.[13]

Many of the most commonly used methods, which utilize electrical field for magnetic storage, rely on the current-induced spin transfer torque (STT).[14] This phenomenon is also based on spin-orbit interaction and consists in the angular momentum transfer from the carrier (current) spin angular momentum to the magnetization angular momentum.

Spin-polarized currents can be also manipulated by using the Rashba effect:[15] it is due to a spin-orbit like interaction and consists in the rotation of the quantization axis in a system with broken symmetry, achieved by an electric field.

Another phenomenon often used to electrically manipulate the spins is the Spin Hall effect (SHE), also originating from the spin-orbit interaction.[16,17] In this case, spin and charge currents are coupled in such a way, that an electric current induces a transverse spin current and vice versa.

A relatively new, but very promising field is antiferromagnetic spintronics. Generally, antiferromagnetic order is much more common than the ferromagnetic order, therefore managing to employ antiferromagnets in spintronics would open the field to a huge amount of new possibilities. It was shown in several studies [18-21] that some of the phenomena used in spintronics, which often require the presence of a ferromagnet, can be successfully exploited also by using antiferromagnetic materials.

Since antiferromagnetic materials give rise to very low spontaneous magnetic fields, they generate virtually no stray fields, avoiding the problem of possible magnetic interference between nearby devices. Moreover, for the same reason, the magnetic storage based on antiferromagnets is particularly stable, robust and not affected by possible external magnetic perturbations.

Therefore, antiferromagnetic materials are particularly suitable for storing, writing and reading information in spintronic and quantum computing devices. Moreover, they can be

used as efficient spin-current transmitters, spin current generators and SHE spin injectors.

From the short overview reported above, one can easily see the reasons why $Au_{25}(SR)_{18}$ clusters, in particular antiferromagnetic 1D polymers of these clusters can be considered particularly suitable for spintronic applications. First of all, they have the right and highly controlled nanometric size, which allows them to be used for building tiny spintronic devices. Second, they show a semiconductor behavior in the solid state, therefore a higher spin lifetime is expected, compared to the more common metal devices. Third, as we saw in Chapter 3, they are characterized by a high spin-orbit coupling constant, which can allow an efficient electrical control of electron spins in this material, by using the many different phenomena reported above. In addition, the formation of linear chains of clusters can suppress spin relaxation, leading to even longer spin lifetimes. Moreover, the presence of antiferromagnetic and ferromagnetic orderings with relatively high exchange coupling constants allows the use of these materials also at high temperatures, near to room temperature. Finally, being molecular systems, they can be chemically tuned in a highly controlled and fine way to obtain the desired properties. For example, as we saw, intercluster interaction can be efficiently modulated by simply changing the protecting ligands.
In addition to their huge applicative potential, the 1D antiferromagnetic chains are very interesting from the theoretical point of view: indeed they constitute quasi-ideal physical systems on which the predictions of fundamental physical theories can be experimentally verified. The simplest model for 1D chains of exchange-coupled spins is the Ising model, which will be explained below.

In this chapter, an EPR study on a series of $Au_{25}(SR)_{18}$ clusters protected with alkyl ligands of different length is reported. The aim of this work was to investigate the ability of the clusters to form 1D chains and the dependence of the exchange interaction on the ligands length. The understanding of this dependence would allow to tune the exchange interactions in order to obtain the desired magnetic properties. We also studied the resulting magnetic and optical properties, such as spin relaxation and photoinduced electron transfer.

5.2. Results and discussion

The CW-EPR measurements were performed on a series of Au_{25} neutral clusters protected with alkyl ligands of different length, specifically $Au_{25}(C_3H_7)_{18}$, $Au_{25}(C_4H_9)_{18}$, $Au_{25}(C_5H_{11})_{18}$ and $Au_{25}(C_7H_{15})_{18}$ (which hereafter will be called respectively C3, C4, C5, C7). As already done for the $Au_{25}(C_2H_4Ph)_{18}$ cluster (see Chapter 4), we studied different solid-state samples for each ligand: polycrystalline samples and amorphous films prepared by solvent evaporation. This was done in order to investigate the effect of crystal order and possible 1D chains formation on the intercluster interactions and on the overall magnetic and optical properties. Additionally, a polycrystalline $Au_{25}(C_2H_4)_{18}$ (C2) sample, prepared by slow solvent evaporation was studied.

5.2.1. Amorphous films.

In analogy with the procedure followed for $Au_{25}(C_2H_4Ph)_{18}$, we started with the investigation of amorphous films. The spectra were recorded at different temperatures, from 5 K to 80 K. At higher temperatures the signals become very weak and broad, therefore their integration would not be reliable. All the films studied so far apparently show only the usual paramagnetic signal, which we already observed for the $Au_{25}(C_2H_4Ph)_{18}$ (subsequently called C2Ph). However, the intensity of the signals and the temperature dependence of the double integrals is different for different ligands, as will be shown subsequently. Just by visually comparing the spectra of the different films, reported in Figure 5.2, it can be seen that the C7 film signal shows a remarkably lower intensity, with respect to the other films, although the total amount of clusters in the films was the same.

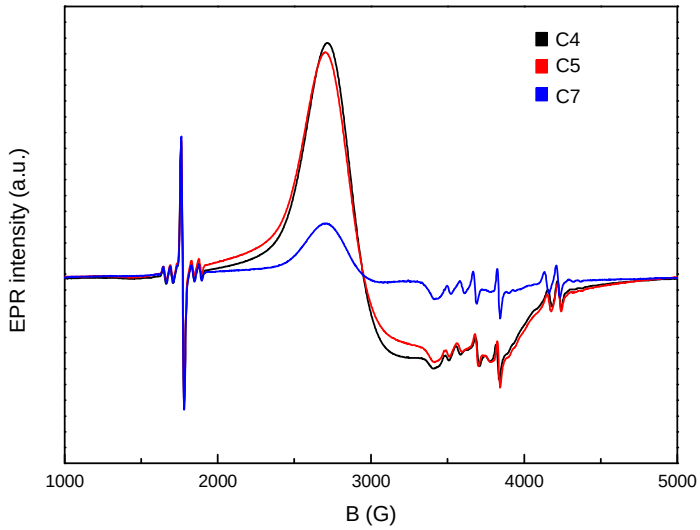

Figure 5.2. CW-EPR spectra of $Au_{25}(SC_4H_9)_{18}$, $Au_{25}(SC_5H_{11})_{18}$ and $Au_{25}(SC_7H_{15})_{18}$ amorphous films at 5 K.

The spectra of the four films at different temperatures with the corresponding simulations are reported in Figure 5.3. For the C3 film, the paramagnetic component alone was sufficient to satisfactorily simulate the spectra. As for the other films, in spite of the fact that no other signal, apart from the paramagnetic one was detected by the visual analysis of the spectra, the simulations revealed that the spectra are far more complex than it seemed. Indeed, the C4, C5 and C7 spectra could not be well simulated with the paramagnetic signal alone, not even changing the parameters with respect to those used for the simulations of the C2Ph film. The best fit was obtained when two components were used for the simulations: one characterized by parameters very close to those of C2Ph, corresponding to the isolated paramagnets and one broader and even more anisotropic component, presumably corresponding to interacting clusters. Additional information was obtained from the double integration of the signals and from the analysis of the temperature dependence of the integrals. As we have already seen previously, the double integrals are proportional to the magnetic susceptibility and thus allow deducing the nature and the intensity of the magnetic interactions taking place in the analyzed system, through the analysis of Curie-like plots (Figure 5.4).

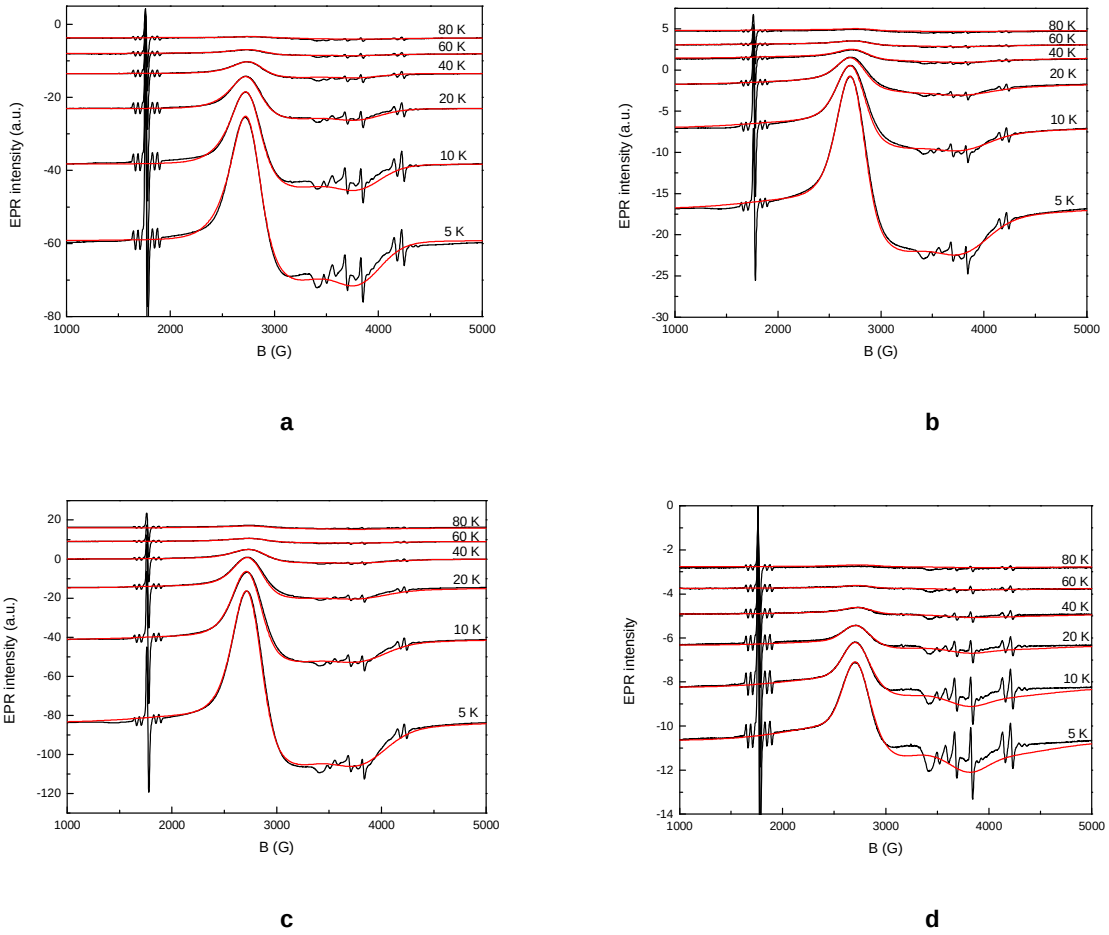

Figure 5.4. CW-EPR experimental (black) and calculated (red) spectra of $Au_{25}(SC_3H_7)_{18}$ (a), $Au_{25}(SC_4H_9)_{18}$ (b), $Au_{25}(SC_5H_{11})_{18}$ (c) and $Au_{25}(SC_7H_{15})_{18}$ (d) amorphous films at different T.

Starting from the shortest ligands, i.e. the C3 clusters, the paramagnetic signal shows a plot very similar to the one we reported for C2Ph: a linear Curie-like temperature dependence with a positive non-zero intercept is observed at higher temperature, while a deviation from linearity takes place below 40 K. The intercept calculated from a linear fit of the high temperature values is of 36 K. The fact that this value, corresponding to the Weiss parameter in the Curie-Weiss approach, is positive, shows that ferromagnetic-like intercluster interactions take place in the film, with lower intensity (lower exchange constant *J*) compared to C2Ph. It must be noted, that this effect can be due to both ferromagnetic exchange and dipolar interactions, both leading to a partial parallel alignment of the magnetic moments.

Concerning the C4 film, the integrals of the paramagnetic component showed a similar Curie-Weiss plot, with a similar intercept value (29 K). The integrals of the second

component are not very reliable, because of its broad linewidth, low intensity and to the fact that it is completely overlapped to the paramagnetic signal. However, an approximate trend could still be extracted, which shows an opposite temperature dependence, compared to the first component. Indeed, its relative weight with respect to the paramagnetic component increases with lowering the temperature, which is an indication of the fact that this signal is due to antiferromagnetically interacting clusters (as explained in Chapter 2 and in the introduction to this Chapter).

The C5 film shows the same features of C4, although the presumably antiferromagnetic signal contribution is higher. The same trend is observed also for the temperature dependence of the C7 spectra, suggesting that this cluster can give antiferromagnetic couplings as well, in spite of the longer ligand length. Surprisingly, the relative weight of the antiferromagnetic component in this case is even higher than for C5.

The presence of the antiferromagnetic component in the spectra of the three films was attributed to the fact that the samples are not perfectly amorphous: the clusters partially crystallize, forming aggregates in which they are magnetically coupled. This explains also the low intensity of the signals in the C7 film spectra: a significant fraction of the clusters is antiferromagnetically coupled, giving rise to an intrinsically weak antiferromagnetic signal, superimposed to the paramagnetic one. The resulting intensity is therefore comparatively low.

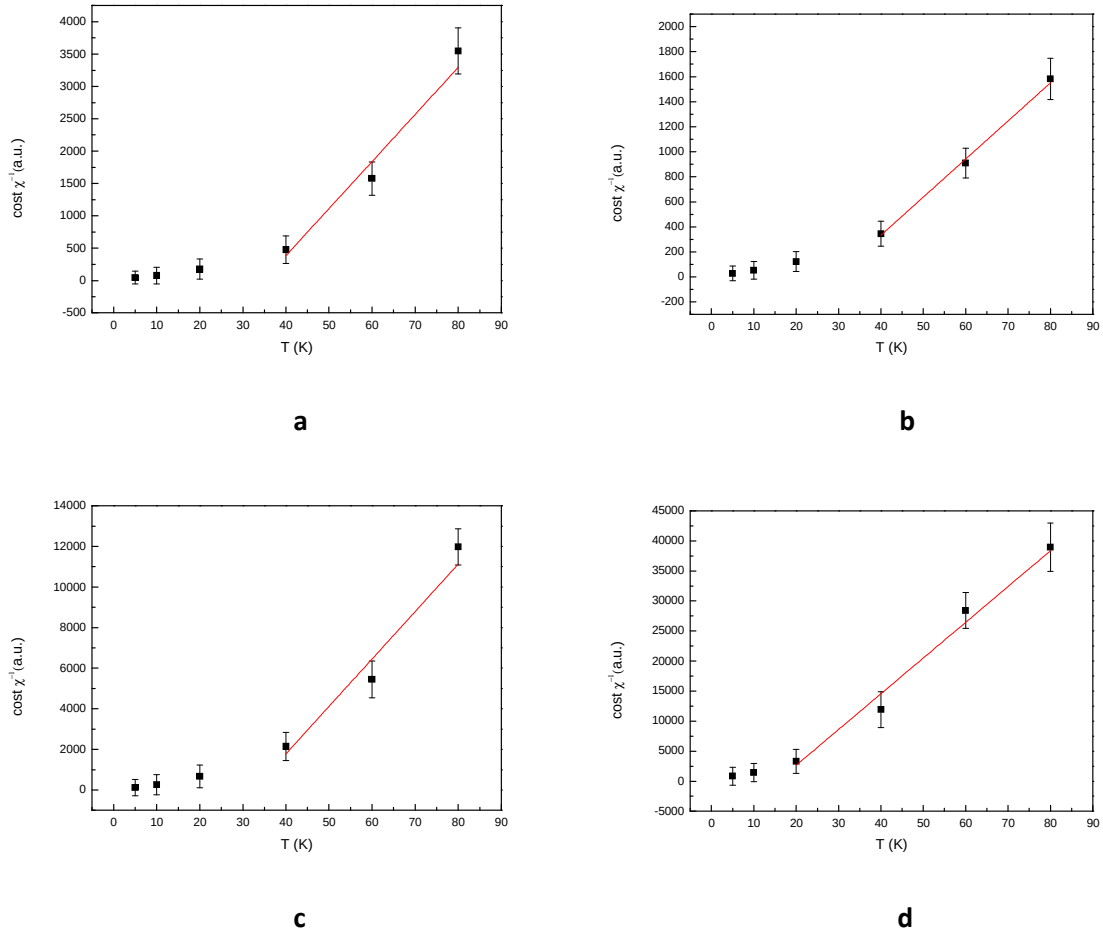

Figure 5.4. Reciprocal of the double integrals of the CW_EPR spectra of $Au_{25}(SC_3H_7)_{18}$ (a), $Au_{25}(SC_4H_9)_{18}$ (b), $Au_{25}(SC_5H_{11})_{18}$ (c) and $Au_{25}(SC_7H_{15})_{18}$ (d) amorphous films.

The parameters obtained from the simulations and from the linear fit of the temperature dependence of the double integrals (at high temperature) are summarized in Table 5.1. As already mentioned, the parameters used for the simulation of the paramagnetic component are very close to those used previously for C2Ph film and all the Au_{25} clusters in solution. However, the g_x value is slightly different for the different ligands. Moreover, for all the films, the g_x value moderately decreases at higher temperatures, which can be seen as a line shift and narrowing, usually observed for superparamagnetic systems. This is another indication of the fact that weak ferromagnetic interactions between the clusters can possibly take place, as already observed for C2Ph.

Table 5.1. Paramaters obtained from the simulation of amorphous films at 5 K and the intercept (Tc) obtained from the linear fitting of the high temperature double integrated spectra.

Ligand\parameter	paramagnetic component				antiferromagnetic component				
	g_x	g_y	g_z	Δ	g_x	g_y	g_z	Δ	T_c
C3	2.49	2.38	1.82	25	-	-	-	-	36
C4	2.49	2.38	1.82	25	2.48	2.46	1.85	155	29
C5	2.51	2.38	1.82	25	2.48	2.46	1.85	155	33
C7	2.54	2.38	1.82	25	2.28	2.06	1.95	155	17

The linear fits of the high temperature paramagnetic region of the Curie-Weiss plots show (Figure 5.4) that C3, C4 and C5 films are all characterized by similar intercept values, corresponding to a Curie temperature of about 30 K. This value is approximately one half of the value obtained for C2Ph (see chapter 4). This shows that, even in an amorphous film with no crystalline and magnetic order, the interactions between the clusters are strongly mediated by the ligands. Specifically, as in the crystals, the ferromagnetic interaction is probably favored by the stacking of the phenyl rings also for the films. Nevertheless, it must be noted that, in these experiments less experimental points were available at high temperature, compared to the C2Ph case because the signal fades above 80 K. Therefore, the obtained values used for the comparison could be somewhat underestimated. In any case, the comparison of the three films with the C7 film, the analysis of which was performed on the same number of experimental points, confirms the importance of the ligands for the intercluster interactions in these systems. Indeed, the Curie temperature for C7 is much smaller than for the other shorter ligands. This means that with such long ligands, in an amorphous environment, the intercluster distance is higher, giving rise to weaker magnetic interactions.

5.2.2. Antiferromagnetic crystals.

We then turned to the crystalline samples, which we supposed, considering our previous studies on C2Ph and C4, to be magnetically ordered. We started by studying longer ligands, i.e. C5 and C7 (Figures 5.5 and 5.7). From some preliminary XRD data we knew that C5 forms linear 1D chains, just like C4, but with a smaller distance between the neighbor clusters inside a chain. For this reason, we expected C5 to be antiferromagnetic, and possibly even more antiferromagnetic (with a higher, more negative, *J*) than C4. An indication of the possible antiferromagnetism of C5 was also provided by the

measurements on C5 amorphous films, reported in the previous paragraph.

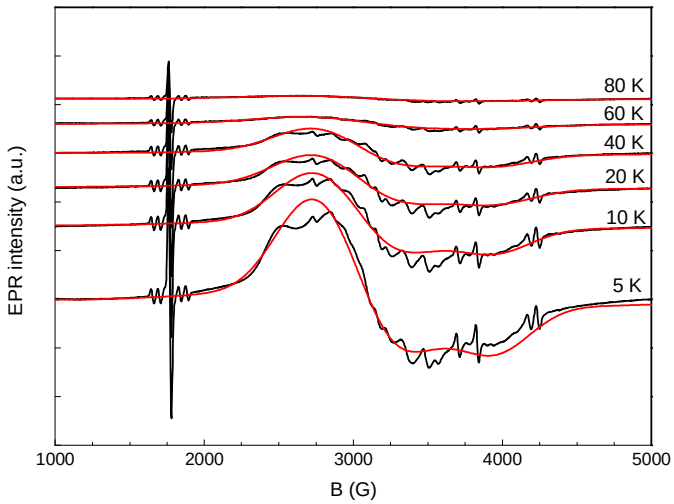

Figure 5.5. CW-EPR experimental (black) and calculated (red) spectra of $Au_{25}(SC_5H_{11})_{18}$ electrocrystallized crystals at different temperatures.

Actually, the spectra of the C5 crystals (Figure 5.5) show broad signals reminding those of C4. Some narrow features superimposed to the broad signal are observed, due to a few larger crystals. Moreover, some features of the paramagnetic signal are visible, which suggest the incomplete crystallization of the clusters. Due to the complexity of the spectrum, reflecting the heterogeneity of the sample, precise simulations are prohibitive. Nevertheless, the spectra corresponding to each temperature were approximately simulated, trying to fit the broadest component, and the signals were double-integrated. In this way, an estimated temperature dependence of the susceptibility was determined. The principal values of the **g** tensor extracted from the simulations are similar to those used for the simulation of the films (g_x=2.53 g_y=2.38, g_z=1.82), but the linewidth is considerably higher Δ=55.

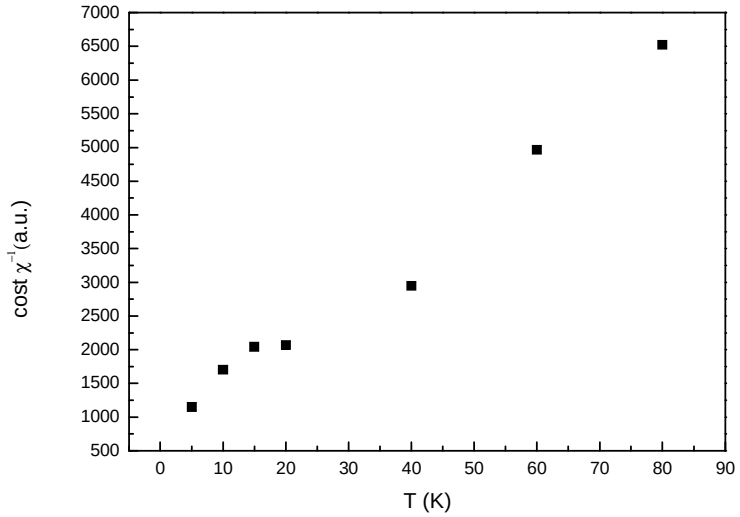

Figure 5.6. Reciprocal of the double integrals of the CW-EPR spectra of $Au_{25}(SC_5H_{11})_{18}$ crystals.

As can be seen in Figure 5.6, the susceptibility, estimated by the double integrals, increases with decreasing temperature, as commonly observed for paramagnets. However, the Curie linear dependence is not followed, and an irregularity around 15 K is observed. These observations are in agreement with the presumed heterogeneity of the sample and indicate that probably for the C5 crystal samples, like for the film, both paramagnetic and antiferromagnetic components are present, due to the amorphous and crystalline regions respectively. This would be also in accordance with the fact that the g factors are similar to those of the paramagnetic films. An alternative (or complementary) hypothesis can be suggested, which demonstrates that in reality also the antiferromagnetic signal intensity can increase with decreasing temperature in certain cases. This explanation is based on the Monte Carlo simulations, which use the aforementioned Ising model, and which will be illustrated in the following paragraph.

Concerning the C7 clusters, the same amount of C7 crystals give much weaker signals, compared to the C5 sample (Fig. 5.7). This can be possibly due to a stronger antiferromagnetic interaction (higher *J*). Moreover, just by a visual inspection of the spectra, it can be clearly seen that the signal intensity decreases at lower temperature, which is in agreement with the strong antiferromagnetism hypothesis.

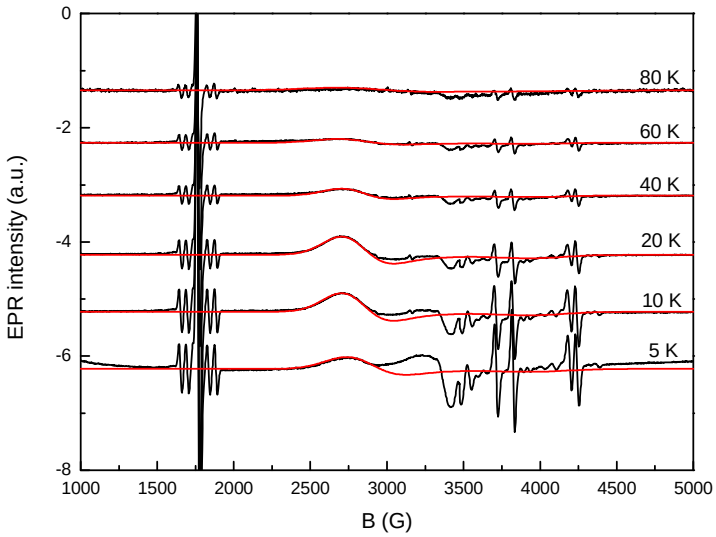

Figure 5.7. CW-EPR experimental (black) and calculated (red) spectra of $Au_{25}(SC_7H_{15})_{18}$ electrocrystallized crystals at different temperatures.

The spectra were satisfactorily simulated with the following parameters, which in this case are significantly different from those obtained for the paramagnetic films: (g_x=2.60 g_y=2.25 g_z=1.75, Δ=40).

The plot of the reciprocal of the double integrated simulated signals vs temperature is reported in Figure 5.8. The graph clearly shows that a minimum is present at 10 K. This is a typical plot for an antiferromagnet with a Néel temperature of 10 K. In agreement with this, a linear fit of the high temperature points, corresponding to the paramagnetic region, give a slightly negative intercept on the x axis, corresponding to a negative Weiss parameter, typical of antiferromagnets.

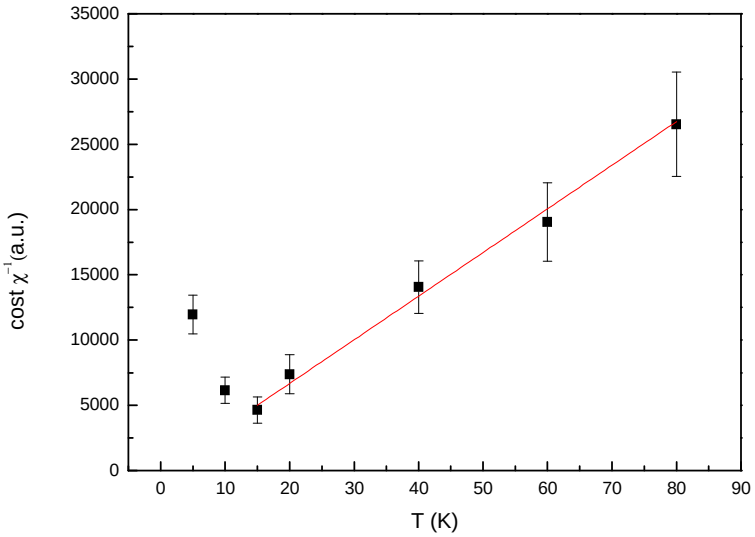

Figure 5.8. Reciprocal of the double integrals of the CW-EPR spectra of $Au_{25}(SC_7H_{15})_{18}$ crystals.

5.2.2. Ferromagnetic crystals.

We then continued by studying the clusters protected with shorter ligands, propanethiolate and ethanethiolate, which is the shortest ligand ever used so far to protect Au_{25} clusters. From the single crystal XRD structures we knew that these clusters don't form linear polymers in the solid state. Therefore, our aim was to understand if exchange interactions are still present for such short ligands and whether these interactions are ferromagnetic or antiferromagnetic. For C3 crystals, which were obtained by electrocrystallization, we observed one relatively broad signal at about 2800 G appearing below 20 K (Figure 5.9). By comparison with the corresponding spectra of the amorphous film, it is clear that this signal is quite different from the usual paramagnetic signal, although a contribution of the latter can not be completely ruled out. Differently from the antiferromagnetic samples, i.e. C4 and C7, the signal intensity increases with decreasing temperatures, indicating that most likely the crystals are not antiferromagnetic. More importantly, the signal shows a small, but evident low-field superparamagnetic shift at low temperatures (between 15 and 5 K) indicating a ferromagnetic interaction between the clusters, as for C2Ph, but with a much lower anisotropy energy.

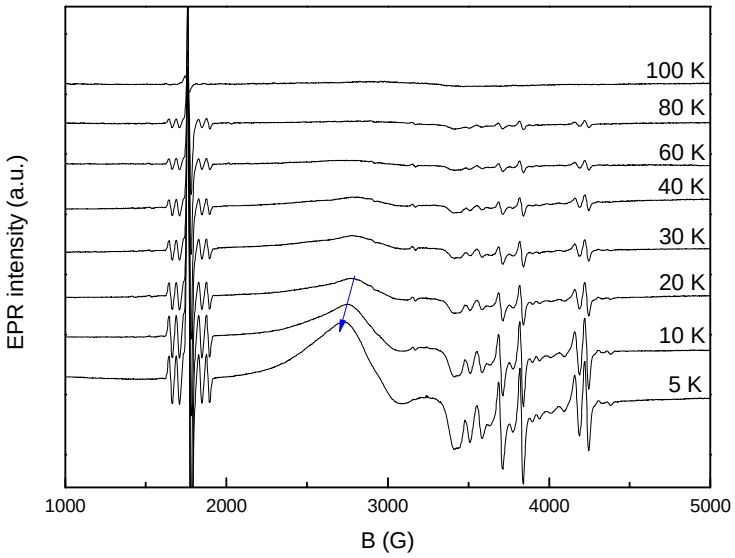

Figure 5.9. CW-EPR spectra of $Au_{25}(SC_3H_7)_{18}$ crystals at different T. The arrow shows the superparamagnetic shift.

Regarding the C2 clusters, due to their poor stability, we did not manage to obtain crystals by electrocrystallization so far, as for the other crystals presented above, but only by slow evaporation. These crystals gave a complex spectrum, which is very similar to the spectrum observed for C2Ph small crystals, consisting in a superposition of a superparamagnetic signal, due to the crystalline, ferromagnetically ordered fraction and the usual paramagnetic signal at low temperature, due to the amorphous fraction (Fig. 5.10). The superparamagnetic contribution is significantly lower, compared to the spectrum of the C2Ph polycrystalline sample, but it can still be clearly identified from the remarkable low field shift at low temperatures. It is noteworthy that also the high temperature resonance shifts strongly resemble those observed for C2Ph.

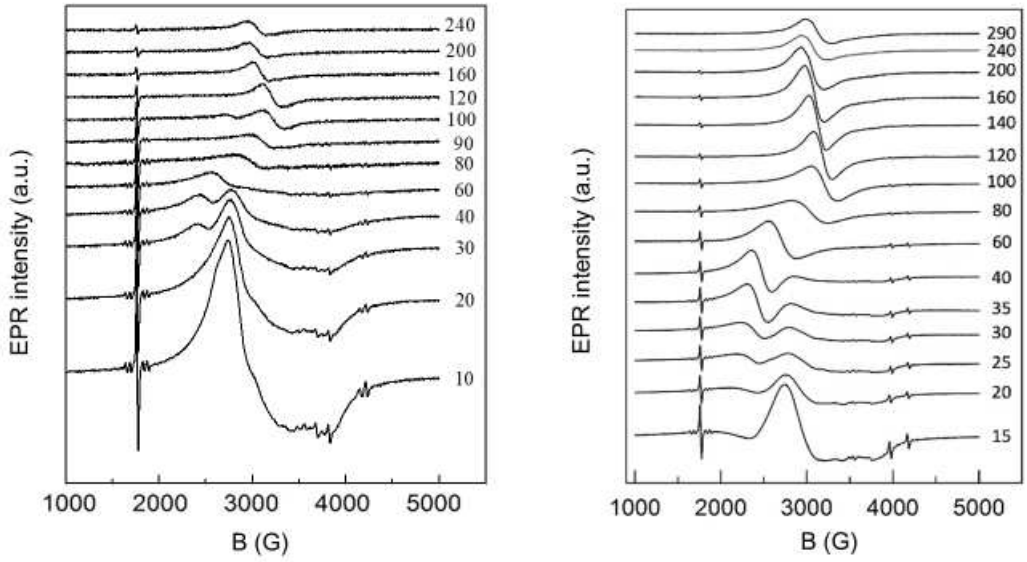

Figure 5.10. CW-EPR spectra of $Au_{25}(SC_2H_5)_{18}$ (left) and, for comparison, $Au_{25}(SC_2H_4Ph)_{18}$ (right) crystals at different T.

Besides showing the ferromagnetism of C2 and C3, these measurements demostrate once again the ability of the electrocrystallization technique to give higher quality crystalline material, compared to the crystals obtained by other methods. In effect, for the electrocrystallized crystals, the paramagnetic signal, due to the amorphous fraction of the sample, was absent or relatively weak. Instead, it always constituted a relevant contribution to the spectra of all the other samples.

In addition to the reported CW-EPR spectra, some preliminary power saturation studies were performed on both crystalline and film samples of the aforementioned clusters in order to investigate the dependence of spin relaxation on the morphology and dimensionality of the system. As explained in the introduction to this chapter, spin relaxation is of paramount importance for possible spintronic applications of these materials, as it determines the spin lifetime. Obtaining high spin lifetimes is crucial for an efficient control of spin currents. Trial experiments performed on C5 clusters are reported in Figure 5.11. The saturation curves were recorded at different fields and temperatures. As observed in Figure 5.11, in which the saturation curves for the C5 crystals and film are reported, saturation takes place at much lower MW power for crystals, compared to the film, which corresponds to slower relaxation times (see Chapter 2). Apparently, for the film

the curve is given by a superposition of a fast and a slow saturating component, the former being due to the crystalline and the latter to the amorphous fraction. The same components supposedly contribute also to the curve of the crystals, but in that case the fast component prevails. First of all, these measurements definitely prove that both the EPR spectra of crystals and film consist of two components, corresponding to a crystalline and an amorphous fraction of the sample. Moreover, most importantly, the significant difference of spin relaxation rates between the amorphous film and the crystalline samples shows that the formation of 1D linear chains of clusters efficiently suppresses relaxation, as was hypothesized in the introduction to this chapter.

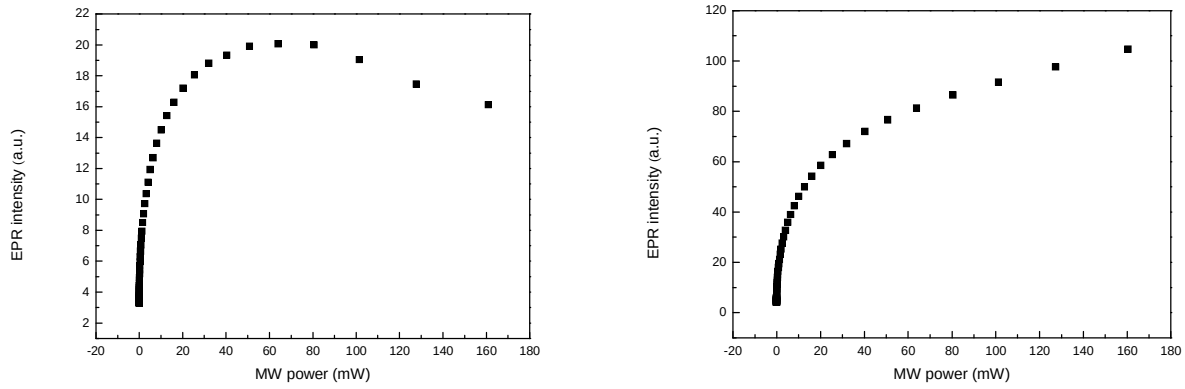

Figure 5.11. Power saturation curves for $Au_{25}(SC_5H_{11})_{18}$ crystals (left) and amorphous film (right) recorded at 10 K at a field of 2000 G.

5.2.4. Monte-Carlo Ising simulations.

As mentioned in the previous paragraph, simulations and integration of the C5 signals at different temperatures shows an increase of susceptibility with decreasing temperature, which is the contrary of what is expected for antiferromagnetic chains and of what we experimentally observed for C4 and C7. However, we know from recent XRD data that C5 clusters form linear chains, just like C4. The intercluster Au-Au distance for C5 is even smaller than for C4, therefore C5 is most likely even more antiferromagnetic than C4. This discrepancy could be explained by the presence of paramagnetic signals due to the poorly crystallized fraction of the sample, overlapping to the antiferromagnetic signal. The paramagnetic signal intensity is higher compared to the antiferromagnetic one and increases at lower temperatures, therefore an overall increase of the double integrals can be predicted.

Here we suggest a different explanation of this trend, which shows that the antiferromagnetic signal intensity can also increase with decreasing temperature. Monte Carlo simulations were performed using the Metropolis algorithm to simulate the temperature dependence of the magnetization in antiferromagnetic cluster chains and give a hint for a possible explanation of the temperature dependence of C5.[22] The Ising model was used for the simulations, valid for 1D exchange-coupled systems. The Ising Hamiltonian is the following:

$$\hat{H} = -J\sum_{\langle ij\rangle}\sigma_i\sigma_j - g\mu_B B\sum_j \sigma_j \tag{5-1}$$

where J is the exchange coupling constant and σ is the spin discrete variable. The simulations were performed by using the following algorithm: the system was initialized by producing a 100x1 vector with a random configuration of spin orientations, expressed by 1 and -1 values. The field was set to 3000 G, which corresponds to the average field intensity used in EPR measurements. A J constant of -26 meV was used (the value obtained for C4 crystals). Then a number of iterations were performed in each of which the energies were calculated, according to equation (5-1). Only exchange interactions between nearest neighbors were considered. Once the interaction energy ΔE is calculated, the spin flip is performed, consisting in changing the value from 1 to -1 or viceversa, with probability

$$p = \exp\left(-\frac{\Delta E}{kT}\right) \tag{5-2}$$

A large number of iterations were performed (specifically 5000), until equilibrium is reached. Then the overall magnetization of the system was calculated by summing up all the spin values. The same operation was performed several times (200) for different temperatures and the average values for each temperature were calculated.

The preliminary simulations show that, while the magnetization actually decreases with decreasing temperature (Figure 5.12) in a high temperature range, under a certain temperature it starts increasing again, giving a possible explanation for the temperature dependence of C5 susceptibility.

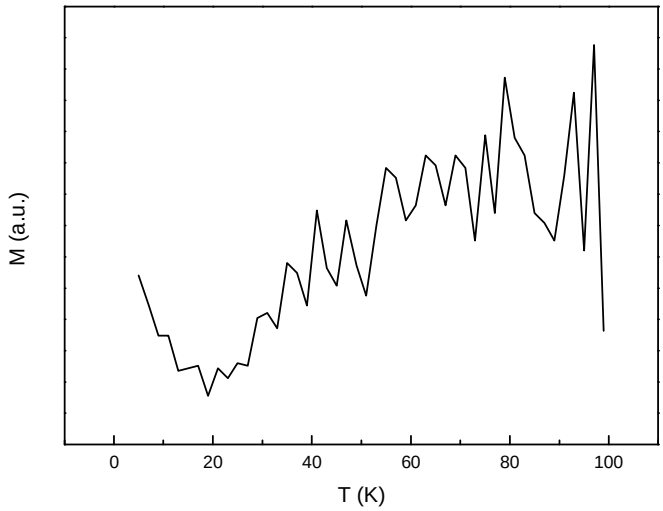

Figure 5.12. Magnetization vs T obtained from trial Monte-Carlo simulations for an Ising 1D antiferromagnetic chain of s=1/2 clusters.

5.2.2. Photoinduced electron transfer.

The results presented so far evidenced that ligands and crystallinity, and in particular the formation of linear 1D chains, strongly affect the magnetic properties of Au_{25} clusters protected with linear alkyl ligands. Subsequently we were interested in investigating other physical properties of the clusters, which could possibly be influenced by the polymeric solid-state structure and by the length of the protecting ligands. Thus, we turned to study the photoinduced behavior of a series of Au_{25} clusters, both in the solid state and in frozen solution, expecting to observe some effect of the aforementioned properties on electron transfer. Eventually, our aim was to obtain a picture of the interplay between the latter and the magnetic, optical and structural properties of these systems.

The measurements were performed on two antiferromagnetic samples, i.e. C4 and C5, in toluene solution and in the crystalline state. These samples were chosen in order to investigate the intercluster distance dependence of the photoinduced electron transfer with and without the linear polymers. The samples were irradiated with a polychromatic visible light lamp. The spectra before, during and after irradiation were recorded (Figure 5.13). At 5 K a significant decrease of the paramagnetic signal intensity was observed for all the samples both in solution and in the solid state for the spectra acquired during the irradiation. The spectra recorded after the light was switched off were instead identical to those before the illumination. The observed decrease of the paramagnetic signal was

attributed to the photoinduced electron transfer process between two clusters. In this process we start from two paramagnetic clusters and the electron transfer between the two leads to the reversible formation of two diamagnetic clusters, one positively and one negatively charged. This obviously gives rise to a decrease of the EPR signal intensity.

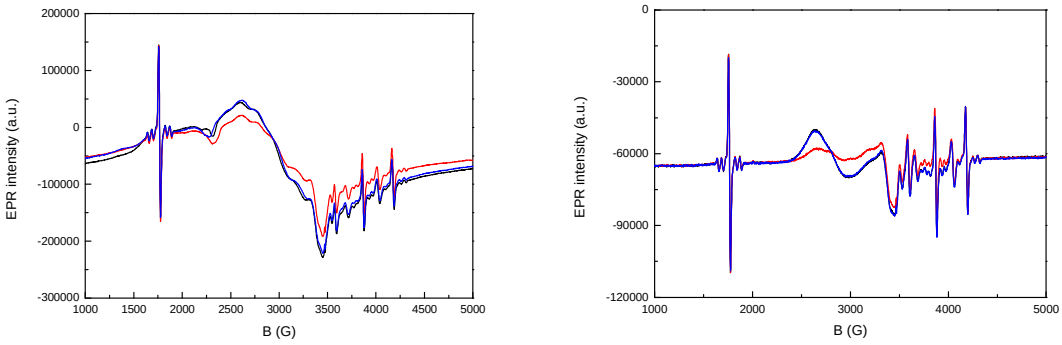

Figure 5.13. CW-EPR spectra of C4 crystals (a) and frozen solution (b) recorded at 5 K before (black), during (red) and after (black) optical irradiation.

Subsequently, in order to investigate the dynamics and the mechanism of this process more in depth, the kinetic traces were recorded, consisting in the intensity of the EPR line maximum vs time right after switching on and switching off the irradiation (Figures 5.14, 5.15). The time traces were fitted by suitable functions (exponential, biexponential or sigmoidal), depending on the sample. It is observed that the kinetics are much slower in solution, compared to the solid state (for instance, in the case of C4: τ_{cryst}=4 s, τ_{sol}=40 s). This is most probably an effect of the intercluster distance: from a simple calculation performed in Chapter 4, it turns out that the clusters are about an order of magnitude nearer in the crystals than in solution. This possibly implies a slower electron transfer in solution, compared to the crystals. Moreover, both in the solid state and in solution the kinetics for C4 are much slower than for C5 (for crystals τ_{C5}=0,2 s, τ_{C4}=4 s), which is also a distance effect: indeed, according to the XRD structures, the mean intercluster distance along a chain is smaller in C5, compared to C4. Finally, it is noteworthy that the relaxation of the clusters in solutions after the light is turned off doesn't follow the exponential law, as for the kinetics during the irradiation, but a sigmoidal, implying that two different mechanisms are involved in the two processes. The fitting values are summarized in Table 5.2.

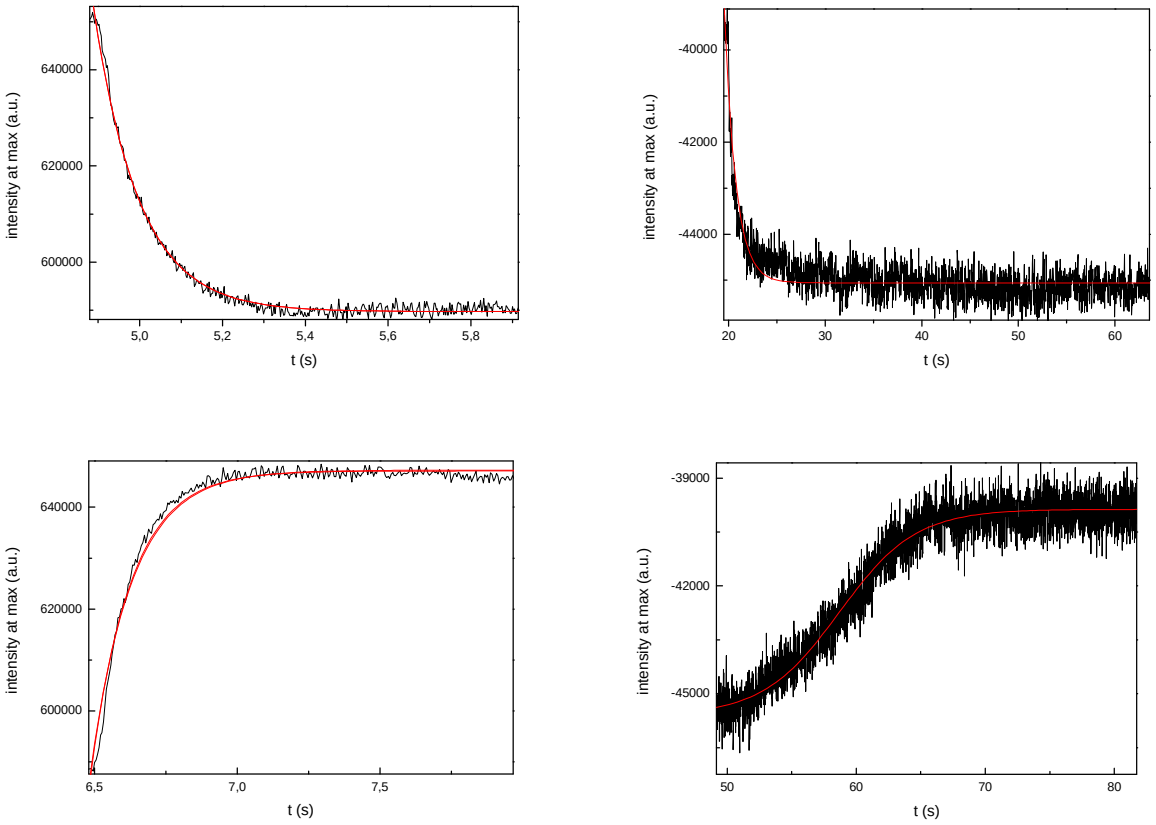

Figure 5.14. EPR intensity of signals of C4 crystals (left) and frozen solution (right) vs time after the irradiation is switched on (above) and off (below).

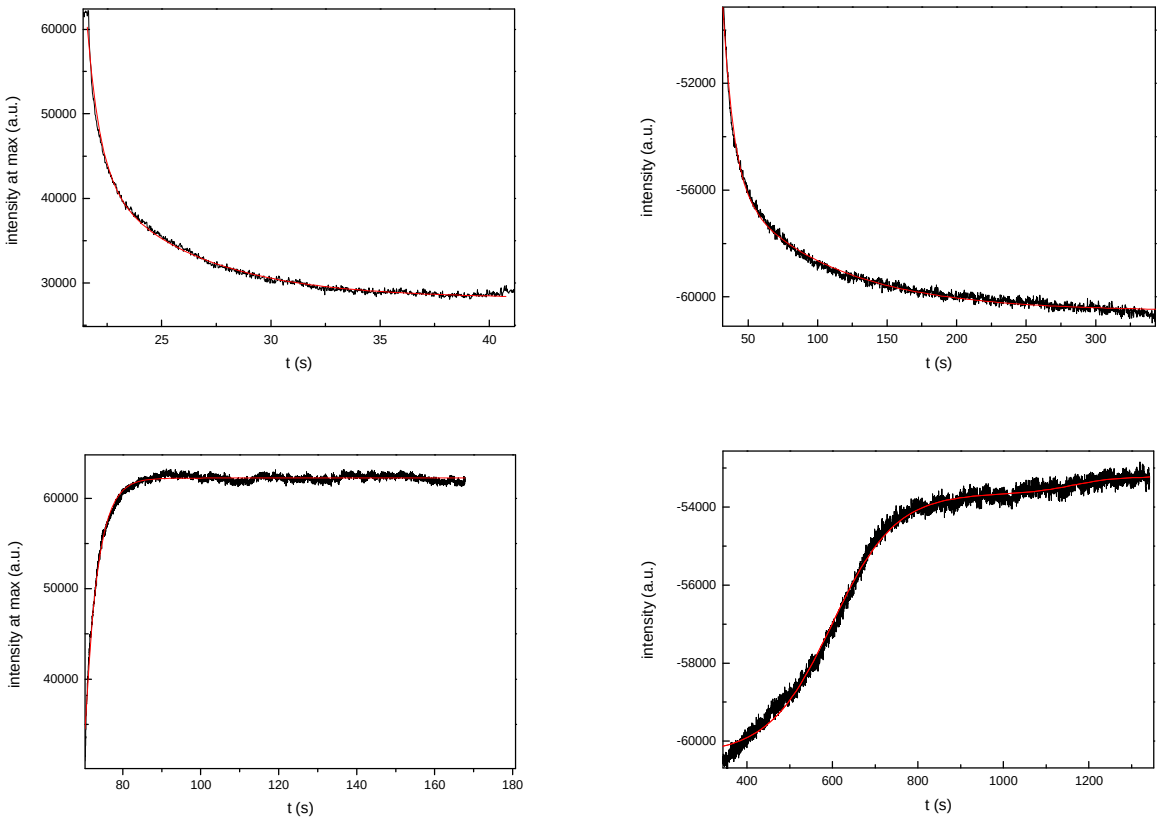

Figure 5.14. EPR intensity of signals of C5 crystals (left) and frozen solution (right) vs time after the irradiation is switched on (above) and off (below).

Table 5.2. Time constants τ obtained from the exponential and biexponential fittings of the time variation of the maximum intensity of the spectra of C4 and C5 crystals and frozen solutions after the irradiation is switched on and off.

	C4 crystals	C4 frozen solution	C5 crystals	C5 frozen solution
lightON	4.5; 1	74; 8	0.17	1.2
lightOFF	3.2	-	0.17	-

Recently we started to investigate the electron transfer properties between Au_{25} and other materials. Thus, we produced a hybrid material, consisting in negatively charged C3 clusters, in the form of an octylammonium salt, adsorbed on TiO_2 nanoparticles with the aim of studying the possible electron transfer between the two compounds. In particular, we were interested in the photoinduced electron transfer reported in literature[23] for such kind of material, which is of particular importance in the field of photovoltaics. Details on the sample preparation are available in the experimental part. The first spectra of the sample recorded both with and without illumination 48 hours after the preparation gave the typical spectrum of TiO_2, with the characteristic defects signals around 3500 G (figure 5.16).

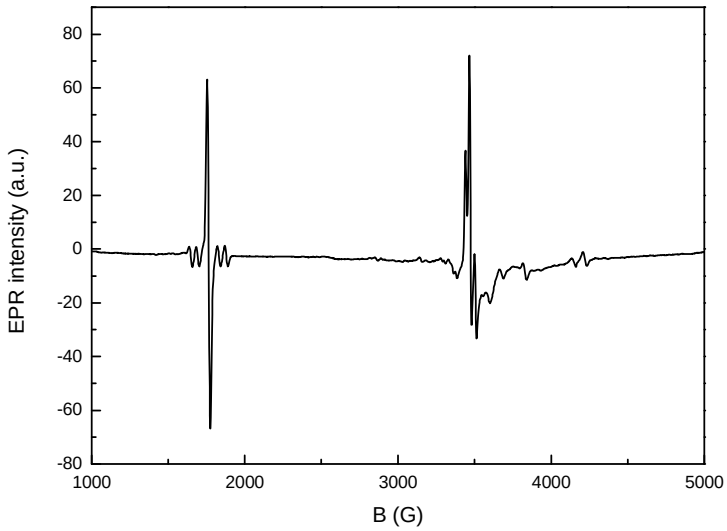

Figure 5.16. CW-EPR spectrum of TiO_2 nanoparicles with adsorbed C3(-) clusters, recorded at 30 K right after the sample preparation and showing the typical defects signals around 3500 G.

These defects are mostly due to various nitrogen species, often present in the commercial titania as impurities or intentionally introduced by N-doping and are of no particular interest for the aims of this study. Additional detailed information on these signals can be found in literature.[23] After leaving the sample in the dark at room temperature for other 48 hours, additionally to the signals due to TiO_2, a low field signal appears below 3000 G, remarkably broader than the N-defects signals. Moreover, the measurements performed at variable temperature (Figure 5.17) showed that this signal exhibits a remarkable resonance shift with lowering the temperature, from 2800 G at 30 K to 2300 G at 5 K. As observed previously for C2Ph(0), C2(0) and C3(0) crystals, this shift is associated with a superparamagnetic behavior, typical of small ferromagnetic particles. First of all, this clearly demonstrates that electron transfer from cluster to titania took place and that this process is slow, irreversible and probably independent on optical irradiation with visible light. Surprisingly, this also shows that TiO_2 in some way promotes the formation of ferromagnetically coupled aggregates of paramagnetic C3 clusters, which we already know to interact ferromagnetically in electrocrystallized crystals. Even more curiously, in these aggregates the magnetic anisotropy is higher compared to the C3(0) crystals we studied before, since the superparamagnetic shift is more evident and is observed at higher temperatures. This may be due to the different dimensions or shape of the crystals.

Ferromagnetism was confirmed by the presence of hysteresis at 30K (Figure 5.18). Hysteresis appears at nearly the same temperature as for C2Ph, but is much weaker. It is remarkable that in this case pure and highly ordered ferromagnetic systems are produced, since no residual paramagnetic signal is visible. This is very surprising, since the paramagnetic signal was still present even in apparently crystalline samples, such as C2Ph and C2 crystals. In summary, these results show that TiO_2 nanoparticles promote both the oxidation and the aggregation of Au_{25} clusters, which form purely ferromagnetic systems.

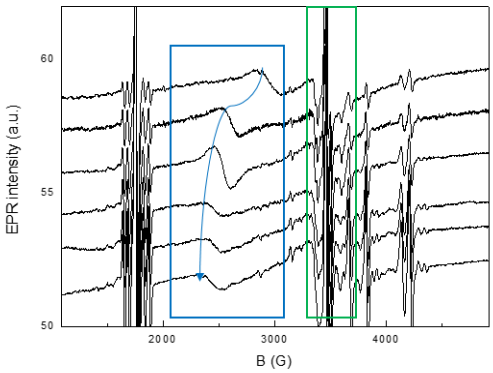

Figure 5.17. CW-EPR spectra of $Au_{25}(SC_3H_7)_{18}^-$ adsorbed on TiO_2 nanoparicles at different temperatures. The TiO2 nitrogen defects are evidenced in green, while the superparamagnetic signal of Au25 aggregates is in blue.

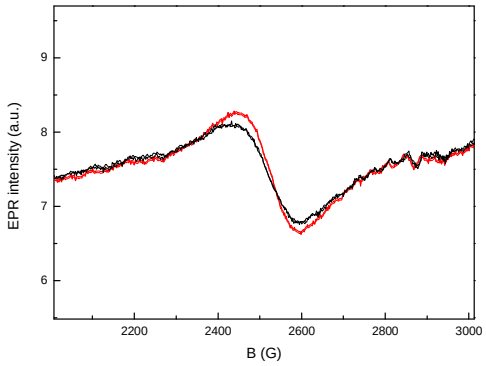

Figure 5.18. Hysteresis of the $Au_{25}(SC_3H_7)_{18}^-$ / TiO_2 system at 30 K, evidenced by the upwards (black) and downwards (red) scans (right) of the CW-EPR spectrum

5.3. Conclusions.

The investigations reported in this chapter show that the formation of linear 1D chains in the crystalline samples gives rise to very different magnetic properties of the Au_{25} clusters, compared to those typical of the amorphous state and that these properties can be

modulated by changing the length of the ligands. While, regardless the ligand used, all the amorphous film samples are essentially paramagnetic, with weak ferromagnetic interactions arising at low temperature (below 40 K in all cases), in the crystalline samples the situation is more complex. Longer ligands (C4, C5, C7) allow the formation of 1D chains, due to the twist-lock mechanism, and thus give rise to antiferromagnetic interactions between neighboring clusters inside a chain. The polymers are not formed with shorter ligands (C2, C3) and in this case the clusters interact ferromagnetically. These interactions are remarkably stronger than in the amorphous films, because of the crystalline and magnetic ordering, but are generally weaker, compared to the case of the C2Ph ligands, extensively discussed in Chapter 4. These findings suggest that the twist-lock mechanism leading to the formation of 1D chains is closely linked to the flexibility of long alkyl chains, while the intercluster ferromagnetic interactions are enhanced by the stacking of phenyl rings. Moreover, we showed that also the magnetic relaxation is affected by the formation of polymeric cluster chains: relaxation is significantly slower in crystals, with respect to the amorphous films. This is most likely due to the reduced dimensionality of the system. We also investigated the response of these systems to optical photoexcitation. These measurements showed a photoinduced electron transfer, taking place both in the crystalline state and in frozen solution, which is also influenced by both the ligands and the aggregation state. Electron transfer between Au_{25} clusters and TiO_2 nanoparticles was also demonstrated, leading to the formation of ferromagnetic aggregates. All these results underline the great scientific and technological interest of these systems, particularly of the linear 1D chains, opening the way to possible applications in spintronics, quantum computing and magneto-optical devices.

5.4. Experimental section.

The synthesis, electrocrystallization and film deposition of the clusters were performed following the procedures described in the previous chapters. The hybrid $Au_{25}(SC_3H_7)_{18}/TiO_2$ material was prepared by simply leaving 20 mg of TiO_2 powder immersed in a 3 mM toluene solution of $(Oct_4N)^+Au_{25}(SC_3H_7)_{18}^-$ for 72 h. The solution was stirred and sonicated approximately every 4 h. The solvent was left to evaporate completely and the procedure was repeated another time, until the powder assumed a grey color, indicating that the cluster was successfully adsorbed. The instrumental settings and parameters used for the EPR measurements were the same reported in Chapter 4.

5.5 References

1. Agrachev, M., Antonello, S., Dainese, T., Gascón, J. A., Pan, F., Rissanen, K., Ruzzi, M., Venzo, A., Zoleo, A.; Maran, F. A Magnetic Look into the Protecting Layer of Au_{25} Clusters. *Chem. Sci.* **2016**, *7*, 6910-6918.

2. Agrachev, M.; Antonello, S.; Dainese, T.; Ruzzi, M.; Zoleo, A.; Aprà, E.; Govind, N.; Fortunelli, A.; Sementa, L.; Maran, F. Magnetic Ordering in Gold Nanoclusters. *ACS Omega* **2017**, *2* (6), 2607-2617.

3. De Nardi, M.; Antonello, S.; Jiang, D.-E. Pan, F.; Rissanen, K.; Ruzzi, M.; Venzo, A.; Zoleo, A.; Maran, F. Gold Nanowired: A Linear $(Au_{25})_n$ Polymer from Au_{25} Molecular Clusters *ACS Nano* **2014**, *8* (8), 8505-8512.

4. Dainese, T.; Antonello, S.; Gascón, J. A.; Pan, F.; Perera, N. V.; Ruzzi, M.; Venzo, A.; Zoleo, A.; Rissanen, K.; Maran, F. $Au_{25}(SEt)_{18}$, a nearly "Naked" Thiolate-Protected Au_{25} Cluster: Structural Analysis by ENDOR and Single Crystal X-ray Crystallography. *ACS Nano* **2014**, *8*, 3904-3912.

5. Bandyopadhyay, S.; Cahay, M. Introduction to Spintronics **2008** CRC Press, Boca Raton.

6. Wolf, S. A.; Awschalom, D. D.; Buhrman, R. A.; Daughton, J. M.; Moln´ar, S. v.; Roukes, M. L.; Chtchelkanova, A. Y. and Treger, D. M. Spintronics: A spin-based electronics

vision for the future, *Science* **2001**, 294, 1488-1495.

7. Coronado, E.; Epsetin, A. J. Molecular spintronics and quantum computing. *J. Mater. Chem.* **2009***, 19*, 1670-1671.

8a. Hossain, M. I.; Bandyopadhyay, S.; Atulasimha, J.; Bandyopadhyay, S. Modulating spin relaxation in nanowires with infrared light at room temperature. *Nanotechnology* **2015***, 26*.

8b. Li, R.; You, J. Q.; Sun, C. P.; Nori, F. Controlling a nanowire spin-orbit qubit via electric-dipole spin resonance. *Phys. Rev. Lett.* **2013***, 111*.

8c. Nautiyal, T.; Rho, T. H.; Kim, K. S. Nanowires for spintronics: A study of transition-metal elements of groups 8-10. *Phys. Rev. B Condens. Matter Mater. Phys.* **2004***, 69*, 193404-1-193404-4.

8d. Nadj-Perge, S.; Frolov, S. M.; Bakkers, E. P. A. M.; Kouwenhoven, L. P. Spin-orbit qubit in a semiconductor nanowire. *Nature* **2010***, 468*, 1084-1087.

8e. Emberly, E. G.; Kirczenow, G. Molecular spintronics: Spin-dependent electron

transport in molecular wires. *Chem. Phys.* **2002***, 281*, 311-324.

8f. Hrkac, G.; Dean, J.; Allwood, D. A. Nanowire spintronics for storage class memories and logic. *Philos. Trans. R. Soc. A Math. Phys. Eng. Sci.* **2011***, 369*, 3214-3228.

9. Patibandla, S.; Pramanik, S.; Bandyopadhyay, S.; Tepper, G. C. Spin relaxation in a germanium nanowire. *J. Appl. Phys.* **2006***, 100*.

10. Nowack, K. C.; Koppens, F. H. L.; Nazarov, Y. V.; Vandersypen, L. M. K. Coherent control of a single electron spin with electric fields. *Science* **2007***, 318*, 1430-1433.

11. Appelbaum, I.; Huang, B. and Monsma, D. J. Electronic measurement and control of spin transport in silicon, *Nature* **2007**, 447, 295.

12. Dyakonov, M. I. and Perel, V. I. Current-induced spin orientation of electrons in semiconductors, *Phys. Lett. A* **1971**, 35, 459.

13a. Datta, S. and Das, B. Electronic Analog of the electro-optic modulator, *Appl. Phys. Lett.* **1990**, 50, 665.

13b. Yang, L.-P.; Sun, C.-P. Indirect control of spin precession by electric field via spin-orbit coupling. *Eur. Phys. J. B* **2015***, 88*, 35-1-8.

14. Wang, K. L.; Kou, X.; Upadhyaya, P.; Fan, Y.; Shao, Q.; Yu, G.; Amiri, P. K. Electric-Field Control of Spin-Orbit Interaction for Low-Power Spintronics. *Proc IEEE* **2016***, 104*, 1974-2008.

15. Rashba, E. I. Properties of semiconductors with an extremum loop, Sov. Phys. Solid State **1960**, *2*, 1109.

16. Y. K. Kato, R. C. Myers, A. C. Gossard, and D. D. Awschalom, Observation of the spin Hall effect in semiconductors, *Science* **2004**, 306, 1910.

17. B. A. Bernevig, T. L. Hughes, and S.-C. Zhang, Quantum spin Hall effect and topological phase transition in HgTe quantum wells, **2006**, *314*, 1757.

18. Jungwirth, T.; Marti, X.; Wadley, P.; Wunderlich, J. Antiferromagnetic spintronics. *Nat. Nanotechnol.* **2016***, 11*, 231-241.

19. Gomonay, O.; Jungwirth, T.; Sinova, J. Concepts of antiferromagnetic spintronics. *Physica Status Solidi Rapid Res. Lett.* **2017***, 11*.

20. Sklenar, J.; Zhang, W.; Jungfleisch, M. B.; Jiang, W.; Saglam, H.; Pearson, J. E.; Ketterson, J. B.; Hoffmann, A. Spin Hall effects in metallic antiferromagnets - Perspectives for future spin-orbitronics. *AIP Adv.* **2016***, 6*.

21. Sklenar, J.; Zhang, W.; Jungfleisch, M. B.; Jiang, W.; Saglam, H.; Pearson, J. E.; Ketterson, J. B.; Hoffmann, A. Spin Hall effects in metallic antiferromagnets - Perspectives

for future spin-orbitronics. *AIP Adv.* **2016***, 6*.

22. Grandi, B. C. S.; Figueiredo, W. Monte Carlo simulation of an antiferromagnetic Ising model at two competing temperatures. *Phys Rev E.* **1999***, 59*, 4992-4996.

23. Kumar, C.P.; Gopal, N.O; Wang, T.C.; Wong, M.-S.; Ke, S.C. *J. Phys. Chem. B* **2006**, *110*, 5223.

Chapter 6.

Intrinsic Exchange Reactivity of the Inner and Outer Ligands in $Au_{25}(SR)_{18}$ Clusters

6.1 Introduction

As reported in Chapter 1, the study of the properties of gold nanoclusters protected by thiolate monolayers is a fast-pace growing research area in nanosciences and nanotechnologies.[1-3] In applications, such as sensing, catalysis and biomedicine,[4,5] the nature and number of functional groups displayed by the monolayer play an essential role in driving the action and performance of the MPC. Proper functionalization, on the other hand, requires implementing strategies suitable to prepare the sought MPCs in a controlled fashion.[6] This can be achieved by carrying out the MPC synthesis directly from a mixture of appropriate thiols, *via* reactions of reactive groups present on the outermost part of the capping monolayer, or by taking advantage of ligand-place exchange reactions. In the latter, the thiolates of preformed MPCs are exchanged with exogenous thiols, a pathway opened several years ago by the Murray's group.[7] Exchange reactions are particularly useful, *e.g.*, to introduce expensive/less easily available thiols, when the target thiols carry groups that are unstable during the reducing, direct-synthesis conditions, or when solubility issues would prevent controlling the MPCs' size in direct syntheses. An early study,[8] later confirmed by further investigations on better defined MPCs,[9,10] already identified that these reactions proceed by an associative mechanism where the exchanged ligands are released as thiols. A similar conclusion was later reached also by density functional theory calculations.[11,12] Because of the number of thiolates protecting the native MPC, ligand place exchange typically leads to polysubstitution,[13,14] partially controllable by adjustment of reaction conditions such as time and relative concentrations. Separation of the substituted clusters requires high-performance liquid chromatography.[15,16] The fact that for clusters larger than 2 nm the starting MPC is not monodisperse with atomic precision further complicates the preparation and analysis of the ligand-exchanged clusters.

As described in the previous chapters, $Au_{25}(SR)_{18}$ is a particularly stable molecular MPC with a metal core diameter of only 1 nm.[1, 17] It also is fully representative of the general properties of this class of ultrasmall MPCs, such as the presence of a HOMO-LUMO gap[18], a very distinct electrochemical behavior,[18,19] and charge-dependent magnetic properties that can be nicely evidenced by NMR[20] and electron paramagnetic resonance.[21,22] $Au_{25}(SR)_{18}$ thus provides an ideal candidate for exploring fine details of the ligand place-exchange reactions under fully controlled conditions. It has been already used to provide the first information on the kinetics of ligand exchange on a well-defined molecular cluster,[10,23] its native ligands were exchanged to affect its electrochemical behavior,[24,25] its monolayer could be fully exchanged,[24,26] the single-crystal X-ray crystallographic structure of an exchanged $Au_{25}(SR)_{18}$ cluster (by two ligands) has been described.[27]

In this chapter, the results of a study are reported aimed to obtain molecular insights into the kinetics of ligand place-exchange reactions. As described in Chapters 1 and 3, due to the presence of six equivalent staples, surrounding a central 13 Au atoms icosahedral core, the 18 ligands of $Au_{25}(SR)_{18}$ split into two families of 6 outer and 12 inner ligands, a feature maintained as one goes from phenylethanethiol[1] down to ethanethiol, the shortest thiol ever used.[28] This suggests that the protecting thiolates are bound to gold with different energy and thus that reactivity could, in principle, be different. The objective of this study was to assess if and to what extent the ligands belonging to these two families are exchanged with intrinsically different rates. The results reported so far in literature on this subject are quite contradictory. Computational studies predicted a preferential exchange in the inner position.[29] This is in agreement with most of the experimental results, based mainly on single crystal XRD.[30,31] However, at least one other study, carried out by means of NMR spectroscopy, states the opposite, i.e. that the outer ligands exchange rate is higher.[32] These inconsistent outcome points out that the ligand exchange reactions are probably more complex than it was assumed and that several factors must be considered for an accurate description, such as the statistical factors and the ligand-dependence of the process.

To make the reactive sites of the monolayer as accessible as possible to the incoming thiols, we prepared the cluster $Au_{25}(SPr)_{18}$, whose single-crystal X-ray crystallographic structure is described in Chapter 3. The kinetic study was carried out by taking advantage of precise control of the cluster charge state and full knowledge of the ^{1}H NMR

spectroscopy behavior for each ligand family. Analysis of the kinetic data highlighted a remarkable site- and thiol-dependent exchange, but also the importance of taking into account statistical factors

6.2 Results and discussion

6.2.1. Preliminary NMR and MALDI analyses

The synthesis of the $Au_{25}(SR)_{18}$ cluster was carried out in tetrahydrofuran as already described for similar clusters.[33] The as-prepared diamagnetic, anionic cluster was quantitatively oxidized to its neutral paramagnetic form *via* a column chromatography method.[28] The rationale of using a paramagnetic cluster is that most of the ^{1}H NMR resonances undergo a significant downfield shift compared to the diamagnetic form. This, together with the use of short thiols for preparing the MPC and performing the exchange (see below), was thus strategic to make the NMR pattern span across a much wider chemical-shift range than for the corresponding diamagnetic cluster, thereby allowing for good separation of the peaks to be studied during the ligand-place exchange reaction and thus precision in the kinetic analysis.

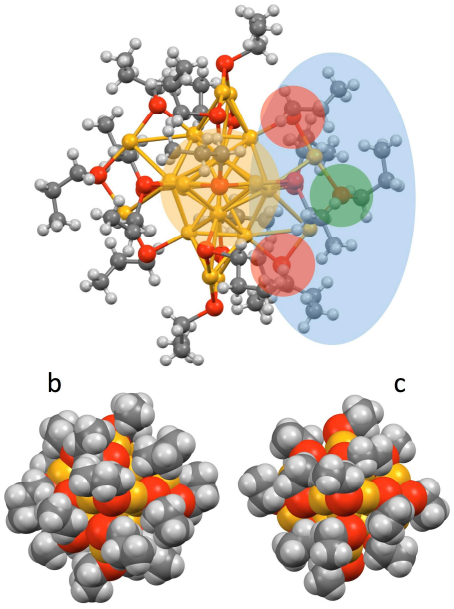

Figure 6.1. (a) Projection showing the X-ray crystal structure of $Au_{25}(SPr)_{18}$. Au = yellow, S = red, C = gray, H = white. For clarity, the icosahedral core (yellow), one of the staples (blue), and the corresponding inner- (red) and outer-ligands (green) have been highlighted. Also shown is a comparison between the space-filling models of (b) $Au_{25}(SPr)_{18}$ and (c) $Au_{25}(SEt)_{18}$.

$Au_{25}(SPr)_{18}$ could be prepared in very pure form and easily crystallized. As for the other known $Au_{25}(SR)_{18}$ structures,[1,27,28,34] the 25 gold atoms can be regarded as forming two shells (Figure 6.1): an inner icosahedral core, consisting of a central Au atom with 12 Au atoms directly interacting with it, and an outer shell of 12 Au atoms protected by thiolate groups to form staple-like structures. The space-filling model (Figures 6.1b), shown in comparison with that of $Au_{25}(SEt)_{18}$ (Figure 6.1c),[28] illustrates the important aspect that because of the short ligand employed and independently of the ligand site, all sulfur atoms are indeed easily accessible to exogenous thiols.

For the exchange reactions, we used ethanethiol (EtSH), 3-mercaptopropionic acid methyl ester (PESH) and ter-butylthiol (tBuSH). EtSH was meant to compare the NMR spectra of the exchanged clusters to that of $Au_{25}(SEt)_{18}$.[29] PESH was chosen to provide a prototype of ligand that could eventually be activated for carrying out functionalization reactions. Both thiols avoid introducing structural factors that could cause specific interactions between neighboring ligands (other than van der Waals) within the monolayer. Moreover, to gain insights into a possible ligand-length effect, whereas one of the thiols was chosen to be a bit shorter than PrSH, the other was a bit longer. tBuSH instead was chosen as a bulky ligand in order to study the influence of sterical hindrance and inter-ligand interactions on ligand exchange reactions kinetics. Figure 6.2 compares the ^{1}H NMR spectra of $Au_{25}(SPr)_{18}$, $Au_{25}(SEt)_{18}$, PrSH, and EtSH in benzene-d_6. In paramagnetic $Au_{25}(SR)_{18}$, the ^{1}H NMR behavior of the ligands is very sensitive to the specific position occupied in the MPC.[20] Figure 6.1a shows that, whereas in the 6 outer ligands the sulfur atom is bound to two Au atoms of the outer shell, in the 12 inner ligands one of the two S-Au bonds involves one of the icosahedron Au atoms. The effect of the unpaired electron is particularly felt by the resonances closer to the icosahedral gold core, *i.e.*, those of the groups in the positions α, β and γ of the inner ligands and the position α of the outer ligands.[30] The spectra of both $Au_{25}(SPr)_{18}$ and $Au_{25}(SEt)_{18}$ display the inner- and outer-ligand resonances in a precise 2:1 ratio. The only peak not shown in Figure 6.2 is the very broad $(\alpha\text{-}CH_2)_{in}$ resonance (25 ℃) that occurs at about 25 ppm for both $Au_{25}(SPr)_{18}$ and $Au_{25}(SEt)_{18}$. Figure 6.2 highlights that some resonances of the clusters and free thiols are particularly well separated. A similar comparison can be made for $Au_{25}(SPr)_{18}$, PESH and tBuSH.

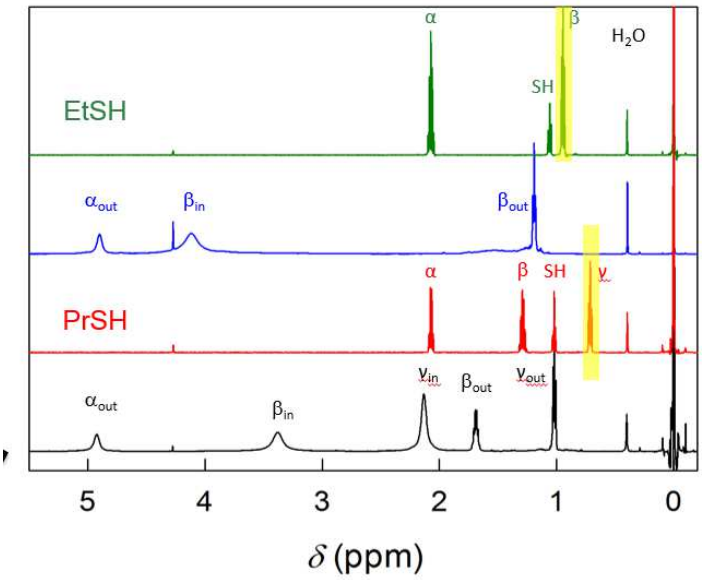

Figure 6.2. Comparison of 1H NMR spectra of free EtSH and PrSH ligands (green and red respectively), $Au_{25}(SEt)_{18}$ and $Au_{25}(SPr)_{18}$ clusters (blue and black respectively).

The exchange reactions were carried out using 2 equiv of thiol with respect to the concentration of $Au_{25}(SPr)_{18}$, 3 mM, in benzene. The reactions were quenched after 1, 4 or 18h. Because the two exogenous thiols and PrSH are very volatile, the reactions could be easily quenched by quick, simultaneous rotary evaporation of solvent and thiols, to leave only the exchanged cluster as a solid. Just before quenching, a tiny fraction of the reaction solution was collected and checked by UV-vis spectroscopy. This allowed us to verify that the concentration of Au_{25} did not change during the experiments, within 1%, and therefore, that in the selected experimental conditions the cluster integrity was maintained quantitatively. Small changes of the UV-vis spectrum were observed only for the tBuSH-exchanged cluster, as will be discussed later.

The solids were analyzed by matrix-assisted laser desorption ionization time-of-flight (MALDI-TOF) mass spectrometry under conditions suitable to avoid fragmentation of the clusters. Figure 6.3 shows a comparison between the mass spectra obtained after exchange with PESH and EtSH after 1, 4 and 18 h.

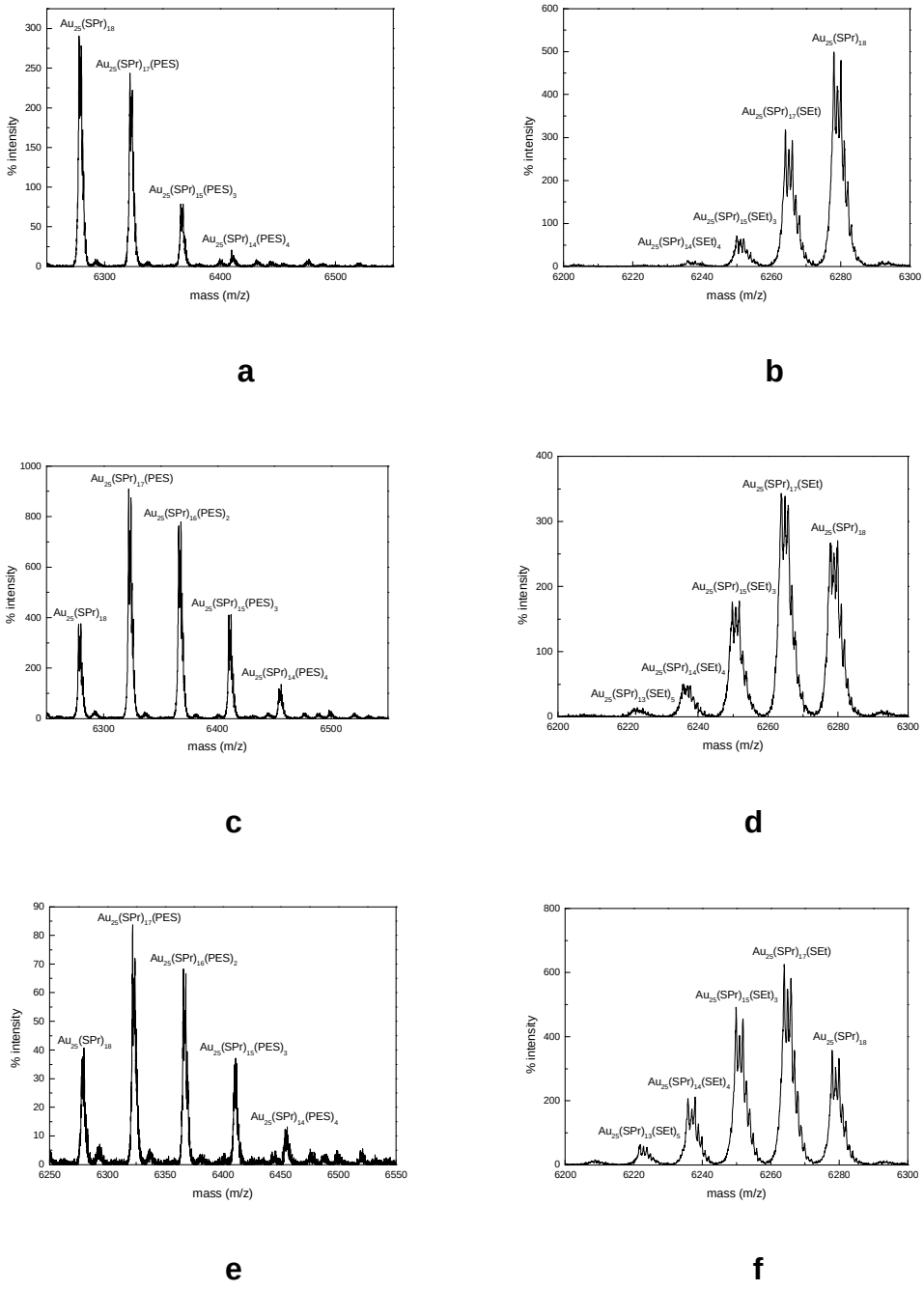

Figure 6.3. MALDI-TOF spectra of $Au_{25}(SPr)_{18}$ partially exchanged with PESH after 1 h (a), 4 h (c) and 18 h (e) and with EtSH after 1 h (b), 4 h (d) and 18 h (f).

The spectra show a progressive increase of polysubstitution. For example, after 1h the mean numbers of ligands exchanged are 0 (55%), 1 (35%), 2 (8%) and 4 (2%), after 4 h they are 0 (30%),1 (38%), 2 (22%), 3 (7%) and 4 (3%), whereas after 18 h they are 0 (20%),1 (35%), 2 (27%), 3 (13%), 4 (3%) and 5 (2%), which correspond to an average of ca. 1.5 equivalents exchanged. A similar trend is observed for PESH, although after 18 h

the extent of exchange is larger, corresponding to 1.7 equivalents (Figure 6.3f). For tBuSH instead, the amount of ligand exchanged after 18 hours is significantly smaller, being equal to about 0.7 (Figure 6.4). Moreover, additional regularly spaced peaks appear at higher masses of the MALDI spectrum, which cannot be assigned to a simply ligand-exchanged Au25 cluster. This feature will be addressed in more detail further on.

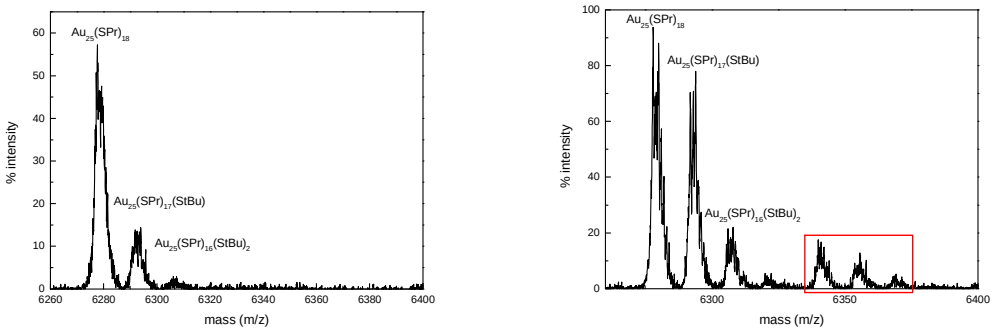

Figure 6.4. MALDI-TOF spectra of $Au_{25}(SPr)_{18}$ partially exchanged with tBuSH after 4 h (a) and 18 h (b).

6.2.2. NMR monitoring of ligand exchange and signals attribution

For the NMR kinetic study, the ligand exchange reactions were carried out directly in the NMR tube and the reactions were monitored in real time by NMR. Figure 6.5 illustrates the time evolution of most NMR resonances during the exchange with 2 equiv EtSH.

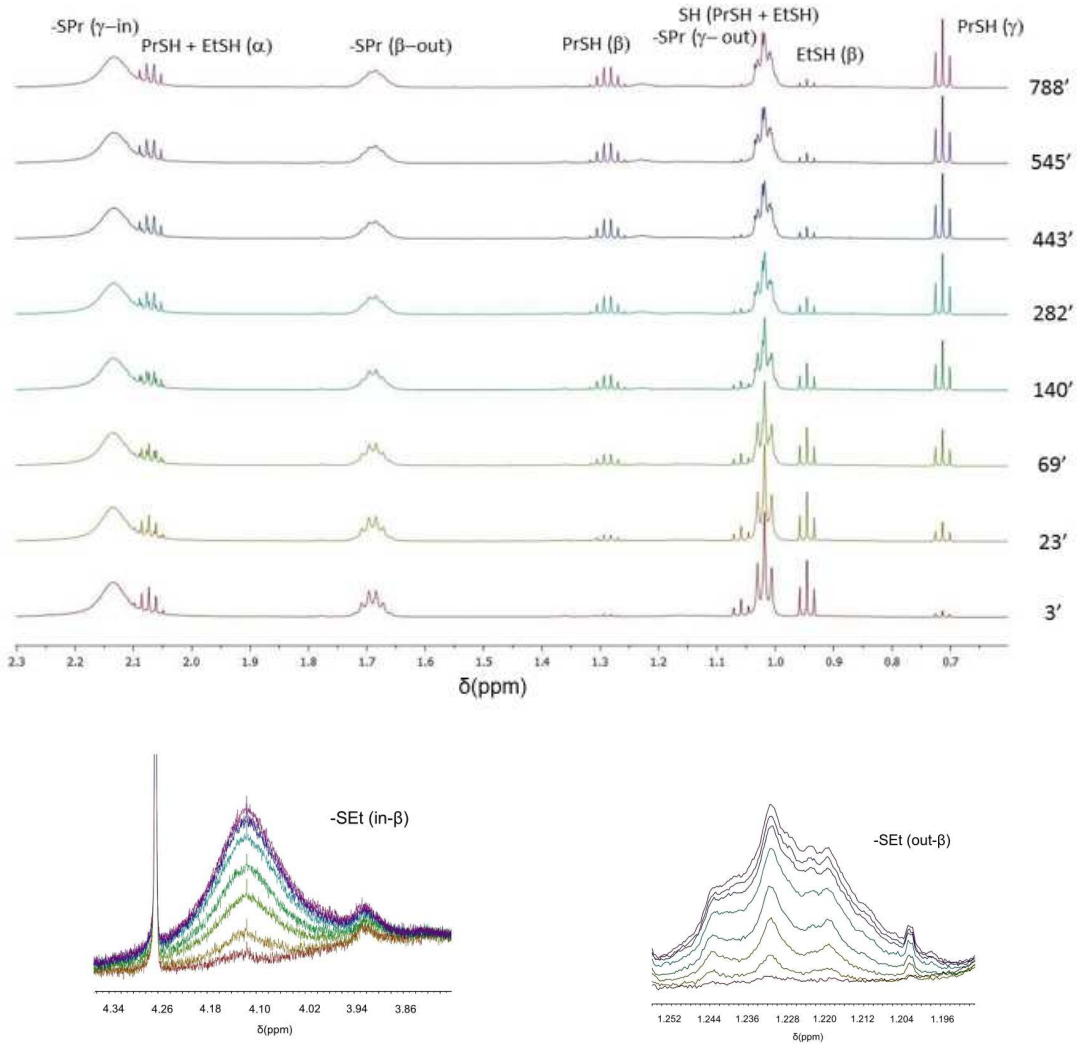

Figure 6.5. Evolution of a portion of the NMR spectra during the ligand exchange reaction of $Au_{25}(SPr)_{18}$ with EtSH (from red to violet).

Comparison with the spectra of $Au_{25}(SPr)_{18}$ and $Au_{25}(SEt)_{18}$ illustrates the decrease of the peaks related to the inner and outer ligands of the native MPC and the growth of the corresponding peaks typical of $Au_{25}(SEt)_{18}$. Interestingly, the position of the peaks does not change remarkably. Nevertheless, some $Au_{25}(SPr)_{18}$ signals slightly broaden and become more asymmetric (Figure 6.6). This phenomenon can be ascribed to the appearance of new peaks, slightly shifted with respect to the original ones. These peaks are due to the change of the chemical environment around the -SPr ligands as the exchange reaction goes on: the -SPr ligands interact with the newly introduced -SEt ligands and this changes the chemical shift of the corresponding signals. This effect is even more evident for PESH and tBuSH, as will be discussed later.

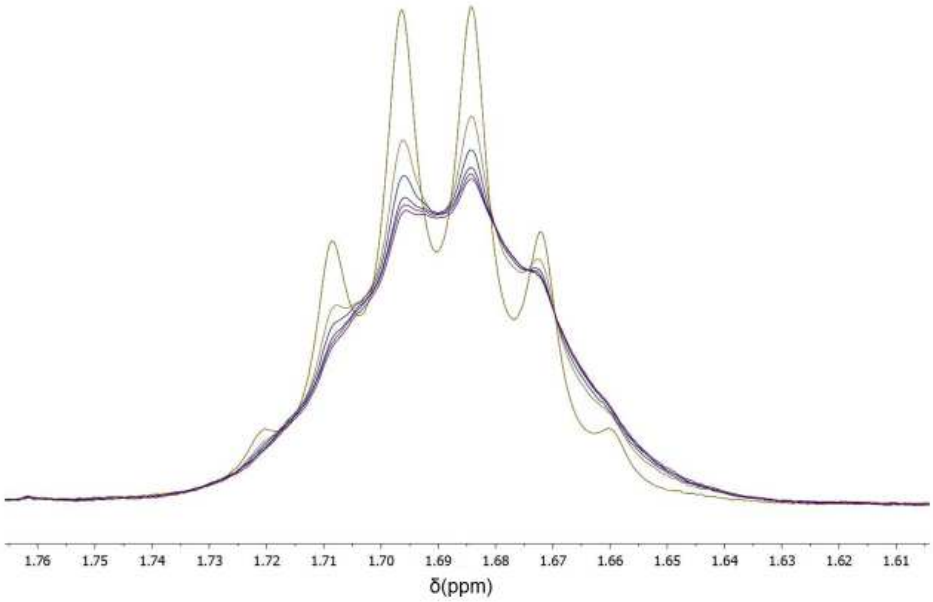

Figure 6.6. Modification of $Au_{25}(SPr)_{18}$ β-out signal with the proceeding ligand exchange with EtSH (from yellow to violet).

No further peaks are detected in the spectra relative to clusters exchanged with EtSH (and PESH, discussed further). On the contrary, some additional peaks, not related to the Au25 cluster or free ligands, appear when the reaction is carried out with tBuSH, as will be seen later. Concerning the free thiol ligands, a progressive disappearance of the resonances of free EtSH, and the corresponding increase of the peaks related to freed PrSH are observed.

To monitor accurately the extent of the exchange reaction, two couples of corresponding resonances for the endogenous and exogenous ligands are particularly suited for EtSH: for the inner ligands (SPr and SEt), $(\beta\text{-}CH_2)_{in}$ (δ 3.29) and $(\beta\text{-}CH_3)_{in}$ (δ 4.12); for the outer ligands, $(\beta\text{-}CH_2)_{out}$ (δ 1.73) and $(\beta\text{-}CH_3)_{out}$ (δ 1.19). Also the signals of the two free ligands were monitored: β for EtSH (δ 0.95) and γ for PrSH (δ 0.72). In the case of signal overlaps, these were corrected by subtracting suitably weighted integrals of clean signals.

While the NMR resonances of $Au_{25}(SPr)_{18}$ were already identified previously (see Chapter 3), this was not the case for signals of PESH and tBuSH bond to the cluster. Therefore, first of all, the identification of the signals and their attribution to the corresponding proton groups had to be performed.

The signals of the PESH ligands bond to the cluster were identified by an accurate analysis of the evolution of all the signals visible in the 1D ^{1}H spectra recorded during the reaction (Figure 6.7) and the 2D COSY (Figure 6.8) and TOCSY (Figure 6.10) spectra.

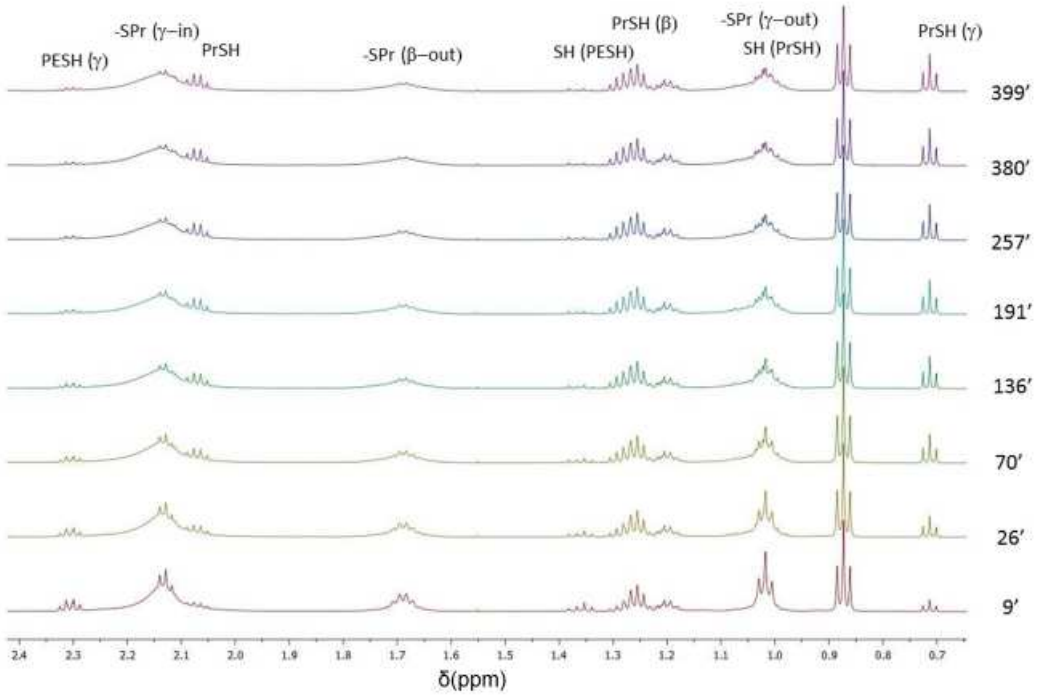

Figure 6.7. Evolution of a portion of the NMR spectra during the ligand exchange reaction of $Au_{25}(SPr)_{18}$ with PESH (from red to violet).

Concerning the out-α signal at 5 ppm, other three signals partially overlapping to it appear as the reaction proceeds, one at lower and two at higher fields (Figure 6.8a). While the out-α signal of the pure $Au_{25}(SPr)_{18}$ cluster decreases, as expected, the other three signals increase during the reaction.

From the COSY spectrum in Figure 6.8 we see that the two signals at both sides of the -SPr out-α signal correlate with the -SPr out-β signal. They are attributed to -SPr out-α protons of partially exchanged $Au_{25}(SPr)_{18}$, interacting with nearby ester ligands, similarly to what was observed for the cluster partially exchanged with EtSH. However, whereas for the latter it appears only as a line broadening and distortion, here the two new peaks are more separated and can be distinctly observed, indicating a stronger interaction between adjacent ligands. Instead, the signal at higher field (5.2 ppm) correlates with another signal at about 2.45 ppm, which doesn't appear in the pure $Au_{25}(SPr)_{18}$ spectrum (Figure 6.8).

Therefore, these two signals are attributed respectively to out-α and out-β -PESH protons bond to the cluster.

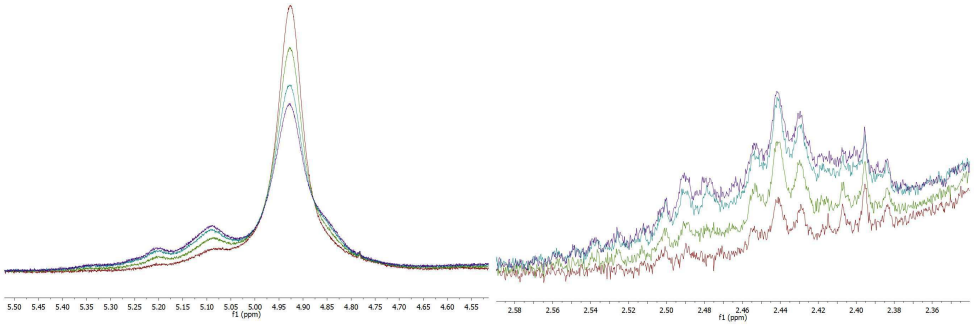

a **b**

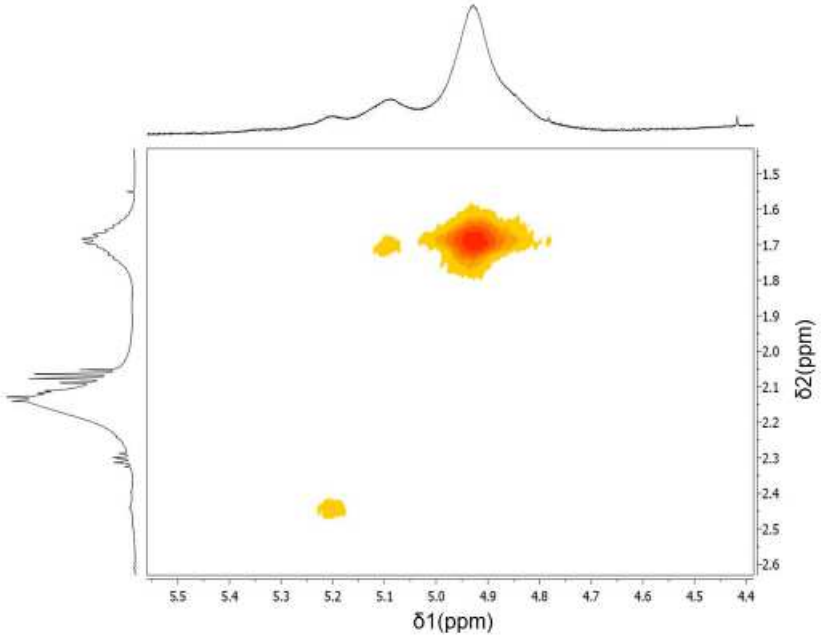

c

Figure 6.8. Evolution of the 1D NMR -SPr out-α (a), -SPr out-β (b); portion of the COSY spectrum of $Au_{25}(SPr)_{18}$ partially exchanged with 2 equiv. of PESH after 18 hours (c).

The -SPr out-β signal at 1.69 ppm, originally a sextet, decreases, broadens and becomes more complex during the exchange reaction (Figure 6.9). This is also due to the –SPr ligands interacting with the bonded ester ligands, as for the correlated -SPr out-α signal and for the cluster exchanged with EtSH.

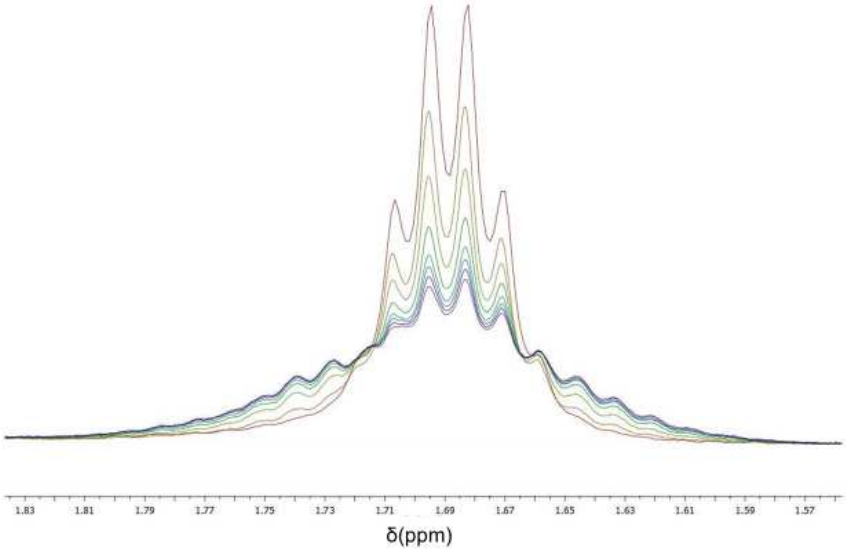

Figure 6.9. Evolution of $Au_{25}(SPr)_{18}$ β-out signal with the proceeding ligand exchange with PESH (from red to violet).

These attributions were also confirmed by TOCSY (Fig. 6.10): whereas the signals attributed to –PrSH out-α bond to the cluster show two correlations, with out-β and out-γ, the signal attributed to the out-α ester protons shows only one correlation with out-α protons. This is in agreement with the fact that PESH ligands have no γ protons.

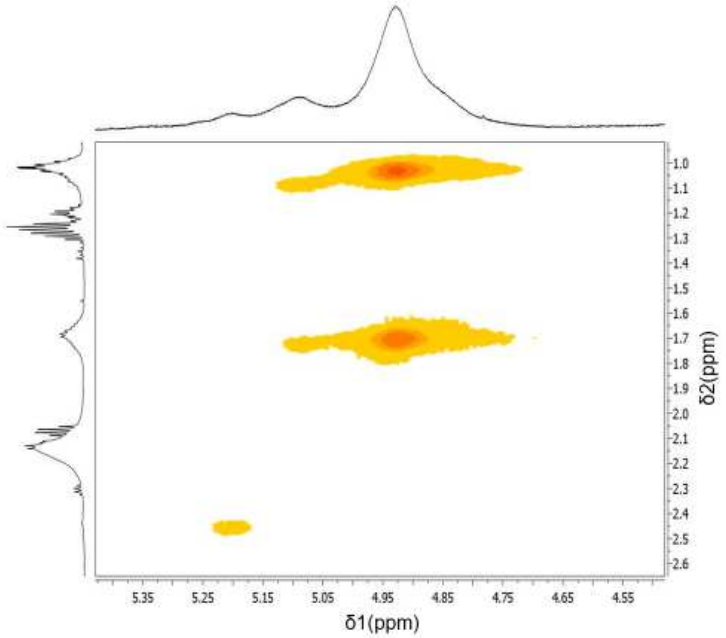

Figure 6.10. Portion of the TOCSY spectrum of $Au_{25}(SPr)_{18}$ partially exchanged with PESH (with 2 equiv. after 18 hours).

Concerning the group of resonances around 3.4 ppm (Figure 6.11), while the -SPr in-β signal decreases in time, a shoulder appears at a slightly higher field (about 3.43 ppm) and then increases as the reaction goes on. It was attributed to the in-β protons of the ester bond to the cluster.

At lower fields (at about 3.2 ppm), together with the -OCH_3 signal of the free ester, there is a group of signals appearing and increasing in time. These resonances can be attributed to the -OCH_3 protons of the ester ligand bond to the cluster and interacting with other ligands next to it. It is most probably due to an overlap of out and in -OCH_3 protons.

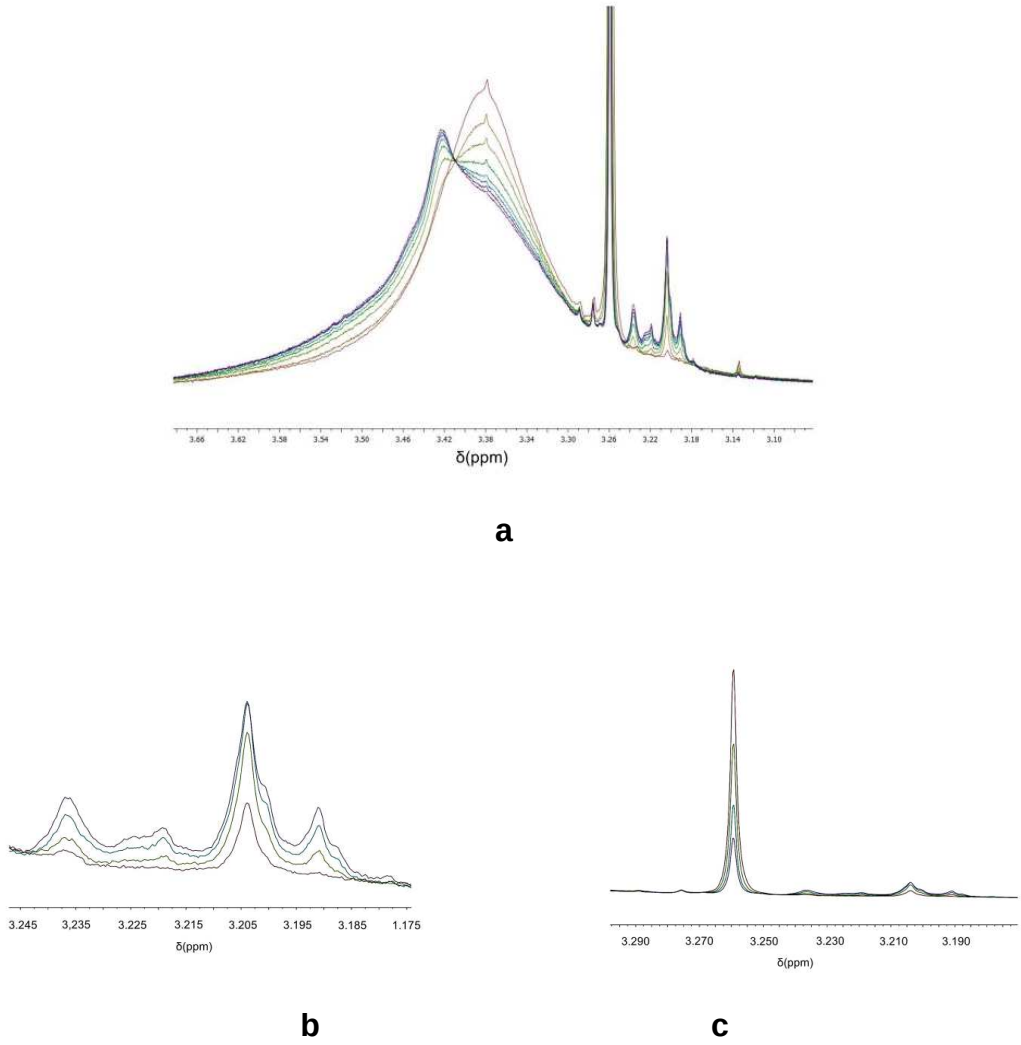

Figure 6.11. Time evolution of the signals of $Au_{25}(SPr)_{18}$ partially exchanged with PESH around 3.2-3.4 ppm with the proceeding of the reaction (from red to violet): -SPr in-β (a), -PES in-β (b) and -OCH_3 in and out (c).

In summary, the attributions for the PESH ligand bonded to the cluster are the following: 5.2 ppm - out-α; 2.45 ppm: out-β; 3.43 ppm - in-β; 3.2 ppm - -OCH_3. The out-α signal is most likely overlapping to the out-α signal of -SPr, as it happens for all the other ligands. For the kinetic analysis, the out-β (-PES) and out-β (-SPr) signals were used for the outer ligands, as well as the in-γ (-PES) and the γ resonance of the PrSH free ligand. The overlapping signals were corrected by means of proper subtractions, as in the case of EtSH.

In Figure 6.12 the evolution of some selected resonances during the exchange with tBuSH is illustrated. For the identification of the signals of the signals of tBuSH bond to the cluster, HMQC and HMBC spectroscopies were used (Fig. 6.13).

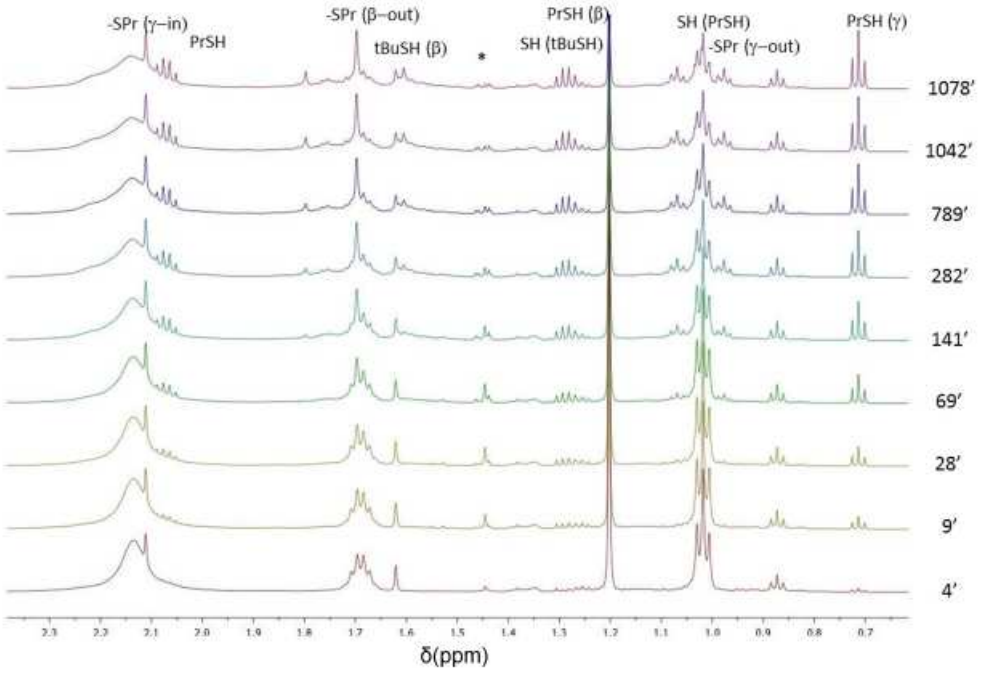

Figure 6.12. Evolution of a portion of the NMR spectra during the ligand exchange reaction of $Au_{25}(SPr)_{18}$ with tBuSH (from red to violet) The signal corresponding to a possible by-product is marked by an asterisk.

It is clear from the HMQC spectrum of $Au_{25}(SPr)_{18}$ partially exchanged with tBuSH (blue) that there is a signal (apparently a singlet) overlapping to the $Au_{25}(SPr)_{18}$ out-β resonance, at 1.7 ppm (^{1}H), 44 ppm (^{13}C). Since this signal apparently increases during the exchange

process, and since there is no such correlation in the $Au_{25}(SPr)_{18}$ HMQC spectrum (red), it is attributed to the tert-butylthiol bonded to the cluster.

This is confirmed by the HMBC spectrum (Fig. 6.13), in which the correlation of the tBu proton group (δ=1.7 ppm) with the alfa carbon is observed (δ=62 ppm). This attribution is compatible with the fact that the correlation does not appear in the HMQC spectrum, since there are no directly bond protons, and in the spectra of the pristine $Au_{25}(SPr)_{18}$ cluster, in which there is no quaternary carbon.

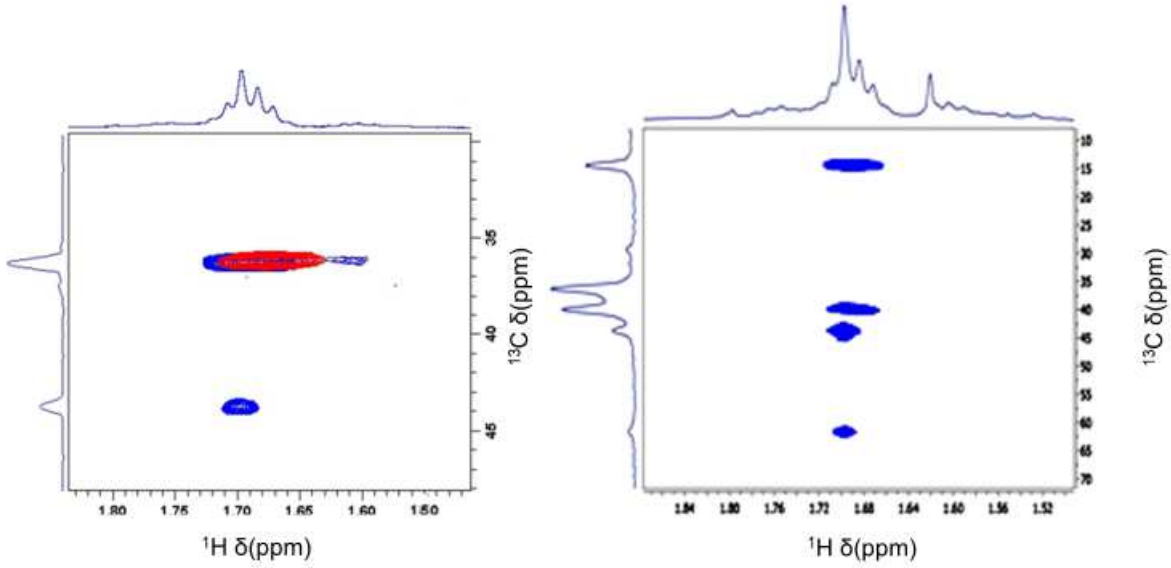

a **b**

Figure 6.13. Portion of the HMQC (a) and HMBC (b) spectra of $Au_{25}(SPr)_{18}$ partially exchanged with tBuSH (with 2 equiv. after 18 hours).

The inner -tBuS signals were not identified from the 1D and 2D NMR spectra. This is an indication of the fact that probably this ligand does not exchange in the inner position.

Another feature of the 1D ^{1}H NMR spectra is the presence of two signals at both sides of the -SPr in-α (4.93 ppm) in-β (3.39 ppm) and in-γ (1.03 ppm) resonances (Fig. 6.14). These signals increase during the exchange process, and thus they can be attributed to partially exchanged $Au(SC_3H_7)_{18}$ cluster. They are due to the same proton group (-SPr in-γ and in-α) with slightly different chemical shifts due to the presence of the sterically hindered -StBu ligands near to it, in particular, most probably to dipolar interactions with the near tBu protons. A shoulder at 3.5 ppm, near to -SPr in-β signal, growing as the

exchange reaction goes on, is most likely due to the same phenomenon. A similar but much less pronounced effect was observed for the exchange with EtSH and PESH as well.

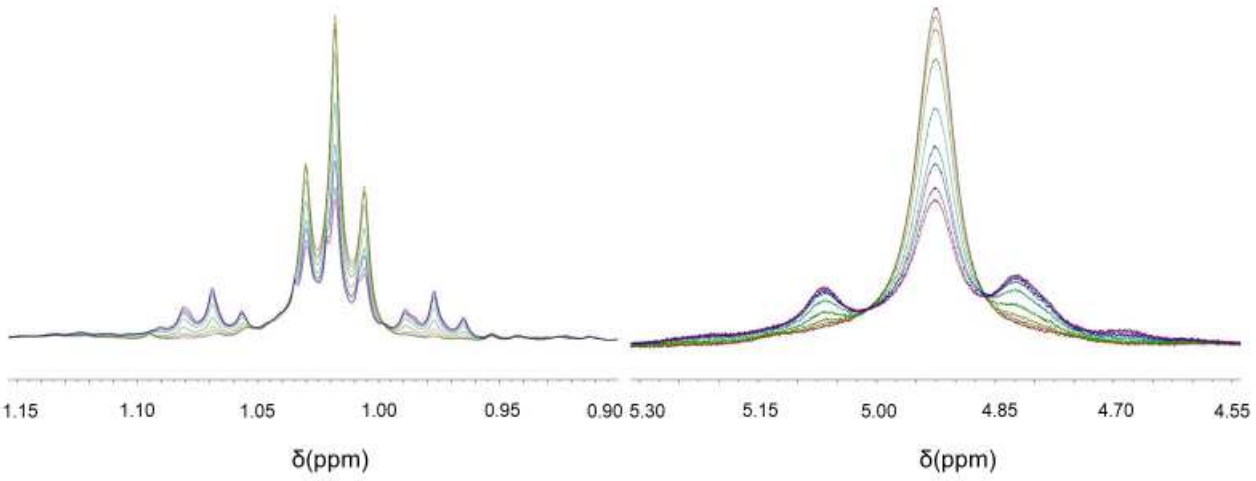

Figure 6.14. Modification of the out-α, out-β and in-γ -SPr signals of $Au_{25}(SPr)_{18}$ partially exchanged with BuSH with the proceeding of the reaction (from red to violet) due to the interactions with adjacent ligands.

As aforementioned, in this case several signals appear and vary during the reaction, which are not associated to Au_{25} clusters or free ligands, such as the group of resonances around 1.45 ppm, marked with an asterisk in figure 6.12. These signals are most probably due to the formation of new species, different from Au_{25}, whose presence was already evidenced by the MALDI spectra.

After the signals assignment, the following resonances were chosen for the kinetic analysis: out-β (-StBu) and out-γ (-SPr) and the usual γ signal of the PrSH free ligand. The signals relative to the inner ligands were not analysed, since, as already mentioned, their integrals do not decrease during the reaction.

6.2.3. Kinetic analysis of the NMR and MALDI data.

For the kinetic analysis, we used a model in which all possible substitution patterns are considered. This procedure is thus based on considering each cluster of the family $Au_{25}(SPr)^{in}_{12-n}(SPr)^{out}_{6-m}$ $(SR)^{in}_{n}(SR)^{out}_{m}$, where the subscripts "in" and "out" have the usual meaning, n = 0, 1,... 12, and m = 0, 1,...6. The total number of species in solution is thus given by the two thiols, PrSH and the exogenous thiol RSH, and 91 possible MPCs. All

exchange reactions are considered as second-order reactions (first order in both the MPC and the thiol) and reversible, with rate constants that depend on the exchange site (in or out) and the specific thiol, but not on the extent of exchange. Hence, we define the following rate-constant values: $(k_{in})_{EtSH}$, $(k_{in})_{PrSH}$, $(k_{out})_{EtSH}$, and $(k_{out})_{PrSH}$. The first few reactions, exemplifying the whole set of reactions considered are the following:

$$Au_{25}(PrS)_{in12}(PrS)_{out6} + EtSH \rightleftharpoons Au_{25}(PrS)_{in11}(PrS)_{out6}(EtS)_{in} + PrSH$$

$$k_{+1} = k_{in(EtSH)1} \quad k_{-1} = k_{in(PrSH)1}$$

$$Au_{25}(PrS)_{in12}(PrS)_{out6} + EtSH \rightleftharpoons Au_{25}(PrS)_{in12}(PrS)_{out5}(EtS)_{out} + PrSH$$

$$k_{+1} = k_{out(EtSH)1} \quad k_{-1} = k_{out(PrSH)1}$$

$$Au_{25}(PrS)_{in11}(PrS)_{out6}(EtS)_{i} + EtSH \rightleftharpoons Au_{25}(PrS)_{in10}(PrS)_{out6}(EtS)_{i2} + PrSH$$

$$k_{+1} = k_{out(EtSH)2} \quad k_{-1} = k_{out(PrSH)2}$$

$$Au_{25}(PrS)_{in11}(PrS)_{out6}(EtS)_{in} + EtSH \rightleftharpoons Au_{25}(PrS)_{in11}(PrS)_{out5}(EtS)_{in}(EtS)_{out} + PrSH$$

$$k_{+1} = k_{out(EtSH)1} \quad k_{-1} = k_{out(PrSH)1}$$

$$Au_{25}(PrS)_{in12}(PrS)_{out5}(EtS)_{in} + EtSH \rightleftharpoons Au_{25}(PrS)_{in11}(PrS)_{out5}(EtS)_{in}(EtS)_{out} + PrSH$$

$$k_{+1} = k_{out(EtSH)1} \quad k_{-1} = k_{out(PrSH)1}$$

$$Au_{25}(PrS)_{in12}(PrS)_{out5}(EtS)_{in} + EtSH \rightleftharpoons Au_{25}(PrS)_{in12}(PrS)_{out4}(EtS)_{in}(EtS)_{out2} + PrSH$$

$$k_{+1} = k_{out(EtSH)2} \quad k_{-1} = k_{out(PrSH)2}$$

…

where k_{+1} and k_{-1} are the kinetic constants of the direct and reverse reactions respectively. Importantly, our kinetic model takes into account the statistical factor. This is because the probability of exchanging an endogenous ligand decreases as more exogenous thiol is introduced into the monolayer. The probability of exchanging the i-th ligand is equal to (12+1-i)/12 for the inner and to (6+1-i)/6 for the outer ligands. Within the formalism introduced above: for i>1, $k_{in\ i}=[(13-i)/12]k_{in\ 1}$, $k_{out\ i}=[(7-i)/6]k_{in\ 1}$. For example, the probability of exchanging the forth ligand of the same ligand type decreases to 9/12 (inner ligands) or 3/6 (outer ligands) of the value corresponding to the first substitution. A set of differential equations describing the time variation of the concentration of the 93 species was written and solved with a Matlab code written ad hoc. The time variations of the integrals of NMR resonances corresponding to inner and outer cluster-bond ligands were fitted and the aforementioned kinetic constants were thus obtained. The so-determined *k* values were

then used to fit the variation of the triplets of the methyl groups of free exogenous (decreasing) and endogenous (increasing) ligands. We note that these resonances alone could not be used for the kinetic analysis because they do not discriminate the specific ligand type causing their change in time. Whereas the NMR signals corresponding to the thiolates are sensitive to the ligand type, MALDI-TOF is not. However, whereas NMR only shows the average extent of exchange, MALDI-TOF provides insights into the actual distribution of exchanged clusters. We thus used the relative MALDI-TOF intensities to test whether the observed *k* values could be validated in terms of reproducing the poly-substitution pattern as a function of time. This comparison was used as an indication of the validity of our model to describe the kinetics of ligand-place exchange for the specific reaction

For the exchange reaction with PESH, we were able to fit the kinetic traces of all the chosen signals with one set of kinetic constants (Figure 6.15).

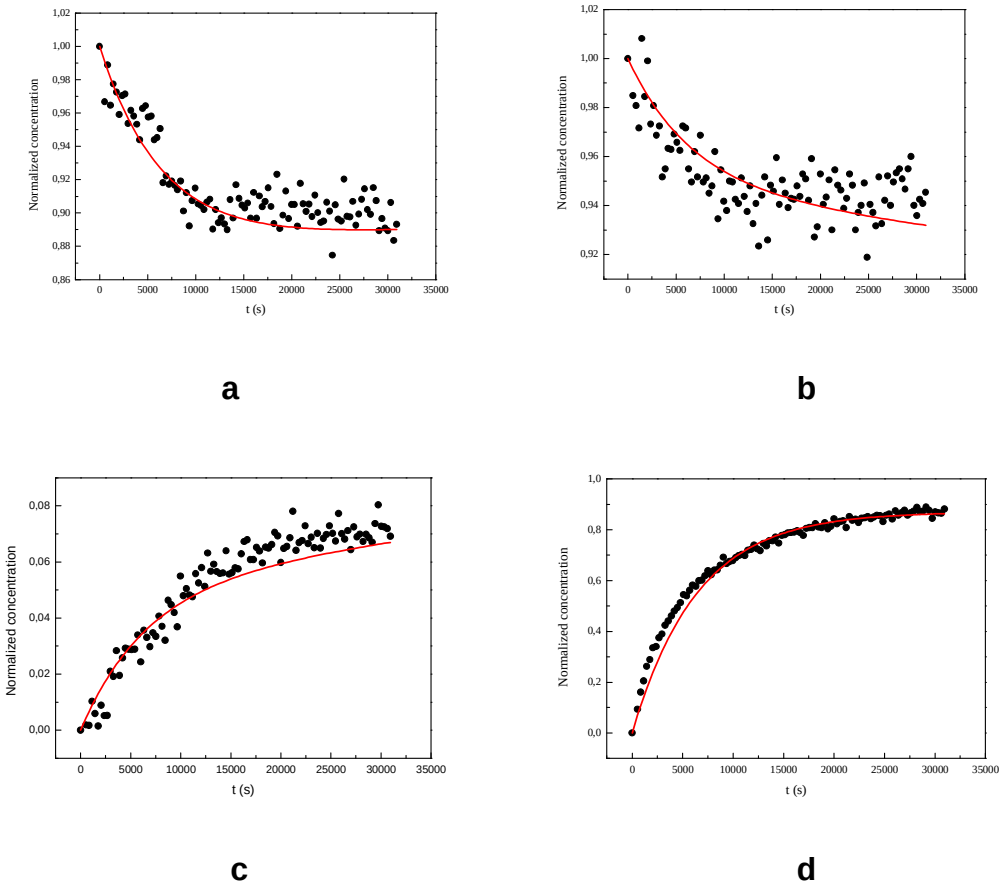

Figure 6.15. Time evolution of normalized integrals of NMR –SPr out-β, -SPr in-γ, -PES out-β and PrSH γ signals (black dots) with corresponding simulations (red lines).

Moreover, the results were perfectly consistent with the MALDI data. Using the kinetic constants obtained from the fitting of the NMR integrals vs time, the fractions of each of the polysubstituted clusters were calculated, as well as the fraction of the reacted ligand. The values calculated in such way are in perfect agreement with those obtained from the MALDI spectra, as shown in Figure 6.16.

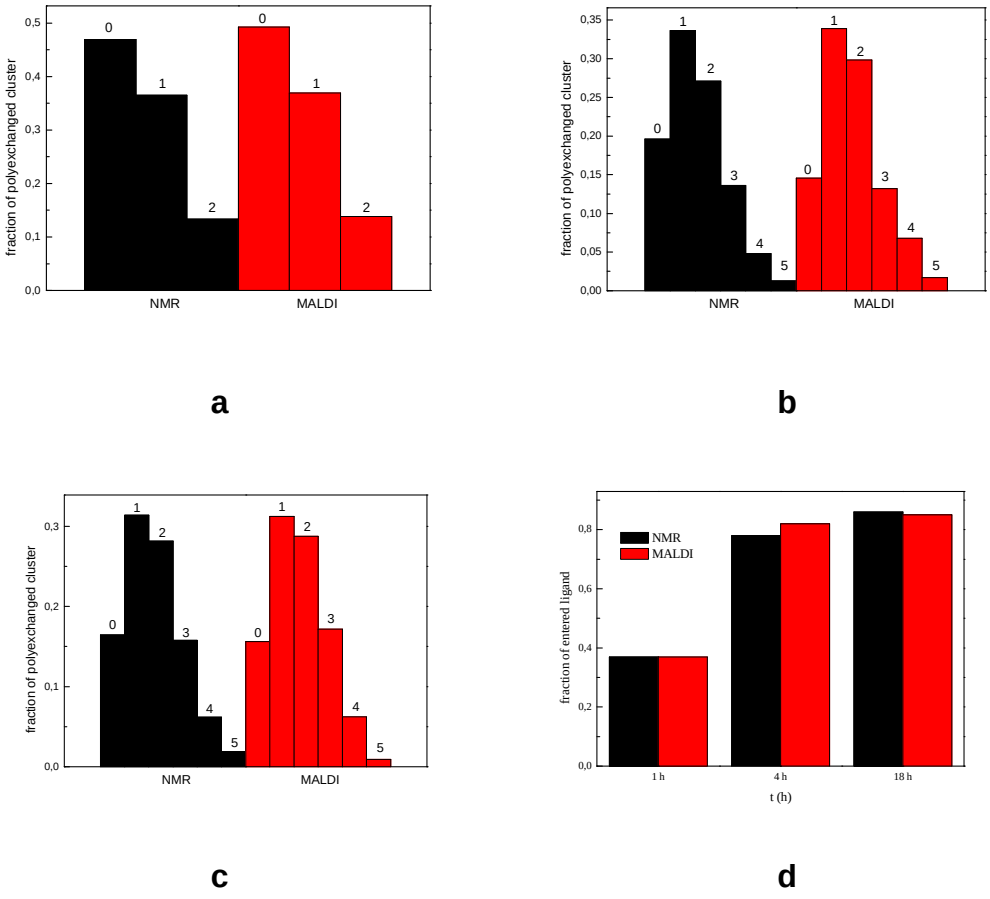

Figure 6.16. Comparison of the polyexchange patterns from MALDI and simulations, based on NMR-derived kinetic constants, after 1 h (a), 4 h (b) and 18 h (c) and of the fraction of ligand entered during the exchange reaction with PESH (d). The numbers indicate the number of exchanged ligands.

Instead, some incongruences were encountered for the reaction with EtSH. Since this reaction turned out to be slower, in was carried out for a longer time, compared to the reaction with PESH, in order to reach the equilibrium. For the exchange with this ligand, the kinetic traces of SPr-in and SPr-out could not be well simulated by the ligand exchange mechanism we considered. In fact, as shown in Fig. 6.17, the integrals of these signals indefinitely increase at long reaction times, from about 20000 s on. Moreover, the

evolution of these signals is not in accordance with other NMR signals (SEt-in, SEt-out and the -CH_3 signals of the free EtSH and PrSH ligands). These signals are also affected by another anomaly: their decrease at the beginning of the reaction appears to be much faster than the variation of both the –SEt and the free ligands. Also the agreement with the MALDI data is somewhat worse, compared to the PESH kinetics (Figure 6.19).

These two phenomena can not be explained in the framework of a simple ligand exchange process, without invoking any other chemical or physical phenomenon affecting the concentration of the species or the signal intensities. Indeed, according to the associative mechanism we hypothesized, which perfectly describes the reaction with PESH, one would expect all the signals to change with the same rate and eventually reach equilibrium at the same time.

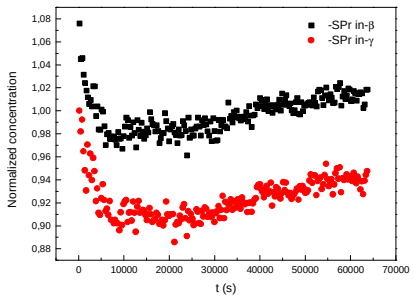

a

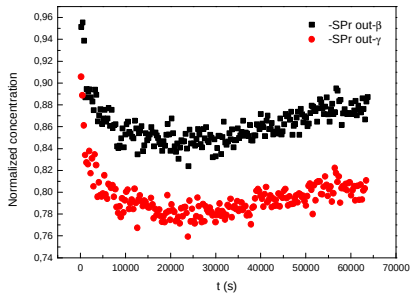

b

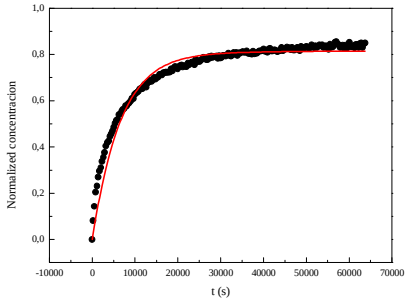

c

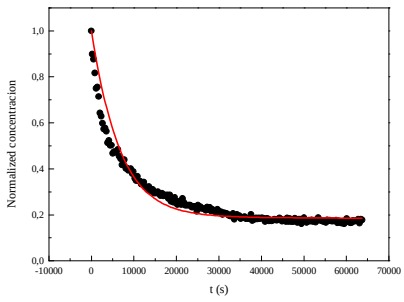

d

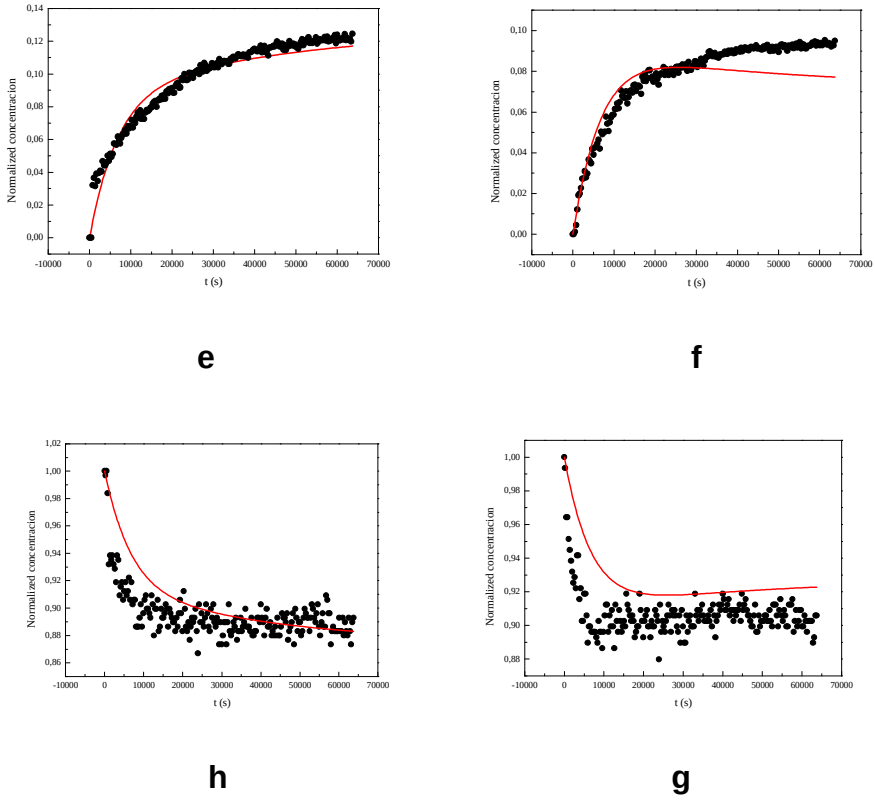

Figure 6.17. Time evolution of the integrals of NMR –SPr in-β, -SPr in-γ (a), -SPr out-β and -SPr out-γ (b) signals. Time evolution of normalized integrals of NMR PrSH γ (c), EtSH β (d), –SEt out-β (e), –SEt in-β (f), –SPr out-β (g) and –SEt in-β (h) signals (black dots) with corresponding simulations (red lines).

There are different possible explanations for the unusual behavior of these signals: the first one is that ligand exchange follows a different mechanism, possibly competitive with the associative one. This could be a dissociative mechanism, which is in contrast with the more commonly accepted associative mechanism hypothesis. Since the model used for the simulations is based on the latter, our approach would not allow to satisfactorily reproduce the reaction kinetics. Moreover, a dissociative mechanism can lead to the formation of by-products or intermediates, whose NMR signals may overlap to those of $Au_{25}(SPr)_{18}$ and whose concentration change during the reaction, thus altering the kinetic traces.

A possible mechanism is suggested here, which could rationalize the much faster experimental decrease of the cluster -SPr signals, compared to the increase of the cluster –SEt signals. This can not be explained with a purely associative second order mechanism assumed in our simulations, in which case the two rates must be

approximately equal and is one of the reasons why the experimental data could not be well reproduced.

This mechanism is based on the one suggested by Murray et al.[35] to explain the ligand exchange kinetics they observed for larger Au MPCs (with a core diameter of about 1-2 nm) in presence of oxygen and it involves a reactive $Au(SR)^+$ intermediate. Recently metal exchange was observed for $Au_{25}(SR)_{18}$, suggesting that this mechanism is possible for these clusters as well.[36]

$$Au_{25}(SR)_{18} \rightleftharpoons Au_{24}(SR)_{17}^- + Au(SR)^+$$
$$Au(SR)^+ + R'SH \rightleftharpoons Au(SR')^+ + RSH$$
$$Au_{24}(SR)_{17}^- + Au(SR')^+ \rightleftharpoons Au_{25}(SR')_{18}$$

The first step is a dissociation. However, it is not the PrSH ligand to dissociate, but the $Au(SPr)^+$ complex, which does not contribute to the PrSH signal. PrSH and EtSH are only involved in the second step instead and this is in agreement with the fact that their rates are equal.

A simulation (Figure 6.18) performed assuming one ligand exchange with this mechanism actually shows that the decrease rate of -SPr is higher than –SEt decrease rate, while the rates of the free thiols PrSH and EtSH are approximately equal, in accordance with the experimental data.

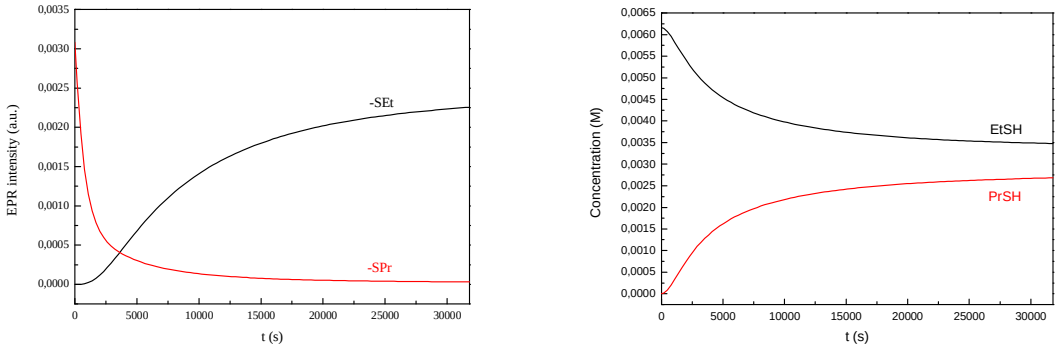

a b

Figure 6.18. Calculated time evolution of –SEt, -SPr (a), EtSH and PrSH (b) concentrations based on the dissociative mechanism explained in the text, considering the exchange of one single ligand.

Another possible reason for the appearance of the drifts is the following: the unexpected variations of the integrals is not due to the concentration changes, but to the variation of the intrinsic integral of the single proton. This could be due to the changes of electron and spin density around the ligand protons, which can lead to variations of relaxation times, which in turn determine changes in linewidth and intensity (see Chapter 2).

None of the two hypotheses can be completely ruled out. Therefore, both these phenomena can contribute to the observed discrepancies.

To overcome these problems, the drifts were empirically corrected and the kinetic analysis was limited to 4 hours for the most critical signals. For such short times, the effects described above should be negligible.

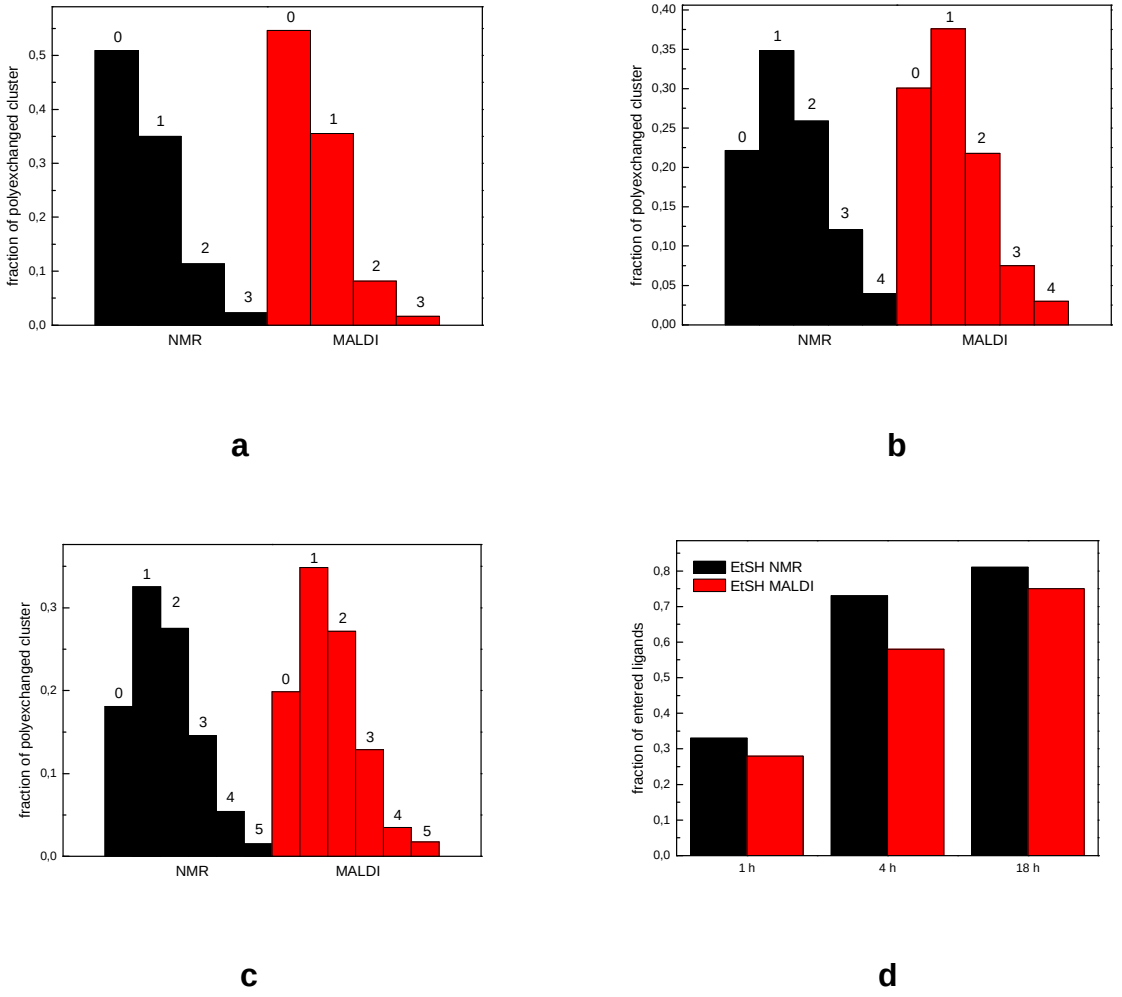

Figure 6.19. Comparison of the polyexchange patterns from MALDI and simulations, based on NMR-derived kinetic constants, after 1 h (a), 4 h (b) and 18 h (c) and of the fraction of ligand entered during the exchange reaction with EtSH (d). The numbers indicate the number of exchanged ligands.

Despite these corrections, the fitting of the different kinetic traces is still not as good as in the case if PESH. In particular, the experimental traces corresponding to the $Au_{25}(SPr)_{18}$ signals are still not well reproduced. Moreover, the comparison with the MALDI data shows that the kinetic analysis based on NMR slightly overestimates the reacted fraction of the ligand (Figure 6.19). This again demonstrates that to satisfactorily describe the reaction in this case, other phenomena must be taken into account, such as those described above, i.e. the variation of nuclear magnetic relaxation or another exchange mechanism. This overestimation also suggests that the -SEt signals are probably affected by the drifts as well. For these reasons, the kinetic constants obtained for this reaction are somewhat approximate. Nevertheless, they can still be used for comparative analysis, and, in particular, to compare the exchange rates of inner and outer positions.

Concerning the kinetics with tBuSH, we observed a completely different situation: as mentioned before, a group of unidentified signals appears while the reaction goes on. From the in-depth analysis of the 2D HMQC and HMBC spectra, it turns out that these signals are not associated to the exchanged Au_{25} cluster. They are therefore most probably due to reaction intermediates or by-products, possibly corresponding to different clusters, other than Au_{25}. The decomposition of the Au core and the formation of other products is also suggested by the changes in the UV-vis spectrum of the exchanged cluster, compared to the *pristine* one (Figure 6.20). These variations were not observed for the other two reactions: after the exchange with both EtSH and PESH the UV-vis spectra were identical to those recorded before the reaction.

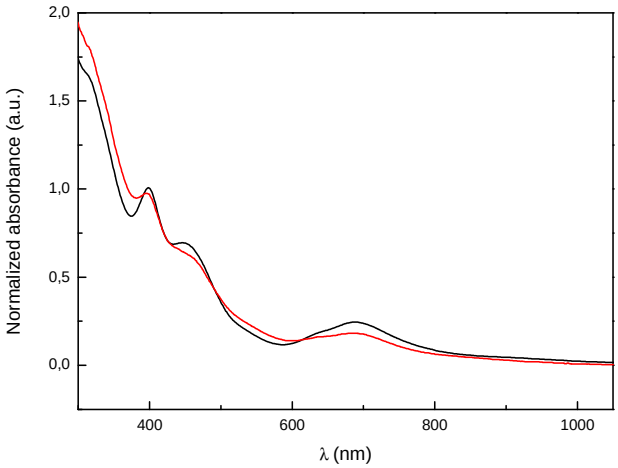

Figure 6.20. UV-vis absorption spectra of $Au_{25}(SPr)_{18}$ before (black) and after (red) 18 hours of ligand exchange reaction with 2 eq. of tBuSH.

Furthermore, an additional and most striking evidence of the formation of new clusters, different from $Au_{25}(SR)_{18}$, comes from the MALDI spectrum: After 18 h of exchange, a series of peaks appear at high masses, which cannot be assigned to a Au25 cluster (Fig. 6.4b). The first, strongest peak is around 6340 m/z and the mass separation between neighboring peaks is 14.03, which corresponds to $MW_{EtSH} - MW_{PrSH}$.

The reason for the instability of the $Au_{25}(SR)_{18}$ cluster with tBuSH is probably the steric hindrance of this ligand. Indeed, tBuSH is likely too much hindered to stabilize $Au_{25}(SR)_{18}$ when several such ligands are bonded, because of interactions between neighboring ligands, which we experimentally observed by NMR to be stronger in this case, compared to the other two ligands. However, it can possibly better stabilize other Au clusters, which are formed during the reaction. This is in agreement with some previous studies, suggesting that tert-butyl and similar bulky ligands with quaternary alkyls do not stabilize well $Au_{25}(SR)_{18}$ clusters. Indeed, it was shown that, adopting the procedure typically used for the synthesis of $Au_{25}(SR)_{18}$ clusters, $Au_{23}(SR)_{16}$ clusters form instead if tBuSH or similar bulky ligands are used.[37,38] It was shown, both experimentally and theoretically, that clusters protected with bulky ligands are characterized by a much higher structural and stoichiometric freedom, compared to those protected by slim alkyl chains.[39] The calculation of the masses corresponding to the possible stoichiometries compatible with the masses determined by MALDI allows us to tentatively suggest that $Au_{26}(SR)_{16}$ is formed, with one, two and three PrSH ligands substituted by tBuSH. This stoichiometry

seems quite reasonable, since this cluster is characterized by a lower ligand/metal ratio, compared to $Au_{25}(SR)_{18}$. The ligands are therefore expected to be more distanced and the steric hindrance would not prevent the cluster stabilization.

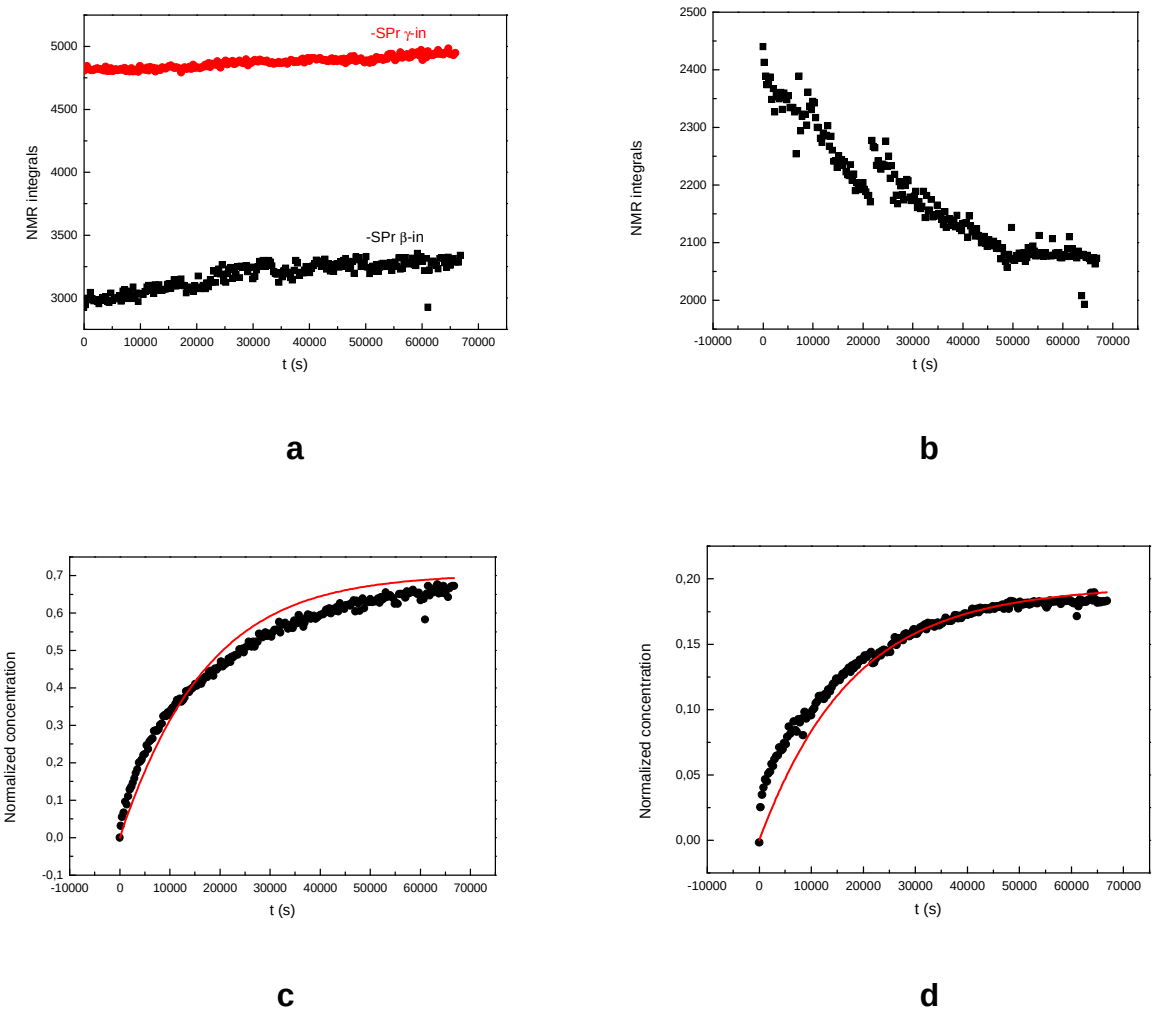

Figure 6.21. Time evolution of the integrals of NMR –SPr in-β, -SPr in-γ (a) and -SPr out-γ (b) signals and of normalized integrals of NMR PrSH γ (c) and –SPr out-β (d) signals (black dots) with corresponding simulations (red lines).

Another feature which can be immediately predicted from the visual inspection of the experimental data (Figure 6.21) is that exchange in the inner position does not seem to take place for this ligand. Indeed, while the integrals of the outer ligands decrease as the reaction goes on, the ones due to the inner ligands do not. Instead they exhibit a slight linear drift, probably due to the same causes already discussed for PESH. The drift was corrected for the cluster signals and the analysis was limited to a few, selected signals,

which do not overlap with any other product or by-product signal and are therefore the most reliable.

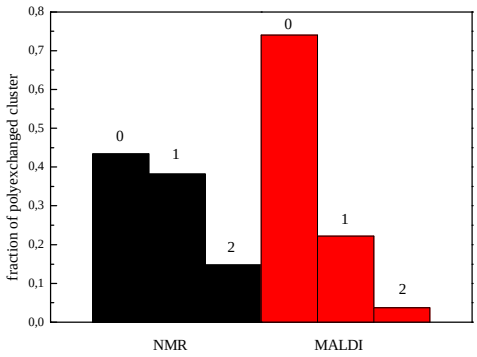

a

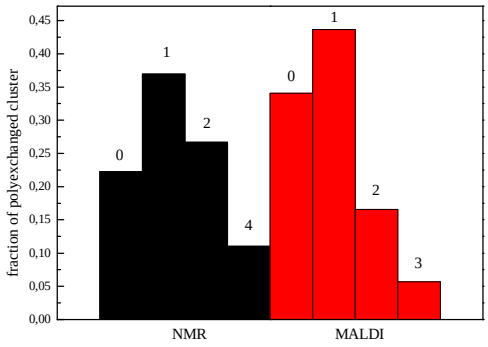

b

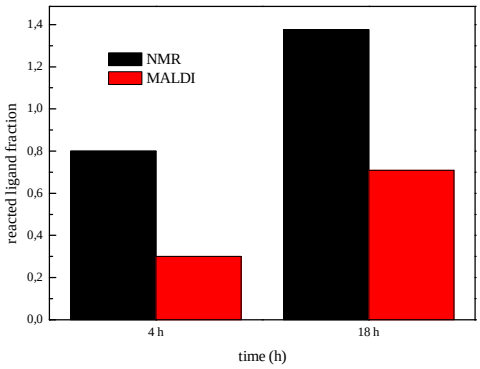

c

Figure 6.22. Comparison of the polyexchange patterns from MALDI and simulations, based on NMR-derived kinetic constants, after 4 h (a) and 18 h (b) and of the fraction of ligand entered during the exchange reaction with tBuSH (c). The numbers indicate the number of exchanged ligands.

As could be expected, for tBuSH the agreement with MALDI is even poorer, than for EtSH: in this case NMR highly overestimates the reaction degree (Figure 6.22). This is reasonable, since, as just shown, not only ligand exchange takes place, but the species present in solution also react to give rise to different by-products, detected both by MALDI and NMR. Since the MALDI measurements were performed on the quenched solutions, we can not exclude that these reactions were completed in the solid state.

Table 6.1. Kinetic constants obtained from the simulations of the ligand exchange reactions with PESH, EtSH and tBuSH. For PrSH the kinetic constants for the three reactions are reported.

	PESH	PrSH (reaction with PESH)	EtSH	PrSH (reaction with EtSH)	tBuSH	PrSH (reaction with tBuSH)
k_{in}	0.0030	0.0040	0.0021	0.0060	0.0003	0.006
k_{out}	0.0014	0.0024	0.0022	0.0034	0.0015	0.003

The kinetic constants obtained for the three reactions are summarized in Table 6.1. The data show that for PESH and EtSH the exchange rate of the inner ligands is twice the rate of the outer ligands. For EtSH the two rates are nearly identical. The fact that the inner and outer rates are virtually the same for the shortest thiol and are remarkably different for longer alkyl chains suggests that the selectivity is associated with the length of the ligand. This indicates, in turn, that the different reactivity of the two sites is mainly due to steric factors. It is conceivable that the inner and outer sites are equally accessible for short ligands, but the faster exchange in the inner position for longer ligands may seem surprising, as one could think that the inner position is less accessible than the outer one. However, the fact that the inner exchange is favored is in agreement with several previously reported results.[29,30,31] Indeed the inner site turned out to be more solvent-accessible, and so an associative mechanism is expected to lead to a preferential exchange in this position. The fact that the two rates are equal for the exchange with EtSH is in agreement with the possible contribution of a dissociative mechanism, which we considered as a possible alternative pathway. Moreover, the exchange kinetics of EtSH is slightly slower, compared to the reaction with PESH. This could be also linked to the different mechanisms involved in the two cases.

Instead, as already anticipated, the kinetic analysis for tBuSH showed that virtually only the outer position is involved in the ligand exchange. The high outer-site selectivity can be ascribed to the remarkable steric hindrance of tBuSH, which is too bulky to access the inner positions. This is confirmed by the stronger interactions between the adjacent ligands, evidenced by stronger and more separated satellite signals, compared to the other two exchange reactions. It must be stressed, that, as just showed for PESH and PrSH, ligands with relatively long, but not bulky, alkyl chains preferentially exchange at the inner position.

6.3 Conclusions

We assessed the kinetics of ligand place-exchange reactions as a function of the ligand site and of the length and bulkiness of the thiolate. The endogenous protecting thiolate was chosen to be short to make all 18 sulfur atoms of $Au_{25}(SPr)_{18}$ easily accessible by exogenous thiols. The selected exogenous thiols were of different length and steric hindrance, in order to study these kinds of effects on the ligand exchange reactions. Instrumental to this study has been the knowledge of the X-ray crystallographic structures of the clusters, the precise understanding of the NMR behavior of the paramagnetic Au_{25} clusters, and the validation of the observed rate-constant values *via* a strict comparison between the NMR and the mass-spectrometry results.

By taking into account the statistic factors in the exchange process, we were able to study the intrinsic reactivity of the inner and outer ligand positions and to understand the influence of other factors, such as the steric hindrance.

We showed that generally the inner ligands exchange significantly faster than the outer ligands and that this difference is sensitive to ligand length and steric hindrance. Very short ligands enter in the inner and outer positions with nearly equal rate. For longer linear chains, instead, the inner positions are more accessible than the outer sites and this gives rise to twice as large kinetic constant values. On the contrary, using an extremely hindered ligand, such as tBuSH, virtually only the outer ligands are exchanged. This study clearly shows that the steric hindrance of the protecting ligands strongly affects the ligand exchange kinetics in a non-trivial way. Ligand length and ligand hindrance have, therefore, opposite effects on the site selectivity. Moreover, we show that an associative ligand exchange mechanism describes very well reactions with thiols of intermediate length, such as PESH. Instead, different competitive mechanisms appear to take place both for very short (EtSH) and very bulky ligands (tBuSH). For the latter, reactions involving the metal core must be taken into account.

6.4 Experimental section

6.4.1 NMR spectroscopy.

$Au_{25}(SPr)_{18}$ was prepared using an approach previously described (Chapter 3). ^{1}H and ^{13}C NMR spectra were obtained at 3 mM MPC concentration in benzene-d_6 (100%, 99.96% d_6, Aldrich) We used a Bruker Avance DMX-600 MHz spectrometer equipped with a 5 mm

TX-1 x,y,z-gradient powered, triple resonance inverse probe operating at 599.90 and 150.07 MHz, respectively. To ensure a complete relaxation for all the resonances, integral values for the proton spectra were obtained by a pre-scan delay of 10 s. the temperature was controlled at 25.0 ± 0.1 ℃ with a Bruker BVT-300 automatic temperature controller. Chemical shifts are in ppm units (δ with reference to tetramethylsilane. The proton assignments were performed by chemical shift correlations and 2D correlation spectroscopy (COSY) and total correlation spectroscopy (TOCSY) experiments. ^{13}C chemical shift values were obtained and assigned through 2D-heteronuclear correlation experiments (heteronuclear multiple quantum coherence, HMQC and heteronuclear multiple bond coherence, HMBC).

6.4.2 Mass Spectrometry.

MALDI-TOF mass spectra were obtained with an Applied Biosystems 4800 MALDI-TOF/TOF spectrometer equipped with a Nd:YAG laser operating at 355 nm. The laser firing rate was 200 Hz and the accelerating voltage was 25 kV. Trans-2-[3-(4-*tert*-butylphenyl)-2-methyl-2-propenylidene] malononitrile (DCTB) was used as the matrix. The laser pulse intensity was kept at threshold values to avoid fragmentation of the clusters.

The clusters were dissolved in benzene containing the matrix, DCTB, to obtain 0.1 mM solutions with a 1:400 MPC/matrix ratio. 2 μl of solution were dropcasted onto the sample plate and air-dried before loading into MALDI-TOF. The spectra were recorded using the reflectron positive-ion mode. As a standard, we used $Au_{25}(SC_2H_4Ph)_{18}$, which has a MW of 7394.

6.5 References.

1. Parker, J. F.; Fields-Zinna, C. A.; Murray, R. W. The Story of a Monodisperse Gold Nanoparticle: $Au_{25}L_{18}$. *Acc. Chem. Res.* **2010**, *43*, 1289-1296.

2. Häkkinen, H. The Gold-Sulfur Interface at the Nanoscale. *Nature Chem.* **2012**, *4*, 443-455.

3. Tsukuda, T. Toward an Atomic-Level Understanding of Size-Specific Properties of Protected and Stabilized Gold Clusters. *Bull. Chem. Soc. Jpn*. **2012**, *85*, 151-168.

4. Li, G.; Jin, R. Atomically Precise Gold Nanoclusters as New Model Catalysts. *Acc. Chem. Res*. **2013**, *46*, 1749-1758.

5. Saha, K.; Agasti, S. S.; Kim, C.; Li, X.; Rotello, V. M. Gold Nanoparticles in Chemical and Biological Sensing. *Chem. Rev.* **2012**, *112*, 2739-2779.

6. Kurashige, W.; Niihori, Y.; Sharma, S.; Negishi, Y. Recent Progress in the Functionalization Methods of Thiolate-Protected Gold Clusters. *J. Phys. Chem. Lett.* **2014**, *5*, 4134-4142.

7. Templeton, A. C.; Wuelfing, W. P.; Murray, R. W. Monolayer-Protected Cluster Molecules. *Acc. Chem. Res.* **200**, *33*, 27-36.

8. Hostetler, M. J.; Templeton, A. C.; Murray, R. W. Dynamics of Place-Exchange Reactions on Monolayer-Protected Gold Cluster Molecules. Langmuir **1999**, *15*, 3782-3789.

9. Donkers, R. L.; Song, Y.; Murray, R. W. Substituent Effects on the Exchange Dynamics of Ligands on 1.6 nm Diameter Gold Nanoparticles. *Langmuir* **2004**, *20*, 4703-4707.

10. Guo, R.; Song, Y.; Wang, G.; Murray, R. W. Does Core Size Matter in the Kinetics of Ligand Exchanges of Monolayer-Protected Au Clusters? *J. Am. Chem. Soc.* **2005**, *127*, 2752-2757.

11. Heinecke, C. L. ; Ni, T. W.; Malola, A.; Mäkinen, V.; Wong, O. A.; Häkkinen, H.; Ackerson, C. J. Structural and Theoretical Basis for Ligand Exchange on Thiolate Monolayer Protected Gold Nanoclusters. *J. Am. Chem. Soc.* **2012**, *134*, 13316-13322.

12. Hadley, A.; Aikens, C. M. Thiolate Ligand Exchange Mechanisms of Au_1 and Subnanometer Gold Particle Au_{11}. *J. Phys. Chem. C* **2010**, *114*, 18134-18138.

13. Dass, A.; Stevenson, A.; Dubay, G. R.; Tracy, J. B.; Murray, R. W. Nanoparticle MALDI-TOF Mass Spectrometry without Fragmentation: $Au_{25}(SCH_2CH_2Ph)_{18}$ and Mixed Monolayer $Au_{25}(SCH_2CH_2Ph)_{18-x}(L)_x$. *J. Am. Chem. Soc.* **2008**, *130*, 5940-5946.

14. Hassinen, J.; Pulkkinen, P.; Kalenius, E.; Pradeep, T.; Tenhu, H.; Häkkinen, H.; Ras, R. H. A. Mixed-Monolayer Protected Au_{25} Clusters with Bulky Calix[4]arene Functionalities. *J. Phys. Chem. Lett.* **2014**, *5*, 585-589.

15. Knoppe, S.; Azoulay, R.; Dass, A.; Bürgi, T. In Situ Reaction Monitoring Reveals a Diastereoselective Ligand Exchange Reaction between the Intrinsically Chiral $Au_{38}(SR)_{24}$ and Chiral Thiols. *J. Am. Chem. Soc*. **2012**, *134*, 20302-20305.

16. Niihori, Y.; Matsuzaki, M.; Pradeep, T.; Negishi, Y. Separation of Precise Compositions of Noble Metal Clusters Protected with Mixed Ligands. *J. Am. Chem. Soc*. **2013**, *135*, 4946**-**4949.

17. Murray, R. W. Nanoelectrochemistry: Metal Nanoparticles, Nanoelectrodes, and Nanopores. *Chem. Rev.* **2008**, *108*, 2688-2720.

18. Lee, D.; Donkers, R. L.; Wang, G.; Harper, A. S.; Murray, R. W. Electrochemistry and Optical Absorbance and Luminescence of Molecule-like Au38 Nanoparticles. *J. Am. Chem. Soc.* **2004**, *126*, 6193-6199.

19. Antonello, S.; Holm, A. H.; Instuli, E.; Maran, F. Molecular Electron-Transfer Properties of Au_{38} Clusters. *J. Am. Chem. Soc.* **2007**, *129*, 9836-9837.

20. Venzo, A.; Antonello, S.; Gascón, J. A.; Guryanov, I.; Leapman, R. D.; Perera, N. V.; Sousa, A.; Zamuner, M.; Zanella, A.; Maran, F. Effect of the Charge State (z = **-**1, 0, **+**1) on the Nuclear Magnetic Resonance of Monodisperse $Au_{25}[S(CH_2)_2Ph]_{18}^{z}$ Clusters. *Anal. Chem.* **2011**, *83*, 6355-6362.

21. Zhu, M.; Aikens, C. M.; Hendrich, M. P.; Gupta, R.; Qian, H.; Schatz, G. C.; Jin, R. Reversible Switching of Magnetism in Thiolate-Protected Au_{25} Superatoms. *J. Am. Chem. Soc.* **2009**, *131*, 2490-2492.

22. Antonello, S.; Perera, N. V.; Ruzzi, M.; Gascón, J. A.; Maran, F. Interplay of Charge State, Lability, and Magnetism in the Molecule-like $Au_{25}(SR)_{18}$ Cluster. *J. Am. Chem. Soc.* **2013**, *135*, 15585-15594.

23. Parker, J. F.; Kacprzak, K. A.; Lopez-Acevedo, O.; Häkkinen, H; Murray, R. W. Experimental and Density Functional Theory Analysis of Serial Introductions of Electron-Withdrawing Ligands into the Ligand Shell of a Thiolate-Protected Au_{25} Nanoparticle. *J. Phys. Chem. C* **2010**, *114*, 8276-8281.

24. Guo, R.; Murray, R. W. Substituent Effects on Redox Potentials and Optical Gap Energies of Molecule-like $Au_{38}(SPhX)_{24}$ Nanoparticles. *J. Am. Chem. Soc.* **2005**, *127*, 12140-12143.

25. Holm, A. H.; Ceccato, M.; Donkers, R. L.; Fabris, L.; Pace, G.; Maran, F. Effect of Peptide Ligand Dipole Moments on the Redox Potentials of Au_{38} and Au_{140} Nanoparticles. Langmuir **2006**, *22*, 10584**-**10589.

26. Meng, X.; Xu, Q.; Wang, S.; Zhu, M. Ligand-Exchange Synthesis of Selenophenolate-Capped Au_{25} Nanoclusters. *Nanoscale* **2012**, *4*, 4161-4165.

27. Ni, T. W.; Tofanelli, M. A.; Phillips, B. D.; Ackerson, C. J. Structural Basis for Ligand Exchange on $Au_{25}(SR)_{18}$. *Inorg. Chem*. **2014**, *53*, 6500**-**6502.

28. Dainese, T.; Antonello, S.; Gascón, J. A.; Pan, F.; Perera, N. V.; Ruzzi, M.; Venzo, A.; Zoleo, A.; Rissanen, K.; Maran, F. $Au_{25}(SEt)_{18}$, a Nearly Naked Thiolate-Protected Au_{25} Cluster: Structural Analysis by Single Crystal X-ray Crystallography and Electron Nuclear Double Resonance. *ACS Nano* **2014**, *8*, 3904-3912.

29. Fernando, A.; Aikens, C. M. Ligand Exchange Mechanism on Thiolate Monolayer Protected Au25(SR)18 Nanoclusters. *J. Phys. Chem. C* **2015***, 119*, 20179-20187.

30. Hossain, S.; Kurashige, W.; Wakayama, S.; Kumar, B.; Nair, L.V.; Niihori, Y. and Negishi, Y. Ligand Exchange Reactions in Thiolate-Protected Au25 Nanoclusters with Selenolates or Tellurolates: Preferential Exchange Sites and Effects on Electronic Structure *J. Phys. Chem. C* **2016** *120* (45), 25861-25869.

31. Ni, T. W.; Tofanelli, M. A.; Phillips, B. D.; Ackerson, C. J. Structural basis for ligand exchange on $Au_{25}(SR)_{18}$. *Inorg. Chem.* **2014***, 53*, 6500-6502.

32. Pengo, P.; Bazzo, C.; Boccalon, M.; Pasquato, L. Differential reactivity of the inner and outer positions of $Au_{25}(SCH_2CH_2Ph)_{18}$ dimeric staples under place exchange conditions. *Chem. Commun.* **2015***, 51*, 3204-3207.

33. Antonello, S.; Arrigoni, G.; Dainese, T.; De Nardi, M.; Parisio, G.; Perotti, L.; René, A.; Venzo, A.; Maran, F. Electron Transfer through 3D Monolayers on Au_{25} Clusters. *ACS Nano* **2014**, *8*, 2788-2795.

34. De Nardi, M.; Antonello, S.; Jiang, D.; Pan, F.; Rissanen, K.; Ruzzi, M.; Venzo, A.; Zoleo, A.; Maran, F. Gold Nanowired: A Linear $(Au_{25})_n$ Polymer from Au_{25} Molecular Clusters. *ACS Nano* **2014**, *8*, 8505-8512.

35. Song, Y.; Huang, T.; Murray, R. W. Heterophase ligand exchange and metal transfer between monolayer protected clusters. *J. Am. Chem. Soc.* **2003***, 125*, 11694-11701.

36. Wang, S.; Song, Y.; Jin, S.; Liu, X.; Zhang, J.; Pei, Y.; Meng, X.; Chen, M.; Li, P.; Zhu, M. Metal exchange method using Au25 nanoclusters as templates for alloy nanoclusters with atomic precision. *J. Am. Chem. Soc.* **2015***, 137*, 4018-4021.

37. Das, A.; Li, T.; Nobusada, K.; Zeng, C.; Rosi, N. L.; Jin, R. Nonsuperatomic $[Au_{23}(SC_6H_{11})$ 16]- nanocluster featuring bipyramidal Au15 kernel and trimeric $Au_3(SR)_4$ motif. *J. Am. Chem. Soc.* **2013***, 135*, 18264-18267.

38. Hesari, M.; Workentin, M. S. Facile synthesis of $Au_{23}(SC(CH_3)_3)_{16}$ clusters. *J. Mater. Chem. C* **2014***, 2*, 3631-3638.

39. Crasto, D.; Barcaro, G.; Stener, M.; Sementa, L.; Fortunelli, A.; Dass, A. $Au_{24}(SAdm)_{16}$ nanomolecules: X-ray crystal structure, theoretical analysis, adaptability of adamantane ligands to form $Au_{23}(SAdm)_{16}$ and $Au_{25}(SAdm)_{16}$, and its relation to $Au_{25}(SR)_{18}$. *J. Am. Chem. Soc.* **2014***, 136*, 14933-14940.